FLOW IN LARGE-AREA NETWORK-STRUCTURED FLUIDIC FABRICS OF PERSONAL THERMAL MANAGEMENT

TANG SHENGYANG

PhD

The Hong Kong Polytechnic University

2025

The Hong Kong Polytechnic University

School of Fashion and Textiles

Flow in Large-Area Network-Structured Fluidic Fabrics of Personal Thermal Management

Tang Shengyang

A thesis submitted in partial fulfilment of the requirements

for the degree of Doctor of Philosophy

August 2024

CERTIFICATE OF ORIGINALITY

I hereby declare that this thesis is my own work and that, to the best of my knowledge and belief, it reproduces no material previously published or written, nor material that has been accepted for the award of any other degree or diploma, except where due acknowledgement has been made in the text.

(Signed)

Tang Shengyang (Name of student)

Abstract

With the advancement of human society, more activities under extreme external environments occurs such as firefighting, industrial operations, outdoor building construction, military drills, sports and space exploration. This prompts the development of personal wearable thermal management systems – an innovative multidisciplinary technology for managing body's microclimate. Fluid is a common medium used in wearable management systems. Air-conditioned clothing, water-cooled mattresses, cold/hot therapy machines, spacesuit are typical applications widely used for outdoor body temperature management.

Large-area fluidic fabric heat transfer panels, light in weight, three-dimensionally deformable and good in conformability to curvilinear shapes, are used in wearable devices for thermal management, pain management, sports and injury recovery. However, conventional fabric heat transfer panels comprising single tubes or channels with limited branches have high energy loss, low heat transfer efficiency and high latency in low-high temperature cycles across large areas in a short time span. Inspired by nature, this thesis demonstrates novel structure fluidic fabrics that can self-adjust and homogenize the flow field through an engineered network structure and guide vanes to overcome these shortcomings.

The body-mounted network-structured heat transfer panel can perform two temperatures switching in ~10 s with fast fluid velocity and uniform surface temperature mapping. This study redesigns guide vanes to make the fluid channel with only two major corners to reduce the head loss. Then reinforcement dots are added to form network structures with different parameters and allocate to four different function areas. The guide vanes and reinforcement dots together

control the flow rate at different parts and facilitate the heat transfer panel more effective heat distribution with faster flow velocity and uniform temperature mapping. Heat transfer panels for lower limbs are successfully applied to the rapid contrast therapy with temperature switching from 5°C to 40°C for fast sports recovery of elite athletes.

The fluid field in network structures of these fluidic fabrics is analysed by computational fluid dynamics simulations and flow visualization experiments. The simulation results, confirmed by flow visualization experiments, reveal three different flow regimes in network structures. They are pure laminar flow; transitional flow and turbulence dominate transitional flow. A 4-step mass transfer mechanism is proposed: (i) Velocity gradient and vorticity induced rotary mixing and elongation; (ii) Wake alternative vortex shedding induced mixing; (iii) High-pressure region splitting; (iv) Low-pressure region suction. It further explains the long-time flow field homogenization of network structure and the uniform temperature mapping of the wearable heat transfer panels.

The power loss calculations of flow field guide the manipulation of local pressure drops due to inertial and viscous forces in the transitional flow field. The calculation results obtained by energy balance equation show PL4 dominates the total power loss in pure laminar regime while PL3 in transitional flow with more turbulent factors. The two power loss types show equivalent contribution when the flow regime is transitional flow. Also, the flow regime is together affected by the network structure parameters defined as “D”, “R” and “r”. This further affects the power loss and local pressure drop of different network structures. The calculation promotes the engineering design and optimization of network-structured fluidic fabric heat transfer panels. By allocating network structure appropriately in the four function areas of wearable heat transfer panels, it finally can perform two different temperatures switching in 10 s.

Publications arising from the thesis

Referred Journal Paper

Shengyang Tang, Fuwang Zhao, Guosai Liua, Jing Yang, Ying Xiong, Lin Shu, Hui Tang, Qingyan Chen, Robert Joseph Young, Xiaoming Tao, Network-structured fluidic fabrics for wearable thermal management system. Engineering. (Under review).

Jing Yang, Ying Xiong, Jinli Piao, Manyui Leung, Guosai Liu, Mingyue Zhu, **Shengyang Tang**, Lisha Zhang, and Xiaoming Tao Wearable Fluidic Fabric with Excellent Heat Transfer Performance for Sports Recovery, Advanced Science, 2024, 2411691.

Junhong Pu, Kit-ming Ma, Yonghui Luo, **Shengyang Tang**, Tongyao Liu, Jing Yang, Jing Liu, Manyui Leung, Ruomu Hui, Ying Xiong, Xiaoming Tao, Textile electronics: manufacturing and post-processing for wearable applications, International Journal of Extreme Manufacturing, 2023, 5:042007.

Referred Patent

Xiaoming Tao, Ying Xiong, **Shengyang Tang**, Jing Yang, Mingyue Zhu, "A system for multi-cyclic rapid contrast temperature therapy", China National Invention Patent, EM/P25426CN00, 2023. (Under review)

Acknowledgements

As I reflect on the journey of my PhD studies, a myriad of captivating memories come to mind. This academic pursuit has been an incredibly enriching experience, offering moments of joy that fueled my love for learning, alongside challenges that have spurred personal growth. I am profoundly grateful to the many individuals who have offered their unwavering support and guidance throughout my academic and personal endeavors.

Firstly, I wish to extend my deepest gratitude to my chief supervisor, Professor Tao Xiaoming. Her exemplary qualities as a scientist, mentor, and educator have made her one of my most significant role models. Professor Tao's guidance has been instrumental in the development and execution of my project, illuminating my path in both the textile and dynamics fields. Her extensive expertise not only encompasses textile, electronic materials, and physics research but also the nurturing of students. The weekly group meetings, characterized by diverse and interdisciplinary discussions, have been a profound source of inspiration. I am especially thankful for the support and autonomy she provided, allowing me the freedom to innovate within my research. Her scientific insights and valuable suggestions have been pivotal to my advancement in this novel research area.

I am equally grateful to my co-supervisor, Professor Chen Qingyan from the Department of Building Environment and Energy Engineering. The stimulating discussions with Professor Chen have sparked my creativity, leading to the development of innovative ideas. His assistance with fluid dynamics simulations and experiments, coupled with his guidance in results analysis and paper revision, has been invaluable.

I owe a debt of gratitude to my colleagues in the COOLWEAR group. Special thanks to Dr. Xiong Ying, Ms. Yang Jing, Ms. Zhu Mingyue, Ms. Leung Manyui, Ms. Liu Guosai, and Mr. Jin Dian. This project was both challenging and time-consuming, yet we persevered together, overcoming countless obstacles.

The COOLWEAR technical support from the Industrial Center of the Hong Kong Polytechnic University was crucial. I am thankful to Dr. Cheung Ching-ching, Mr. Cheng Wai-leung, Mr. Yu Bun, Dr. Xiao Mingxiang, Mr. Ma Chun-ming, Mr. Tam Yau-chuen, and Mr. Ng Sai-choi for their contributions.

I also extend my appreciation to Professor Tang Hui from the Department of Mechanical Engineering for his help with flow visualization experiments, and to Dr. Zhao Fuwang and Dr. Zeng Lingwei for their support in the Water Tunnel Laboratory.

In addition, heartfelt thanks to all group members for their support in both my studies and daily life: Dr. Fang Bo, Dr. Lin Shuping, Dr. Zhang Lisha, Dr. Zhang Ziheng, Dr. Pu Junhong, Dr. Liu Su, Dr. Li Jun, Dr. Qi Bao, Dr. Liu Jin, Dr. Yang Su, Dr. Ding Xujiao, Ms. Piao Jinli, Ms. Wang Savannah, Ms. Li Ying, Ms. Ma Linlin, Mr. Liu Shirui, Mr. Wu Jingyang, Mr. Balilonda Andrew, Mr. Chen Xiaobin, Mr. Luo Heng, Ms. Ma Kitming, Mr. Wang Shuo, Mr. Luo Yonghui, Ms. Wong Kelly, Ms. Liu Tongyao, Ms. Li Ke, and Ms. Li Wenbo.

I am grateful to the review panels for their dedication and feedback throughout this process. I also appreciate the postgraduate scholarship from The Hong Kong Polytechnic University and the technical support from laboratory staff, general officers, and technicians.

Finally, I would like to express my heartfelt thanks to my family and friends for their unwavering support during my studies in Hong Kong. My parents, Mr. Cheng Shaobo and Mr. Gu Fadong have been my pillars of strength throughout this journey.

Table of Contents

List of Figures

Figure 3.13 Temperature maintenance ability testing results of thermoelectric (TE) module by attaching to COOLWEAR system. (a) Temperature vs. time during five cycles with 8 TE modules turned on, the original state of water tank in this test is 1.5 liter room temperature water mixed 1.5 liter ice in cold water tank and 3 liter 50ºC hot water in hot water tank; (b) Temperature vs. time during five cycles without TE modules, the original state of water tank in this test is 1.5 liter room temperature water mixed 1.5 liter ice in cold water tank and 3 liter 50ºC hot water in hot water tank; (c) Temperature vs. time during five cycles with 4 TE modules turned on, the original state of water tank in this test is maintained under 5ºC in cold water tank and 3 liter 50ºC hot water in hot water tank; (d) Temperature vs. time during five cycles with 8 TE modules turned on, the original state of water tank in this test is maintained under 5ºC in cold water tank and 3 liter 50ºC hot water in hot water tank.

Figure 4.1 SANDEN KS_4000T welder for making network-structured devices. By ratio-frequency welding two pieces composite fabrics of polyamide fabric laminated with a thermoplastic polyurethane film in an aluminum mold.

Figure 4.2 (a-b) Manufacturing process of the network-structured fluidic fabric were first cut out shape of layers and then adhering two pieces composite fabrics and PVC tubes by ratio-frequency welding; (c) The full leg network-structured heat transfer panel contains reinforcement dots and guide vanes for controlling the flow field inside, the two kinds of welding units formed the nature inspired network-structured wearable heat transfer panel for large area rapid thermal management; (d) The laminated fabric was soft and can be adapted to complex shapes for the purpose of wearable, the heat transfer fluid can go through the channels formed by these reinforcement dots and guide vanes to conduct large area rapid thermal management.

Figure 4.3 (a) Two-layer network structure with single fabric material; (b) Three-layer network structure with 3 kinds of fabric materials which can fill two different fluids (e.g. water and air); (c) Four-layer network structure with 3 types of materials for pneumatic actuating, anisotropy flexible fluidic fabric upside and inextensible fluidic fabric downside.

Figure 4.4 Experimental set up of the network structure device fluid field observation by an infrared camera. (a) The fluid field observation is obtained by the temperature distribution during water injection and different temperature water switching, the temperature is observed by an infrared camera on top of the network structure device. (b) Fluid control section consists of two water pumps, two flowmeters and two liquid manometers are placed at inlet and outlet.

Figure 4.5 Traditional commercial single tube wearable heat transfer panels, all the fluid channels of these wearable heat transfer panels are allocated arbitrary. (a) Water-cooling mattress; (b) Water-cooling T-shirt.

Figure 4.6 Traditional commercial single tube wearable heat transfer panel – Game Ready wrap for full leg. (a) Schematic diagram of Game Ready wrap for full leg – constructed by curved guide vanes and numerous reinforcement dots. (b) This wearable heat transfer panel contains a wide fluid channel with many reinforcement dots and turnings. (c-e) The wearable heat transfer panel is ~4.27 mm in thickness when injected with water and ~1.27 mm in thickness of welded fabrics. The diameter of reinforcement dots is ~4.28 mm.

Figure 4.7 The temperature distribution of Game Ready wrap for full leg, the outlet temperature reaches a steady state after 164s. Also, the temperature distribution of this wearable heat transfer panel is uneven due to the low flow velocity inside.

Figure 4.8 Numerical simulation calculation results of Game Ready wrap for full leg, the inlet velocity is set as 0.15m/s. (a-b) The temperature distribution at 90 s and 160 s. (c) The velocity magnitude distribution of this Game Ready wrap when the flow field is fully developed. (d) The pressure distribution of this Game Ready wrap when the flow field is fully developed.

Figure 4.9 Network structure in rivers follows the natural topology of landscape, while that of trees and capillaries are self-adjustable when one branch is blocked and can distribute fluid and mass in large area.

Figure 4.10 (a-b) Schematic diagrams of single tube/network structure fluidic fabrics filled with fluid, network fluidic fabrics contains numerous reinforcement dots for flow field manipulation with wider fluid channel. (c) The fabricated network fluid channel, fluid can pass through the channels formed by the reinforcement dots and the curved walls formed by the laminated fabrics. (d-e) The cross-section view of network structure device filled with fluid inside.

Figure 4.11 Schematic of network-structured fluid channel and electric-fluidic analogy

Figure 4.12 (a) This full leg network-structured wearable heat transfer panel showed much faster thermal management than one commercial product on sale, the heat efficiency was obviously enhanced due to fast fluid velocity inside thus less circulation time and large temperature gradient between heat transfer panel and surface skin, the outlet temperature of network-structured heat transfer panel in this work went to a stable state in 6 s and the temperature difference value between outlet and inlet is less than 3 ℃, fast fluid velocity and uniform temperature distribution means the local power loss of each part of this heat transfer

panel was in a reasonable level; (b) Outlet temperature comparison of final version of this work, FHTP with inappropriate network structure and single tube arrangement in Figure 4.27 by the same pumping system. With appropriate network structure, the final version of our FHTP showed faster thermal management, while the water took ~ 12 s to the water outlets and more than 24 s for temperature uniform distribution. The lower fluid velocity causes the outlet flow temperature to drop more slowly. Also, with the potential safety problems caused by high pressure.

Figure 4.13 Applications of the network-structured wearable heat transfer panels for thigh. (a) Demonstration of thigh experiment by thermal management system. An infrared camera was placed nearby for recording surface temperature; (b-c) Skin temperature before & after 1-min cold therapy. The heat transfer panel can effectively decrease the temperature on the thigh uniformly; (d-e) Surface temperature mapping on human body of the thigh heat transfer panel during cold therapy and the temperature switch period. This uniform heat performance can also be achieved when worn on the human body.

Figure 4.14 An athlete is using the thermal management system with network-structured calf wearable heat transfer panels for fast contrast therapy after training on field.

Figure 4.15 Rapid and uniform thermal performance of full leg network-structured heat transfer panels. (a-b) A well-designed network-structured wearable heat transfer panel for whole leg (~0.32 m^2) with 4 functional areas (FA) for the purpose of dispersion (FA1), fast transfer (FA2), connection (FA3) and large area heat transfer (FA4), appropriate control of network-structured parameters can make the heat transfer panel with fast fluid velocity,

uniform heat performance and suitable power loss; (c) Equivalent fluidic circuit diagram for network structure heat transfer panel with four functional areas.

Figure 4.16 The heat transfer panel for whole leg can be filled with water quite fast in ~6 s (V_0 = 0.8 m/s) and show uniform heat performance due to appropriate control of network-structured parameters in different parts of this wearable heat transfer panel, this fulfilled the requirement of fast contrast temperature therapy for fast recovery of athletes after training.

Figure 4.17 Numerical simulation calculation results of wearable heat transfer panel for full leg (V_0 = 1.0 m/s). (a) The velocity magnitude distribution of this wearable heat transfer panel when the flow field is fully developed; (b) The pressure distribution of this wearable heat transfer panel when the flow field is fully developed; (c) The vorticity distribution of this wearable heat transfer panel when the flow field is fully developed.

Figure 4.18 Numerical simulation calculation results of wearable heat transfer panel for full leg (V_0 = 0.5 m/s). (a) The velocity magnitude distribution of this wearable heat transfer panel when the flow field is fully developed; (b) The pressure distribution of this wearable heat transfer panel when the flow field is fully developed; (c) The vorticity distribution of this wearable heat transfer panel when the flow field is fully developed.

Figure 4.19 Temperature mapping of wearable heat transfer panel for full leg (V_0 = 0.5 m/s) at different times. It takes ~44 s for the cold water to replace the hot water.

Figure 4.20 Temperature mapping of wearable heat transfer panel for full leg (V_0 = 1.0 m/s) at different times. It takes ~10 s for the cold water to replace the hot water.

Figure 4.21 Rapid and uniform thermal performance of network-structured heat transfer panels for thigh and calf. The two well-designed network-structured wearable heat transfer panels also contain 4 functional areas (FA) as illustrated in the previous full leg wearable heat transfer panel.

Figure 4.22 Wearable heat transfer panels for thigh and calf, respectively, show uniform temperature, implying that water can be filled in 4 s (V_0 = 1.0 m/s) and 3 s (V_0 = 1.1 m/s) appropriate control of network-structured parameters can make the heat transfer panel with fast fluid velocity, uniform heat performance and suitable power loss.

Figure 4.23 Numerical simulation calculation results of wearable heat transfer panel for thigh (V_0 = 0.5 m/s). (a) The velocity/V_0 distribution of this wearable heat transfer panel when the flow field is fully developed; (b) The pressure distribution of this wearable heat transfer panel when the flow field is fully developed; (c) The vorticity distribution of this wearable heat transfer panel when the flow field is fully developed.

Figure 4.24 Temperature mapping of wearable heat transfer panel for thigh (V_0 = 0.5 m/s) at different times. It takes ~12 s for the cold water to replace the hot water.

Figure 4.25 Numerical simulation calculation results of wearable heat transfer panel for calf (V_0 = 0.5 m/s). (a) The velocity/V_0 distribution of this wearable heat transfer panel when the flow field is fully developed; (b) The pressure distribution of this wearable heat transfer panel when the flow field is fully developed; (c) The vorticity distribution of this wearable heat transfer panel when the flow field is fully developed.

Figure 4.26 Temperature mapping of wearable heat transfer panel for calf (V_0 = 0.5 m/s) at different times. It takes ~6 s for the cold water to replace the hot water.

Figure 4.27 Wearable heat transfer panels with inappropriate network structures and tube arrangements. (a) Calf heat transfer panel with an inappropriate tube arrangement; (b) Full leg heat transfer panel with an inappropriate network structure; (c) Full leg heat transfer panel with a single tube arrangement; (d-g) Calf heat transfer panel with an inappropriate tube arrangement showing poor heat transfer evenness and extremely low fluid velocity due to unreasonable head loss manipulation; (h-k) Full leg heat transfer panel with an inappropriate network structure showing extremely low water velocity and low heat transfer efficiency. Too many dots resulted in a very high pressure at the inlet and further caused water leakage; (l-o) Full leg heat transfer panel with a single tube arrangement that also shows extremely low water velocity and low heat transfer efficiency. Too much head loss at the corner also results in very high pressure at inlet and further causes water leakage.

Figure 5.1 (a-c) Schematic diagram of the three parameters (*R*, *D*, *r*) used to define the reinforcement dots arrangement and thickness of the heat transfer panel; (d) Cross-section of the inflated heat transfer panel obtained by a spatial digitizer; (e) Hexagonal unit cell definition for evaluating the power loss density and the three lines (red, green and black) for extracting the time averaged velocity.

Figure 5.2 (a-c) Grid distribution of the computation domain, the grid type used in this work is polyhedral grid, grid quantity is ~394 million with 5 layers of boundary grid; (d) Distribution of Y plus, the maximum value is less than 1.2.

Figure 5.3 Location of three monitoring points in computation domain, for the purpose of identifying the fully developed flow field.

Figure 5.19 Flow visualization of ink stream split by high-pressure region – step (iii) & (iv) (V_0 = 0.1 m/s), (a-c) marked in red showed the streamline is approaching the high-pressure region, (d-f) marked in purple and red showed the split stream line by high-pressure region and the sucked ink by low-pressure region, the stream line was finally divided into three parts.

Figure 5.20 Flow visualization of ink stream sucked by low-pressure region – step (iv) (V_0 = 0.1 m/s), the ink marked in pink was sucked by low-pressure region and the ink marked in yellow went forward, the stream line was divided into two parts.

Figure 5.21 Self-homogeneity adjusted flow field with location of high- & low-pressure area with different attack angles when V_0 = 0.1 m/s: (a,d) 0 °; (b,e) 15 °; (c,f) 30 °.

Figure 5.22 CFD time-averaged simulation results of velocity magnitude contour in the x-y plane. (a) V_0 = 0.025 m/s; (b) V_0 = 0.05 m/s; (c) V_0 = 0.075 m/s; (d) V_0 = 0.1 m/s; (e) V_0 = 0.2 m/s; (f) V_0 = 0.3 m/s; (g) V_0 = 0.4 m/s; (h) V_0 = 0.5 m/s; (i) V_0 = 0.6 m/s; (j) V_0 = 0.8 m/s; (k) V_0 = 1.0 m/s.

Figure 5.23 CFD time-averaged simulation results of pressure contour in the x-y plane. (a) V_0 = 0.025 m/s; (b) V_0 = 0.05 m/s; (c) V_0 = 0.075 m/s; (d) V_0 = 0.1 m/s; (e) V_0 = 0.2 m/s; (f) V_0 = 0.3 m/s; (g) V_0 = 0.4 m/s; (h) V_0 = 0.5 m/s; (i) V_0 = 0.6 m/s; (j) V_0 = 0.8 m/s; (k) V_0 = 1.0 m/s.

Figure 5.24 (a) Time-averaged V/V_0 magnitude contour in the x-y plane (V_0 = 0.1 m/s) and the velocity magnitude comparison of simulation and experiments results at the place marked by red broad line , regions with high velocity gradient around the dots are mixing area; (b) Time-averaged pressure coefficient (Cp) depicted the crossed layout of high- & low- pressure region (V_0 = 0.1 m/s).

Figure 6.20 Average power loss density of different parameters network structure hexagon region at each row of reinforcement dots shown in **Figure 5.1**. (a) D = 5mm, R = 15mm, r = 25mm, 5-15-25; (b) D = 5mm, R = 20mm, r = 45mm, 5-20-45; (c) D = 5mm, R = 25mm, r = 45mm, 5-25-45; (d) D = 5mm, R = 30mm, r = 45mm, 5-30-45.

Figure 6.21 Inlet pressure vs. inlet velocity of different network structures, the 5-20-25 network structure shows the low inlet pressure with relative lower water consumption (suitable parameter for FA4) while the 5-30-45 network structure shows the lowest power loss density together with relative lower inlet pressure (suitable parameter for FA1), other network structures can be used for control the mass rate of flow in other FAs for the purpose of uniform heat performance and fast velocity.

CHAPTER 1 Introduction

1.1 Background

Heat stress is a critical concern for individuals who engage in physical exertion or work in extreme climates[1], where the body's natural cooling mechanism—primarily through evaporation—is challenged[2]. This can lead to a dangerous accumulation of heat within the body, manifesting in symptoms such as cognitive impairment, profuse sweating, elevated heart rate, and an increase in core body temperature[3]. These physiological responses not only impair physical and mental performance but also pose serious risks to the cardiovascular system and overall health, potentially resulting in fatal outcomes. In work environments such as mining, construction, foundry work, horticulture, and agriculture are particularly susceptible to heat stress due to the hot conditions they often operate in, coupled with the demanding physical nature of their tasks[4]. To mitigate the adverse effects of thermal stress, strategies such as the implementation of personal thermal management systems, modification of the work environment, and regulation of work activities are essential[5]. These measures are designed to enhance the body's ability to maintain thermal equilibrium, ensuring the safety and health of individuals in heat-stressed conditions[6].

Traditional methods of environmental temperature control, such as heating, ventilation, and air conditioning (HVAC) systems, are not always efficient or practical, especially in outdoor or non-stationary contexts. Wearable systems, an emergent class of personal technology, are designed to be worn on the body, either as accessories or as part of the user's clothing. These systems, by virtue of their design and functionality, have the potential to revolutionize the way

humans interact with and adapt to external environments[7]. Wearable thermal management systems are an innovative class of technology designed to regulate the body's microclimate, providing personalized heating and cooling to the wearer. Advancements in materials science, thermoelectric components, and energy-efficient design have enabled the development of wearable devices that can provide localized temperature control[8–10]. These systems can be integrated into clothing, accessories, or standalone devices that come into contact with the skin. Wearable thermal management systems are widely applied in personal comfort, energy savings, outdoor work, wellness, military, aerospace industry, medical services and athletic performance enhancement[11]. These applications draw forth different kinds of wearable thermal management devices such as air-conditioned clothing, water-cooled mattresses/cushions, cold/hot therapy machines[12], spacesuit[13] and so on.

Fluid is a common medium in wearable systems for mass transfer, heat exchange and energy transfer. It is widely used in thermal management systems mentioned above. Fluidic fabrics with engineered network flow-channel structure, being lightweight and fluid-tight, are ideal user interface in such thermal management systems due to their mechanical strength, flexibility and adaptability for complex shapes, irregular surfaces and deformability for desired configurations by the need for comfort, unobtrusiveness, and aesthetic appeal. Fluids flowing within the fluidic fabrics act as heat-exchange agents or as load-bearing elements used in conjunction with different fabrics. They can be gases, liquids, their mixtures or even those under phase-transition[14,15]. A large variety of strong fiber materials offers excellent choices for normal and extreme operational conditions, such as extreme temperatures, radiation, chemical corrosion and high pressure[16]. The fluidic fabrics filled with fluid flow facilitate a wide range of industrial applications including aerospace[17], production in heavy industry[18], medical

and healthcare[19]. On the other hand, fluidic fabrics have been widely used in sensory stimulations of virtual reality/augmented reality applications as flexible functional components such as haptic gloves[20], pneumatic actuators[21,22], soft robotics[23,24] and programmable functional structures[25].

Fluidic fabric is a kind of composite structural material consisting of at least two layers of fluid-tight fabrics. The type and physical parameters of fabric (e.g. fabric construction, fiber material, thickness) and fluid-tight materials (e.g. adhesive membrane or coating) can be designed for numerous functional devices with multilayer fluid channels. The flow channels are formed by adhering at selected locations of two fluidic fabrics stacked together. Hence fluid can pass through the channels between the sealed dots or walls. Routes of fluid can be tuneable by selecting the positions of sealed points and shapes of dendric lines. Most wearable heat transfer panels transfer fluid just by a single channel and control the flow rate by traditional hard valves. This is not desirable to the wearable requirements of lightweight and flexibility.

Wearable fluidic devices usually have a relatively high mass flow rate with large covering area and light weight. The Reynolds number may reach ~10^4 in some parts of the fabric interior. Most previous investigations on enclosed structures like microfluidics have been confined to laminar flow with a definite volume[26], where the analogue of Poiseuille's law of fluidics and the Ohm law of electricity[27] has been used for fluid field control, by changing the channel shape and adding obstacles. Furthermore, energy efficiency is a key limiting consideration for such devices that demand light weight including batteries as the main power supplier for wearables. The conventional cumbersome single tube arrangement has a large head loss and cannot distribute fluid rapidly in a large area with uniform distribution[28]. Large energy dispersions in a moving fluid field should be avoided in devices like fluid filters[29] and

hydrofoils[30], while appropriate power loss due to turbulence flow is necessary to achieve better heat transfer efficiency in heat transfer panel[31]. Although numerous studies of oscillators[32], valves[33], logics[34] and energy sources[35,36] have enabled the development of fluid driven automatic soft robots[37,38], up to now, few have been reported on the analysis and control of interior flow fields for the fluidic fabrics in wearable systems.

Nature itself shows us that network arranged fluid channels are self-adjustable and can distribute fluid in a large area based on the balance of flow resistance caused by power loss in different dendric channels. Thus, no floods occur in regions with plentiful river systems[39,40], capillaries are self-adjusting between hot and cold environment for temperature and pressure control[41], water and nutrition can be distributed to numerous terminals by thousands of branches in a tree. The appropriate control of power loss in different parts of a network with fluid channels can effectively control the flow field for desired flow distribution with higher flow velocity. Thus, the heat performance of wearable heat transfer panels can be significantly enhanced. This work proposed a new network-structured wearable heat transfer panel with low head loss for fast and uniform flow velocity inside, and studied the mass transfer mechanism, flow field evolution and local head loss of this network structure.

1.2 Problem Statement

Wearable thermal management systems play a crucial role in a variety of extreme environments, ensuring that individuals can acquire and maintain a desired temperature despite external conditions. Water is our daily life access material with the highest specific heat capacity. It can transfer large amounts of heat during the interaction with objects of temperature gradient around.

Many heat transfer panels use water as the heat exchange medium for better heat exchange efficiency such as space suit, water cushions in wearables and cooling tower, high performance computer cooling systems in other thermal management systems. Traditional water-based wearable heat transfer panels usually have high head loss due to the single-tube arrangement with limited branches of fluid channel and relatively large density of water, which results in low flow velocity and suboptimal heat transfer capabilities, the effectiveness of these systems is often hampered by the limitations inherent in traditional wearable fluidic heat transfer panels.

The fluid needs to take more time to go through the whole circulation, this may cause poor heat transfer efficiency as the head loss is very high due to lots of turnings, corners and narrow diameter of tube inside, then the fluid velocity cannot be very high. This further cause the uneven heat exchange rate at inlet and outlet, as the temperature gradient near inlet is very large and more heat can be exchanged at this place, while the temperature gradient near the outlet is much smaller as the majority heat exchange has been conducted previously. This caused poor heat performance and imposed restrictions on increasing the total heat transfer ability of wearable heat transfer panel. To enhance the performance of wearable thermal management systems to transfer large amount of heat rapidly, several potential research areas need to be explored are listed follows:

1. **Thin, light and flexible wearable heat transfer panel with limited power supplier.**

   The soft surface of wearable heat transfer panel may burst if the inlet flow rate is forced to increase. Even though it is beneficial for better heat exchange ability since the flow contains high amount of turbulence with increased flow rate, the head loss will be quite high when the velocity magnitude is increased. The wearable thermal management

systems are worn on the human body and powered by a limited energy source (e.g. portable rechargeable batteries). Also, simply increasing the fluid volume inside wearable heat transfer panel will make the heat transfer panel heavier and too thick to be worn on human body. Safety and energy usage efficiency need to be considered first. Thus, designing a wearable heat transfer panel with less fluid consumption and higher flow rate inside can significantly enhance the heat performance and make it easier to use.

2. **Lack of comprehensive flow field analysis for wearable heat transfer panels.**

A significant knowledge gap exists in the comprehensive understanding of flow fields within wearable heat transfer panels. Also, the fluid channel of heat transfer panels in this work is brand new designed. The flow rate distribution determines the heat transfer capability in different parts of heat transfer panel, and the uniform heat performance strongly relies on the flow velocity evenness. The reinforcement dots inside not only exist for reducing water consumption, but also play the key role of flow manipulation by separating the incoming flow into two streams thus acquired the purpose of manipulating flow field by different arrangement of these reinforcement dots. This study seeks to bridge this gap through meticulous mapping and analysis of the flow field dynamics using computational fluid dynamics (CFD) simulations, complemented by experimental validation. Such detailed scrutiny is expected to unveil stagnation points or zones of inefficient heat transfer, thereby informing design modifications that optimize fluid distribution and thermal regulation.

3. **Needs for optimization of kinetic energy transfer and flow resistance.**

   The role of kinetic energy transfer during fluid circulation in wearable heat transfer panels, and its impact on system performance remains underexplored. Head loss is ubiquitous during the process of fluid moving, adding obstacles in fluid field not only can separate the incoming flow, but also causes energy dissipation then to reduce the fluid velocity. Since this work aims to make the large area wearable heat transfer panel with uniform heat performance and extreme fast temperature time, the velocity of flow inside should be fast and the flow resistance at different places ought to be meticulously controlled to make sure the uniform heat performance. This makes the head loss manipulation of reinforcement dots at different parts of the wearable very important, as low head loss can increase the fluid velocity but appropriate head loss for flow field homogenization and turbulence can improve the flow field evenness and heat convection for better heat transfer capability.

By delving into these research areas, we can develop wearable thermal management systems that offer superior heat transfer capability to individuals operating in various environments. These improvements will not only enhance personal safety but also expand the potential applications of wearable thermal management in fields such as aerospace, military operations, and outdoor sports.

1.3 Objectives

To develop the new network-structured wearable heat transfer panel with fast flow velocity inside is meaningful and important. The goal can be achieved by 1) designing network structure channel heat transfer panel with fewer corners and reinforcement dots; 2) study the flow field inside the network structure; 3) calculate and compare the local head loss of different network structures; 4) arrange different network structures at suitable regions of the wearable heat transfer panel for desired properties. The specific objectives are listed as follows:

1. **To design body-mounted heat transfer panels**

   A network structure wearable heat transfer panel will be designed which incorporates limited numbers branching channels and optimized flow paths. This could control the flow rate of different areas for heat transfer panel and facilitate more effective heat distribution with faster flow velocity. Also, developing scalable solutions that can be customized to fit different body shapes and sizes will ensure that a wider range of users can benefit from these new wearable heat transfer panels.

2. **To conduct CFD simulations, flow field visualization experiments of network structure and thermal modelling of potential application**

   Advanced computational models can help predict the performance of wearable heat transfer panels under various conditions, aiding in the design and testing process. This research will study the flow field evolution under different boundary conditions by CFD simulations and explore the mass transfer mechanism. Then the thermal modelling of a

rapid contrast therapy for human leg will be performed for the application evaluation of the network structure wearable heat transfer panel.

3. **To improve energy efficiency of the heat transfer panels**

Improving the energy efficiency of wearable thermal management systems is essential, particularly for scenarios where power supply is limited. This could involve the use of phase change materials (e.g. ice) or thermoelectric elements that leverage body heat as an external energy source. This research will employ power loss theory to conduct a comparative analysis of power loss types and magnitudes across various network structure flow channel designs. The objective is to identify configurations that minimize energy dissipation while maximizing heat exchange efficiency. This may involve the design of passive flow elements (reinforcement dots and buckling) to balance the contribution of viscosity and turbulent factors in total power loss, thereby enhancing heat transfer without necessitating an increasement in pumping power.

4. **To develop guidance for engineering design and safety**

Establishing design guidelines and safety standards for wearable heat transfer panel will be important to ensure user safety and promote widespread adoption. This research will list the general guidelines of designing different shapes of wearable heat transfer panel for the purpose of customization.

1.4 Methodology

To solve these research problems and achieve the goals of objectives, research methodology of this research ought to be listed in a comprehensive review to find out the key issues of designing rapid wearable heat transfer panel, network structure flow field analysis and flow rate control by local head loss calculation. This work adopts the following methodology:

1. **Wearable thermal management strategy selection for large area rapid temperature switch.**

   The thermal management strategy is numerous, such as air/liquid cooling, micro fans ventilation, phase change materials, etc. And they are selected based on the scenarios it will be applied, such as outdoor workers for air cooling, heavy industry workers for liquid cooling and athletes cooling garments during sports for passive cooling materials. Here this work chooses fast contrast therapy for after sports recovery of elite athletes as the scenario of designing this rapid wearable heat transfer panel. This therapy requires a high level of heat transfer and temperature switch in a large variety. By acquiring this requirement, the rapid heat transfer panel can meet the extreme thermal transfer requirement in wearables and have the potential to be applied in other areas. Based on the thermal modelling and simulation of this rapid contrast therapy, the amount of heat transfer can be roughly calculated. Then, after the most suitable strategy is selected, the control logics need to be designed for acquiring the best heat efficiency. Last, other potential strategies also need to be tested and evaluated for further improvement of the current rapid thermal management system.

2. **Design a nature-inspired network structure to acquire high flow rate for wearable heat transfer panel to perform large area rapid thermal management.**

   Inspired by nature, the network structure owns lots of advantages of distribution fluid such as large coverage area, adjustable flow rate and relatively low head loss. First, this study will redesign the fluid channel inside to reduce the large head loss at corners and turnings. Then, reinforcement dots will be added into the fluid channels to reduce the water consumption of this wearable heat transfer panel. Third, based on the previous allocation of guide vanes and reinforcement dots, three wearable heat transfer panels for the purpose of rapid temperature switch will be designed (full leg, thigh, calf). Fourth, specific simulations and experimental validation will be conducted for testing the above five rapid wearable heat transfer panels. Last, analysis on previous simulations and experiments helps give a tentative design principle on design such kind of rapid temperature switch wearable heat transfer panels.

3. **The study of network structure flow field evolution and mass transfer mechanism for explaining flow field behaviour of rapid wearable heat transfer panel.**

   The heat performance of wearable heat transfer panel strongly relies on the flow field evolution inside the fluid channel. First, the network structure parameters will be defined to describe the structure difference among them. And detailed instantaneous simulation of a specific network structure will be performed under different inlet velocity to study the fluid field evolution of network structure, the velocity field, pressure field and vorticity field will be detailed investigated respectively together with the periodic analysis of fluid field. Second, with the tentative understanding of network

structure fluid field, flow field visualization experiments will be conducted for the validation of the simulation results previous and the study of mass transfer mechanism inside the network structure. The results here will explain the fluid field behaviour of wearable heat transfer panels in the previous section. Last, the time-averaged simulation will be performed to help understand the long-time behaviour of network structure, as the heat transfer panel will be covered on human body for at least several minutes. Based on the analysis of local fluid field behaviour of network structure, we can understand the macro behaviour of heat transfer panel which is consists of hundreds of reinforcement dots and set up the foundation of the following flow field manipulation by appropriate local head loss control.

4. **Research on large area flow field manipulation by local head loss control of different network structure and the design guidance of soft heat transfer panel for different purposes.**

To do the head loss calculation of the heat transfer panel, the energy balance equation directly deduced from Navier-Stokes equations is applied in this work. First, power loss calculation of a network structure with inlet velocity from 0.025 m/s to 1 m/s will be performed, the analysis of different power loss sections is based on the flow field evolution and mass transfer mechanism analysis in previous section. This part will detailed investigate the power loss constitution with the change of inlet velocity together with the spatial distribution of different power loss type. Second, the power loss visualization of instantaneous and time-averaged flow field will be conducted to find out the power loss generating region and the triggering factor. Third, the water temperature of network structure surface and inside will be compared together with the

surface Nusselt number to evaluate the heat transfer capability of different inlet velocity. Fourth, power loss calculation will be performed on other representative network structures for comparison, the time-averaged velocity field and pressure field will be analysed first to have a general understanding of these different network structures. Then, instantaneous velocity field evolution and time-averaged power loss and surface Nusselt number map will be extracted for comparison. Fifth, a general manipulation principle of flow field for wearable heat transfer panels will be proposed and shed light on other potential applications.

1.5 Project Significance

Wearable personal thermal management system offers a novel solution by localizing climate control, thereby reducing the need for other cumbersome equipment. This thesis delves into the role of light, thin and flexible wearable heat transfer panel in providing personalized thermal regulation-focusing on the flow field manipulation analysis for enhanced heat performance. With the successful making of these three customized wearable heat transfer panels, the novel fluid channel design principle shows excellent fluid field manipulation capability. This thesis has delivered the following positive outcomes.

1. A nature-inspired network structure is proposed for wearable thermal transfer fluidic fabric devices by flow field manipulation to achieve rapid and uniform temperature with large coverage area. The nature-inspired network structure is exemplified by a rapid-contrast-therapy heat transfer panel fluidic fabric designed for fast sports recovery of elite athletes, which offers a series of temperature cycles switching from 5^{o}C to 40^{o}C in

a record short period of time in less than 10 s with uniform surface temperature covering body area, over 6 times of conventional single-tube heat transfer panel. This network-structured fluidic fabric is made by adhering two pieces of composite fabrics together with welded reinforcement dots and guide vanes, when inflated with fluid, those cylindrical dots cluster formed spatial curved walls, which forms the network-structured flow field. They are equipped with appropriate power loss control of the ratio components due to inertial and viscous forces in the transitional flow field.

2. Based on the successful making of the network-structured wearable heat transfer panel, self-adjusting fluid field and mass transfer mechanism in the network structure are further analysed for better understanding the behaviours of wearable heat transfer panels. The self-adjusting fluid field constructed by numerous curved walls formed by reinforcement dots shows the evolution details from pure laminar flow regime to turbulence dominate transitional flow regime, which reveals the fundamental interactions between the fluid and the novel network-structured fluidic fabric. It shows the similarities and differences between the flow field of the network structure and the traditional flow field around the cylinders and clarifies the basic flow situation in the network structure. The 4-step mass mixing mechanism inside the network structure was induced by cross layout of high- & low-pressure region inside the network structure flow field thus facilitates the automatic homogeneity adjusted flow field. It also unveils stagnation points or zones of inefficient heat transfer- recirculation bubble.

3. Power loss calculation results of different network structures were analysed to reveal energy transfer in the fluid circuit, and further shows the principle of manipulating fluid field. The power loss of the network structure for homogenization fluid field can be

controlled by changing their parameters, therefore the power loss components of different types are regulated for a desired purpose. The numeric simulations show the kinetic energy transfer in the fluid circuit and energy dissipation in a 4-step mass mixing process, offering engineering guide of parameter selection and optimization for the network-structured fluidic fabrics. The excellent performance of these heat transfer panels was realized by design of appropriate network structures at different parts of heat transfer panels. It helps find suitable network structure for wearable heat transfer panel with much less power loss in flow field homogenization.

This work shed new light on the development of fluidic fabric heat transfer panels. It illustrates their great potentials in other thermal management devices with large cover area such as air-conditioned clothing, thermal management system in space exploration, quick charging lithium battery in electric automobile, effective cooling of computers and other machines and so on. Through this exploration, this novel fluid field manipulation methodology may contribute to the ongoing discourse on the integration of technology with human physiology and the environment, paving the way for sustainable and inclusive technological advancements.

1.6 Structure of the Thesis

In this work, a kind fluidic wearable heat transfer panel with novel fluid channel for fast uniform fluid transfer has been developed. The content is organized in 7 chapters, with the respective focal points listed as follows:

Chapter 1 is the introduction, consisting of background description, problem statement, objectives, research methodology, project significance and thesis structure. This part gives the background and prospects of wearable thermal management systems, reveals the drawbacks of current fluidic based wearable heat transfer panels and lists the objectives for improving these drawbacks. Then, methodology for realizing these objectives is clarified and the significance of this research is stated.

Chapter 2 is a comprehensive review of wearable thermal management systems. This part first gives a brief description of wearable thermal management systems, and traditional human thermoregulation methods are stated. Following the review of mediums for thermal transfer in wearable thermal managements systems. Then, different personal thermal management strategies and capacity evaluation methods are described. Last, is the review of fluid dynamics research on traditional rigid heat transfer panel and propose the current problems and potential solutions of wearable heat transfer panel development.

Chapter 3 is the whole thermal management system feasibility evaluation. This section first calculates the heat transfer amount during the rapid contrast therapy of 5 cycles, which need extremely huge thermal transfer between skin and heat transfer panel interface. Then the potential methods for realizing this purpose are proposed and give a detailed description. Last is the exploration of other advanced methods.

Chapter 4 is the design of network structure wearable heat transfer panels for full leg, thigh, calf, knee and ankle. This section mainly focuses on the design and analysis of full leg wearable heat transfer panel. First, the general layout thinking of guide vanes is proposed and then is the arrangement of reinforcement dots. Second, is the simulation results and experiments analysis.

Third, is the application of design principle on other four wearable heat transfer panels and their simulation and experiment results analysis.

Chapter 5 is the flow field evolution and mass transfer mechanism of network structure. This part first describes the fluid field evolution of one representative network structure under different inlet velocity. Then, flow field visualization experiments are performed for simulations validation and study on mass transfer mechanism. Last, the time-averaged simulation results are presented show the long-time flow field condition of network structure.

Chapter 6 is power loss analysis of representative network structures and the propose of network structure fluid field manipulation principles. This section first lists the power loss of a representative network structure with different inlet velocities. Then, detailed analysis on power loss type constitution and spatial distribution is presented. Based on the power loss calculation, the thermal transfer performance of network structure is also analysed. Last, other representative network structures are analysed and compared, and the general manipulation principle of flow field for wearable heat transfer panels will be proposed and shed light on other potential applications.

Chapter 7 gives a summary of the whole research work, this part also discusses the limitations of present research work and gives suggestions the outlook of future work for the improvement of large area fluid field manipulation.

CHAPTER 2 Literature Review

2.1 Introduction

Thermal comfort is a multidisciplinary area involves different scientific domains – including thermal physiology, building science, psychology and so on. As a crucial aspect of thermal physiology, thermoregulation is gaining prominence due to global warming[42]. Thermal comfort can be described as "that condition of mind which expresses satisfaction with the thermal environment" defined by the American Society of Heating, Refrigerating, and Air-conditioning Engineers (ASHRAE) Standard 55-66[43]. Achieving thermal comfort necessitates the maintenance of thermal homeostasis in the body, which is influenced by the heat produced through human metabolism and the heat exchange with the surrounding environment[44].

With the progress and development of human society, some people need to work in hot or humid environments such as firefighting, industrial work, military tasks, and sports. Thermal physiological strain poses a threat on human, thus leading to the diminish of their endurance and performance[45]. Air conditioners are widely used for human thermal regulation when performing indoor activities[46]. However, for outdoor activities, alternative methods for body temperature are needed and this prompt the study for wearable thermal management technologies.

Garments play a crucial role in personal thermoregulation by influencing the exchange of heat between the human body and its environment[47]. Although the human body possesses intrinsic mechanisms to adjust its temperature, such as by modulating metabolic rates, blood flow,

sweating, and pore adjustments, these natural processes can be insufficient under extreme environmental conditions[9]. In hot weather, the body may increase sweating and blood circulation to dissipate heat more effectively. However, in situations where these self-regulation abilities are overwhelmed—such as in extreme temperatures or adverse environmental conditions—functional garments become essential for maintaining thermal comfort.

Personal thermal garments are emerging as a key technology for mitigating health issues caused by thermal extremes and providing an environmentally friendly answer to the rising energy demand[48]. As global temperatures rise, there is increasing pressure to ensure personal comfort in hot climates. With projections indicating that global energy consumption could triple by 2050, the need for advanced thermoregulation garments is more pressing than ever[49]. In recent decades, there has been extensive research dedicated to developing intelligent thermoregulation garments, with personal heating garments making substantial strides and gaining a strong market foothold. These garments leverage cutting-edge heating materials, such as carbon nanotubes[50,51], carbon fibers[52,53], graphene[54,55], and metallic nanowire meshes[56,57], to offer effective heating solutions. Meanwhile, there is an equally strong demand for cooling garments designed for use in situations like intense physical activity in heat and specialized protective wear for astronauts, medical staff, and firefighters.

The idea of personal cooling garments was initially introduced in 1958[58], yet it wasn't until 1962 that the first refrigeration garment for personal use was manufactured for the aerospace sector. Following this development, various types of cooling garments—including fluid-cooled, radiative-cooled, and thermoelectric (TE)-cooled versions—have been designed and assessed. Nevertheless, the technical challenges in attaining highly efficient cooling effects in garments have resulted in the PCG market evolving more slowly.

Recently, driven by the rapid advancement of smart and functional textiles and the increasing global demand for energy-efficient solutions, significant efforts have been made to advance personal thermal management garments. This has involved exploring new materials, cooling technologies, and optimizing device structures. In this review, we concentrate on cutting-edge developments in the field of personal thermal management garments. We categorize these garments into two groups based on whether they require an external power source for their heating or cooling functions: passive cooling and active cooling. Additionally, we outline the primary challenges faced in developing these garments and highlight future directions aimed at accelerating progress in personal thermal management solutions.

2.2 Human thermoregulation and self-adjustment process

Human thermal production is a critical aspect of physiological processes, primarily driven by cellular metabolic activity. This process involves the conversion of over 80% of metabolic energy into heat. In cellular metabolism, energy is initially stored in adenosine triphosphate (ATP)[59]. During activities that require energy, such as maintaining basal metabolic rates or conducting physical work, ATP breaks down into adenosine diphosphate (ADP) and a free phosphate, releasing heat. Notably, only about 25–30% of this metabolic heat is applied to mechanical work like muscle contractions, while the remaining 70% is retained within the body, serving no direct physiological function. The regulation of thermogenic activity involves both neural and humoral factors, with sympathetic nervous excitation and hormones such as

adrenaline and thyroid hormones enhancing metabolic rates and thus increasing heat production[60,61].

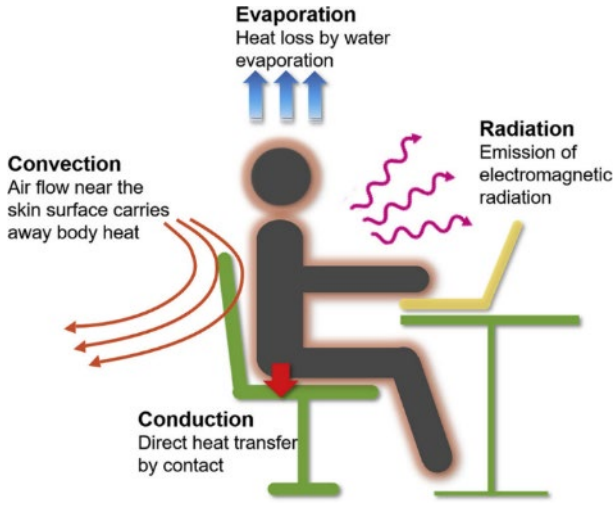

Figure 2.1 Heat dissipation routes of the human body[7]. The human body generally dissipates heat via four routes: radiation, conduction, convection, and evaporation.

Simultaneous heat loss is managed predominantly through the skin via radiation, conduction, convection, and evaporation, governed by the temperature and vapor pressure differences between the skin and the environment[7] (**Figure 2.1**). When environmental conditions render physical heat loss insufficient, evaporative processes, including insensible perspiration and sweating, become vital. Additionally, respiratory activities contribute to heat dissipation, with processes in the respiratory tract causing expired air to carry away heat through both evaporation and convection, highlighting the complexity and efficiency of the body's thermal regulatory systems.

The JOS-3 model provides a comprehensive framework for simulating the human body's structure and thermal dynamics by incorporating 85 meticulously defined nodes, which include a central blood node, multiple arterial, venous, and superficial vein nodes, core nodes, muscle nodes, fat nodes, and skin nodes (**Figure 2.2**)[62]. The body is divided into 17 distinct segments, accounting for all major anatomical parts, such as the head, neck, chest, and limbs. This segmentation allows for precise modelling of physiological characteristics and processes specific to each region. The standard body in JOS-3 is characterized by a body surface area of 1.87 square meters and a weight of 74.43 kilograms, serving as a baseline for simulations. Adjustments to heat capacity, thermal conductance, blood flow, and basal metabolic rate are made using ratios derived from these baseline values, enabling the simulation of various body sizes and conditions[63–65].

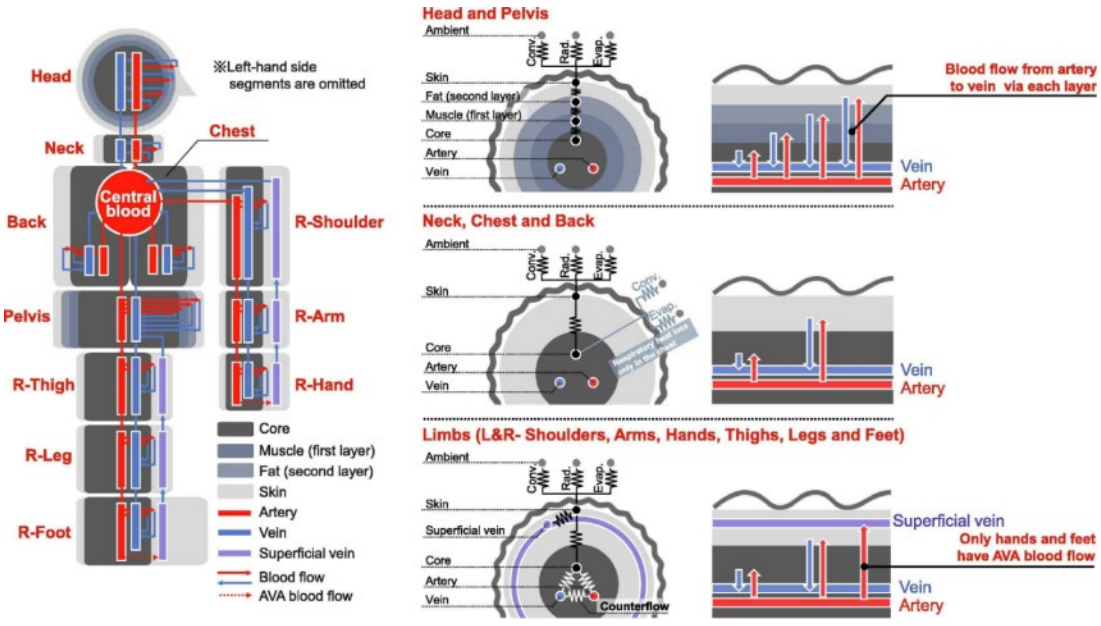

Figure 2.2 Concept of joint system thermoregulation model (JOS-3)[62]. JOS-3 has four layers in the head and pelvis only to maintain sufficient prediction accuracy. In fact, the head

does not have a muscle or fat layer like the other parts of the body, but it is described as a thermal layer. Although the layers can be called the first or second layer, we call it muscle and fat for ease of understanding.

The generation and regulation of body heat is a dynamic process primarily occurring in the core and muscle layers and involving intricate mechanisms of heat transfer. In the human body, heat produced internally is conveyed to the skin through conduction between adjacent layers and through blood flow, which serves as a primary medium for thermal exchange. Conduction facilitates the movement of heat through tissues directly, while the counterflow heat exchange system is particularly relevant in narrower segments such as the shoulders, arms, hands, thighs, legs, and feet, where arterial and venous pathways facilitate efficient heat exchange. Blood flow, originating from a central node, traverses through arteries, tissue layers, and veins in a systematic circulation across seven designated routes that end at major body extremities such as the head, chest, back, and limbs. The complexity of heat distribution underscores the importance of various factors in calculating heat loss, especially across the skin and through respiration. Skin heat loss is assessed through sensible and latent heat components, where sensible heat is influenced by convective and radiative heat transfer coefficients alongside clothing thermal insulation, all of which vary with posture and are measured using advanced thermal manikin techniques[66,67]. Latent heat transfer is calculated using the Lewis Ratio alongside factors such as clothing thermal resistance and vapor permeation efficiency[68,69]. Additionally, respiration contributes to heat loss, closely linked to metabolic activity, with significant respiratory heat exchange delineated in the core chest region in the JOS-3 model. This comprehensive understanding of body heat generation and loss, leveraging critical data

from thermal manikin studies, offers valuable insights into adaptive physiological responses and informs applications in biomedical research and environmental conditioning strategies.

Human thermoregulation is an intricate physiological process that ensures the maintenance of optimal body temperature, essential for homeostasis and overall health. This complex system involves both autonomic and behavioral responses to environmental stimuli, mediated by the integrated functions of the skeletal muscles, respiratory system, nervous system, endocrine system, and skin[70]. Autonomic thermoregulation relies on thermosensors distributed throughout the body that detect temperature changes and relay this information to the central nervous system[71]. The brain processes these signals and initiates responses via the autonomic nervous system to thermoeffectors such as cutaneous blood vessels, sweat glands, skeletal muscles, and adipose tissue[72]. These responses are crucial for either dissipating excess heat or conserving and generating heat, but they require significant energy, involve complex circulatory adjustments, and affect the body's water balance[73]. In contrast, behavioral thermoregulation involves conscious actions aimed at maintaining core body temperature, often by modifying environmental exposure or engaging in specific activities. Common examples include changing clothing layers, adjusting posture, or using air conditioning, demonstrating how humans actively manage their thermal environment[74]. The dual pathways of autonomic and behavioral thermoregulation highlight the body's remarkable ability to manage thermal stress through both involuntary physiological adjustments and voluntary lifestyle choices, crucial for adapting to varying environmental challenges.

2.3 Passive personal thermal management strategies

Passive personal thermal management strategies do not require external power[75–77] and it can be classified into two main types: phase change materials thermal management and radiation thermal management.

2.3.1 Ice cooling and phase change materials (PCMs) thermal management

Phase change materials (PCMs) present a promising solution for enhancing human thermoregulation by effectively utilizing the latent heat absorbed or released during phase transitions to manage the microclimate between garments and the body[78]. A classic example is the incorporation of ice in cooling garments (**Figure 2.3**), which rely on the phase change from solid to liquid to absorb body heat and lower skin temperature, providing thermal comfort in hot conditions[79]. These garments, widely used in industries such as protective clothing[80,81], sportswear[6,82,83], and military uniforms[84,85], demonstrate significant physiological and subjective benefits, as confirmed by studies like those conducted by Juhani et al. and Cooter et al.[86], which noted improved work efficiency and endurance performance. However, traditional ice cooling garments suffer from drawbacks such as weight, bulkiness, and potential skin irritation due to prolonged contact, limiting their practical application[87]. This has spurred research into more flexible and effective options, such as gel ice technology[88–90], although findings by Dehghan et al.[88] and Chesterton et al.[89] highlight existing challenges in achieving optimal cooling effects without sacrificing wearability and comfort.

Figure 2.3 Illustration of an ice cooling vest[79].

The pursuit of advanced materials underscores the limitations of conventional frozen PCMs, such as inconsistencies in cooling efficacy and temporal limitations. Emerging research endeavors focus on developing innovative PCMs that provide more controlled and enduring thermal regulation for wearable applications[78,91–93]. For instance, Li et al.[94] introduced a lightweight phase change material garment that showcased significant cooling efficiency with a manageable weight, emphasizing easy integration into daily attire. Techniques to incorporate PCMs into textiles—such as impregnation and filling with hollow fibers[95], melt spinning[96], coating[97] and composite fiber fabrication[98]—have gained traction over the past decade[99–101]. This is illustrated by V. Skurkyte-Papieviene et al.[98], who enhanced PCM microcapsules' heat storage and release capabilities with thermally conductive additives, and Yang et al.[100], who designed a 3D-printed, flexible PCM nonwoven fabric that maintained thermal stability through extensive use. Such advancements reflect a trend towards multifunctional, durable textiles capable of effective thermoregulation in varying conditions.

One innovative approach to evaporative cooling in textiles is the three-layer laminate design, which efficiently uses evaporation to cool the wearer[14]. This design stands out due to its simplicity and convenience (**Figure 2.4**), as the garment does not need to be fully soaked in water for activation; instead, it features a filling opening that allows easy water replenishment without needing to remove the garment. This feature is particularly advantageous for athletes, enabling them to maintain cooling through specialized t-shirts or headbands without the discomfort of being wet. Furthermore, the laminate's low thermal resistance ensures that even when cooling is not needed, the body temperature does not rise due to the dry laminate's insulating properties. This design also facilitates direct contact with the skin, enhancing cooling efficiency compared to designs with air gaps, which can increase thermal resistance and reduce performance.

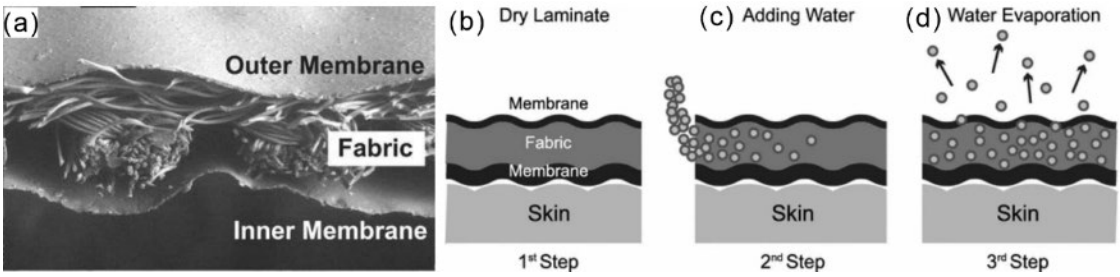

Figure 2.4 Three-layer laminate based on membrane evaporation[14]. (a) Scanning electron microscope picture of the three-layer laminate; from top to bottom outer Sympatex membrane (thickness 10 μm), textile fabric made of polyester multifilament (100 μm), inner Sympatex membrane (15 μm); (b-d) Diagram of the three-layer laminate and the principle of water evaporation from the reservoir.

The primary benefits of this evaporative cooling garment are its lightweight and flexible nature, making it highly portable. However, its effectiveness can vary significantly depending on environmental conditions. In extremely humid climates, the cooling performance can be considerably diminished due to the lower vapor pressure difference between the garment's outer membrane and the ambient environment. This reduced difference inhibits efficient mass transfer, which is critical for effective evaporative cooling. Thus, while this design offers convenience and portability, its reliance on environmental conditions can be a limitation, necessitating consideration of the intended use environment to ensure optimal performance.

The commercialization and widespread acceptance of wearable PCMs hinge on ongoing advancements in material science and textile technology, as exemplified by Outlast® Technologies[102]. Their innovative integration of PCM microencapsulation in fibers underscores a significant leap in managing thermal loads, minimizing perspiration by nearly half under high-temperature conditions. This achievement stems from the ability to create breathable, flexible garments that address the core weaknesses of traditional PCM applications. The enhanced thermo-regulating capabilities and user comfort potential position PCM textiles for extensive deployment in personal cooling technologies, marking a pivotal direction in the evolution of cooling garments. As research continues to push boundaries in PCM performance and integration, the potential for large-scale implementation of adaptive PCM textiles becomes ever more feasible, offering promising pathways for future developments in personal and occupational thermal management.

2.3.2 Radiation thermal management

Advanced textiles designed for human thermoregulation through radiation and moisture control represent a cutting-edge approach to maintaining thermal comfort and reducing energy

consumption. Radiation cooling (RC) utilizes the atmospheric window in the infrared (IR) spectrum between 8 to 13 μm, which allows human heat to be directly radiated into space without consuming external energy[103]. As textiles serve as the interface between the human body and its environment, they play a crucial role in managing heat exchange. However, traditional textiles often overlook the potential for controlling thermal radiation. Novel radiative cooling and warming textiles require precise engineering of IR optical properties, tailored for either retaining or dissipating heat. This new wave of textiles aims to enhance personal comfort while contributing to lower energy demands in climate control systems.

Numerous innovative textiles have emerged in the market, leveraging various fibers and technologies to optimize thermal management. Brands like Columbia's Omni-heat and Dupont's CoolMax focus on harnessing unique fiber structures to enhance moisture transport and reflect body heat, respectively. Nike's AeroReact adjusts its pore size in response to moisture, altering breathability dynamically. Similarly, Verycool by Yonex integrates xylitol for a cooling sensation, and Under Armour's HeatGear relies on strategic compression to improve muscle performance[7]. Each of these textiles utilizes distinct mechanisms to address heat and moisture management, confirming the industry's focus on integrating advanced materials for enhanced comfort and functionality. Dual-layer knitted fabrics further capitalize on contrasting hydrophilic properties to improve one-way sweat transport, showcasing how engineered textiles can effectively manage moisture and improve thermal comfort[7].

For cooling purposes, recent developments have resulted in textiles like the IR-transparent visibly opaque fabric (ITVOF), designed by Tong et al.[104] Utilizing low IR-absorptive polyethylene fibers structured to minimize IR reflection while maintaining opacity, these textiles focus on maintaining visibility and thermal regulation simultaneously (**Figure 2.5**).

NanoPE, another breakthrough material, incorporates nanoporous structures that exploit Mie scattering to maintain IR transparency[105]. These pores enable NanoPE films to scatter visible light while preserving mid-IR transparency, offering energy-efficient cooling benefits. The recent progress in scaling NanoPE for fabric production allows for improved softness and durability, making it suitable for everyday use. Peng et al.'s work demonstrates that garments made from NanoPE fibers can reduce skin temperature by approximately 2.3°C compared to conventional cotton, which correlates with a significant reduction in building energy consumption[106]. This highlights the crucial potential of advanced textiles in substantially lowering energy costs associated with thermal management.

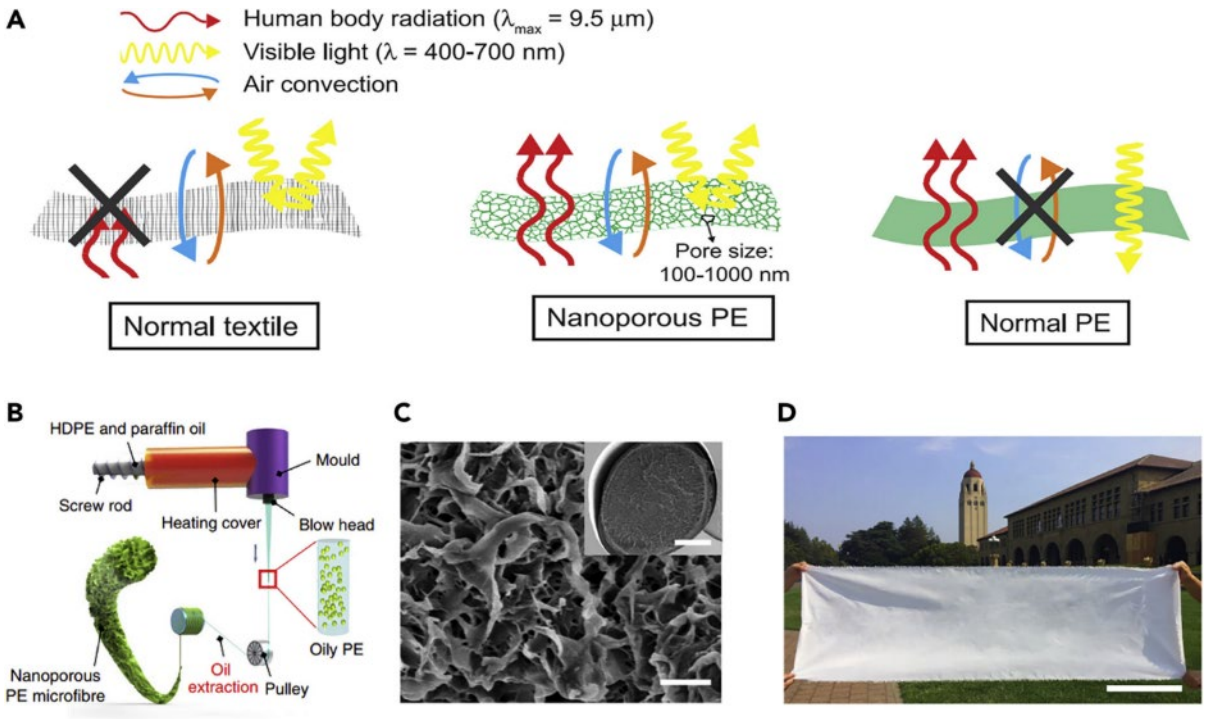

Figure 2.5 Textiles for radiative cooling[105,106]. (a) Schematics of comparison among normal textile, NanoPE, and normal PE. Only NanoPE satisfies IR transparency and visible

light opacity at the same time. (b) A schematic diagram of the manufacturing process for the NanoPE microfiber. (c) Scanning electron microscope (SEM) image of the cross-section view of a nanoPE microfiber. Scale bar, 2 μm. The inset shows a lower-magnification SEM image of the well-preserved cross section of the microfiber. Scale bar, 50 μm. (d) A photograph of a large woven NanoPE fabric. Scale bar, 0.35 m.

Radiative warming textiles have also been the focus of innovative material design, aiming to reflect human body thermal radiation effectively (**Figure 2.6**). Traditional metallic fibers, despite offering high thermal reflection, are often not practical due to their weight and rigidity[107,108]. Newer approaches involve metal-polymer composite yarns with improved flexibility and surface-modified textiles using metallic nanomaterials[57,109–111]. Silver nanowires, as illustrated by Hsu et al.[57], create conductive networks within fabrics to enhance thermal insulation through reflective and active heating mechanisms. However, optimizing mid-IR reflectance remains challenging, prompting further research[109,112,113]. Enhanced designs like nanoporous silver textiles based on NanoPE, as developed by Cai et al.[109], feature improved reflectivity and a significantly reduced thermal emissivity, allowing for a notable decrease in energy set points. Alternative strategies using composites of materials like woven Kevlar fiber with metallic nanowires and reduced graphene oxide showcase high IR reflectivity, providing localized warming effects and advancing the capabilities of modern thermal textiles[114,115]. These developments reflect a growing trend towards employing advanced materials and innovative design strategies to manage heat more effectively, promising enhanced thermal regulation for diverse applications.

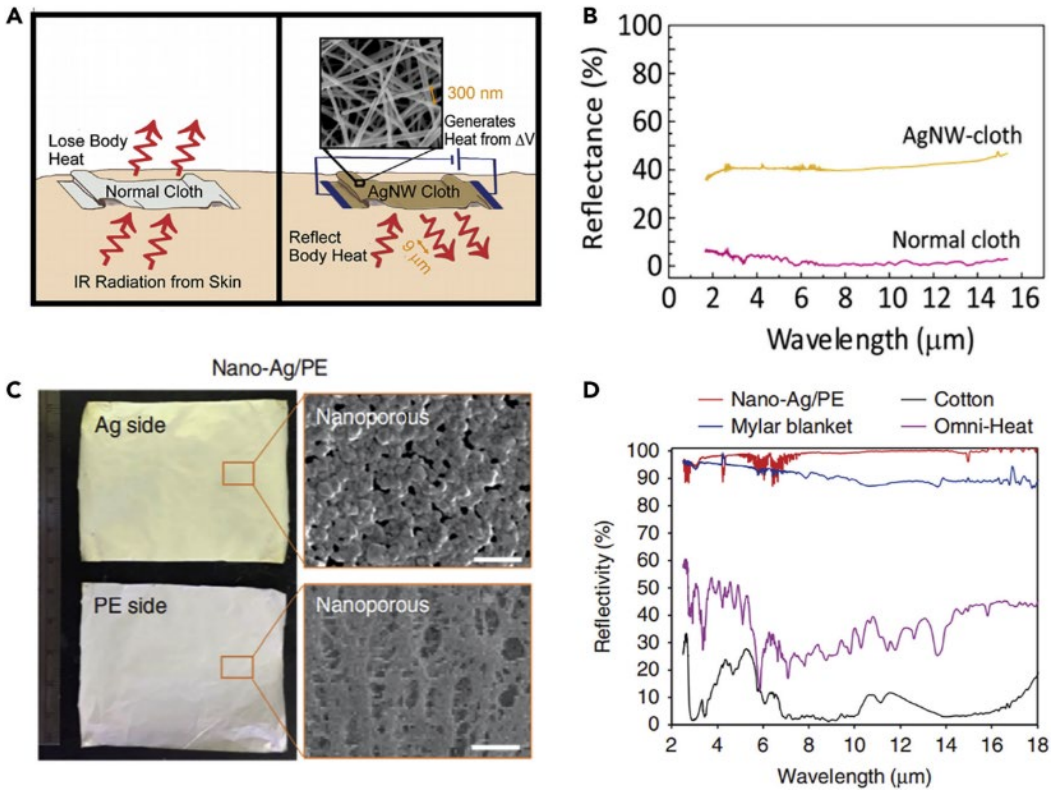

Figure 2.6 Textiles for radiative warming[57,109]. (a) Concept illustration of Ag nanowire cloth with thermal radiation insulation and active warming. (b) Reflectance measurement of normal cloth and AgNW cloth. (c) Photographs and SEM images of the silver side and PE side of Nano-Ag/PE. Scale bar, 1 μm. (d) Measured total Fourier transform infrared (FTIR) spectroscopy reflectance of the Ag side of Nano-Ag/PE, cotton, Mylar blanket, and Omni-Heat.

2.4 Active personal thermal management strategies

With the rapid advancement of wearable electronic technology, integrating electronic devices into intelligent thermal management garments has become a key focus area. In this context, personal thermal management garments powered by external sources have continually evolved. Currently, the primary types of garments in this domain include fluid-driven thermal management garments and thermoelectric (TE) thermal management garments.

2.4.1 Fluid driven thermal management garments

Air and liquid thermal management garments represent a significant advancement in wearable cooling technologies, leveraging longstanding strategies to provide effective thermal regulation in various environments. Air-cooling garments (ACGs) function by channeling air through the microclimate between clothing and the body (**Figure 2.7**), offering benefits such as affordability, lightweight design, and portability[116,117]. Initially developed for aerospace and military applications to mitigate heat stress in protective gear for pilots and soldiers, ACGs have since expanded into broader fields[44]. Conversely, liquid cooling garments (LCGs) employ a network of circulating water tubes integrated with a micro pump system to transfer cold liquid across the inner garment layer, effectively lowering body temperature (**Figure 2.8**)[44,118]. The inaugural use of LCGs was for astronauts, underscoring their effectiveness in extreme conditions. Through extensive research, both ACGs and LCGs have become pivotal in sectors like military[119], mining[120], and sports. Recent innovations include hybrid personal cooling vests (PCVs) that combine phase change materials (PCMs) with ventilation fans, as demonstrated by Ni et al.[121], highlighting their practicality and efficiency in hot, humid environments. Furthermore, research by Lou et al. exploring the interaction of body

position with air tubing networks and thermoelectric cooling plates provides insights for enhancing the integration and comfort of these garments in everyday use[122]. As such, air and liquid thermal management garments continue to evolve, offering promising solutions for thermal comfort across diverse applications.

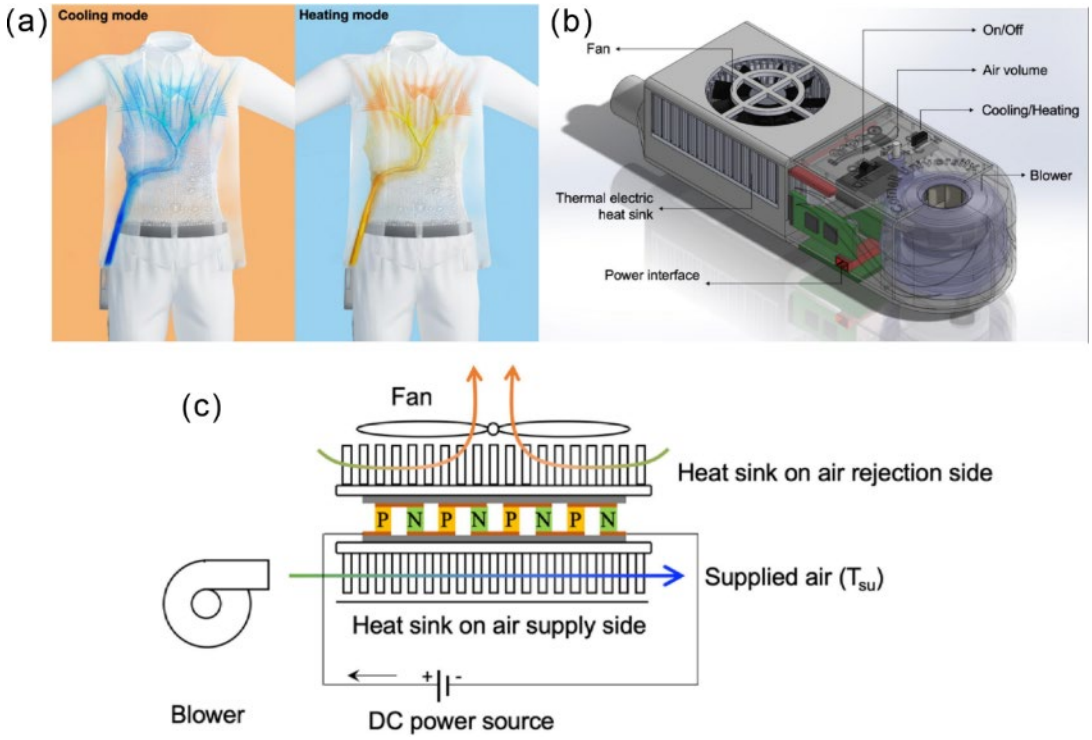

Figure 2.7 Introduction of the TACUS[123]. (a) Design and functions of TACUS in cooling and heating modes; (b) 3D perspective of the integrated TECU; (c) Mechanism of the TECU.

Thermoelectric (TE) thermal management systems offer promising solutions for small-scale solid-state cooling applications, particularly in industries requiring lightweight, cost-effective options[124–126]. TE cooling plates (TECPs) have been successfully commercialized,

facilitating practical applications in wearable cooling devices like the Embr wave bracelet and Sony Reno pocket, which deliver localized cooling to the skin[127,128]. Innovative applications, such as the undergarment embedded with a TECP cooling system developed by Luo et al.[123], demonstrate the potential of these systems in personal thermal management. This TE module, incorporating a heatsink and tubing network, offers significant energy efficiency, achieving 15% savings in indoor heating, ventilation, and air conditioning (HVAC) systems. Despite these benefits, the bulkiness and rigidity of traditional heatsinks pose challenges to the wearability and flexibility of TE applications.

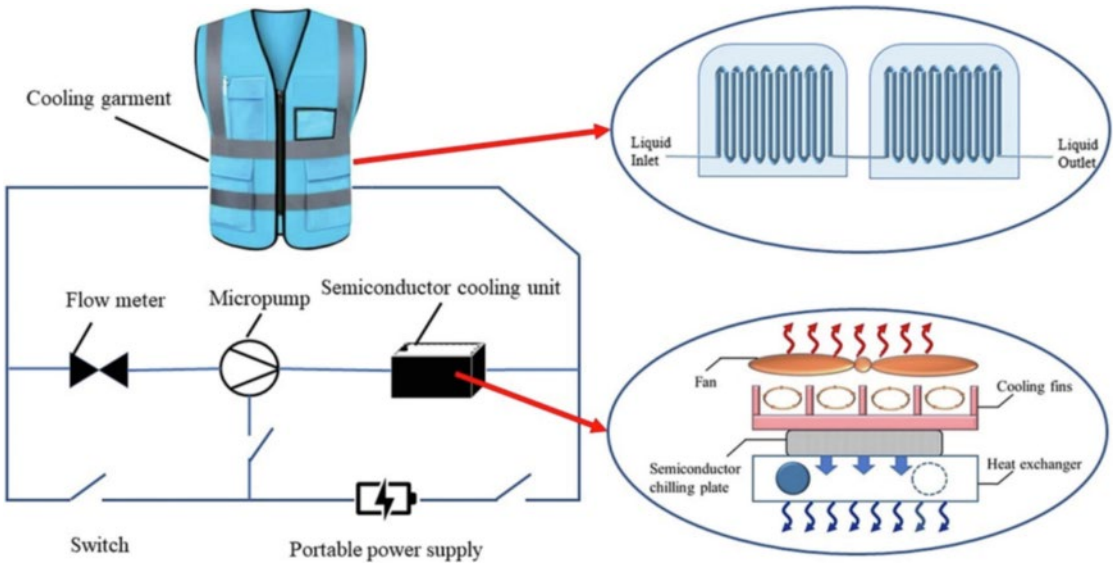

Figure 2.8 Schematic diagram of the basic composition of the cooling clothing system[128].

Air-cooled garments (ACGs) and liquid-cooled garments (LCGs) offer promising solutions for personal cooling but come with inherent limitations largely due to their reliance on external devices to cool the circulating fluids. This dependency imposes a restriction on the mobility

and effective working range of individuals wearing these garments, rendering them unsuitable for a variety of applications where portability and flexibility are essential. In response to these limitations, Ernst et al. developed a portable cooling system utilizing a vapor compression cycle with R-134a as the refrigerant[129], as shown in **Figure 2.9**. While vapor compression systems are common in HVAC applications—comprising a condenser, evaporator, expansion valve, and compressor—they typically depend on electrical power, which is impractical for portable garments. To address this, Ernst et al. proposed incorporating a fuel-driven engine to power the compressor, albeit at the expense of increased system bulkiness. The designed wearable garment features a tri-layer construction consisting of an aluminum foil layer and a refrigerant tube layer functioning as the evaporator, separated from the condenser by an insulation layer. Although the system delivers a notable cooling capacity of 100–300 W at ambient temperatures between 37.7 and 47.5 °C, its substantial weight of approximately 5.31 kg poses a challenge for extended use. Future research should focus on reducing the overall weight of the system, potentially by substituting lightweight batteries for the fuel-driven engine, while carefully considering energy density requirements. Additionally, exploring alternative refrigerants beyond R-134a could enhance the cooling capacity, offering more efficient and portable solutions for wearable cooling garments.

Due to the high specific heat capacity of water, such kinds of liquid driven cooling wraps are widely used for sports recovery[130]. Typical example is GameReady® company offers a range of products (GRPro 2.1 Cold and Compression Therapy System & Med4 Elite) tailored toward injury recovery and rehabilitation, primarily using a combination of cold therapy and compression[131].

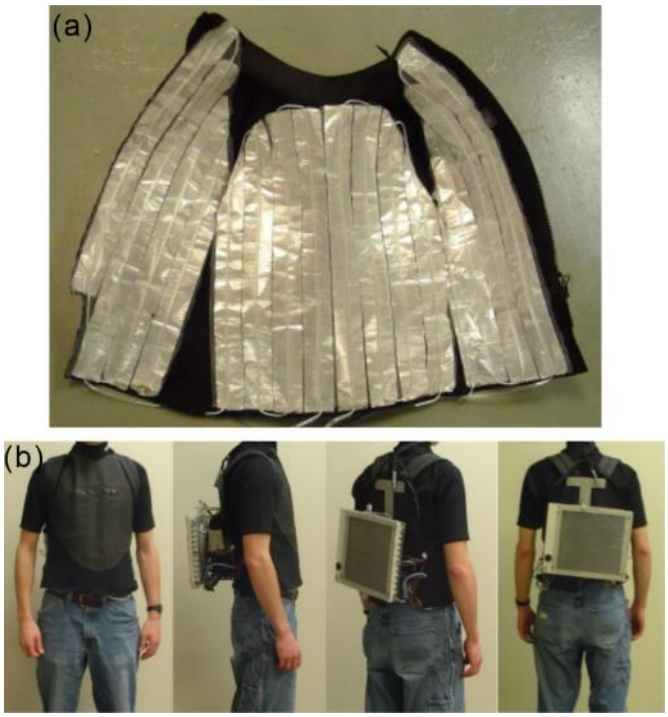

Figure 2.9 Wearable cooling garment working based on the vapor compression cycle[129].

Gas expansion cooling garments provide an innovative approach to thermal management that operates based on the vaporization of liquefied carbon dioxide (CO2), eliminating the need for external power. This technology leverages the rapid expansion and phase change of compressed CO2, dispensed through an expansion valve, to absorb heat from the environment. As the liquefied CO2 vaporizes, it extracts energy in the form of the heat of vaporization, effectively lowering the surrounding temperature. Zhang et al. demonstrated that this method can enhance cooling effects when the vaporized CO2 is directed over a pure cotton fabric, promoting increased sweat evaporation on the skin's surface[132,133], as shown in **Figure 2.10**. Despite these benefits, careful monitoring of CO2 concentrations is essential, as excessive levels can be toxic. Zhang et al. observed that CO2 concentrations could reach ten times the normal level

during tests in a 29.5 m^3 enclosed space, highlighting the importance of safety measures. The primary advantages of gas expansion cooling garments include their lightweight nature (approximately 1.3 kg), cost-effectiveness, portability, and low operational risk. However, these garments provide only moderate cooling capacities and are limited by their short operational duration, with a single CO2 bottle providing cooling for approximately 25 minutes. Future development of these systems could focus on extending operational duration while ensuring safe CO2 management to optimize their practicality and effectiveness.

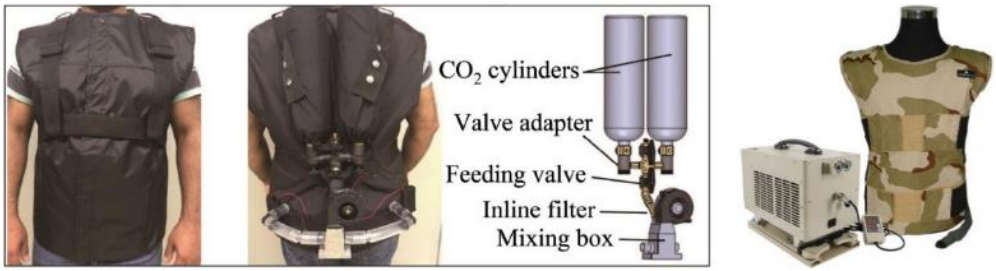

Figure 2.10 Front view, back view, and the air treatment system of the cooling garment [132,133].

Fluid-driven thermal management garments, while effective in achieving substantial cooling performance, face significant challenges when adapting to complex living and working conditions that demand enhanced comfort and safety. The inherent design of these garments often results in bulky and heavy configurations, which restrict their practicality and widespread adoption in everyday life. This bulkiness is primarily due to the embedded heavy devices essential for their operation, which also introduces safety risks such as potential skin burns from steam formation[134]. Consequently, there is a pressing need to innovate and refine these

cooling systems to ensure not only improved efficiency but also enhanced safety and user comfort. Advances in lightweight materials and safer cooling mechanisms must be prioritized to overcome these limitations, potentially expanding the applicability and attractiveness of fluid-driven thermal management garments in diverse settings.

2.4.2 Electricity driven thermal management garments

Individual wearable cooling devices have traditionally relied on air and liquid cooling methods, which are often criticized for being cumbersome due to their bulky air or fluidic channels, leading to inconsistent and unreliable cooling performance[135]. These limitations have spurred interest in homeostatic solid-state cooling technologies, such as electrocaloric[136,137], magnetocaloric[138], and thermoelectric (TE) cooling systems[139]. Among these, TE cooling, coupled with joule heating, stands out as a promising option for industrial-scale thermal management due to its consistent performance and compact design[140]. Unlike traditional cooling garments, TE cooling systems can be applied directly to the skin without the need for a thermal exchange medium, enhancing both efficiency and user convenience[141]. This direct contact capability makes wearable TE cooling and joule heating devices an attractive alternative for achieving personal thermal comfort, offering a sophisticated solution that aligns with the evolving demands of modern wearable technology.

Flexible thermoelectric generators (TEGs) are increasingly popular in wearable applications due to their ability to minimize thermal contact resistance by ensuring robust contact with the skin[142,143]. This strong contact significantly enhances the temperature differential across the TEG, a critical factor for efficient operation. The performance of thermoelectric designs (TEDs) when integrated into wearable devices is influenced by various factors including device geometry, air speed, the body's heat content, placement on the body, and individual anatomical

differences[144]. The TED, exemplified in the design shown in **Figure 2.11**, incorporates optimized heat spreaders that enhance thermal performance while boosting the durability of the associated protective clothing. This design leverages two crucial attributes for maximizing cooling efficiency and power output: low thermal conductivity within the device and high thermal conductivity in the stretched sheets. Additionally, these sheets are stretchable, augmenting the flexibility of the TEGs, thereby aligning with the dynamic and diverse demands of wearable technology applications.

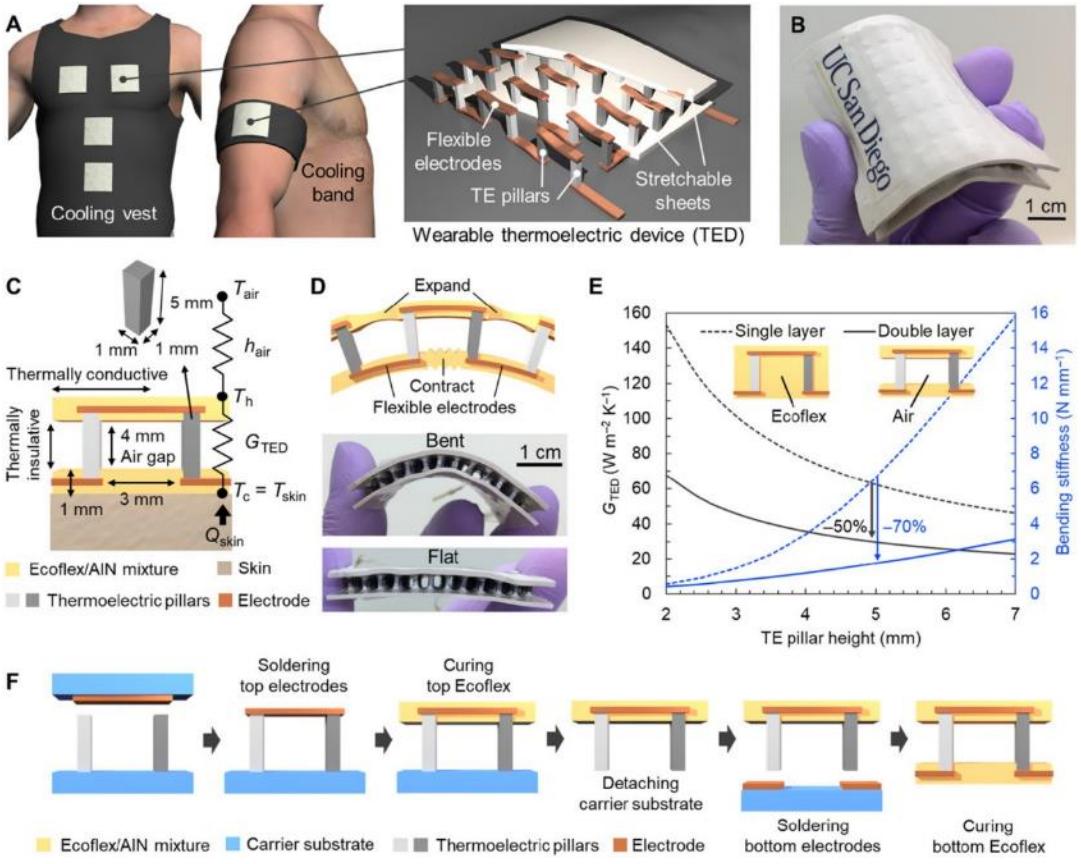

Figure 2.11 Design, fabrication, and working of wearable thermoelectric device[145].

Joule heating textiles represent a significant advance in the development of active thermal management systems, offering enhanced warming capabilities by using the principle of electro-thermal conversion[146,147], as shown in **Figure 2.12**. Unlike passive textiles, which rely solely on regulated radiation and conduction without additional energy, Joule heating textiles incorporate electrically conductive materials like carbon nanotubes[148], graphene[149], metallic nanomaterials[111,150,151], and conductive polymers[152]. These materials can be embedded or applied to textile surfaces to generate heat through decreased electrical resistance when voltage is applied. This feature is particularly beneficial in wearable applications, where such textiles must provide effective heating while maintaining durability under mechanical stress. For instance, the integration of a nanowire percolation network within polymers delivers a robust electrothermal effect that remains stable even during stretching or bending[151]. Metallic materials, in addition to their Joule heating capabilities, further enhance the functionality of textiles through superior thermal radiation reflectance, making them suitable for a variety of environmental conditions[57,114,115,153].

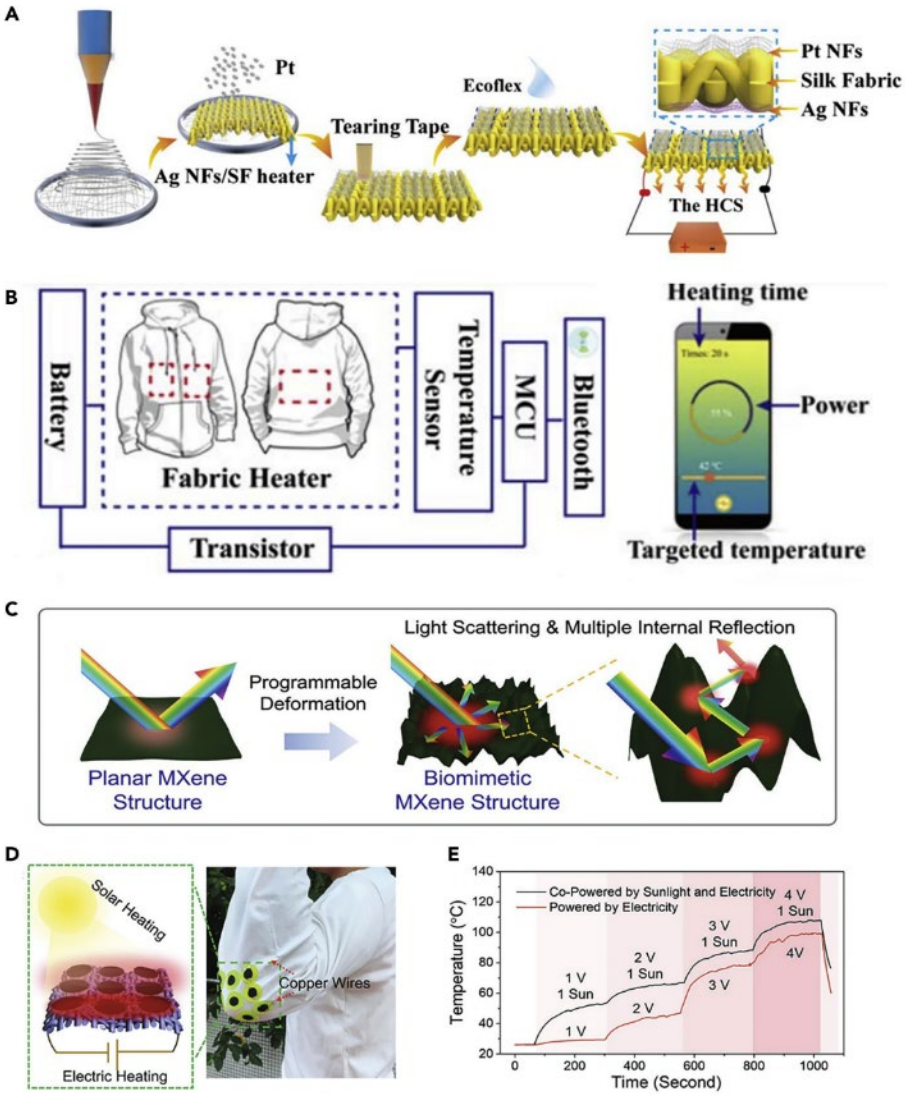

Figure 2.12 Active Warming Textiles Based on Joule-Heating and Light-to-Heat Conversion [150,154].

The integration of smart control systems into Joule heating textiles transforms them into sophisticated personal thermal management devices. An exemplary innovation by Huang et al. introduced a sandwich-structural textile combining Ag nanofibers and Pt nanofibers to serve dual functions as a heater and temperature sensor, respectively[150]. This design exhibits high

thermal stability and precise temperature control and can be managed interactively via smartphone[150]. The system enables users to set desired temperatures through a mobile app, which communicates with a microcontroller unit (MCU) via Bluetooth to adjust the power input to the textile's Joule heating elements. Although the fully integrated application of such smart textiles with temperature control has yet to be realized, this work charts a promising course for future developments in the domain of interactive and responsive clothing technology. By enabling real-time adjustment and monitoring of thermal conditions, these advanced textiles could significantly enhance user comfort and energy efficiency in personal apparel[150].

Beyond the Joule heating mechanism, advancements in dual-mode heating textiles further expand the versatility of active warming solutions. Li et al. leverage biomimetic MXene textures inspired by the black scales of Bitis rhinoceros to develop stretchable textiles that combine solar and electric heating[154]. These textiles exploit a highly hierarchical structure for broad-spectrum light absorption, achieving up to 93.2% efficiency in light-to-heat conversion. By mimicking natural textures, these MXene-coated textiles offer dual heating capabilities that utilize both sunlight and electrical power. This innovative approach not only enhances the efficiency of heating but also paves the way for the development of integrated solar-electric dual-heated textiles. The success of this technology hinges on advancing the MXene coating process, allowing it to uniformly cover individual fibers[154]. Such progress would enable scalable production and further elevate the functionality of active warming textiles, providing sustainable and efficient heating solutions for various applications.

2.5 Conclusions and outlook

It is obvious that wearable thermal management is gaining more and more attention of scientific researchers due to its wide application. From this brief review, we see that the wearable thermal management system can be simply divided into four major groups: passive phase change materials wearable thermal management strategy, passive radiation wearable thermal management strategy, active fluidic wearable thermal management strategy and active electricity driven wearable thermal management strategy. Even though all these wearable thermal management systems are applied in numerous scenarios, the heat transfer capability is still limited in some specific conditions, and the volume and weight of wearable thermal management system is also cumbersome for some people. In all these four categories of thermal management strategies, the fluid driven wearable thermal management system is the one have the potential to perform large heat transfer combined with lightweight and relative comfort. This is due to the nature of fluid: relatively large heat capacity and no fixed shape. However, all current wearable fluidic thermal management systems are limited due to the low fluid velocity inside. This is due to the inappropriate design of fluid channel and small power input of fluid pump. But all the research works up to now are still lack of the fluid dynamics design of fluidic wearable thermal management systems. And this thesis will focus on solving this problem to develop a wearable heat transfer panel with large fluid velocity and even surface temperature mapping for wearable thermal management.

CHAPTER 3 Wearable Thermal Management Strategy and System Evaluation

3.1 Introduction

Wearable thermal management systems have garnered significant attention in recent years due to their potential applications in various fields, including sports recovery[82], healthcare[19], and personal comfort[155]. These systems can be broadly categorized into passive and active thermal management devices. Passive systems, such as phase change materials (PCMs)[156] and thermally conductive fabrics[57], rely on inherent material properties to regulate temperature. In contrast, active systems, including thermoelectric coolers (TECs)[145] and liquid cooling garments[157], utilize external power sources to achieve precise thermal control. Despite their promise, both categories face limitations. Passive systems often suffer from limited thermal regulation capacity and slow response times, while active systems can be bulky, energy-intensive, and complex to integrate into wearable formats.

In the realm of sports recovery, effective thermal management is crucial for enhancing muscle recovery, reducing inflammation, and improving overall athletic performance[158]. Sports competition is no longer the effort of the athletes themselves, but also with the technologies applied to them. The speedy recovery between and after tournaments is of great importance for athletes to release their potential abilities in the next competition. The main strategies employed in wearable thermal management for sports recovery include localized heating and cooling, dynamic temperature modulation, and hybrid systems that combine both heating and cooling functionalities. The rapid contraction therapy (RCT) by hot and cold water immersion has been

used to help the athletes provide short effective recovery by increasing the blood flow in human body, reducing the muscle swelling and mitigate the pain during strenuous exercise[159]. However, current wearable sports recovery devices are hindered by their low heat transfer capabilities. Most existing devices are designed to operate at a single temperature during one cycle and lack the ability to perform rapid temperature switches, which is essential for optimizing therapeutic outcomes. Also, taking these tools for RCT to the competition site is unrealistic in most cases, because the equipment is too large. Developing a portable RCT device can help athletes get better performance in their following competition.

This chapter will focus on the research of several critical issues for the development of a novel wearable RCT device. First, evaluating the thermal transfer quantity between human body and hot/cold water in immersion RCT through thermal simulation. Such simulations can provide insights into the efficiency and effectiveness of heat transfer mechanisms, guiding the design of more advanced systems. Second, the development of control logistics is crucial for enhancing energy efficiency, ensuring that the devices can deliver the desired thermal effects without excessive power consumption. Third, exploring innovative designs for external hot and cold sources can significantly improve the performance and versatility of wearable thermal management systems.

3.2 Methodology

3.2.1 Heat transfer model and numeric simulation set up for water immersion rapid contrast therapy (RCT)

As illustrated in **Figure 3.1a**, the model setup for the heat transfer simulation is presented. The dimensions of the human thigh are defined as having a length of 45 cm and a diameter of 14 cm. The leg is composed of skin, muscle, blood vessels, connective tissues, and bones. Skeletal muscles are crucial for rapid recovery post-exercise. Given that the skin is approximately 1 mm thick and consists of about 60% water, comparable to muscle tissue which contains about 70% water, the skin's thermal properties have been neglected in this simulation. Similarly, blood vessels and connective tissues occupy a minimal proportion of the leg, and their thermal impact is reduced as blood vessels constrict during cooling and dilate during heating cycles. Hence, the thigh in this simulation is modelled solely with muscle tissue.

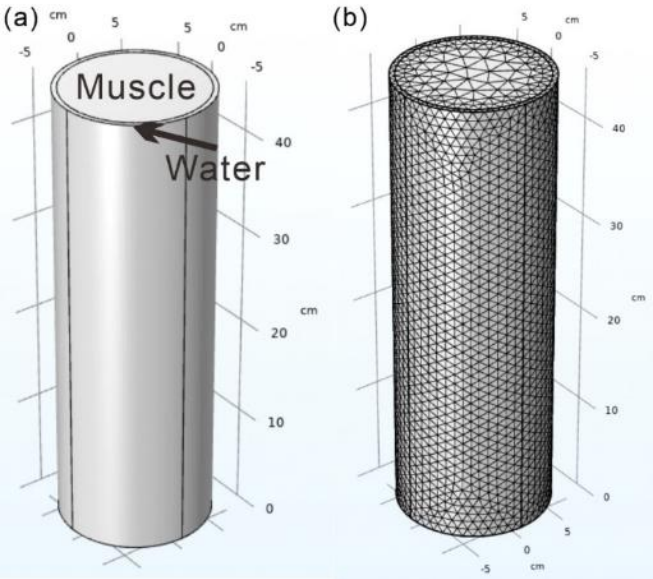

Figure 3.1 Schematics of the thigh model set up and grid distribution of the computation domain. The cylinder is assumed as an adult's thigh filled with muscle by covering a thin water layer with constant temperature switching between 5ºC and 40ºC.

The outer surface of the leg is assumed to be covered with a 0.5 cm layer of water, and the temperature of this layer is maintained constant throughout the designated period. To evaluate the maximum heat transfer, the temperatures for the hot and cold cycles are set to 40°C and 5°C, respectively. The cold cycle is applied for 1 minute, followed by the hot cycle for 2 minutes, with a total of five hot and cold cycles being administered. The simulation utilized the predefined material properties for muscle and water in COMSOL Multiphysics 6.0.

During the whole heat transfer period, the heat transformation between the human leg and water should obey the following time-dependent equations [160]:

$$\rho C_p \frac{\partial T}{\partial t} + \rho C_p \vec{u} \cdot \nabla T + \nabla \vec{\mathrm{q}} = Q + Q_{ted} \tag{3-1}$$

$$\vec{q} = -k\nabla T \tag{3-2}$$

Where ρ is the density of muscle, C_p is the heat capacity of muscle, T is temperature, t is the time, $\vec{u}$ is the velocity vector of translational motion, $\vec{q}$ is the heat flux by conduction, Q contains additional heat sources = 0 in this case, Q_{ted} is the thermoelastic damping and accounts for thermoelastic effects in solids, k is the thermal conductivity of muscle, ∇ is Laplace operator.

To determine the upper limits of heat transfer, the muscle temperature is set to 45 °C. The water region is initially set to 5 °C for the first 60 seconds, then switches to 40 °C for the next 120 seconds, reflecting the conditions of rapid contrast therapy. This process is repeated for a total of five cycles. The interface between the muscle and the water, which is assumed to be continuous as depicted in **Figure 3.2**, serves as the boundary for calculating the energy transfer between the water and the thigh.

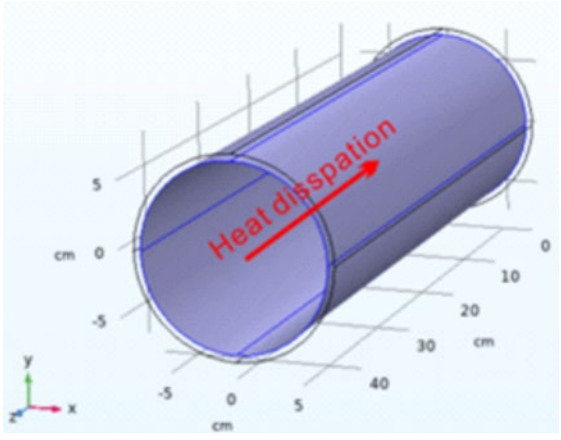

Figure 3.2 The surface for calculating the energy transfer (between water and leg). By integrating the heat flux on this plane, the total heat flux consumption can be calculated.

The boundary condition between the leg and water can be expressed as the following thermal contact equation [160]:

$$-\overrightarrow{n_d} \cdot \overrightarrow{q_d} = \overrightarrow{n_u} \cdot \overrightarrow{q_u} \tag{3-3}$$

Where the subscripts *u* and *d* refer to the upside and downside of the slit, respectively.

All simulations were conducted using the commercial finite element software COMSOL Multiphysics 6.0. The assumptions employed in this study include heat transfer in solids and fluids and laminar flow conditions. The mesh size for all simulations was set to "normal" (as shown in **Figure 3.1b**). The mesh type was specified as free quadrilateral, and it was automatically generated by COMSOL Multiphysics 6.0.

3.2.2 Switch logics and external hot/cold source design

The control strategy of this wearable thermal management system starts by proposing the water circulation route inside. The switch logical design of this wearable thermal management system, especially for rapid contrast therapy is based on the on/off control of 5 solenoid values, 2 pumps and 1 drain pump. A prototype for realizing this switch logic is also prepared.

The external hot/cold source plays the role of supporting water with stable temperature continuously for the circulation of therapy. This work explores the potential of adding extra heating and cooling components by comparing the one without heating/cooling component.

This test is conducted on the fast wearable thermal management system – COOLWEAR, developed by our research team.

The fast wearable thermal management system originated from the elite athlete's requirement for fast contrast therapy beside the sports field as a water bathtub is cumbersome. Also, the current commercial portable wearable thermal management systems can only perform single temperature therapy, and other indoor thermal management systems cannot perform fast switching temperature (they usually take more than 1 min to change temperature). We have demonstrated that our self-developed fast wearable thermal management system is portable and can perform the temperature switch in 10s. The whole wearable thermal management system (developed by our research group) contains two parts: an all-in-one thermal management box for cold and hot water circulation and switching, a soft heat transfer panel for heat transfer to the human body. This wearable heat transfer panel is made by a traditional textile processing technology – laminating. The thermal management box contains two water tanks, one for hot water and the other for cold water. This thermal management box can perform both water injection and sucking, together with the function of high-pressure air massage. The user can adjust the water temperature inside the two water tanks and control the hot/cold therapy time separately for his/her preference.

3.3 Results and discussion

The chapter mainly focuses on (1) the simulation analysis of heat transfer during the water immersion contrast temperature therapy (2) the determination of switch logics for valve control temperature gradience and (3) thermal management source of thermoelectric (TE) module.

3.3.1 Heat transfer model and numeric simulation for water immersion rapid contrast therapy (RCT)

Water immersion rapid contrast therapy, often referred to as contrast water therapy (CWT), involves alternating between hot and cold water immersion. This technique is popular among athletes for its potential benefits in recovery, reducing muscle soreness, and improving circulation. By preparing two hubs with adjustable temperature settings, the hot water should be comfortably warm, typically around 38-43°C, while the cold water should be quite cold, around 5-15°C. Immerse part of the body in the cold water for 1-2 minutes. This causes blood vessels to constrict, which can help reduce inflammation and muscle soreness. Quickly switch to the hot water for 2-4 minutes. This helps to dilate blood vessels and increase blood flow to the muscles. Alternate between hot and cold water immersions for a total of 3-4 cycles.

Figure 3.3 is the calculated temperature gradient distribution of the thigh in cross-section view. From the four pictures during the first cooling cycle. Even after 120 s of immersion in cold water, the temperature inside the thigh is still very high. This means that during the fast contrast temperature therapy, only the periphery part of the leg will be effectively affected.

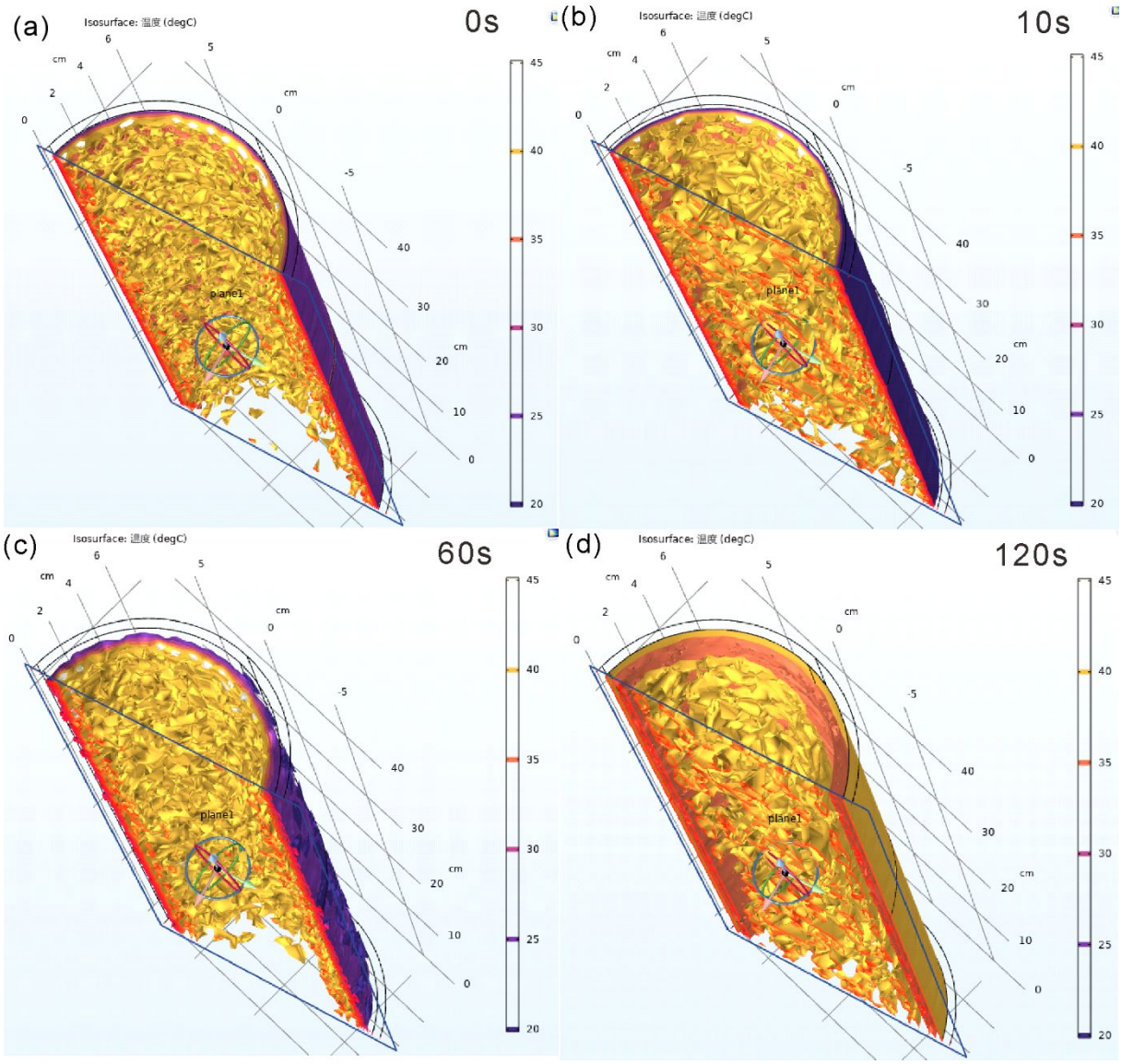

Figure 3.3 Temperature gradient distribution of a leg in cross-section view during the first cooling cycle at 0s, 10s, 60s and 120s.

The simulation results show that the temperature on the surface of the thigh decreases/increases sharply before and after the switch of the water temperature (**Figure 3.4**). The thermal flux power is high at the beginning, which is up to ~6 kw, this can be explained by the $\frac{\partial T}{\partial t}$ section in

equation (3-1), as the temperature gradient is really high at the beginning, this makes the heat transfer quite fast. Later, the thermal flux slowly come down, as the temperature of periphery part of the leg is decreasing, which also reduce the value of $\frac{\partial T}{\partial t}$ in equation.

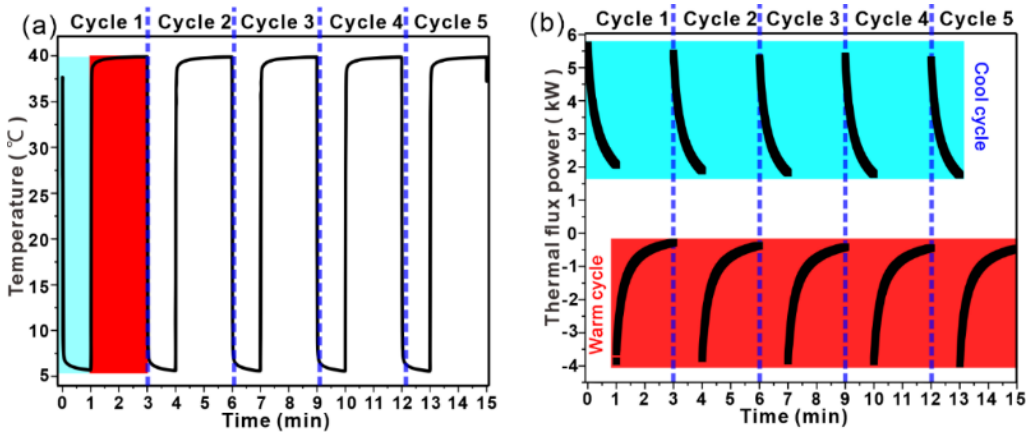

Figure 3.4 (a) The calculated temperature on the surface of the leg vs. time, (b) the calculated thermal flux power through the surface in **Figure 3.2** between the leg and water.

Figure 3.5 shows the overall thermal flux consumption in one thigh, which is integration result of the thermal flux power curve over the time in **Figure 3.4b**. The energy consumption in the cool cycles is much higher than that in warm cycles, this is also because the temperature difference, ΔT, in cool cycles is almost 40 °C. With the number of cycle increase, the thermal flux in cool cycles is decreasing and increases in warm cycles. This is also caused by the change of $\frac{\partial T}{\partial t}$. In first cycle, the surface temperature of the leg is 45 °C, much higher than 5 °C of the cold water, this makes the cycle consume the most thermal flux energy in all 10 cycles. However, with the increasement of cycle number, the overall temperature of the leg has

decreased, this makes the thermal flux energy consumption decreased in the following 4 cycles. When it comes to the warm cycle part, the thermal flux energy consumption is increasing, which is the same reason as mentioned above. The overall temperature of the leg is decreased and the increasement of $\frac{\partial T}{\partial t}$ makes more heat transfer between leg and warm water.

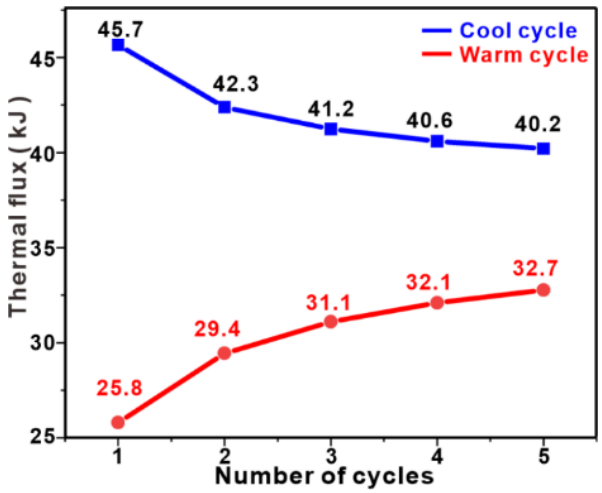

Figure 3.5 Overall thermal flux consumption of one thigh during the five RCP therapy cycles.

In all, the requirement of energy consumption in the fast contrast temperature therapy has been figured out. Guidance can be given for the selection of components for rapid contrast therapy device. The potential highest heat transfer between skin surface and the wearable heat transfer panel is ~360 kJ in 15 min. The thermal transfer is quite large for wearable thermal management systems, so water is selected as the heat transfer medium for wearable heat transfer panel in the following experimental tests. The fast switch between hot and cold therapy poses extreme high requirement on the fast water injection and short hot/cold water alternating period. The ideal

time gap is less than 10s. Obviously, traditional wearable heat transfer panel cannot reach this standard, and the fluid channel need to be redesigned based on the study of internal fluid dynamics. Also, as the wearable heat transfer panel need to perform at least two therapies of different temperatures, the valves and pumps control and water mixing of different temperatures need to be optimized.

3.3.2 Determination of switch logics for higher energy efficiency

The rapid thermal management system uses water as heat exchange medium because of its large heat capacity. Different from other water based wearable heat transfer panels which only need to perform therapy with a particular temperature without changing, this wearable heat transfer panel needs to perform at least two different temperatures for contrast therapy, this requires a new switch logic for switching different water temperatures and may cause severe mixing of water with large temperature difference. This would further decrease the energy usage efficiency since the power and space of external hot/cold source is limited. Considering the high heat flux power and limited electric power provided by a portable power bank, the optimization of switch logical design of different pumps can effectively enhance the performance of this rapid contrast therapy system.

The switch logical design was developed in two categories. In these two figures, the number “0” means the state of the valve is close, water cannot go through in this direction, while the number “1” means open and water can pass the valve in this direction (**Figure 3.8**). The first one is the simplest just with hot and water tanks (**Figure 3.6**), for the purpose of portable and boarding. The first configuration needs fewer valves and the whole system is very simple, which will be used in our current device development. the second is the device added the heating and cooling function by additional thermoelectric units (**Figures 3.8a-b**), which makes the loop

logical circuit more complex and the cost for fabrication is higher, together with the energy consumption, but this configuration can heat and cool water inside the water tank. The second configuration will be clarified in the following 3.3.3 section.

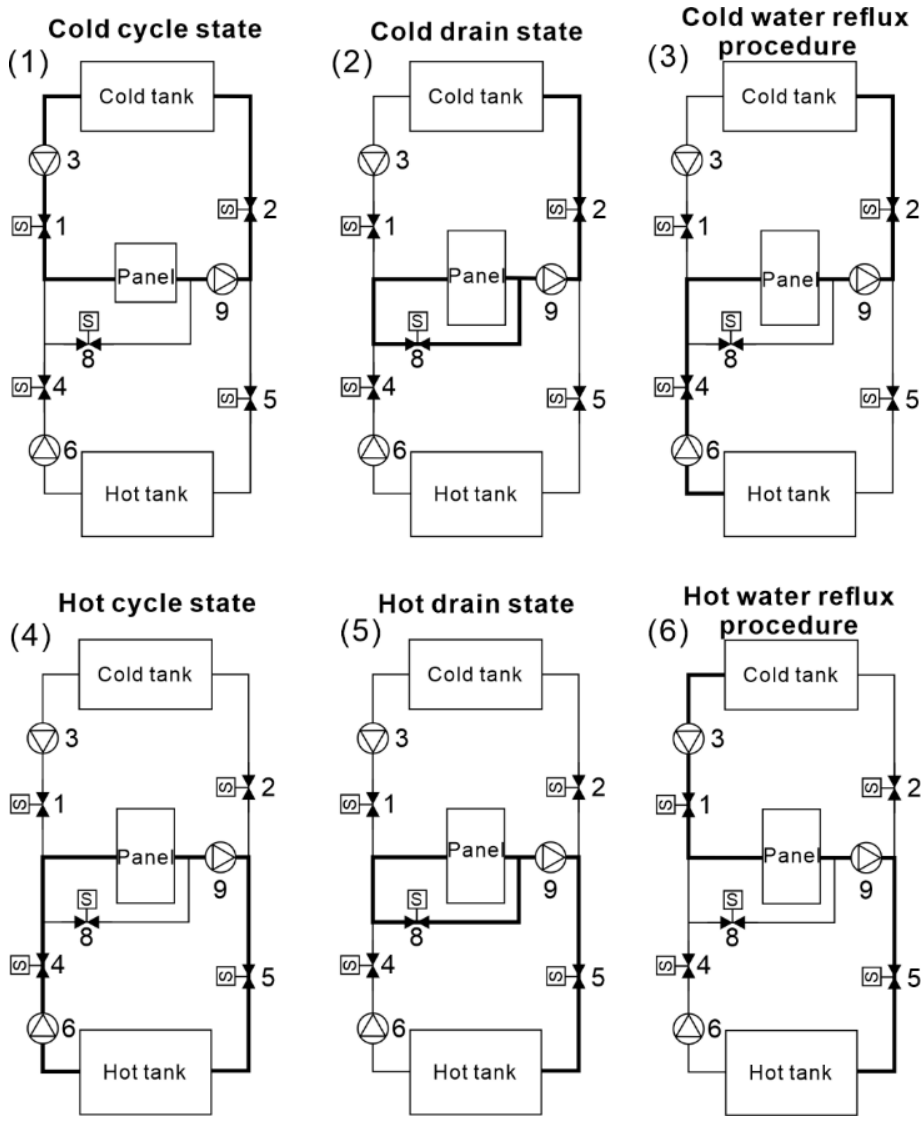

Figure 3.6 Schematic diagram of switch logical design of six different state. (a) cold cycle state, (b) cold drain state, (c) cold water reflux procedure, (d) hot cycle state, (e) hot drain state, (f) hot water reflux procedure.

The whole control system consists of 5 solenoid valves (labels 1,2,4,5,8), 2 pumps (labels 3,6) and 1 drain pump (label 9). Label 7 remains for thermoelectric units in the second configuration. Details of the first configuration are shown in **Figures 3.6**. The prototype for realizing this switch logics is the PLC relay control system as shown in **Figure 3.7**. For higher energy efficiency, the whole circulation is divided into 6 cycle states. Cold/hot cycle states are the longest state for hot/cold therapy. Cold cycle state keeps components 1,2,3,9 on and 4,5,6,8 off, which ensures the cold water circulation between soft heat transfer panel and cold water tank. Hot cycle state keeps components 4,5,6,9 on and 1,2,3,8 off, which ensures the hot water circulation between soft heat transfer panel and cold water tank. Cold/hot drain cycle states are used for sucking the remaining cold/hot water inside the soft heat transfer panel into the cold/hot water tank for reducing the water mixing of different temperatures in the next therapy cycle. Cold drain state keeps components 2,8,9 on and 1,3,4,5,6 off while hot drain state keeps components 5,8,9 on and 1,2,3,4,6 off. This state can extract water both from the inlet tube and outlet tube for shorter sucking period as this state do not perform well in therapy with few and stagnate water inside soft heat transfer panel. Less time in this state the faster switch between two temperatures therapy can be achieved. Cold/hot water reflux procedure are used for further reducing the water mixing of different temperature based on previous cold/hot drain state. Since the remaining water in soft heat transfer panel during previous circulation cannot be completely sucked out, this procedure can use the afterward injected temperature water to push the previous temperature water into the corresponding water tank. The key factor on this procedure is to control the working time of this procedure, otherwise more water of different temperature may be injected into the wrong water tank and caused low energy efficiency. Cold water reflux

procedure keeps components 2,4,6,9 on and 1,3,5,8 off while hot water reflux procedure keeps components 1,3,5,9 on and 2,4,6,8 off.

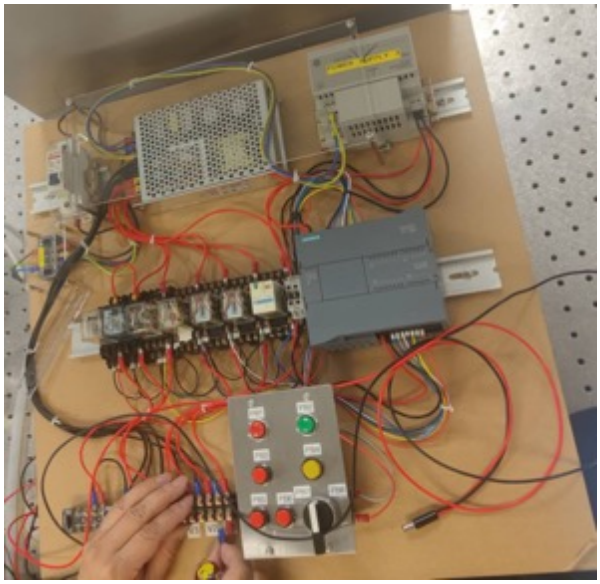

Figure 3.7 PLC/relay control system made in Industrial Center of The Hong Kong Polytechnic University based on the switch logical design above.

By comparing directly injecting the contrast temperature water into the soft heat exchange panel, the appropriate allocation of the 6 cycle states can enhance the energy usage efficiency and obviously enhance the thermal performance of this wearable system. The time relay design is based on the water consumption volume and fluid velocity.

3.3.3 Heating and cooling capability of commercial thermoelectricity (TE) modules

Previous section detailed investigated control logics of hot/cold water circulation control. By appropriate arrangements of the state of valves and pumps in fluid circulation circuit, the energy usage and therapy performance are effectively improved. However, the previous section only contains the hot/cold water tank without heating/cooling function. This part will study the possibility of heating and cooling by thermoelectricity (TE) modules: tests for the heating and cooling ability of TE modules and heating/cooling performance when attached to COOLWEAR thermal management system.

Even though the two logics switch circuits are different (**Figure 3.6** & **Figure 3.8**), the function output is the same: providing the heat transfer device with cold and hot water for time intervals. The output signal of a programmable logic controller (PLC) is the same. **Figure 3.8** is the simplified switch logical design of **Figure 3.6** with the adding of TE modules. **Figure 3.8a** is the cold cycle with TE modules while **Figure 3.8b** is the hot cycle with TE modules. The hot/cold water need to go through the hot/cold planes of TE modules for heat transfer. During the cold cycle, the water passes through the cold water tank, cold plane and leg surface and the hot water only passes through hot water tank and hot plane for heat collection. During the hot cycle, the water passes through the hot water tank, hot plane and leg surface and the cold water only passes through cold water tank and cold plane for cooling down.

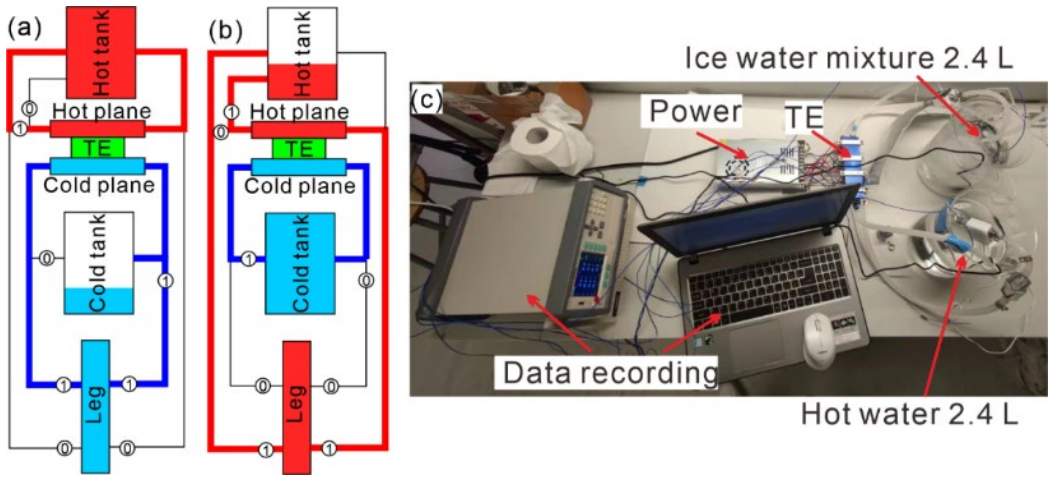

Figure 3.8 Heating ability test of thermoelectric (TE) module. (a) Schematic diagram of switch logical design of cold cycle with TE modules; (b) Schematic diagram of switch logical design of hot cycle with TE modules; (c) Experimental set up of TE heating ability test.

For testing the TE heating ability, four pieces of TE modules are combined for testing. They are powered by a 300-watt power adapter. Two pumps are located in the hot water tank and cold water tank for water circulation. Both hot and cold water tanks contain 2.4 litre water, respectively. Temperature sensors are placed inside these two water tanks for temperature measurement. The initial temperature of cold water tank is set as 0°C, and the initial temperature of hot water tank is set as room temperature (22.4°C). As shown in **Figure 3.9**, is the temperature vs. time when keep the whole test system running. The cold water tank is set and maintained around 0°C with ice. This can help test heat production capability under the worst working condition. The temperature inside hot water tank keeps increasing linearly. It reaches 40°C when 750 s and 50°C when 1336s. The total power consumption of TE modules is ~204 watt. The heat generation during the whole test is ~2.78×10^5 J. The heating power of these four pieces of TE modules is ~208 watt. Thus, the heating power of each TE module unit is ~52 watt.

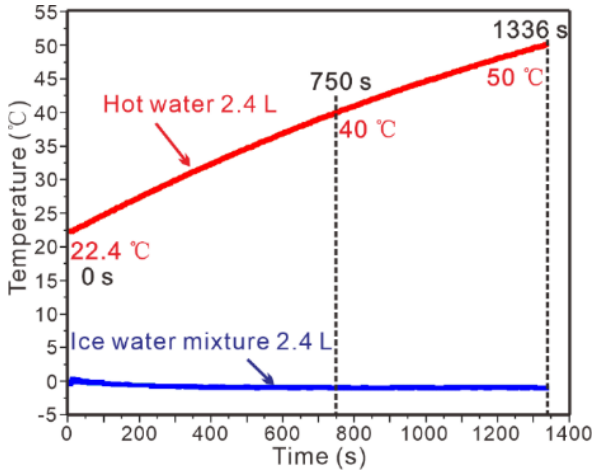

Figure 3.9 Heating ability test result of thermoelectric (TE) module by keeping the cold water around 0ºC and testing the temperature change of hot water side.

For testing the TE cooling ability, eight pieces of TE modules are combined for testing, experimental set up are shown in **Figure 3.10**. They are powered by two 300-watt power adapters. Two pumps are used for water circulation. Hot and cold water tanks contain 800 ml and 300 ml water, respectively. The hot water circulation contains more water for 360 water cooling fans. Temperature sensors are placed inside these two water tanks for temperature measurement. Both initial temperature of cold water tank and hot water tank are set as room temperature (22.4ºC). This experimental set up aims to test the cooling ability of TE modules under the extreme using scenarios – without any ice inside but providing the hot water circulation part with enough heat dissipation facility (two 360 water cooling fans). This experimental set up aims to test the best cooling performance of TE modules under the best heat dissipation condition. Since the thermal management box is designed for portable, the two 360 water cooling fans is the maximum volume for the purpose of portable, otherwise it maybe too large to carry. The temperature inside the hot water tank reaches 42.5ºC and keep as a

constant after 360 s. The temperature inside the cold water tank reaches 5ºC from the beginning 22.4ºC after 240 s. So the heat transfer power from cold plane to hot plane of this TE modules is ~99 watt and the cooling power of each TE unit is ~12.5 watt. This means under the best heat dissipation condition of a portable device, the TE unit can transfer 12.5 J heat energy from cold plane to hot plane every second.

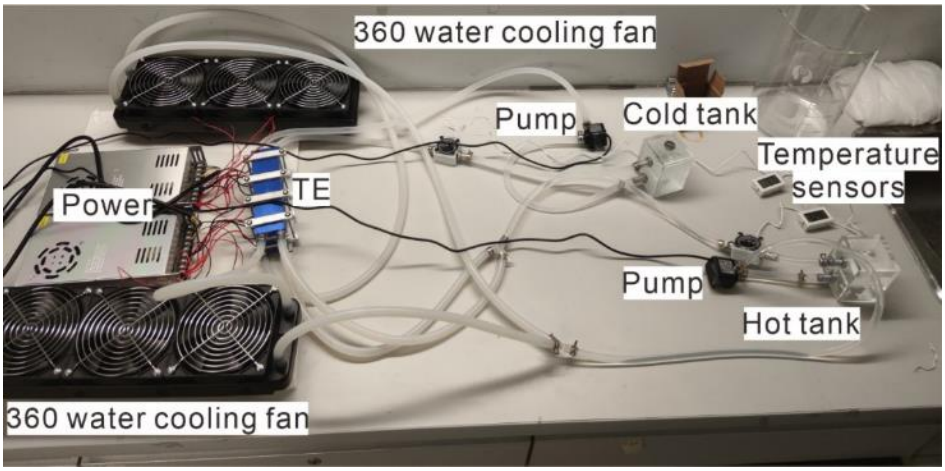

Figure 3.10 Cooling ability test experimental set up of TE heating ability test.

Based on previous data, the TE unit can transfer 12.5 J heat from cold plane to hot plane while generating total 52 J heat on the hot plane at the same time. This means that the generated heat is four times higher than the transferred heat and the adding or extra heat dissipation is necessary. The temperature difference between cold and hot plane strongly affects the heat transfer ability from cold plane to hot plane. When the hot plane is under good heat dissipation condition, the heat transfer ability of TE modules can be enhanced. That's why the temperature curve in **Figure 3.9** is linear while nonlinear in **Figure 3.11**.

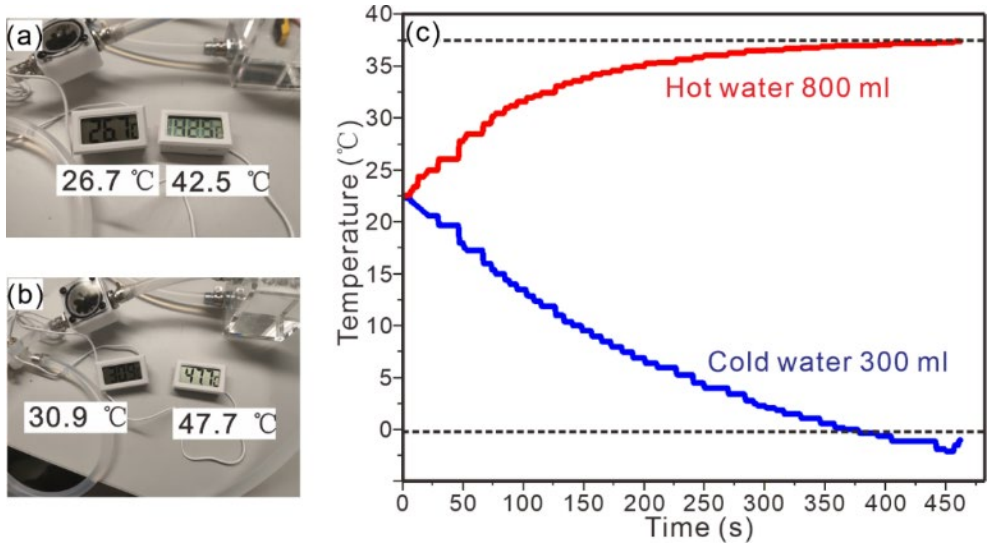

Figure 3.11 Cooling ability test result of thermoelectric (TE) module start when both hot and cold water tank are 22ºC (room temperature). (a) Final temperature of hot and cold water tank with 360 water cooling fans; (b) Final temperature of hot and cold water tank without 360 water cooling fans; (c) Temperature vs time result of TE module with 360 water cooling fans.

The effect of TE modules is still unclear in real application scenerios since the above data of TE modules capability are acquired in extreme conditions. The experimental set up in **Figure 3.12** aims for testing the temperature maintenance ability of TE modules. The temperature maintenance test is performed by attaching the 8 pieces of TE modules to the circulation of our research group developed COOLWEAR fast contrast therapy system. The hot plane is attached to the circulation of hot water tank and the cold plane is attached to the circulation of cold water tank with two water pumps. The eight-pieces TE modules are powered by a 600-watt power adaptor. The room temperature is ~20ºC. The two soft heat transfer panels are expanded on the

ground for controlling the heat dissipation (as the temperature on surface skin is difficult to control). The COOLWEAR performs 5 cycles of contrast therapy. 1 minute for cold water circulation and 2 minutes for hot water circulation. This system can automatically heat the water when temperature is lower than a particular value (50ºC setting in this test) in hot water tank and the maximum power of heating is ~400 watt. Total 5 cycles last for 15 minutes.

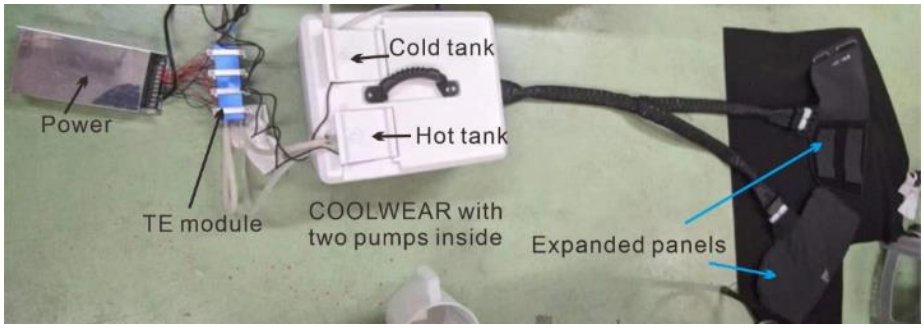

Figure 3.12 Temperature maintenance ability experimental set up of thermoelectric (TE) module by attaching to COOLWEAR system.

As shown in **Figure 3.13**, the temperature maintenance test is under five different primary conditions: (a) cold water tank with 1.5 litre room temperature water and 1.5 litre ice, hot water tank with 3 litre 50ºC water, all 8 pieces TE modules turned on. The total power consumption of this state during water circulation is 600 watts – 1000 watts. (b) cold water tank with 1.5 litre room temperature water and 1.5 litre ice, hot water tank with 3 litre 50ºC water, but all 8 pieces TE modules turned off. The total power consumption of this state during water circulation is ~400 watts. (c) The cold water tank temperature is maintained under 5ºC with enough ice, hot water tank with 3 litre 50ºC water, 4 pieces TE modules turned on. The total power consumption

of this state during water circulation is ~700 watts. (d) The cold water tank temperature is maintained under 5ºC with enough ice, hot water tank with 3 litre 50ºC water, all 8 pieces TE modules turned on. The total power consumption of this state during water circulation is 600 watts – 1000 watts.

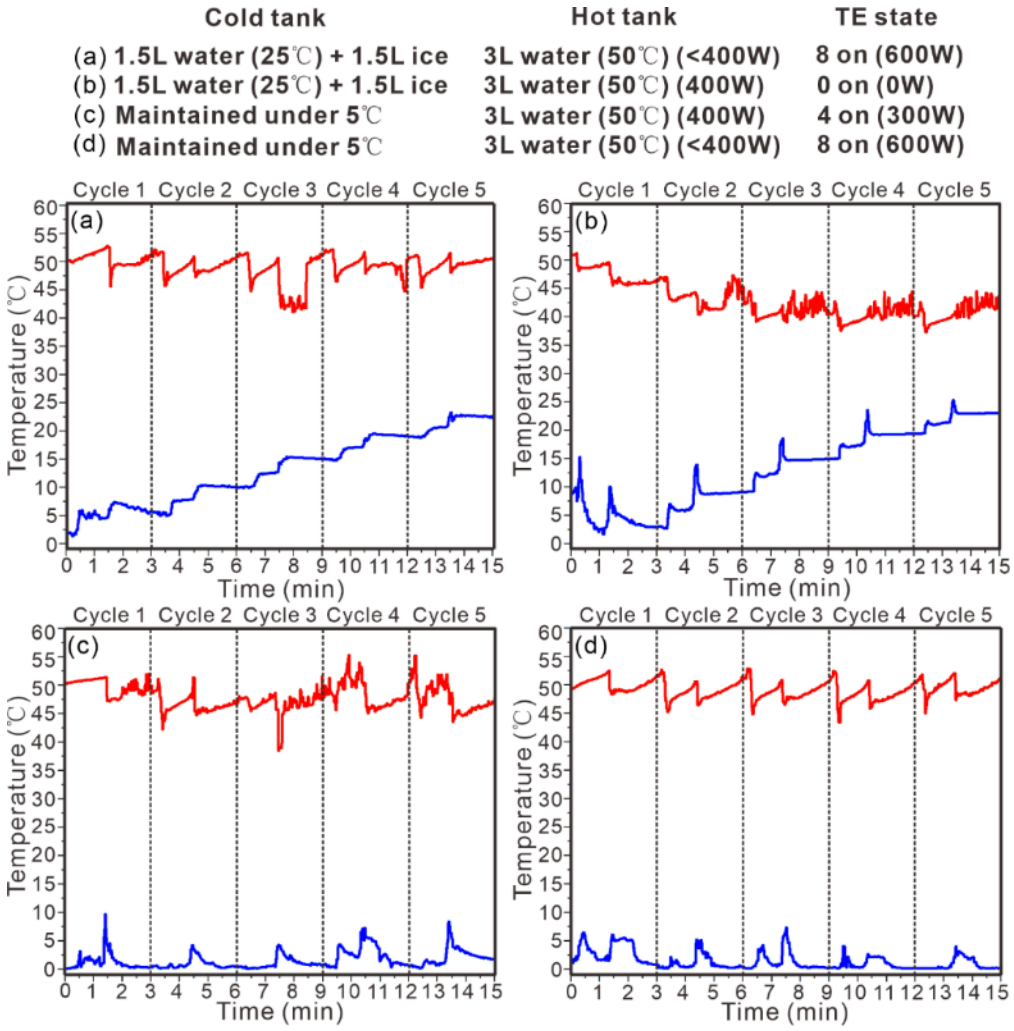

Figure 3.13 Temperature maintenance ability testing results of thermoelectric (TE) module by attaching to COOLWEAR system. (a) Temperature vs. time during five cycles with 8 TE modules turned on, the original state of water tank in this test is 1.5 liter room temperature

water mixed 1.5 liter ice in cold water tank and 3 liter 50ºC hot water in hot water tank; (b) Temperature vs. time during five cycles without TE modules, the original state of water tank in this test is 1.5 liter room temperature water mixed 1.5 liter ice in cold water tank and 3 liter 50ºC hot water in hot water tank; (c) Temperature vs. time during five cycles with 4 TE modules turned on, the original state of water tank in this test is maintained under 5ºC in cold water tank and 3 liter 50ºC hot water in hot water tank; (d) Temperature vs. time during five cycles with 8 TE modules turned on, the original state of water tank in this test is maintained under 5ºC in cold water tank and 3 liter 50ºC hot water in hot water tank.

As shown in **Figure 3.13a**, the temperature in hot water tank is maintained mostly higher than 45ºC. A sudden drop on temperature occurs during the temperature switch period as some cold water may be mixed into the hot water tank is unavoidable. The temperature in cold water tank is increasing with the increment of switching circulations. The final temperature value is around 20ºC which is not suitable for a cold therapy since the temperature is too high. Even though the temperature is slightly dropping during the cold therapy circulation, the TE modules cannot maintain the temperature under a particular value. But the TE modules can total maintain the temperature in hot water tank. This test results show the 8 pieces of TE modules and heater inside can maintain the hot water tank temperature, but the situation is not desirable on the cold water tank side, together with high power consumption. **Figure 3.13b** shows the results without TE modules, the temperature in water tank can also be maintained higher than 40ºC. This means the heating power 400 watts is enough for 5 cycles. However, when comparing the temperature curve in cold water tank in **Figure 3.13a&b**, no obvious difference between these two results. Even though there is a slight temperature decrease in condition (a), the final temperature is just

2ºC lower than that without TE modules. So, the TE modules are not suitable for onsite cold water tank temperature maintenance. They can only be used for the cold water preparing of cold therapy with sufficient time. Since the TE modules can maintain the hot water temperature on the previous two conditions, the following two conditions aim to test the heating ability of TE modules under extreme temperature difference between hot and cold plane. As shown in **Figure 3.13c&d**, temperature can be maintained above 45ºC and this temperature is high enough for hot therapy. In general, due to the nature of TE materials, even though it is small and not noisy when comparing to other cooling devices, it is unavoidable to produce too much extra heat for heat transfer from cold plane to hot plane. This makes them not suitable for onsite portable cold therapy, especially for this kind of contrast therapy with unavoidable hot and cold water mixing during temperature switch.

3.4 Summary

In this chapter, we have explored the potential applicable strategy for the fast contrast therapy, evaluated the controlling logics and temperature maintenance capability of fast contrast therapy system. With the thermal modelling and simulations of water immersion rapid contrast therapy, the strategy for thermal management is cooling/heating by water circulation due to the large heat transfer during water immersion. To reduce the mixing of different temperature water, an optimized switch design is proposed for higher energy efficiency with appropriate sucking and reflux period control. Portable heating/cooling strategies like directly adding ice, heat by heating rod, TE cooling and heating are tested and evaluated. For onsite fast contrast therapy, directly adding ice for cold therapy and heating by heat rod is the most suitable thermal

management strategy. TE modules consume too much energy and large heat transfer amount from cold plane to hot plane. They are more suitable for thermal management without large thermal transfer amount and frequent large difference temperature switching.

CHAPTER 4 Network-Structured Fluidic Fabrics for Large Area Rapid Wearable Thermal Management

4.1 Introduction

Fluidic fabrics are widely used in the realm of wearable technology, offering versatile applications particularly in thermal regulation and force feedback mechanisms. These advanced textiles are used in sports recovery[159] and medical sectors[161] by providing precise thermal control and localized cooling or heating for injury treatment and rehabilitation. In Virtual and Augmented Reality (VR/AR) applications, fluidic fabrics contribute to immersive experiences through haptic feedback, enhancing user interactions by simulating touch and force sensations[162]. Furthermore, outdoor enthusiasts benefit from these fabrics in garments designed for efficient thermal management, ensuring comfort across varying environmental conditions. In extreme environments such as space exploration[163], fluidic fabrics are integral in maintaining astronaut body temperatures, crucial for prolonged missions and extravehicular activities.

The core functionality of these diverse applications lies in the meticulous flow control within the fluidic fabrics. So that, the heat and force can be delivered in the desired way. However, a significant challenge arises in large-area thermal regulation: the slow flow velocity. This limitation often leads to uneven temperature distribution and large time span latency in large cover area, undermining the efficiency and effectiveness of the wearable's thermal management system. Traditionally, wearable heat transfer panels have relied on circulating water, air, or

utilizing phase-change materials for heat transfer. Despite their utility, these methods inherently suffer from the same drawback—single-channel flow systems. This single-channel approach causes the problem of slow and uneven thermal distribution, particularly over expansive areas. To address this issue, large-area fluid distribution network composed of numerous branching structures is proposed.

Inspired by naturally occurring models such as tree branches, river systems, and biological capillaries, these network structures aim to enhance the uniformity and speed of fluid flow[39–41]. The trees can distribute the nutrition to the terminals for leaves due to the numerous branches mass transfer. There are no floods in areas with plenty of rivers. This is because the flow rate can be adjusted when one channel is blocked. Thus, this blocked water can be distributed to other rivers. Biological capillaries can control the flow rate of blood at different temperatures by adjusting the flow resistance at different parts. Then less flood would be transferred to the low temperature region for thermal regulation. All these examples shows that the network structure can effectively manipulate the flow field in a large area by controlling the flow rate at specific channels or areas.

By mimicking these intricate natural patterns, fluidic fabrics can potentially achieve more efficient thermal regulation across broad surfaces, paving the way for more advanced and effective wearable technologies. This work proposed a network structure which can distribute water over a large area for covering human body. For fast fluid velocity and uniform temperature distribution, the flow resistance at different regions of this device is preciously controlled and the turnings of the wearable heat transfer panels are reduced to two for less head loss due to the velocity direction change. Based on this network structure, five wearable heat transfer panels specifically for fast contrast therapy is prepared. The full leg wearable heat

transfer panel can be fulfilled with water in 6 s and perform the different temperature switch in 10 s. The thigh and calf wearable heat transfer panels can be fulfilled with water in 4 s and 3 s, respectively. And both can perform different temperature switch in 10 s. The last two wearable heat transfer panels are for knees and ankles, the area is much smaller when compared to the previous 3 wearable heat transfer panels, both can also perform different temperature switch in 10 s.

This chapter first tells the fabrication method and experimental testing of the wearable heat transfer panels. Secondly, the analysis of experiments and numerical simulation results on a representative traditional wearable heat transfer panel for sports recovery is conducted. Thirdly, the design principles of this network-structured is proposed and the experiment results and numerical simulation results on full leg wearable heat transfer panel are analysed. Last, other two wearable heat transfer panels (thigh, calf) are fabricated based on the previous design principles.

4.2 Methodology

4.2.1 Device fabrication

Three network-structured devices (wearable heat transfer panels for whole leg, thigh and calf) were made by ratio-frequency welding two pieces composite fabrics of polyamide fabric laminated with a thermoplastic polyurethane film in an aluminium mold, using a SANDEN KS_4000T welder (**Figure 4.1**).

Figure 4.1 SANDEN KS_4000T welder for making network-structured devices. By ratio-frequency welding two pieces composite fabrics of polyamide fabric laminated with a thermoplastic polyurethane film in an aluminum mold.

The manufacturing process of the network-structured fluidic fabric is shown in **Figure 4.2**. Firstly, the outline of the wearable heat transfer panel is cut. Then, by ratio-frequency welding, the guide vanes and reinforcement dots are adhered thus the network structure fluid channels are formed. Last, by covering the wearable heat transfer panel over the leg, and injecting fluid inside, the wearable heat transfer panel can perform hot/cold therapy.

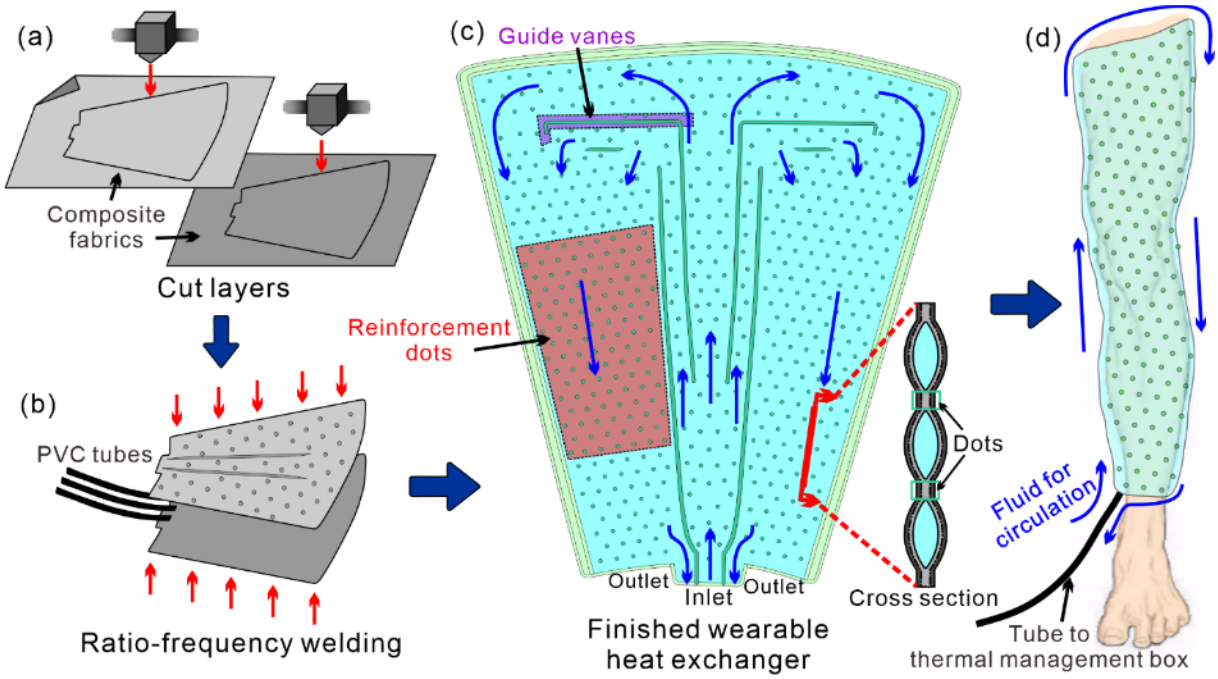

Figure 4.2 (a-b) Manufacturing process of the network-structured fluidic fabric were first cut out shape of layers and then adhering two pieces composite fabrics and PVC tubes by ratio-frequency welding; (c) The full leg network-structured heat transfer panel contains reinforcement dots and guide vanes for controlling the flow field inside, the two kinds of welding units formed the nature inspired network-structured wearable heat transfer panel for large area rapid thermal management; (d) The laminated fabric was soft and can be adapted to complex shapes for the purpose of wearable, the heat transfer fluid can go through the channels formed by these reinforcement dots and guide vanes to conduct large area rapid thermal management.

The making process of network-structured fluidic fabrics can be modified thus making multilayer fluidic fabrics with different functions. **Figure 4.3a** is the two-layer network structure with single fabric material. This can be used for simple wearable heat transfer by

injecting different temperature water. **Figure 4.3b** is the three-layer network structure with 3 kinds of fabric materials which can fill two different fluids. The inner fluid channel can be injected with water for thermal regulation and the outside fluid channel can be injected with compressed air for force feedback (such as massage). **Figure 4.3c** is the four-layer network structure with 3 types of materials for pneumatic actuating, anisotropy flexible fluidic fabric upside and inextensible fluidic fabric downside. By welding the four layers, three types of materials together, the fluidic fabric can provide force feedback with compressed air inside.

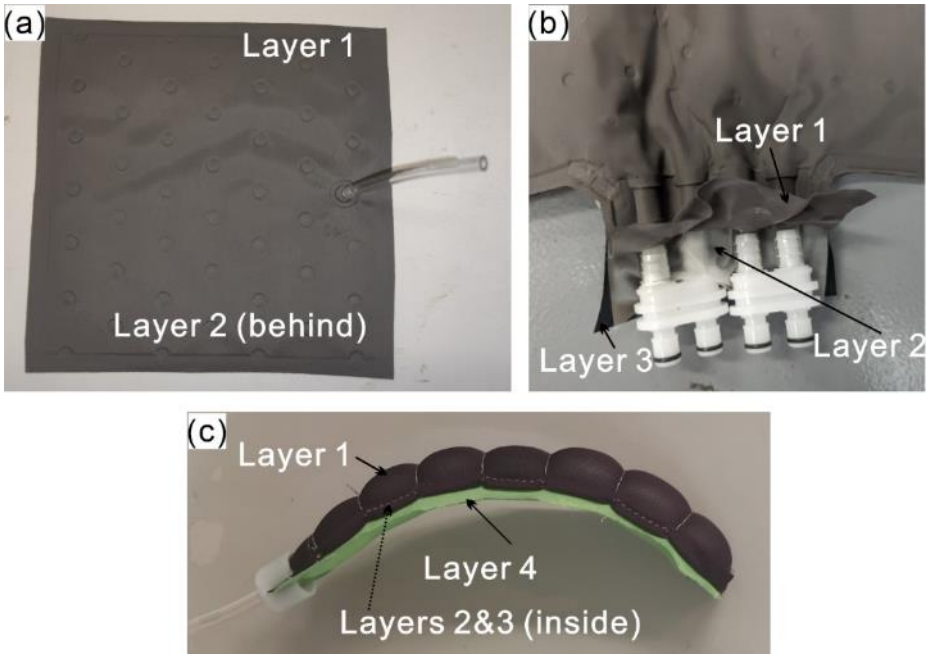

Figure 4.3 (a) Two-layer network structure with single fabric material; (b) Three-layer network structure with 3 kinds of fabric materials which can fill two different fluids (e.g. water and air); (c) Four-layer network structure with 3 types of materials for pneumatic actuating, anisotropy flexible fluidic fabric upside and inextensible fluidic fabric downside.

4.2.2 Numerical simulation and experimental set up

All the reinforcement dots in wearable heat transfer panels are set 5 mm in diameter, and the distance between each dot is different depending on the corresponding function area. Since the dimension in the thickness direction is much smaller than that in the spanwise direction, its flow in the thickness direction is neglected for simplifying to two-dimensional models. This can accelerate the calculation without sacrificing the general flow field characterizing accuracy. Otherwise, the simulation would be tedious and time consuming. The 3D space fluid field simulation of network structure is analyzed in the following chapter with modified parameters for better analyzing. The shapes of the following wearable heat transfer panels are designed to fit the legs, thighs and calves of elite athletes.

The heat transfer inside the wearable heat transfer panels can be expressed as follows[164]:

$$d_Z \rho C_p \frac{\partial T}{\partial t} + d_Z \rho C_p \vec{u} \cdot \nabla T + \nabla \cdot \vec{q} = d_Z Q + q_0 + d_Z Q_p + d_Z Q_{vd} \tag{4-1}$$

$$\vec{q} = -d_Z k \nabla T \tag{4-2}$$

$$\rho = \frac{p_A}{R_S T} \tag{4-3}$$

Where ρ is the density, C_p is the specific heat capacity at constant pressure, T is the absolute temperature, $\vec{u}$ is the velocity vector, $\vec{q}$ is the heat flux by conduction, Q contains heat sources other than viscous dissipation.

The flow of water inside the wearable heat transfer panels can be expressed as follows [164]:

$$\frac{\partial \rho}{\partial t} + \nabla \cdot \left(\rho \vec{V}\right) = 0 \tag{4-4}$$

$$\frac{\partial \vec{V}}{\partial t} + \vec{V} \cdot \left(\nabla \vec{V}\right) = \vec{f} - \frac{1}{\rho}\nabla p + \frac{\mu}{\rho}\nabla^2 \vec{V} + \frac{1}{3}\frac{\mu}{\rho}\nabla\left(\nabla \cdot \vec{V}\right) \quad (4\text{-}5)$$

To fit the boundary conditions mentioned in chapter 3, the primary water temperature inside is set as 40°C and the water temperature from inlet is set as 5 °C. The velocity of the inlet ranges from 0.25 m/s to 1 m/s, which corresponds to the output performance of the pump in our laboratory. No heat transfer with the surroundings. The calculation is time-dependent, and the calculation time is set as 30 s. The physics fields are heat transfer and laminar flow.

Experimental set up of the network structure device fluid field observation is shown in **Figure 4.4**. Since the heat transfer panel is flexible and the measurement of internal fluid field is quite difficult. The fluid field is observed by an infrared camera. When the heat transfer panel is injected with different temperature water, the fluid field evolution can be roughly presented with the temperature mapping. **Figure 4.4a** is the experimental set up, the fluid field observation is obtained by the temperature distribution during water injection and different temperature water switching, the temperature is observed by an infrared camera on top of the network structure device. **Figure 4.4b** is the fluid control section consists of two water pumps, two flowmeters and two liquid manometers are placed at inlet and outlet. The water pumps are for water injecting and sucking. The flowmeters are for measuring the flow velocity. The liquid manometers are for pressure drop measurements.

As the heat transfer panels for legs (full leg, thigh, calf), users prefer to place their legs horizontally on the ground. In the cases from this thesis, the gravity effect can be neglected to reduce the simulation time

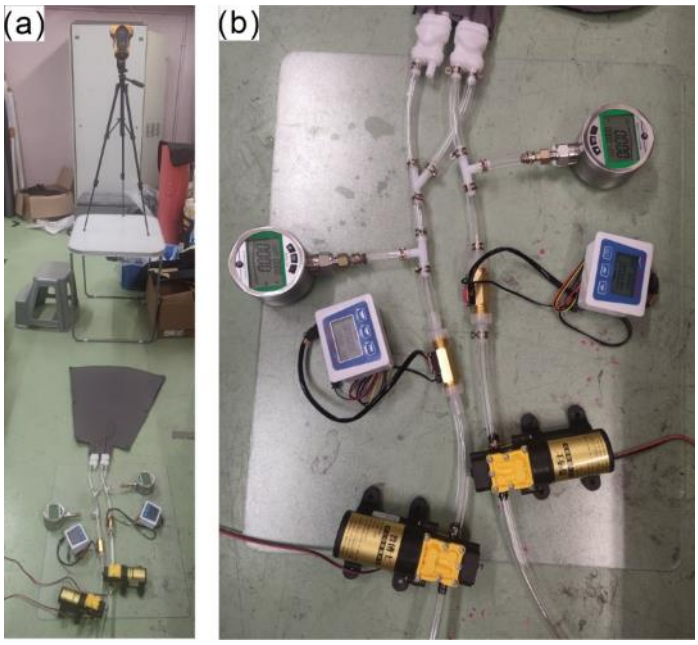

Figure 4.4 Experimental set up of the network structure device fluid field observation by an infrared camera. (a) The fluid field observation is obtained by the temperature distribution during water injection and different temperature water switching, the temperature is observed by an infrared camera on top of the network structure device. (b) Fluid control section consists of two water pumps, two flowmeters and two liquid manometers are placed at inlet and outlet.

4.3 Results and discussion

4.3.1 Traditional wearable heat transfer panels

Traditional wearable heat transfer panels are usually constructed by single tube channel or simple one-way fluid circulation routine, as shown in **Figure 4.5**. Their fluid channels are allocated arbitrary just to cover the heat transfer area without the consideration of heat transfer

efficiency. The channels contain lots of turnings and the flow resistance is very high when increasing the flow velocity inside. This limits the heat transfer quantity during the working time of heat transfer panel.

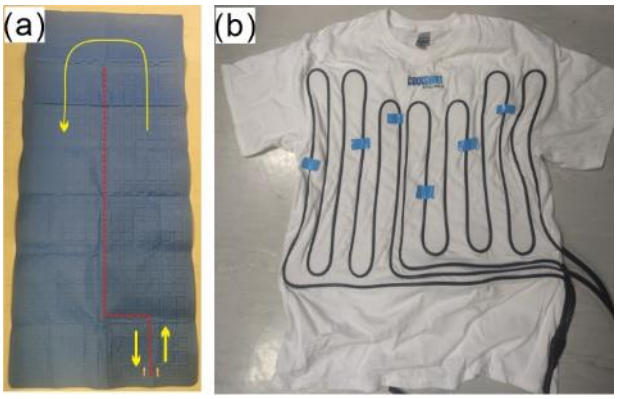

Figure 4.5 Traditional commercial single tube wearable heat transfer panels, all the fluid channels of these wearable heat transfer panels are allocated arbitrary. (a) Water-cooling mattress; (b) Water-cooling T-shirt.

Game ready wrap is a representative wearable heat transfer panel of wide single channel with numerous reinforcement dots (**Figure 4.6**). **Figure 4.6a** is the schematic diagram of Game Ready wrap for full leg. The curved guide vanes along the single fluid channel can mitigate the bucking effect of periphery fabrics. This can further improve the conformability of this wearable heat transfer panel. The reinforcement dots inside are designed for the purpose of reducing the thickness when inflated with cold water. As shown in **Figure 4.6c&d**, the wearable heat transfer panel is ~4.27 mm in thickness when injected with water and ~1.27 mm in thickness of welded fabrics. The dots density is also very high, the diameter of reinforcement

dots is ~4.28 mm. This makes the full leg wearable heat transfer panel light and thin when it is working on human body with water circulating inside. The water consumption of this full leg wrap is ~500 ml.

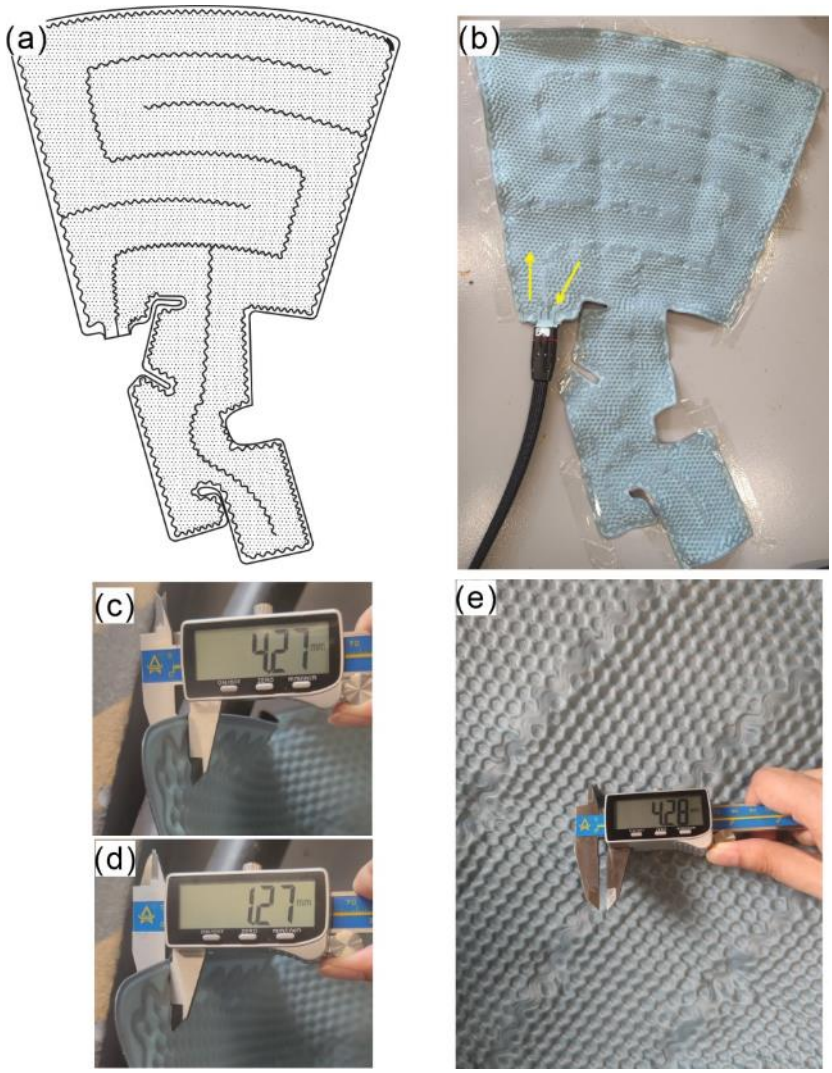

Figure 4.6 Traditional commercial single tube wearable heat transfer panel – Game Ready wrap for full leg. (a) Schematic diagram of Game Ready wrap for full leg – constructed by curved guide vanes and numerous reinforcement dots. (b) This wearable heat transfer panel

contains a wide fluid channel with many reinforcement dots and turnings. (c-e) The wearable heat transfer panel is ~4.27 mm in thickness when injected with water and ~1.27 mm in thickness of welded fabrics. The diameter of reinforcement dots is ~4.28 mm.

The heat transfer coefficient and pressure drop are important criteria for evaluating the thermal performance of all heat transfer panels. Appropriate power loss control and uniform velocity distribution are of great importance due to the characteristics of the flexible wearable heat transfer panel: 1. large coverage area, 2. same position of the water inlet & outlet. Traditional single tube wearable heat transfer panels (**Figure 4.5**) usually contain many corners to ensure the whole panel is filled with water, but this results in high power loss and low fluid velocity.

Figure 4.7 shows the heat performance of this wrap for full leg. It takes ~164 s for this wearable heat transfer panel reaches a steady state. The temperature is uneven, and it is increasing gradually from inlet to outlet along the direction of this single channel tube the water passes by. This is caused by the heat transfer between heat transfer panel and the ambient air. The front water can absorb more heat due to longer heat transfer time and the temperature is higher. This uneven temperature mapping and long fluid field developing time (time for reaching a steady state) can be improved by accelerating the flow velocity inside.

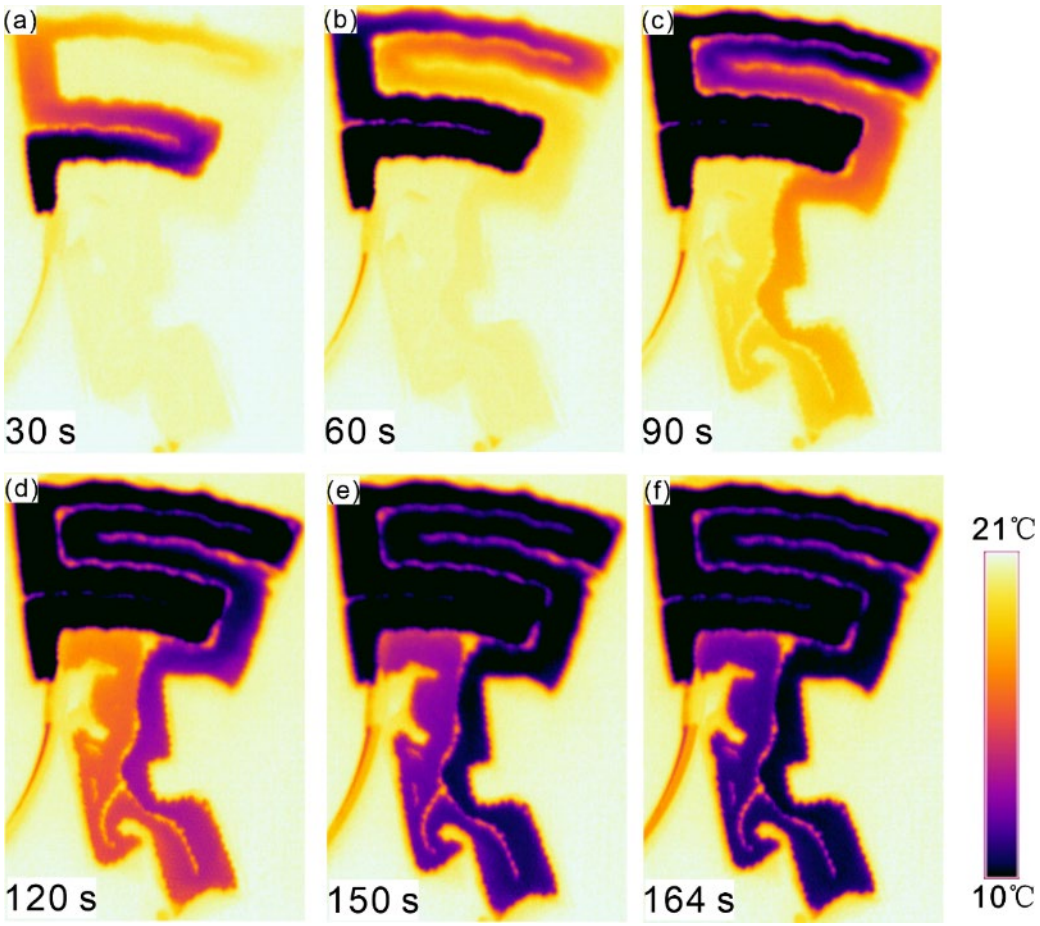

Figure 4.7 The temperature distribution of Game Ready wrap for full leg, the outlet temperature reaches a steady state after 164s. Also, the temperature distribution of this wearable heat transfer panel is uneven due to the low flow velocity inside.

Figure 4.8 shows the numerical simulation calculation results of Game Ready wrap for full leg. The inlet velocity is set as 0.15 m/s, the simulation results show the full leg wrap takes ~160 s to reach a steady state. This corresponds to the previous experimental results. As shown in **Figure 4.8a&c**, the velocity magnitude is higher in the middle part of the wide tube while relatively lower at the corners. A 'die' area with quite low velocity occurs at the bottom part of

this full leg wrap. Due to the nature of single tube and the contribution of numerous reinforcement dots, the velocity evenness inside the tube can be guaranteed. The uniformity of heat transfer can be enhanced by increasing the flow velocity inside. **Figure 4.8d** is the pressure mapping of this full leg wrap. The highest pressure occurs at the inlet while the lowest near the outlet. The pressure drop shows the flow resistance the fluid inside need to overcome. Usually, the pressure drop would increase together with the flow velocity. Simply increase the velocity at inlet by using a larger pump is not acceptable for wearable heat transfer panels. This can make the pressure at the inlet extremely high and further tear the fabric and cause water leakage. The following channel redesigned network-structured wearable heat transfer panel shows uniform temperature mapping and extreme fast flow velocity, which significantly enhance the heat performance of wearable heat transfer panels.

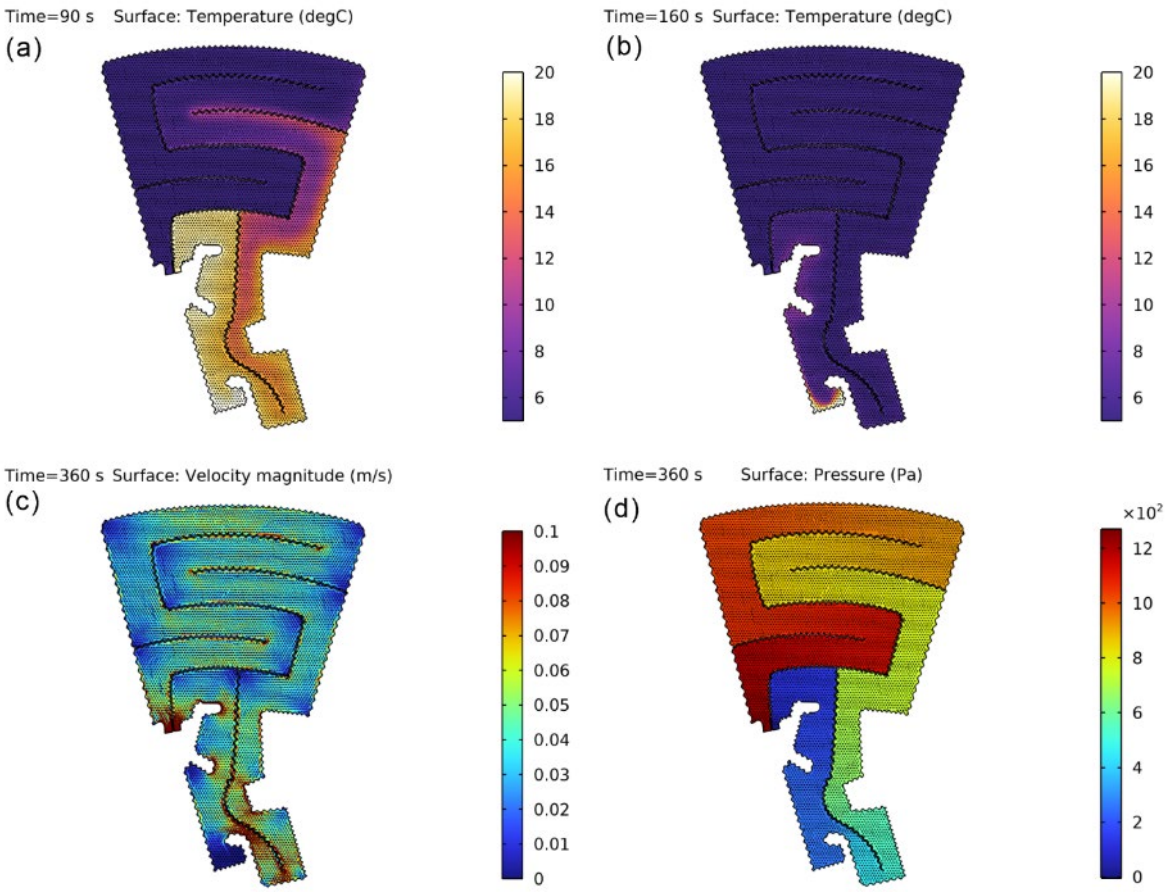

Figure 4.8 Numerical simulation calculation results of Game Ready wrap for full leg, the inlet velocity is set as 0.15m/s. (a-b) The temperature distribution at 90 s and 160 s. (c) The velocity magnitude distribution of this Game Ready wrap when the flow field is fully developed. (d) The pressure distribution of this Game Ready wrap when the flow field is fully developed.

4.3.2 Network-structured wearable heat transfer panel for full leg

The full leg example (**Figure 4.2c**) shows the general procedure of designing and making this rapid wearable heat transfer panel based on the following 2 chapters analysis: A 4-step mass

mixing mechanism, controllable automatic homogeneity by adjusting the flow field and power loss evaluation. Final versions of the three wearable heat transfer panels (full leg, thigh and calf) were acquired based on large amounts of simulation results for different network structure parameters and extensive experimental proof and validation.

4.3.2.1 Design principles of network structures and practical application performance

Network structures are widely present in nature (**Figure 4.9**). They are widely used for mass transfer from limited sources to numerous terminals with extensive coverage. Areas with plenty of rivers can adjust the flow rate of each branch to avoid floods. In life entities, branches of trees are used for distributing water and nutrients to the terminals of leaves and capillaries can easily shrink and expand to control the flow rate of blood. The network structures can effectively control the flow rate of each dendritic channels by adjusting the wall shapes of them. **Figure 4.10a-c** shows schematic diagrams of single tube/network structure fluidic fabrics filled with fluid; network fluidic fabrics contains numerous reinforcement dots for flow field manipulation with wider fluid channel while the single tube can only transfer fluid in a narrow channel with lots of turnings. **Figure 4.10d-e** shows cross-sectional view of network structure device filled with fluid inside. **Figure 4.11** shows the idea of electric-fluidic analogy. The reinforcement dots in the wearable heat transfer panel can be used for the flow field manipulation. Based on the idea of network structure and flow field control by reinforcement dots, the wearable heat transfer panel with fast flow velocity successfully designed.

Figure 4.9 Network structure in rivers follows the natural topology of landscape, while that of trees and capillaries are self-adjustable when one branch is blocked and can distribute fluid and mass in large area.

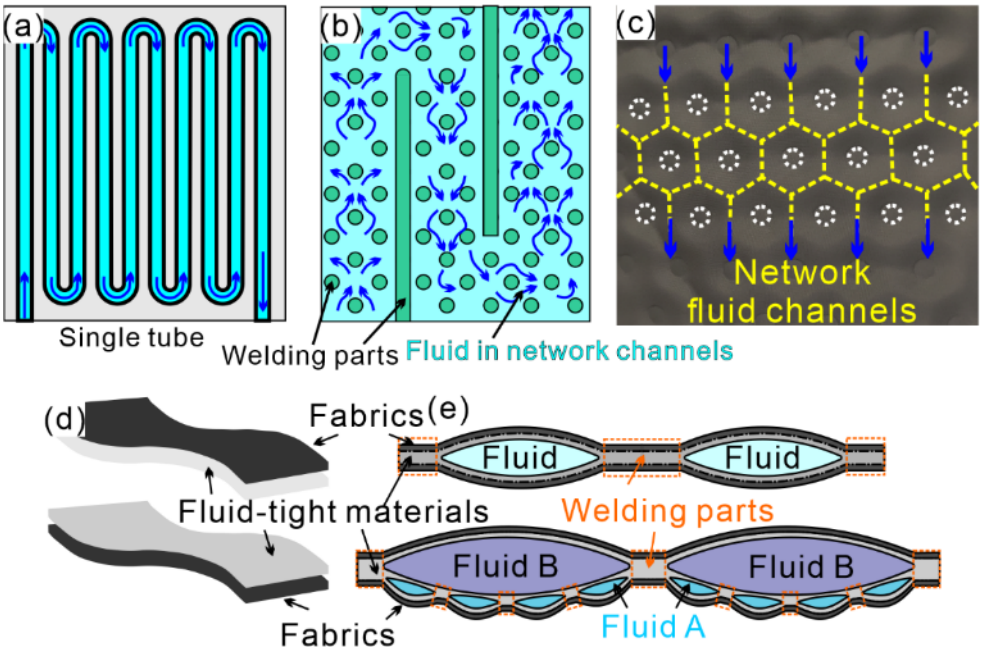

Figure 4.10 (a-b) Schematic diagrams of single tube/network structure fluidic fabrics filled with fluid, network fluidic fabrics contains numerous reinforcement dots for flow field manipulation with wider fluid channel. (c) The fabricated network fluid channel, fluid can pass through the channels formed by the reinforcement dots and the curved walls formed by

the laminated fabrics. (d-e) The cross-section view of network structure device filled with fluid inside.

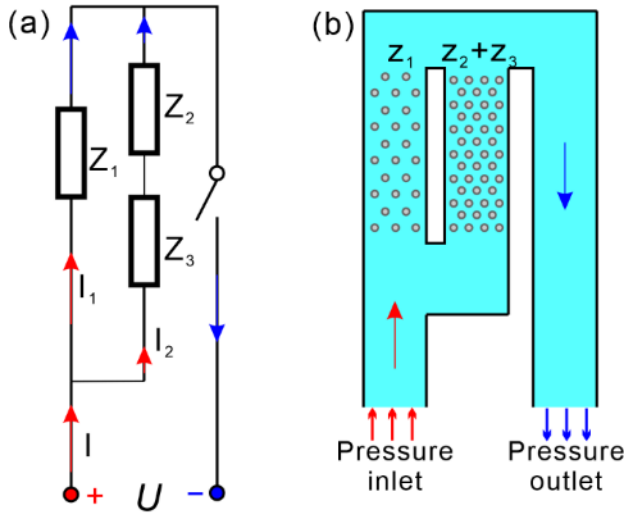

Figure 4.11 Schematic of network-structured fluid channel and electric-fluidic analogy.

This heat transfer panel for a whole leg can be filled uniformly in less than 6 s with a 24 V water pump at the inlet, power ~30 W (**Figure 4.12** & **Figure 4.16**), much faster than traditional commercial wearable heat transfer panels (more than 1 min, **Figure 4.7** & **Figure 4.12**) and those without an appropriate dots and tube arrangement design (**Figure 4.27**). The results showed the appropriate arrangement of network structure can significantly increase the fluid velocity and enhance the performance of wearable heat transfer panels. The heat efficiency was obviously enhanced due to faster fluid velocity inside, leading to a lower circulation time and a large temperature gradient between the heat transfer panel and skin surface. The outlet temperature of the network-structured heat transfer panel in this work reached a stable state in

6 s and the temperature difference between the outlet and inlet was less than 3 ℃. The fast fluid velocity and uniform temperature distribution meant that the local power loss of each part of this heat transfer panel was reasonable.

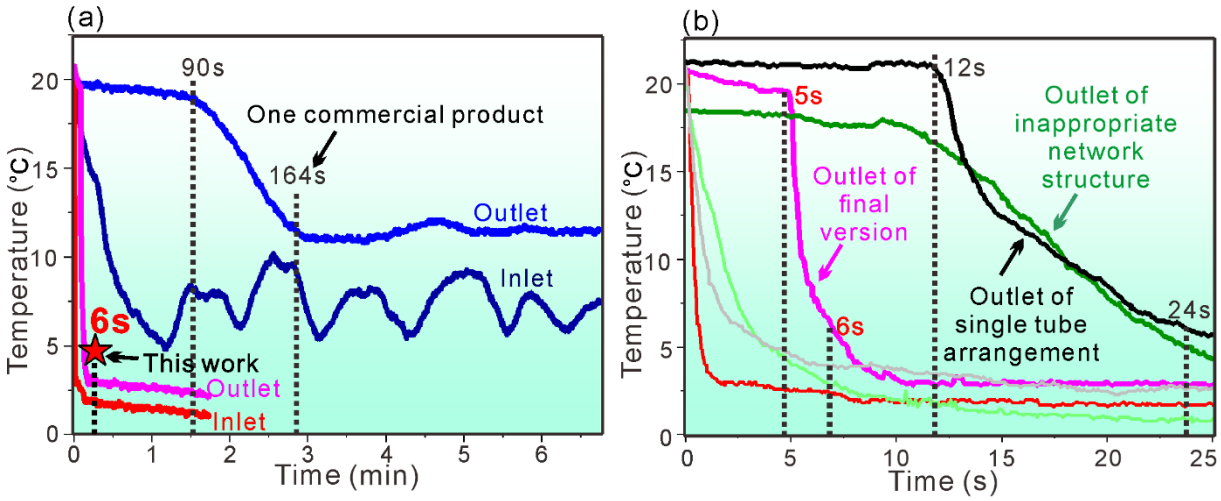

Figure 4.12 (a) This full leg network-structured wearable heat transfer panel showed much faster thermal management than one commercial product on sale, the heat efficiency was obviously enhanced due to fast fluid velocity inside thus less circulation time and large temperature gradient between heat transfer panel and surface skin, the outlet temperature of network-structured heat transfer panel in this work went to a stable state in 6 s and the temperature difference value between outlet and inlet is less than 3 ℃, fast fluid velocity and uniform temperature distribution means the local power loss of each part of this heat transfer panel was in a reasonable level; (b) Outlet temperature comparison of final version of this work, FHTP with inappropriate network structure and single tube arrangement in **Figure 4.27** by the same pumping system. With appropriate network structure, the final version of our FHTP showed faster thermal management, while the water took ~ 12 s to the water outlets

and more than 24 s for temperature uniform distribution. The lower fluid velocity causes the outlet flow temperature to drop more slowly. Also, with the potential safety problems caused by high pressure.

For real application scenarios, another two wearable heat transfer panels were used, thigh and calf, for this wearable thermal management system. An onsite thermal performance test of the thigh wearable heat transfer panel was conducted for this wearable thermal management system (**Figure 4.13**). **Figure 4.13** shows the skin temperature before and after the 1-minute cold therapy with a water temperature of ~ 5 °C, and most of the thigh surface is affected. The areas of the guide vanes and reinforcement dots, however, show higher temperatures. This means the cross-directional thermal conductivity is poor. As the fabric inflates, the welding dots form air gaps between the fabric and skin such that thermal transfer is only by radiation. Our network-structured wearable heat transfer panels have been used by elite athletes for enhancing their competition performance. **Figure 4.14** shows the real scenario with an athlete using the calf network-structured heat transfer panel for fast sports recovery.

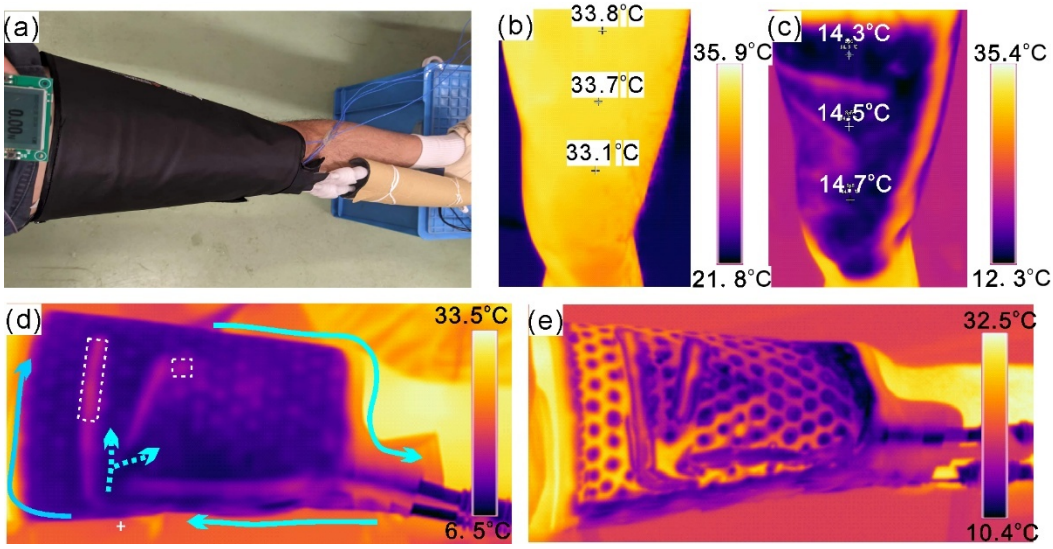

Figure 4.13 Applications of the network-structured wearable heat transfer panels for thigh. (a) Demonstration of thigh experiment by thermal management system. An infrared camera was placed nearby for recording surface temperature; (b-c) Skin temperature before & after 1-min cold therapy. The heat transfer panel can effectively decrease the temperature on the thigh uniformly; (d-e) Surface temperature mapping on human body of the thigh heat transfer panel during cold therapy and the temperature switch period. This uniform heat performance can also be achieved when worn on the human body.

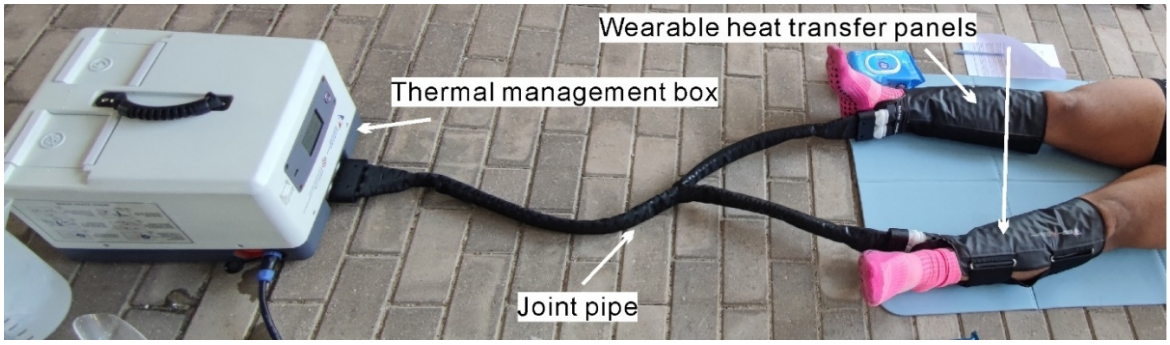

Figure 4.14 An athlete is using the thermal management system with network-structured calf wearable heat transfer panels for fast contrast therapy after training on field.

We designed this network-structured heat transfer panel (**Figure 4.2c**) by changing "R" and "D" and the local pressure drop can be controlled (detailed investigated in chapter 5), thus manipulating the flow field at different parts of heat transfer panel. For reducing kinetic energy loss at the corners of tubes, this heat transfer panel contains only two major corners on the top side (**Figure 4.15a**). Thus, the heat transfer panel is divided into 4 different function areas – function area 1 (FA1), FA2, FA3 & FA4 (**Figure 4.15b&c**). The parameters (this will be detailed discussed in Chapter 5 & 6) of the network structure are different in the 4 function areas. FA1 is close to the inlet tube, and the fluid velocity is very large. The dot density here is smaller leading to less power loss, but large enough for dispersing the velocity from a narrow inlet. After the incident flow is dispersed by FA1, FA2 will distribute the water into three narrow tubes. The flow resistance Z3 of the two tubes on the side was the same. The distance from inlet to outlet of the two side tubes is shorter than that of the central tube in FA2 (**Figure 4.15c** & **Figure 4.16a**). Water will then go to FA3 - the flow resistance Z3 is larger than Z2 to avoid velocity unevenness, so that more water can go to FA3. As the inlet and two outlets are located at the bottom, this will make the water tend to flow to the central axis and reduce the fluid rate at the margin of FHTP thus weaken the heat performance. FA3 was designed with one long and short guide vanes with numerous reinforcement dots. This part is affected not only by the arrangement of dots, but also the change in velocity direction. The two guide vanes formed the three inlets of FA4 and the flow rate on the margin of FHTP is the largest while with lower flow resistance/pressure drop/power loss. The other two outlets are designed for eliminating the "die area" (a second flow formed vortex with extreme low flow velocity) under the long guide vane. The two outlets are much narrower and with higher density of reinforcement dots. This means Z4 + Z2 is smaller than Z5 + Z3, so that water in these two

areas can go to FA4 (main heat transfer area) almost at the same time (**Figure 15c** & **Figure 4.16b&c**) when passing through the two routes. The dot density in FA4 is higher leading to less water consumption (for smaller thermal management box) and better velocity evenness. The velocity in FA4 is much smaller thus making the flow resistance Z7 small. **Figure 4.16** indicated that the appropriate network structure can evidently increase the water velocity for less circulation time thus enhancing the heat transfer coefficient and keeping the pressure drop at a reasonable level.

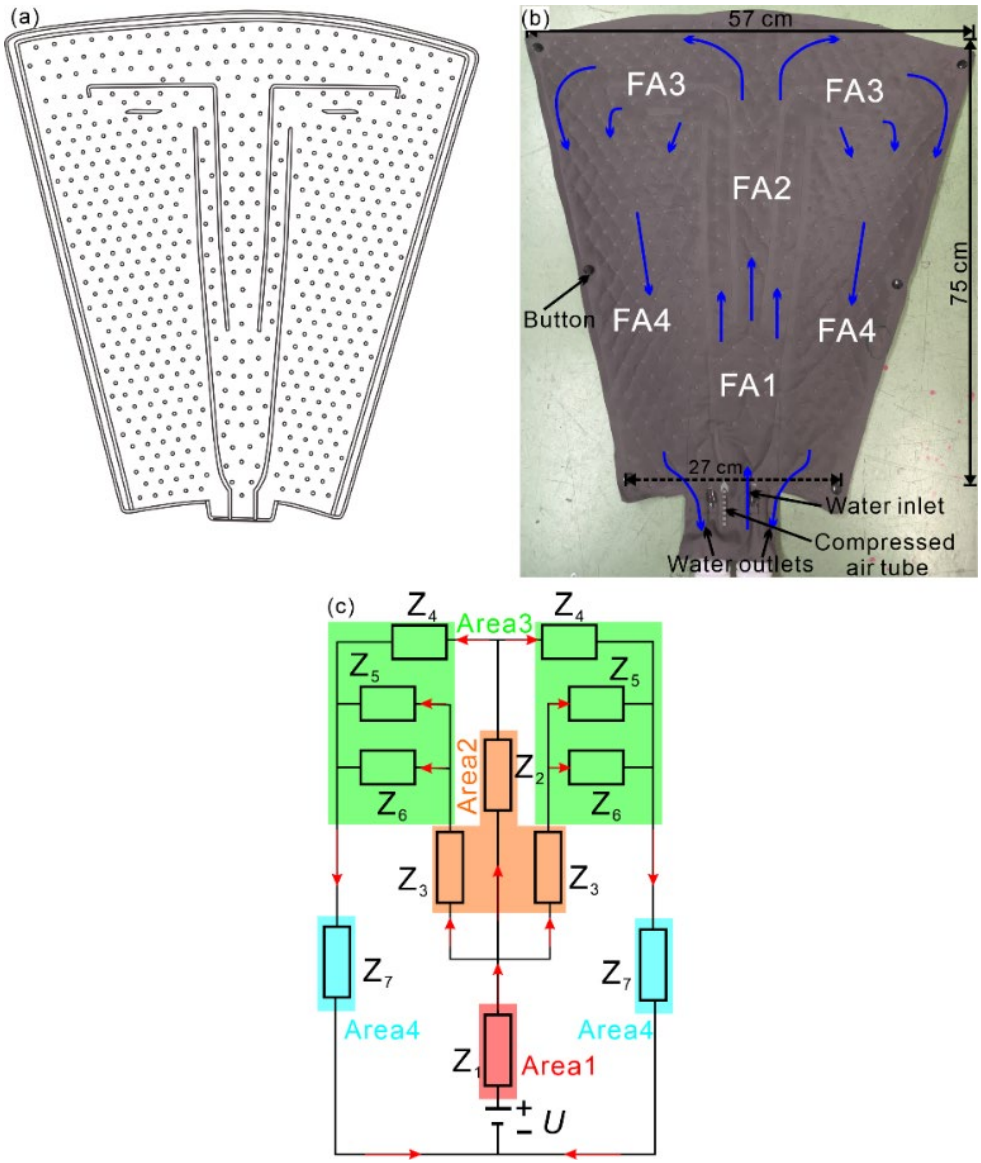

Figure 4.15 Rapid and uniform thermal performance of full leg network-structured heat transfer panels. (a-b) A well-designed network-structured wearable heat transfer panel for whole leg (~0.32 m^2) with 4 functional areas (FA) for the purpose of dispersion (FA1), fast transfer (FA2), connection (FA3) and large area heat transfer (FA4), appropriate control of network-structured parameters can make the heat transfer panel with fast fluid velocity, uniform heat performance and suitable power loss; (c) Equivalent fluidic circuit diagram for network structure heat transfer panel with four functional areas.

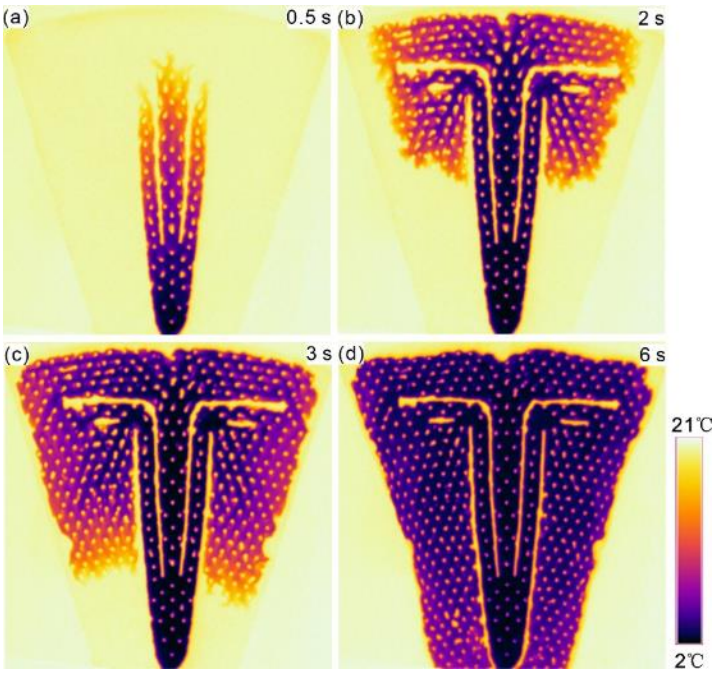

Figure 4.16 The heat transfer panel for whole leg can be filled with water quite fast in ~6 s (V_0 = 0.8 m/s) and show uniform heat performance due to appropriate control of network-structured parameters in different parts of this wearable heat transfer panel, this fulfilled the requirement of fast contrast temperature therapy for fast recovery of athletes after training.

4.3.2.2 Flow field analysis

Previous part tells the design principles of the network-structured full leg wearable heat transfer panel. Experiments and simulation results in this part further reveals the fluid field evolution inside and outward temperature mapping behaviour. However, real applications are always more complicated, since the boundary conditions are different under different usage scenarios. **Figure 4.16** shows the full leg wearable heat transfer panel can be filled with water quite fast in ~6 s. This part mainly focuses on the fluid field analysis when it is fully developed. The purpose of this part is to have a general understanding of the macro fluid field of this full leg

wearable exchanger. The following experiments only focus on the fully developed fluid field indirectly indicated by surface temperature mapping. The simulations only focus on the simplified two-dimensional models. Previous Game Ready wrap simulation shows the calculated results roughly corresponds to the experiment results.

Figure 4.17 & **Figure 4.18** are numerical simulation calculation results of wearable heat transfer panel for full leg. The only difference is the inlet velocity is 0.5 m/s in **Figure 4.17** while 1.0 m/s in **Figure 4.18**. By comparing velocity mapping, the velocity can be nondimensionalized since the flow states are the same. The first reinforcement dot and the following several arrows of reinforcement dots are of great importance, which is named as FA1 for the purpose of dispersion the inlet fluid. The first reinforcement must be placed in the middle part of the fluid channel. If this reinforcement dot is located close to one boundary of inlet guide vane, the uneven flow can affect the following fluid field evolution and cause the flow tend to concentrate in one particular routine and weaken the heat transfer capability of the whole wearable heat transfer panel. Reinforcement dots and guide vanes of inappropriate design is detailed discussed in section 4.3.4. The angle of the inlet guide vanes cannot be too high. The guide vanes at inlet are parallel to the inlet flow direction. After the first reinforcement dot, the angle of guide vanes is set as ~7° with a curve connect to the inlet guide vanes. The connection curve and inlet guide vanes can restrain the backward-facing step flow. The direction of this flow is usually adverse to the inlet flow, this may cause severe energy dissipation and decrease the flow velocity. The following four reinforcement dots are located near the connection curve for restraining the backward-facing step flow. It can be further proved by the vorticity contour map. The following reinforcement dot is located in the middle part of the previous last two reinforcement dots for the purpose of further dispersion. Other following reinforcement dots

are in hexagonal sampling lattice with larger dots distance for smaller flow resistance. When the water goes into the FA2, two extra guide vanes occur. The middle water tunnel continues to expand gradually. The two narrow water tunnels aside the middle water tunnel contain reinforcement dots with higher density. This has been explained in previous part for avoiding too much water goes on the two aside channels and weaken the heat transfer on the margin part of this heat transfer panel. The flow field shows distinct Karman Vortex Street. This is different from most commercial wearable heat transfer panels as most of their fluid field are laminar flow. Transition flow contains both laminar and turbulence factors. It doesn't cost too much energy dissipation but enough for flow field homogenization. Despite the two corners and low velocity regions at the end of the vertical guide vanes, most part of this wearable heat transfer panel show uniform and fast flow velocity. This ensures the excellent heat performance of this wearable heat transfer panel. The pressure contour maps show the highest pressure occurs near the inlet and the lowest near the outlet. The result corresponds to the previous full leg Game Ready pattern simulation results. But the highest pressure is ~1600 Pa when inlet velocity is 1.0 m/s, four times higher than the value ~400 Pa when the inlet velocity is 0.5 m/s. It shows the relationship between inlet velocity and pressure drop is nonlinear.

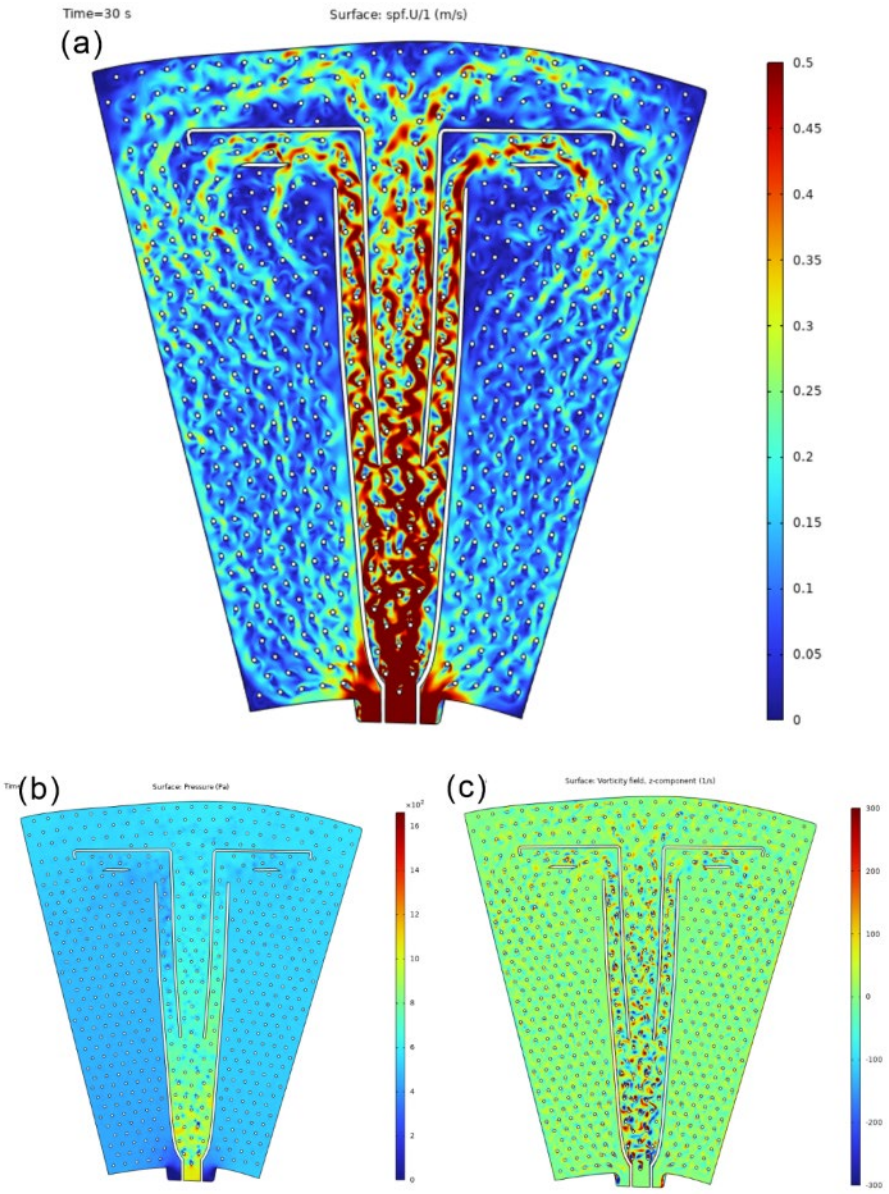

Figure 4.17 Numerical simulation calculation results of wearable heat transfer panel for full leg (V_0 = 1.0 m/s). (a) The velocity magnitude distribution of this wearable heat transfer panel when the flow field is fully developed; (b) The pressure distribution of this wearable heat transfer panel when the flow field is fully developed; (c) The vorticity distribution of this wearable heat transfer panel when the flow field is fully developed.

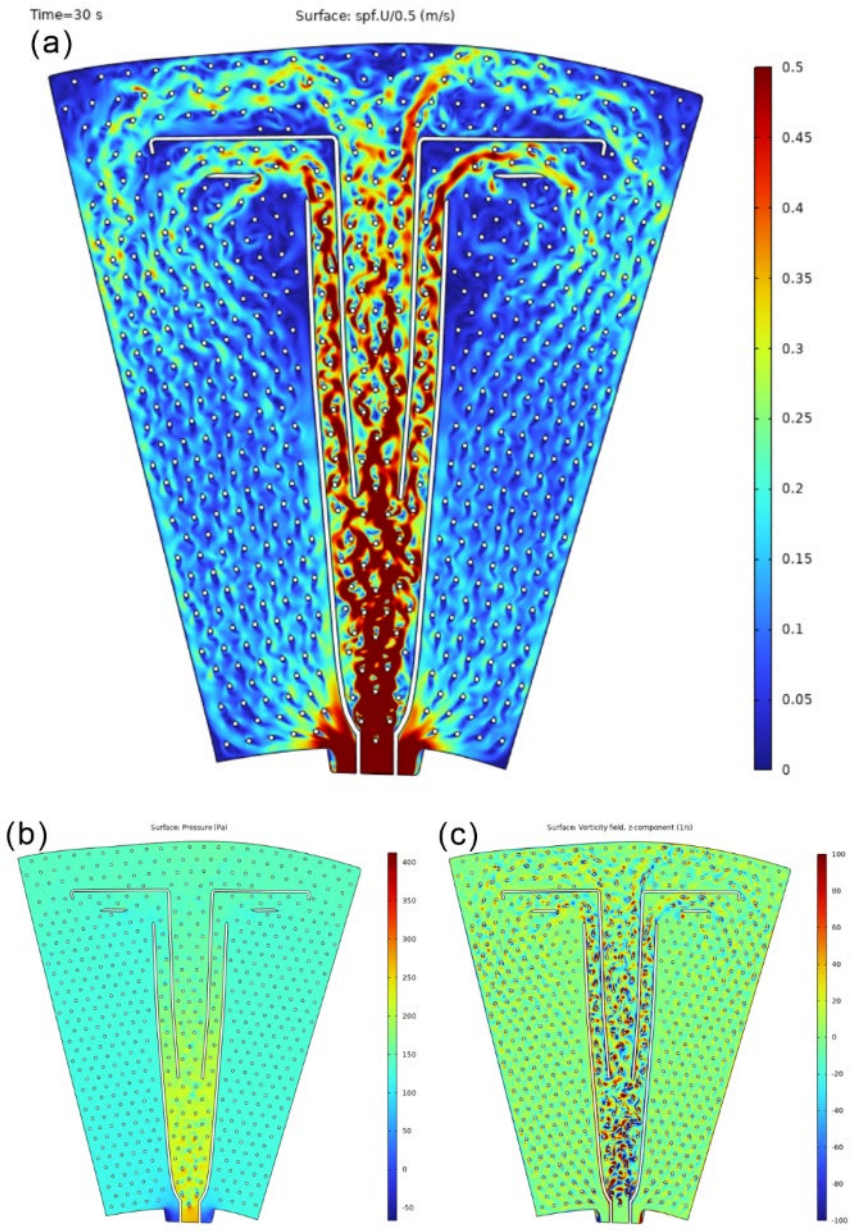

Figure 4.18 Numerical simulation calculation results of wearable heat transfer panel for full leg (V_0 = 0.5 m/s). (a) The velocity magnitude distribution of this wearable heat transfer panel when the flow field is fully developed; (b) The pressure distribution of this wearable heat transfer panel when the flow field is fully developed; (c) The vorticity distribution of this wearable heat transfer panel when the flow field is fully developed.

Figure 4.19 & **Figure 4.20** are the temperature mapping of the full leg wearable heat transfer panel with inlet velocity 0.5 m/s and 1.0 m/s, respectively. This experiment is performed by running this heat transfer panel with hot water into a stable state, the suddenly switching the inlet tube from hot water tank to cold water tank to observe the fluid field indicated by temperature mapping. The difference between the two experiments are the time for the cold water to replace the hot water. It takes ~10 s for the cold water to replace the hot water when the inlet velocity is 1.0 m/s while ~44 s when the inlet velocity is 0.5 m/s. The macro fluid field evolution tendency with different inlet fluid velocity is almost the same, this corresponds to the V/V_0 velocity mapping in simulation results. The difference between simulation results and experiments is the "die" area located at the end of the inlet guide vanes. The "die" area disappeared in experiments because of boundary layer caused extra flow resistance. The flow resistance in other directions is larger than that in the two-dimensional simulation results. The temperature mappings show obvious asymmetry. As shown in **Figure 4.20c-d**, the flow velocity on the right part is always higher regardless of the inlet flow velocity. Two factors make this phenomenon happens: 1. The asymmetry guide vane at inlet for the purpose of air massage affects the following flow field evolution. The large vortex inside this small "die" area affects the inlet velocity direction and lead more fluid turns to the right side. 2. The human leg is naturally asymmetry; right part of this wearable heat transfer panel is smaller than the left part. This caused the right part flow resistance is smaller under the condition of the same reinforcement dots density.

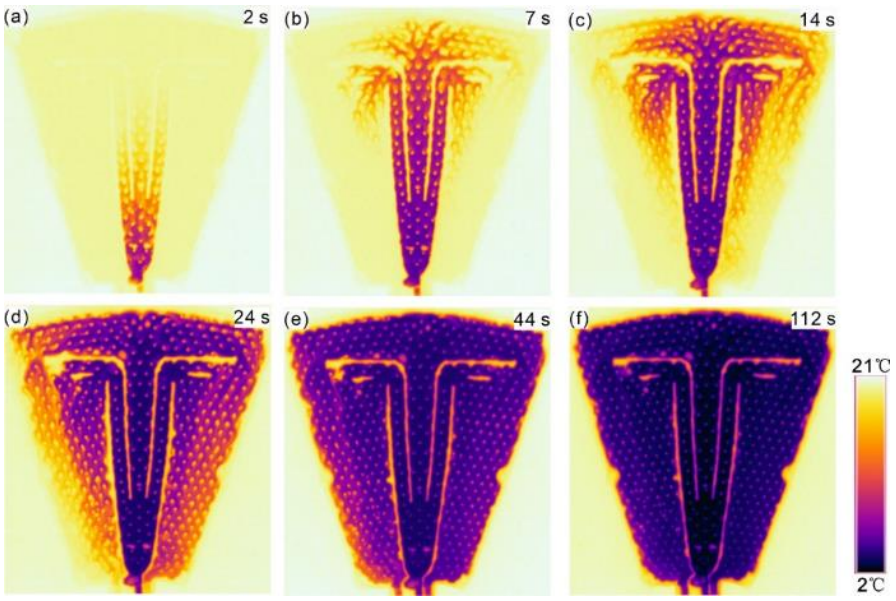

Figure 4.19 Temperature mapping of wearable heat transfer panel for full leg (V_0 = 0.5 m/s) at different times. It takes ~44 s for the cold water to replace the hot water.

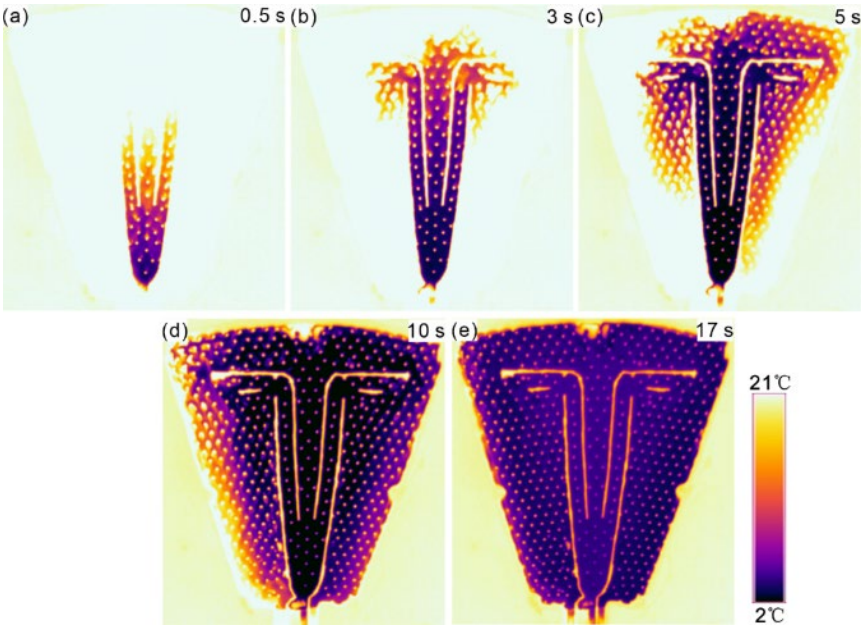

Figure 4.20 Temperature mapping of wearable heat transfer panel for full leg (V_0 = 1.0 m/s) at different times. It takes ~10 s for the cold water to replace the hot water.

4.3.3 Network-structured wearable heat transfer panels for thigh and calf

Another two network-structured wearable heat transfer panels for thigh and calf are also design based on the principle for making the full leg wearable heat transfer panel through an appropriate network structure design at 4 different function areas of the heat transfer panel (**Figure 4.21**). On consideration of the garment fitting and device user friendly, the inlet and outlets are set at the bottom of the wearable heat transfer panel. Thus, the thigh heat transfer panel inlet guide vanes and FA1&FA2 dots arrangement are different from the full leg due to the larger distance vertical to the inlet flow direction. The inlet guide vanes are much shorter, and the angle is increased to ~10^{o}. The two network-structured heat transfer panels for thigh and calf show excellent uniformity for the heat transfer process and extreme short switching times between two different temperatures (**Figure 4.22**).

The thigh wearable heat transfer panel can be filled in 4 s. **Figure 4.23** is the numerical simulation calculation results of this wearable heat transfer panel and **Figure 4.24** is the temperature mapping of wearable heat transfer panel when the cold water is replacing the hot water. Near the inlet, the flow passes through the first reinforcement dot without causing severe backward-facing step flow due to the two slant reinforcement dots besides. However, a large, inflated bulge occurs between the first two reinforcement dots in the middle line of wearable heat transfer panel, and this further causes the poor heat transfer in this region. Same phenomenon also occurs in the two inner turnings near the end of the inlet guide vanes. Although the flow resistance is still not perfect and this makes the flow velocity on the right part lower when comparing to the left side, the thigh wearable heat transfer panel can also perform the water replacement in ~12 s (~8 s when inlet velocity increases to 1.0 m/s).

The calf wearable heat transfer panel can be filled in 3 s. **Figure 4.25** is the numerical simulation calculation results of this wearable heat transfer panel and **Figure 4.26** is the temperature mapping of wearable heat transfer panel when the cold water is replacing the hot water. As the geometry shape of calf wearable heat transfer panel is similar to that of full leg heat transfer panel, the guide vanes and reinforcement dots design strictly follow the principle of full leg heat transfer panel. The performance is better due to smaller area. The calf wearable heat transfer panel can perform water replacing in ~6s (~3 s when inlet velocity increases to 1.0 m/s).

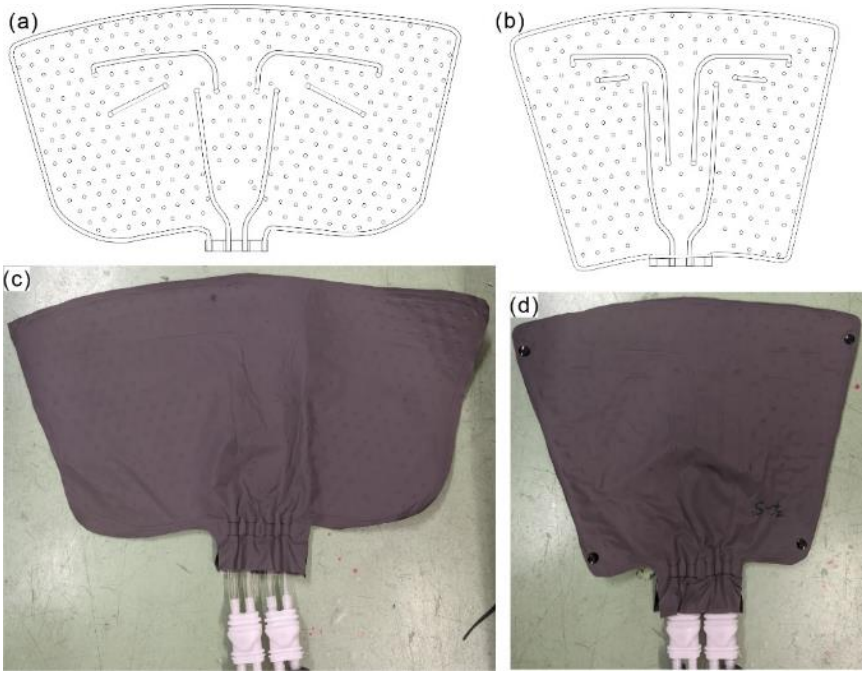

Figure 4.21 Rapid and uniform thermal performance of network-structured heat transfer panels for thigh and calf. The two well-designed network-structured wearable heat transfer panels also contain 4 functional areas (FA) as illustrated in the previous full leg wearable heat transfer panel.

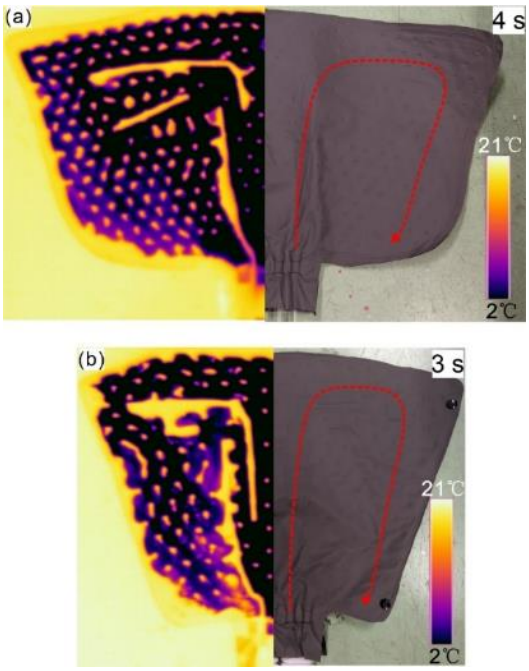

Figure 4.22 Wearable heat transfer panels for thigh and calf, respectively, show uniform temperature, implying that water can be filled in 4 s (V_0 = 1.0 m/s) and 3 s (V_0 = 1.1 m/s) appropriate control of network-structured parameters can make the heat transfer panel with fast fluid velocity, uniform heat performance and suitable power loss.

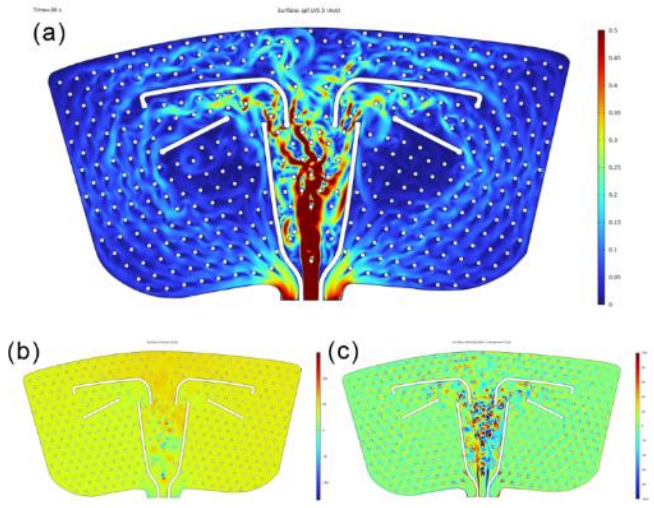

Figure 4.23 Numerical simulation calculation results of wearable heat transfer panel for thigh (V_0 = 0.5 m/s). (a) The velocity/V_0 distribution of this wearable heat transfer panel when the

flow field is fully developed; (b) The pressure distribution of this wearable heat transfer panel when the flow field is fully developed; (c) The vorticity distribution of this wearable heat transfer panel when the flow field is fully developed.

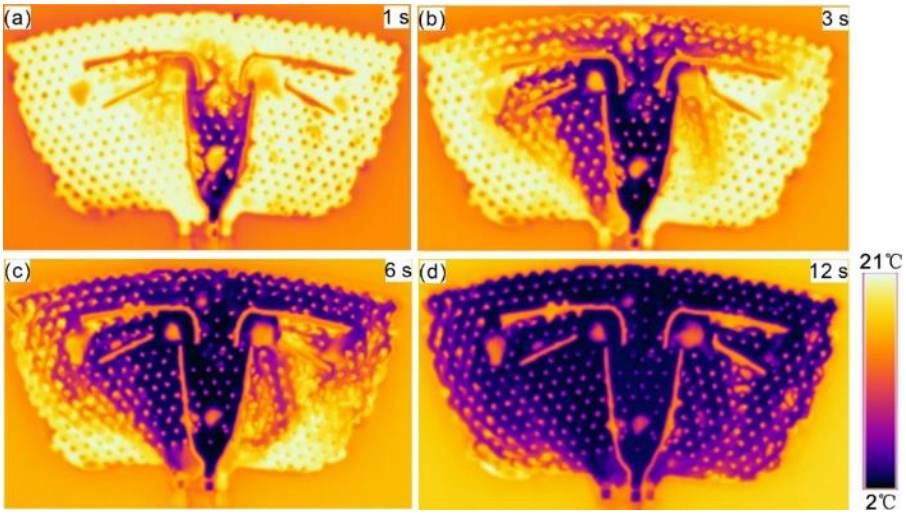

Figure 4.24 Temperature mapping of wearable heat transfer panel for thigh (V_0 = 0.5 m/s) at different times. It takes ~12 s for the cold water to replace the hot water.

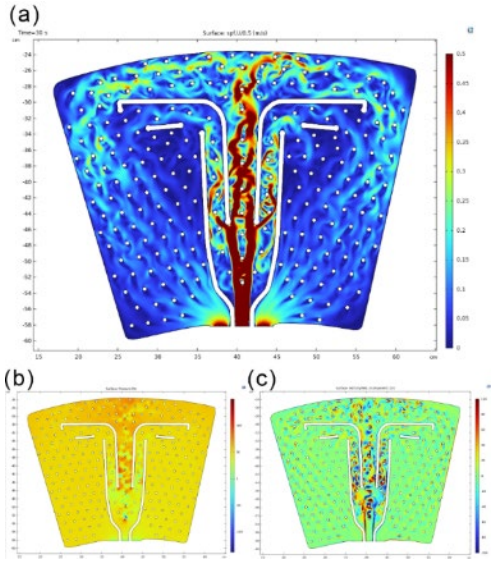

Figure 4.25 Numerical simulation calculation results of wearable heat transfer panel for calf (V_0 = 0.5 m/s). (a) The velocity/V_0 distribution of this wearable heat transfer panel when the

flow field is fully developed; (b) The pressure distribution of this wearable heat transfer panel when the flow field is fully developed; (c) The vorticity distribution of this wearable heat transfer panel when the flow field is fully developed.

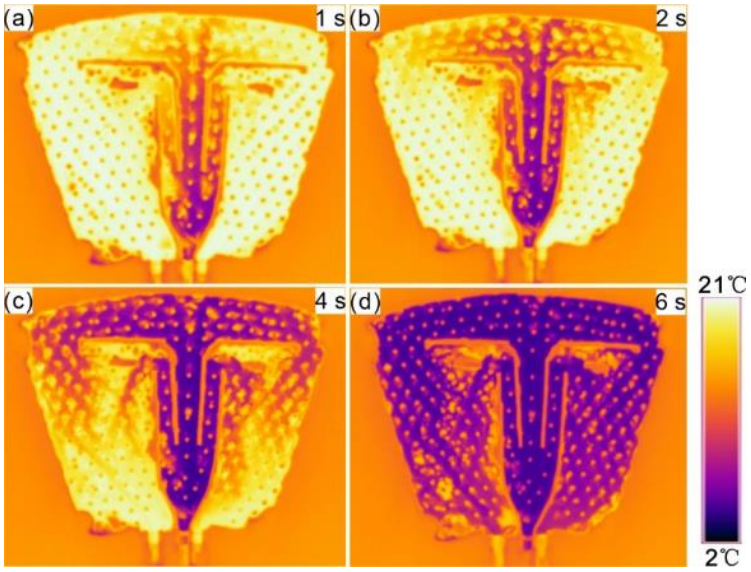

Figure 4.26 Temperature mapping of wearable heat transfer panel for calf (V_0 = 0.5 m/s) at different times. It takes ~6 s for the cold water to replace the hot water.

4.3.4 Wearable heat transfer panels with inappropriate network structure and guide vanes

Figure 4.27 are three typical wearable heat transfer panels with inappropriate network structures and tube arrangements. They show us the consequence without appropriate guide vanes, network structure and single channel. All these three experiments were performed with the same pump for water circulation. **Figure 4.27a&d-g** is the calf heat transfer panel without

appropriate guide vanes. Although the guide vanes and reinforcement dots are located almost in a symmetry pattern, the fast fluid velocity caused the unstable flow field thus make the flow rate distribution uneven. This wearable heat transfer panel even can not be filled. **Figure 4.27b**&**h-k** is the full leg wearable heat transfer panel allocated with high density reinforcement dots. Due to the high head loss caused by the reinforcement dots, it takes ~25 s to fill the whole wearable heat transfer panel. The last one (**Figure 4.27c**&**l-o**) is the same as the gameready full leg wrap in tube and dots arrangement. This single tube arrangement heat transfer panel also takes ~22 s to be filled. Much slower than our record ~6 s. This further shows the huge improvement of our nature-inspired network-structured wearable heat transfer panels.

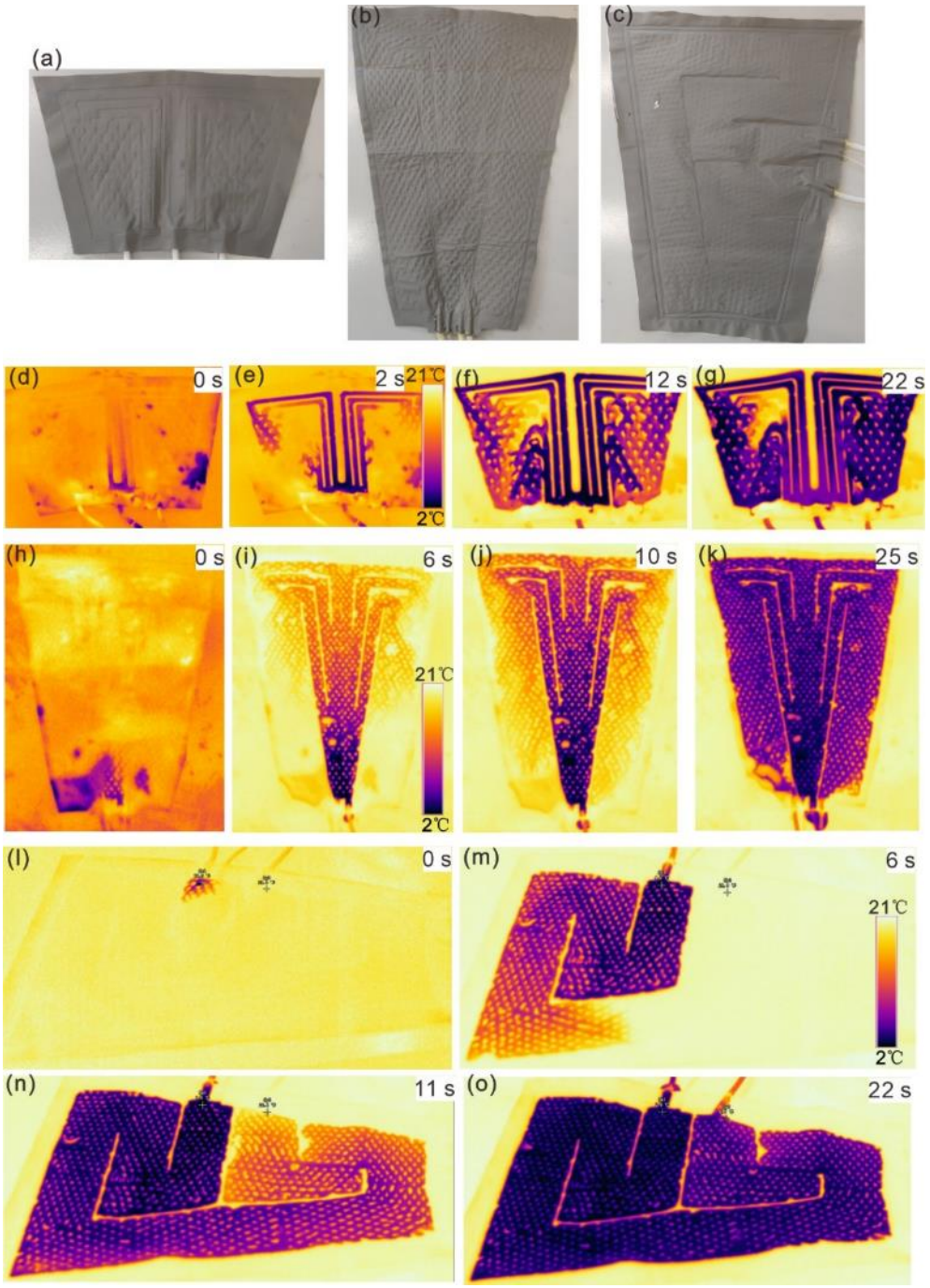

Figure 4.27 Wearable heat transfer panels with inappropriate network structures and tube arrangements. (a) Calf heat transfer panel with an inappropriate tube arrangement; (b) Full leg heat transfer panel with an inappropriate network structure; (c) Full leg heat transfer panel with a single tube arrangement; (d-g) Calf heat transfer panel with an inappropriate tube arrangement

showing poor heat transfer evenness and extremely low fluid velocity due to unreasonable head loss manipulation; (h-k) Full leg heat transfer panel with an inappropriate network structure showing extremely low water velocity and low heat transfer efficiency. Too many dots resulted in a very high pressure at the inlet and further caused water leakage; (l-o) Full leg heat transfer panel with a single tube arrangement that also shows extremely low water velocity and low heat transfer efficiency. Too much head loss at the corner also results in very high pressure at inlet and further causes water leakage.

4.4 Summary

In this chapter, we have designed three novel nature-inspired wearable heat transfer panels (full leg, thigh and calf) which can perform two different temperatures switching in 10 s. Arising from the idea of network structure on flow field and mass transfer adjustments in nature, the fluid channel of these wearable heat transfer panels is redesigned, and the number of corners is decreased to two for reducing the energy loss. The function of reinforcement dots is extended for manipulating the flow field and distribute the fluid to the desired region (not only for reducing the water consumption). The engineered network-structured wearable heat transfer panels show faster fluid circulation velocity and more uniform temperature mapping when comparing to those without appropriate network structure and guide vanes arrangement.

CHAPTER 5 Flow Field Evolution and Mass Transfer Mechanism of Network-Structured Fluidic Fabrics

5.1 Introduction

Wearables are devices designed to be worn on the body, offering seamless integration into daily activities for enhanced connectivity and convenience. As technology advances, wearables are increasingly used for diverse applications, from health monitoring[165] to augmented reality experiences[166]. Fluids used in wearables play a crucial role in enhancing the functionality and comfort of these devices. These fluids can be found in various components such as flexible batteries, cooling systems, and materials that alter their properties in response to environmental changes. Flow field control in wearable devices is pivotal for optimizing their performance and user comfort. This meticulous engineering ensures wearables operate efficiently and reliably, providing users with a seamless and comfortable experience.

In traditional fluid dynamics, passive control and active control are two fundamental approaches to managing fluid flow[167]. Passive control involves the use of fixed design elements, such as surface modifications or streamlined shapes, to influence the flow without the need for external energy input. Active control, on the other hand, employs external mechanisms like actuators or pumps to dynamically adjust and manipulate the flow, often responding to real-time conditions for enhanced efficiency and performance. Both strategies are integral to optimizing the behavior of fluids in various applications, from aerodynamics[168] to industrial processes[169]. However, no such kind of systematic fluid field control strategy is

applied in designing wearable fluidic thermal management devices. Most wearable thermal management devices research just focuses on material design, system integration and garment fitting.

The flow field evolution plays a key role in heat transfer of wearable heat transfer panels. Traditional water-based wearable heat transfer panels typically suffer from high head loss due to their single-tube design with few fluid channels and the relatively high density of water. This design limitation leads to low flow velocity and reduced heat transfer efficiency. Consequently, the performance of these systems is often undermined by the constraints of conventional wearable fluidic heat transfer panels. The fluid takes longer to circulate through the system, resulting in poor heat transfer efficiency due to significant head loss caused by numerous turns, corners, and the narrow diameter of internal tubing. Consequently, the fluid velocity remains low, leading to an uneven heat exchange rate between the inlet and outlet. Near the inlet, where the temperature gradient is large, more heat is exchanged, while near the outlet, the smaller temperature gradient limits heat transfer since most of the exchange has already occurred. This results in subpar heat performance and constrains the overall heat transfer capacity of the wearable heat transfer panel.

In the previous chapter, several nature-inspired wearable heat transfer panels are designed and fabricated. All of them can be filled with water in less than 6 s and perform the temperature switching in less than 10 s. This nature-inspired network structure shows excellent fluid field manipulation capability by controlling the flow resistance at different parts of the network fluid channels. The network structure is composed of guide vanes and numerous reinforcement dots. Results in previous chapter show that the reinforcement dots not only can reduce the water consumption to avoid too much inflation, but also contribute to the fluid field manipulation.

When injected with fluid, the fabric inflates. The reinforcement dots inside and the curved walls form a special kind of special-shaped cylindrical array.

In fluid dynamics, the study of flow around a cylinder is a fundamental problem that has significant applications in engineering and environmental sciences[170]. This research area involves understanding how fluids (such as air or water) behave as they move past a cylindrical object. Researchers investigate various flow patterns that arise at different Reynolds numbers, including laminar, transitional, and turbulent flows[171]. They examine how these flow patterns influence forces such as drag and lift, which are critical in designing efficient structures and vehicles. Additionally, the phenomenon of vortex shedding, where vortices periodically detach from the cylinder at higher Reynolds numbers, is explored due to its implications for vibration and structural noise. Detailed analysis of the boundary layer around the cylinder helps in understanding heat transfer and friction, which are important for optimizing designs in engineering applications like pipelines, bridges, aircraft, and underwater vehicles. However, this kind of special-shaped cylinder has never been investigated.

As the special-shaped cylinders inside the network structure play a key role in flow field manipulation. This chapter studies the flow field evolution of this special-shaped cylinders inside the wearable heat transfer panels and clarifies how the network structure controls the local flow field to give the heat transfer panel excellent performance with faster and uniform fluid velocity.

5.2 Methodology

This part introduces the methodology of flow field on network-structured fluidic fabrics and involves the definition of network structure, numerical simulation and flow visualization experiments set up.

5.2.1 Definition of network structure

Due to the nature of the "balloon effect" of liquid-tight inflatable laminated fabrics, the cross section of inflated network structure consists of various arcs as shown in **Figure 5.1c-d**. This work only considers the power loss when filled with water where the sample reaches the steady state, and no significant deformation occurs during this period. As the wearable heat transfer panel is flexible and its shape is changeable, three main parameters for defining the outline of the network structure are R (length between two reinforcement dots), D (diameter of reinforcement dot) and r (radius of inflated membrane), as shown in **Figure 5.1a-d**. Next, by rotating the Z axis shown in **Figure 5.1b**, one hexagonal unit cell is completely constructed (**Figure 5.1c**). "R" and "D" together define the distance between dots for fluid to go through, "r" reflects mainly the fluid pressure inside the wearable heat transfer panels. All these parameters are controllable when a heat transfer panel is applied with different fluid pressures inside (e.g. the distance between two dots – "R", will decrease and thickness – "r", will increase as the fluid pressure is increased). **Figure 5.1d** is the cross-section of the inflated heat transfer panel obtained by a spatial digitizer.

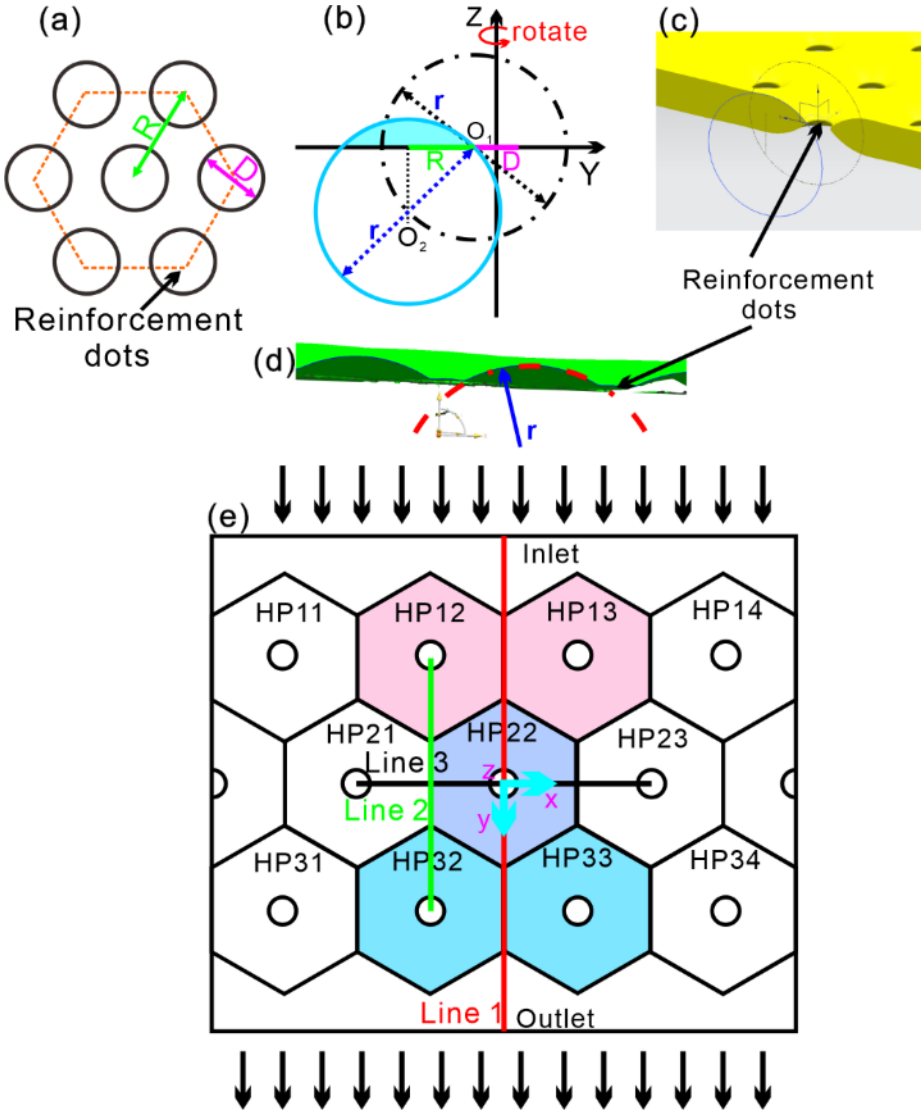

Figure 5.1 (a-c) Schematic diagram of the three parameters (*R*, *D*, *r*) used to define the reinforcement dots arrangement and thickness of the heat transfer panel; (d) Cross-section of the inflated heat transfer panel obtained by a spatial digitizer; (e) Hexagonal unit cell definition for evaluating the power loss density and the three lines (red, green and black) for extracting the time averaged velocity.

This 3D structure is used to simulate the flow field inside the network structure. The whole flow field is divided into 12 hexagonal unit cells to study the flow field evolution and pressure drop inside the network structure. The power loss evaluation was conducted by summation of the energy balance equation which will be discussed in Chapter 6. Three rows of reinforcement dots were placed to make sure that the flow is fully developed inside the network structure.

5.2.2 Numerical simulation set up

The numerical simulations of the fluid field of network fluidic fabrics were conducted using a commercial computational fluid dynamic software ANSYS FLUENT v22.1. The equations were discretized by the finite volume method. High quality mesh generation can ensure the accuracy and convergence of numerical simulations. A tetrahedron structure mesh was generated by ICEM with 5 boundary layers. All these meshes were then transferred into a polyhedral structure mesh by Ansys Fluent (**Figure 5.2a-c**). The average Y plus value was less than 1.2, which meets the required value of the grid Y plus with the SST k-ω turbulence model (**Figure 5.2d**).

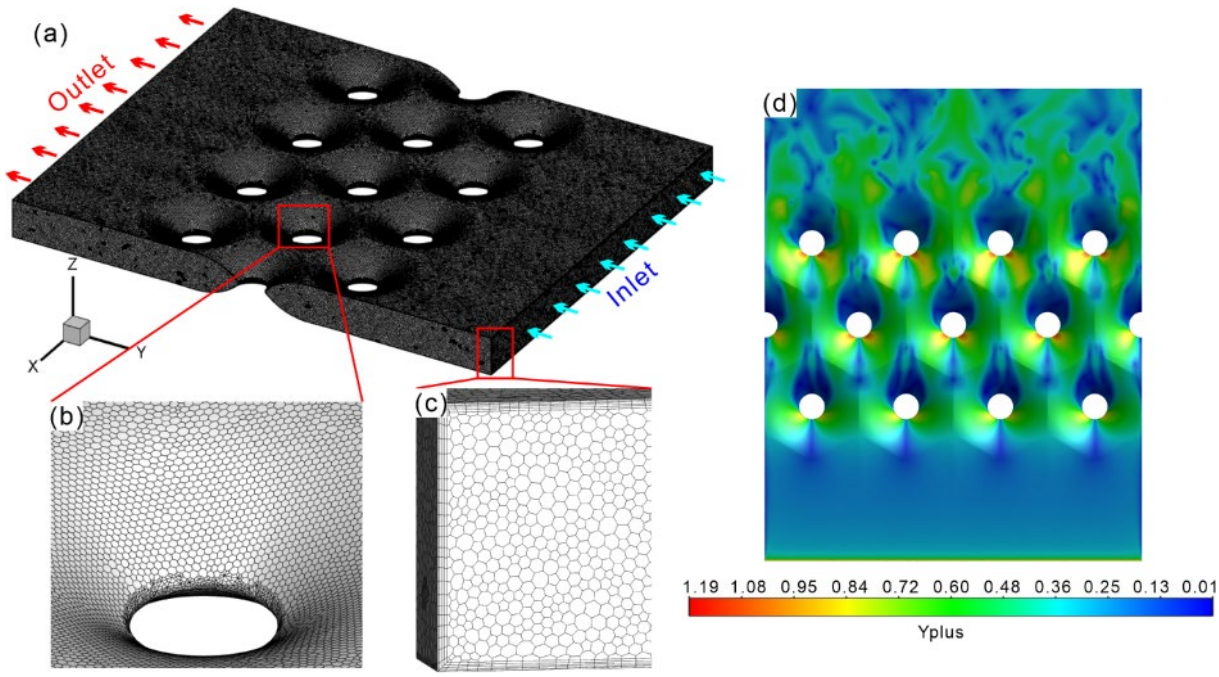

Figure 5.2 (a-c) Grid distribution of the computation domain, the grid type used in this work is polyhedral grid, grid quantity is ~394 million with 5 layers of boundary grid; (d) Distribution of Y plus, the maximum value is less than 1.2.

To ensure that the flow inside the network structure was fully developed, three points were placed as shown in **Figure 5.3** to monitor the fluctuation of the velocity field. Shown in **Figure 5.4** are the velocity magnitude of three monitor points versus flow time. It presents the data for the velocity magnitude for the first 1 s for each inlet velocity from 0.1 m/s to 0.6 m/s. When the flow field is fully developed into a steady state (the velocity magnitude evolves into a periodical fluctuation status), the time-averaged simulation is finished. **Figure 5.8**, **Figure 5.10** and **Figure 5.12** show the velocity magnitude versus flow time for each inlet velocity from 0.025 m/s to 1.0 m/s. Several quasi-periodicities of flow field are included in the simulation for all

inlet velocity conditions; the time-averaged result is acceptable for the power-loss evaluation and flow-field analysis.

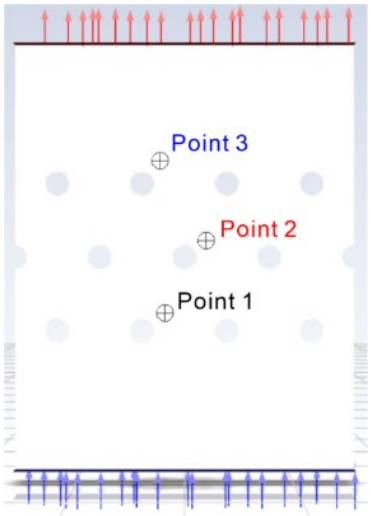

Figure 5.3 Location of three monitoring points in computation domain, for the purpose of identifying the fully developed flow field.

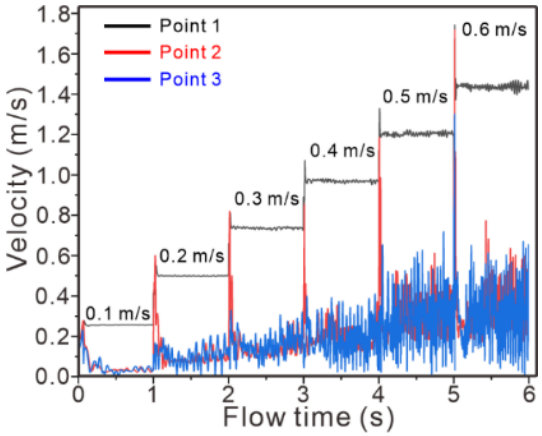

Figure 5.4 Data for steady flow field formation. The velocity evolved into a periodic variation which shows the flow field was fully developed.

Considering that the Reynolds number (Re) calculated from the hydraulic diameter inside the network structure is high (2802 when V_0 = 0.1 m/s, 8405 when V_0 = 0.3 m/s, and 16809 when V_0 = 0.6 m/s) and the flow inside is not pure laminar, Ansys Fluent was used to solve the incompressible 3D steady Reynolds-averaged Navier-Stokes (RANS) equations. In Reynolds decomposition, every instantaneous quantity is decomposed into the time-averaged part and fluctuating part. The governing equations can be expressed as follows[172]:

$$\frac{\partial}{\partial x_i}(\rho\overline{u_i}) = 0 \tag{5-1}$$

$$\frac{\partial}{\partial x_j}\left(\rho\overline{u_i u_j}\right) = -\frac{\partial \overline{p}}{\partial x_i} + \frac{\partial}{\partial x_i}\left[\mu\left(\frac{\partial \overline{u_i}}{\partial x_j} + \frac{\partial \overline{u_j}}{\partial x_i} - \frac{2}{3}\delta_{ij}\frac{\partial \overline{u_k}}{\partial x_k}\right) - \rho\overline{u_i' u_j'}\right] \tag{5-2}$$

where $\overline{u_i}$ and $\rho\overline{u_i' u_j'}$ are the Reynolds averaged velocity vector and the Reynolds stress tensor; u_i' in term $\rho\overline{u_i' u_j'}$ is the fluctuating component of the flow velocity. μ is the dynamic viscosity.

As Re inside the network structure is high, the SST $k-\omega$ turbulence model was used for numerical simulation of network structure. The SST $k-\omega$ turbulence model[173] mainly includes two equations of turbulent energy k and turbulent eddy frequency ω.

$$\frac{\partial(\rho k)}{\partial t} + \frac{\partial}{\partial x_j}\left(\rho\bar{u}_j k\right) = \frac{\partial}{\partial x_j}\left[\left(\mu + \frac{\mu_t}{\sigma_k}\right)\frac{\partial k}{\partial x_j}\right] + P_k - \beta'\rho k\omega + P_{kb} \tag{5-3}$$

$$\frac{\partial(\rho\omega)}{\partial t} + \frac{\partial}{\partial x_j}\left(\rho\bar{u}_j \omega\right) = \frac{\partial}{\partial x_j}\left[\left(\mu + \frac{\mu_t}{\sigma_k}\right)\frac{\partial \omega}{\partial x_j}\right] + \alpha\frac{\omega}{k}P_k - \beta_3\rho\omega^2 + (1-F_1)2\rho\frac{1}{\sigma_{\omega 2}\omega}\frac{\partial k}{\partial x_j}\frac{\partial \omega}{\partial x_j} \tag{5-4}$$

where $\beta' = 0.09$, $\sigma_{\omega 2} = 1/0.856$. The model coefficients σ_{k3}, $\sigma_{\omega 3}$, α_3, β_3 are liner combinations of the corresponding coefficients of basic $k-\omega$ model and $k-\varepsilon$ model. μ_t is the turbulent viscosity and is defined as:

$$\mu_t = \frac{\rho \alpha_1 k}{\max(\alpha_1 \omega, SF_2)} \quad (5\text{-}5)$$

where $\alpha_1 = 0.31$[173], F_2 is a blending function that restricts the limiter to the wall boundary layer, S is an invariant measure of the strain rate.

The boundary conditions are set as follows: the inlet of network structure is set in a particular velocity magnitude from 0.025 m/s to 1.0 m/s and outlet pressure is set at 1 atm. The material inside the network structure used to produce soft heat transfer panel is TPU and the roughness of the TPU surface is 0.5 μm and 2 μm on the fabric surface. Thus, the wall roughness is selected as 0 mm for simplification of the simulation and following analysis. The criterion for solution convergence was set as 10^{-5} and the time step of transient simulation was 0.0002 s.

5.2.3 Experimental set up of flow visualization

The flow visualization experiments were conducted in the Water Tunnel Laboratory located in The Hong Kong Polytechnic University, as shown in **Figure 5.5**. The whole flow visualization system was made up of the following components: a 3D-printed transparent mold with a network structure; a container for water circulation inside the network structure mold; an ink injection machine with three different colors; a high-speed camera for capturing ink streamlines.

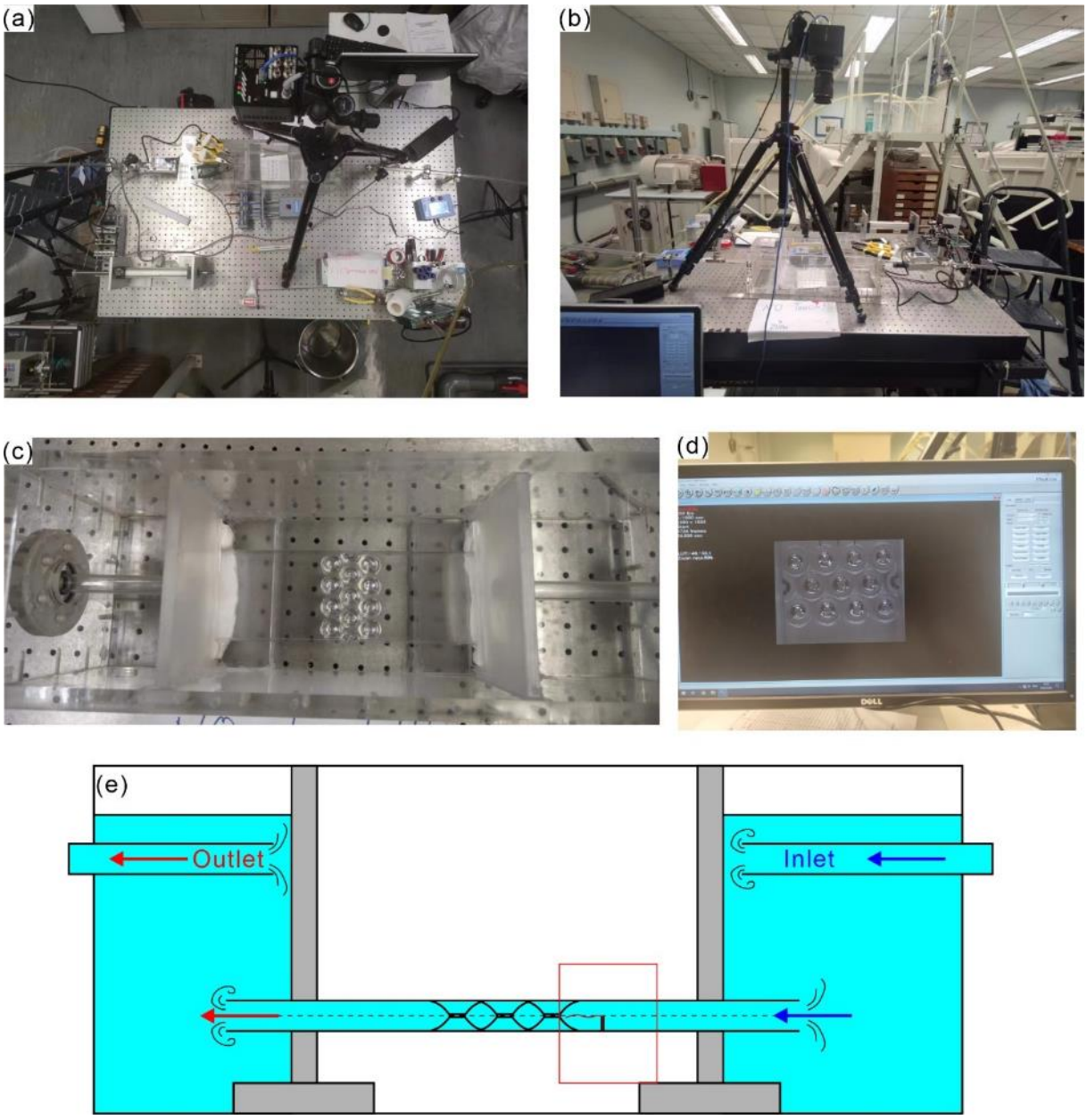

Figure 5.5 (a-b) Top view and front view of the flow visualization experimental set up; (c-d) Top view of the 3D-printed transparent mold with the network structure from the circulation container and high-speed camera; (e) Schematic diagram of cross-section view of the container for water circulation inside the network structure mold.

Figure 5.5e shows the cross-section of the water-circulation container. The network structure (mold, inlet and outlet) was immersed in water. Inlet and outlet were placed on the upper side of the 3D-printed network structure mold and close to the wall ahead to avoid unexpected turbulence in the network structure 3D-printed mold. Three ink release needles were placed as shown in **Figure 5.6** & **Figure 5.16**.

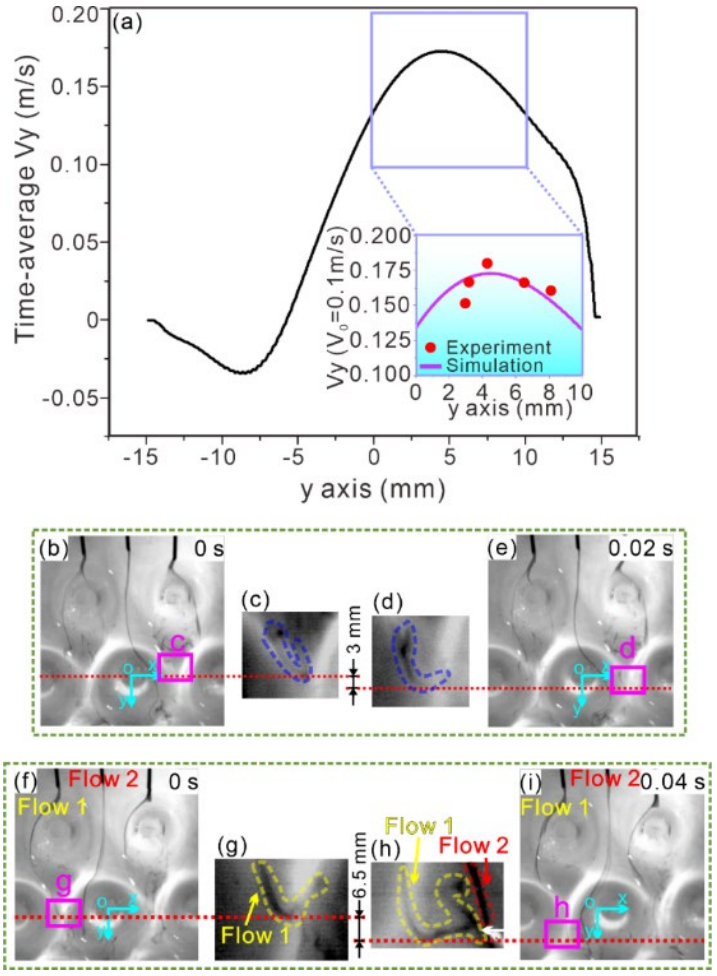

Figure 5.6 (a) Time-averaged velocity in Line 2 (**Figure 5.1**), for comparison with experiment results; (b-i) Two examples of how to acquire the velocity magnitude in flow visualization experiments.

5.3 Results and discussion

5.3.1 Verification of simulation

Verification of the simulation was conducted by grid independent verification and experimental verification. The power loss density calculated by Eq. (6-1) is shown in **Figure 5.7.** We can see that the value of power loss density did not change obviously when the grid quantity was larger than 2.04 million. Finally, we chose a polyhedral structure mesh with a grid quantity of 3.94 million. The power loss density value is different when the row number changes. This may not be important for a single case but is very important for our analysis as we need to quickly compare the flow resistance of different dot arrangements for the device design and choose the appropriate layout strategy in the appropriate part of the network structure. The results show that a power loss density value of around 8000 W/m^3 (**Figure 5.7b**). This means that the power loss value was representative for most dots' power loss inside the network structure when the row number is larger than 3. It can also represent the flow resistance of this kind of dot layout.

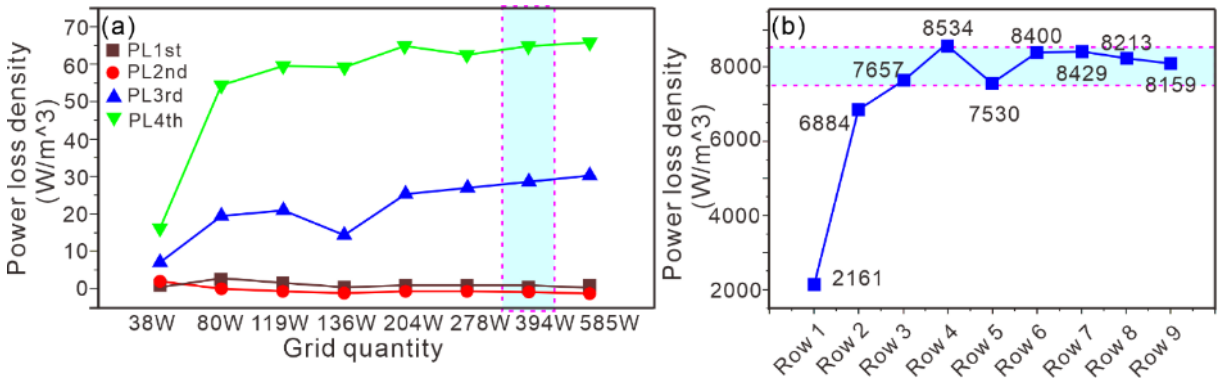

Figure 5.7 (a) Power loss density vs. grid quantity; (b) Total power loss density of each row vs. row number.

Experiments were also undertaken for verification. **Figure 5.6** shows the time-averaged velocity magnitude along line 2 (**Figure 5.1e**) by numerical simulation. **Figure 5.6b-i** depicts the approximate velocity near line 2 (~ 0.15 m/s and ~0.163 m/s, respectively). By comparing the time-averaged data with the experimental data, the acceptable deviation is less than 5% between experimental data and simulation results, we found that the deviation was acceptable. The verification of simulation in this work also considers the fluctuating caused by Karman Vortex Street.

5.3.2 Flow field evolution of network structure

The fluid field of network structure is different with different inlet velocities. On considering the velocity is different at different parts of the network-structured wearable heat transfer panel, the flow field regime needs to be studied under these conditions. This part investigates the flow field regime of inlet velocity ranging from 0.025 m/s to 1.0 m/s. The range of velocity includes almost all possible conditions inside the network-structured wearable heat transfer panel. The inlet velocity can reach up to 1 m/s. The flow field regime only includes two different states in this kind of network structure: pure laminar flow and transition flow regime.

5.3.2.1 Pure laminar flow regime

As shown in **Figure 5.8** is the velocity magnitude of three monitoring points shown in **Figure 5.3** of 2 second time-averaged simulation. The velocity is almost a constant in 2 s. The velocity does not change on the monitoring point near the first row of reinforcement dots and slightly fluctuate when the flow passes through the following two rows of reinforcement dots. These

results show the flow field inside the network structure is pure laminar when the inlet velocity is lower than 0.05 m/s.

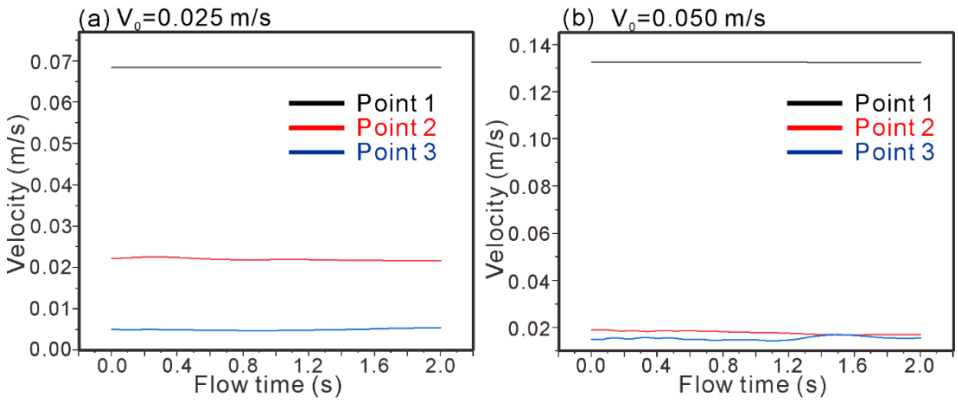

Figure 5.8 Velocity magnitude of three monitoring points shown in **Figure 5.3** of 2 seconds simulation. (a) V_0 = 0.025 m/s; (b) V_0 = 0.05 m/s.

Figure 5.9 is the CFD instantaneous simulation results of velocity magnitude/pressure/vorticity contour in the x-y plane of inlet velocity 0.025 m/s and 0.05 m/s, respectively. On the windward side of the reinforcement dots, the velocity is low and almost drops to nearly zero due to the blockage of reinforcement dots. The fluid pressure is at its maximum in this part. This is like the stagnation point of flow around cylinders. The velocity accelerates as the fluid move away from the stagnation point and slide along the flank part of the reinforcement dots as the flow channel is narrower. But due to the low flow velocity and Reynolds numbers, the separation point tends to occur quite smoothly and symmetrically around the reinforcement dots. Beyond the separation points, the flow forms a wake behind the reinforcement dots. This wake is symmetric and smooth, flowing in parallel layers with minimal mixing across layers, the shape

is “bat-like”. Around the reinforcement dots surface, the pressure is highest at the stagnation point and decreases along the surface to a minimum at the sides of the reinforcement dots, and then it increases toward the back as the boundary layer begins to separate and forms the wake. This varying pressure distribution creates a net pressure drag force on the reinforcement dots.

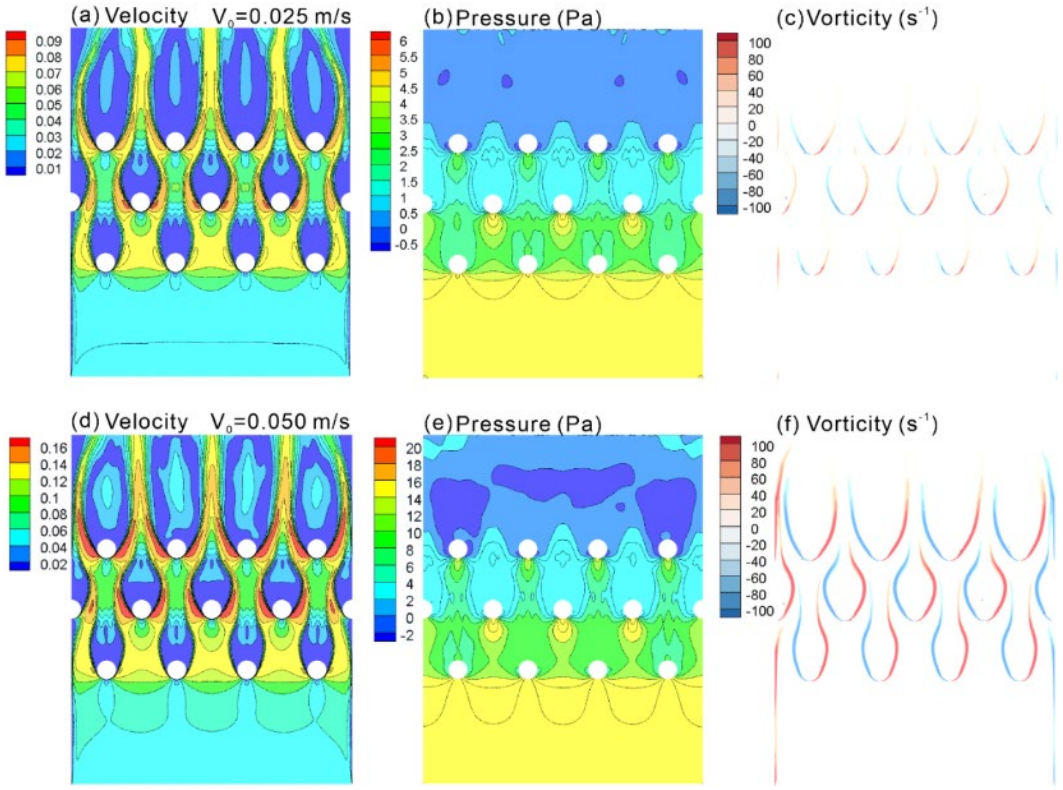

Figure 5.9 CFD instantaneous simulation results of velocity magnitude/pressure/vorticity contour in the x-y plane. (a-c) V_0 = 0.025 m/s; (d-f) V_0 = 0.050 m/s.

5.3.2.2 Transition flow regime

As shown in **Figure 5.10** is the velocity magnitude of three monitoring points shown in **Figure 5.3** of 1 second simulation. Different from the results when the inlet velocity is lower than 0.05 m/s, the velocity magnitude at the monitoring points starts to fluctuate when the inlet velocity

is higher than 0.075 m/s. The fluctuation is weaker when the flow passes through the first row of reinforcement dots and more obvious in the monitoring points of the second and third rows of reinforcement dots. With the increasement of inlet velocity, the magnitude and frequency of velocity go up. This shows the evolution of flow field is periodic.

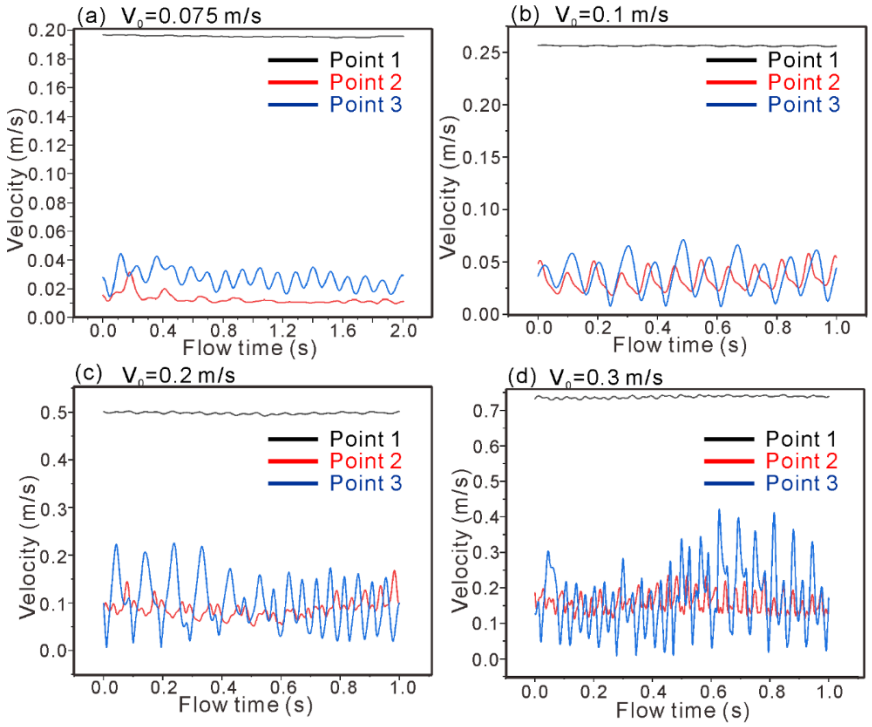

Figure 5.10 Velocity magnitude of three monitoring points shown in **Figure 5.3** of 1 second simulation. (a) V_0 = 0.075 m/s; (b) V_0 = 0.1 m/s; (c) V_0 = 0.2 m/s; (d) V_0 = 0.3 m/s.

Figure 5.11 is the CFD instantaneous simulation results of velocity magnitude/ pressure/vorticity contour in the x-y plane of inlet velocity from 0.075 m/s to 0.2 m/s. The flow regime is obviously in the transitional flow regime occurs between laminar and fully turbulent

flow. This flow regime presents a complex blend of laminar and turbulent characteristics, significantly influencing the flow dynamics and forces experienced by the reinforcement dots. Within this regime, the boundary layer on the reinforcement dots formed walls transitions progressively from laminar at the front to turbulent towards the rear. As shown in **Figure 5.11**, the vortex starts to shed when the flow passes through three rows of reinforcement dots – Karman vortex street, and the location for vortex start to shed is at the rear of the computational domain. Also, no obvious vortex shedding near the reinforcement dots. Initially, the flow remains laminar and well-ordered near the stagnation point but begins to develop turbulent fluctuations further along the surface. As the flow transitions around the rear of the cylinder, the wake becomes more turbulent, and complex compared to the steady, symmetric wake in laminar flow. The wake width in the transitional regime is generally broader than in laminar flow but narrower than in fully turbulent conditions.

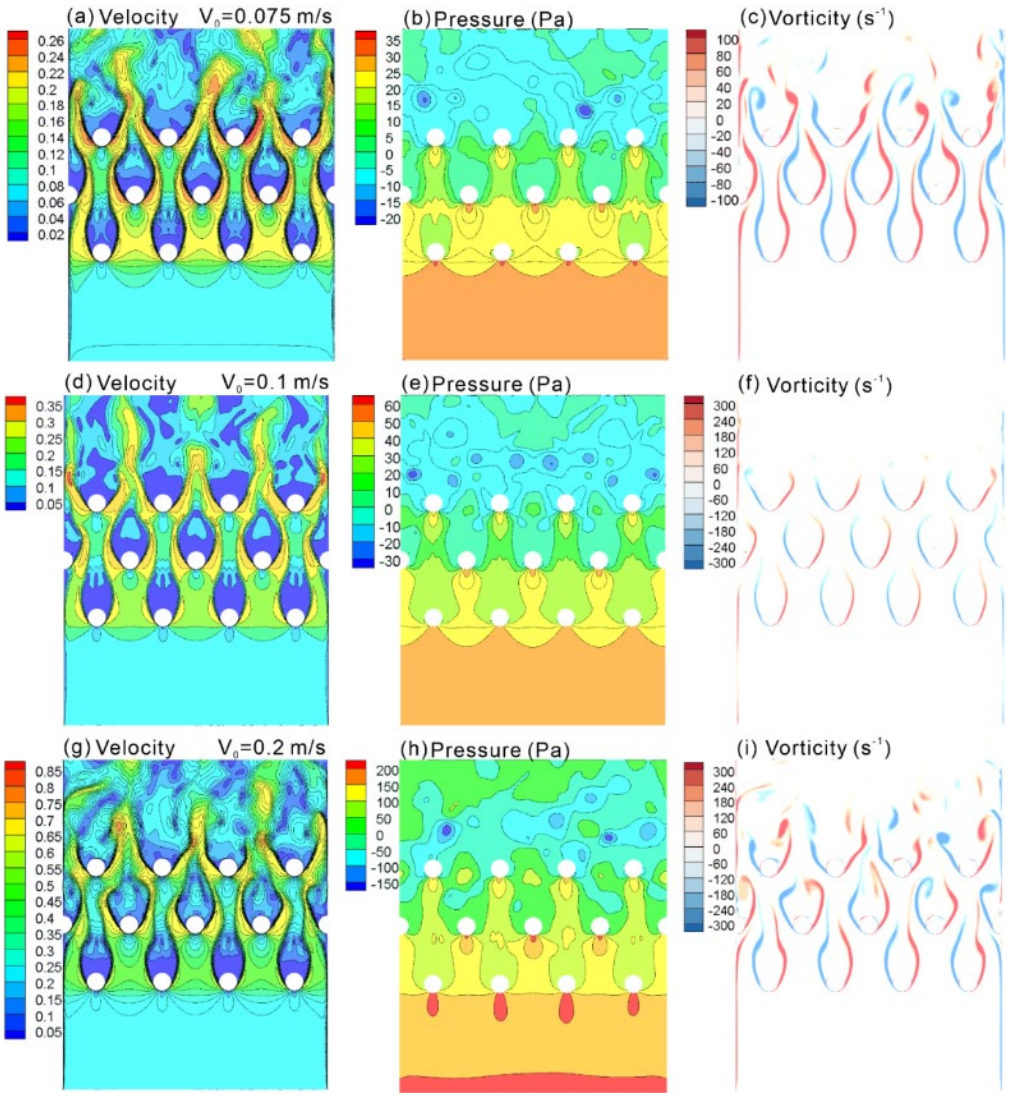

Figure 5.11 CFD instantaneous simulation results of velocity magnitude/pressure/vorticity contour in the x-y plane. (a-c) V_0 = 0.075 m/s; (d-f) V_0 = 0.1 m/s; (g-i) V_0 = 0.2 m/s.

The transition to turbulent flow leads to fluctuations in the pressure and velocity distribution around the reinforcement dots (**Figure 5.10**). Pressure on the forward-facing side of the reinforcement dots remain relatively high, while the rear-facing portion experience low pressure (**Figure 5.11**). Compared to the previous entirely laminar regime, the presence of

turbulent patches in the boundary layer can reduce pressure drag because the turbulent boundary layer can better adhere to the cylinder's surface before separating, thus delaying flow separation and narrowing the wake. However, on condition that the wall roughness is selected as 0 mm for simplification of the simulation, the actual flow regime in wearable heat transfer panels contains more turbulence when compared to the simulation results. Because the roughness of wall surface can induce an earlier transition to turbulence.

5.3.2.3 Transition flow with more turbulent factors

Figure 5.12 is the velocity magnitude of three monitoring points shown in **Figure 5.3** of 1 second simulation. **Figure 5.13** is the CFD instantaneous simulation results of velocity magnitude/pressure/vorticity contour in the x-y plane. The inlet velocity of the above simulation results ranges from 0.4 m/s to 1.0 m/s and the flow exhibits a mix of coherent structures interspersed with chaotic, turbulent patches. The flow regime of this part is also transition, the vortex shedding still remains an important phenomenon, but the vortices are more irregular. The vortex shedding occurs at the second row of reinforcement dots. The flow may exhibit a mix of coherent structures interspersed with chaotic, turbulent patches. The fluctuation of velocity is more intensive with larger magnitude. Intermittent patches of turbulence interspersed within laminar regions. This patchiness grows as the flow moves along the curved walls of reinforcement dots. In the lower part of the transitional regime, the boundary layer may separate from the surface earlier, like laminar flow around a cylinder. As turbulence develops in the boundary layer, it can cause reattachment of the flow downstream of the initial separation point, resulting in a more chaotic and turbulent wake behind the reinforcement dots, also more obvious Karman vortex street (**Figure 5.13**). Due to the increasement of inlet velocity, vortex shedding becomes more irregular compared to the periodic vortex shedding seen in the previous

transition flow regime. This results in the frequency of vortex shedding fluctuates, and the vortices themselves can be more irregular in size and strength. The Strouhal number, which relates the vortex shedding frequency to cylinder diameter and flow velocity, can be less stable and show more variability during transitional flow due to the mixed characteristics of both laminar and turbulent flows.

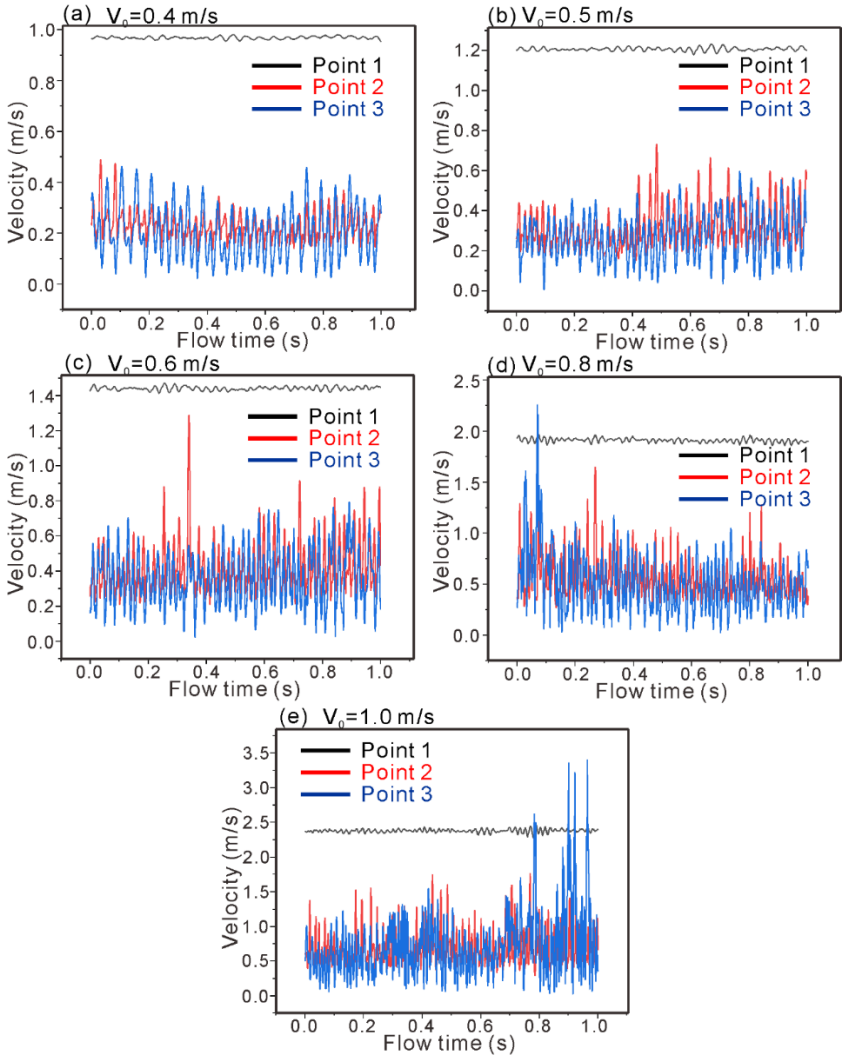

Figure 5.12 Velocity magnitude of three monitoring points shown in **Figure 5.3** of 1 second simulation. (a) V_0 = 0.4 m/s; (b) V_0 = 0.5 m/s; (c) V_0 = 0.6 m/s; (d) V_0 = 0.8 m/s; (e) V_0 = 1.0 m/s.

Initially, as the flow transitions from laminar to turbulent, the drag coefficient might increase due to the enhanced wake turbulence. However, as the flow fully transitions and the turbulent boundary layer adheres better before separation, the drag coefficient may reduce. The lift (or side force) and drag forces on the cylinder are not just averaged values but exhibit considerable temporal fluctuations. This can lead to vortex-induced vibrations (VIV) and noise, where the periodic shedding of vortices synchronizes with the natural frequencies of the cylinder, potentially causing structural fatigue or resonant vibrations. Obvious vibrations can be felt by skin around the FA1 of the wearable heat transfer panel. Luckly, this condition only occurs when the wearable heat transfer panel is small or in experimental test for extreme performance test. As flow regime in most part of network-structured wearable heat transfer panel will not reach this standard. Also, to mitigate this phenomenon at places with high velocity, we can choose fabrics with lower roughness on the surface to reduce the flow resistance as surface roughness elements can trip the boundary layer into turbulence sooner.

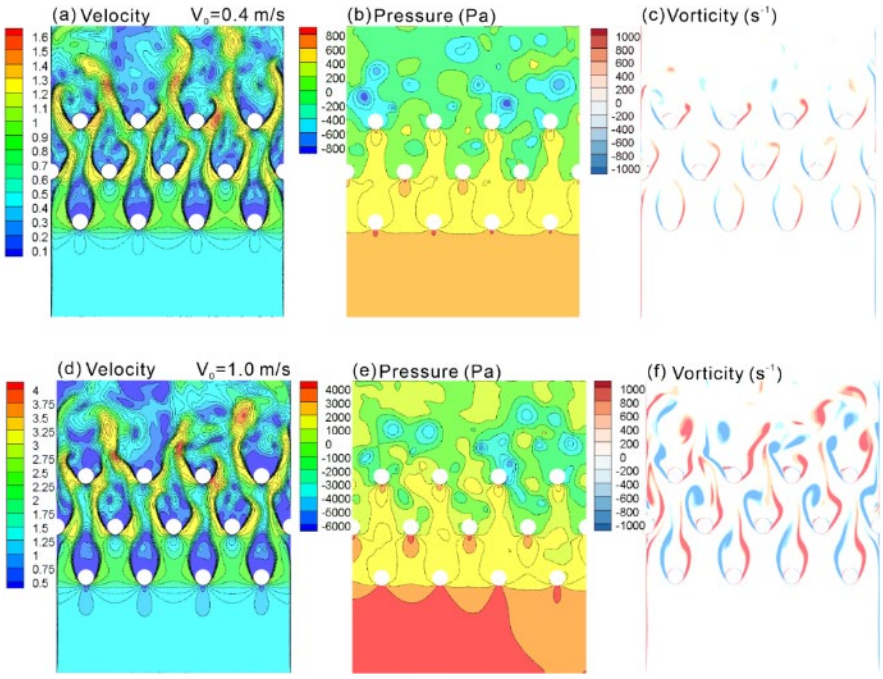

Figure 5.13 CFD instantaneous simulation results of velocity magnitude/pressure/vorticity contour in the x-y plane. (a-c) V_0 = 0.4 m/s; (d-f) V_0 = 1.0 m/s.

5.3.3 Mass transfer mechanism of network structure

The main contribution to mass transfer inside the network structure flow field is by convection. Three ink release needles (yellow, red and blue) were placed as shown in **Figure 5.6** & **Figure 5.16**. Ink visualization experiments depicted vividly mass transfer inside the network structure based on the research of flow field evolution previous. **Figure 5.14** is the schematic diagram of four turbulent areas of flow around a cylinder for comparing with the special shaped cylinder clusters in this work.

Figure 5.15 shows the schematic diagram of the 4-step mass transfer inside the network structure: (i) Velocity gradient and vorticity induced rotary mixing and elongation; (ii) Wake

alternative vortex shedding induced mixing; (iii) High-pressure region splitting; (iv) Low-pressure region suction.

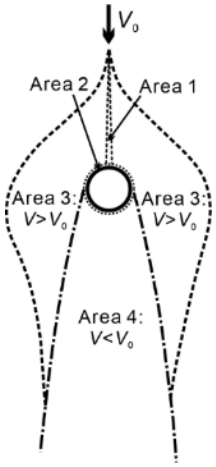

Figure 5.14 Schematic diagram of four turbulent areas of flow around a cylinder [], area 1 (Narrow area of decelerating flow), area 2 (Boundary layer region attached to the surface of the structure on both sides), area 3 (Shear and accelerated flow area on both sides), area 4 (A wide area of downstream separated flow called the wake).

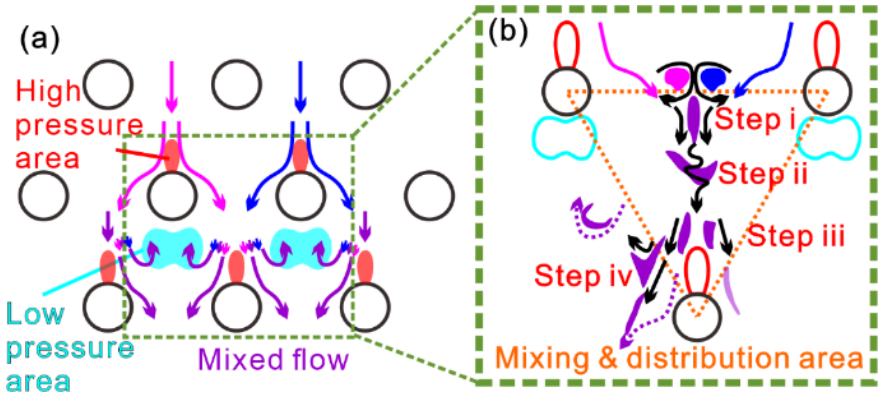

Figure 5.15 Schematic diagram of crossed layout high- & low-pressure region and the 4-step mass transfer behavior inside the mixing area: (i) Velocity gradient and vorticity induced rotate mixing and elongation; (ii) Wake alternative vortex shedding induced mixing; (iii) High-pressure region split; (iv) Low-pressure region suck.

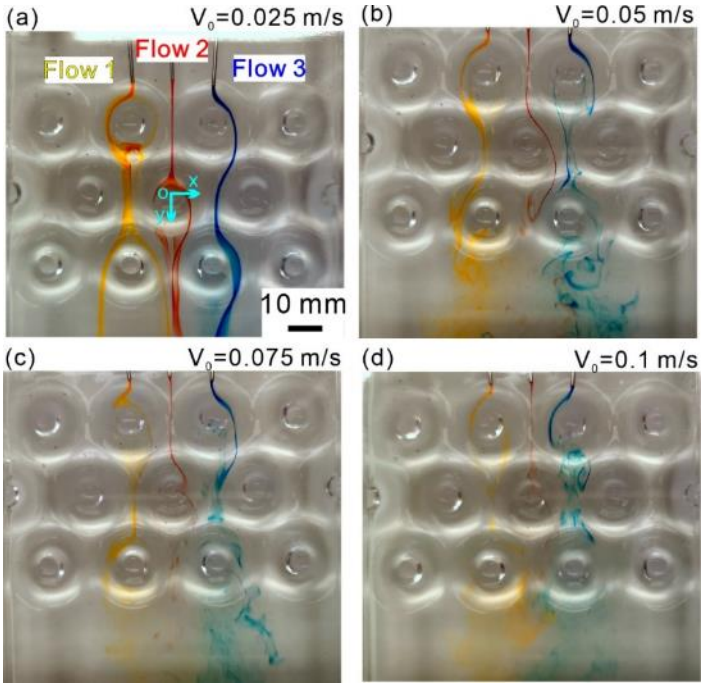

Figure 5.16 A typical flow visualization capture with three ink colors, clearly depicted the interaction of one dot with surrounding dots in different rows, showed the flow evolution from a single streamline into a more homogenous state at different inlet velocities. (a) V_0 = 0.025 m/s; (b) V_0 = 0.05 m/s; (c) V_0 = 0.075 m/s; (d) V_0 = 0.1 m/s.

Steps (i) & (ii) contributed to the mixing behavior of the network structure by the accelerating velocity and alternating positive and negative vortex shedding. Firstly, when two flows go into the middle part of two dots, the two-block mass starts to rotate, mix and becomes elongated due to the velocity gradient and vorticity. **Figure 5.16** shows that the width of the red ink stream is thinner when the flow goes into the middle part of two reinforcement dots, which means that the stream is elongated, and the vortex structure in **Figure 5.16b-d** shows the rotation behavior in step (i) caused by the previous dots. Secondly, as the velocity gradient in X direction is larger, the block mass with larger velocity will go ahead and the other part with lower velocity falls

behind. This makes the ink drop turn into an arc-shape and continue being elongated in the Y direction, as shown in **Figure 5.17** & **Figure 5.18**. Also, due to the alternative vortex shedding effect downstream of the dots, the ink drop acquires momentum in the X direction. This contributes to both the mixing effect and the step (ii) splitting procedure.

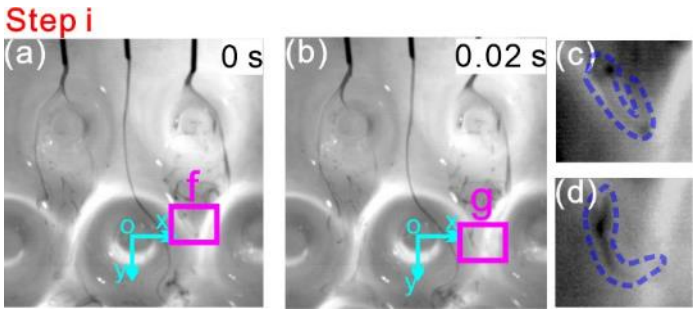

Figure 5.17 Shape change of a typical ink drop – step (i) & (ii) induced the rotation and distortion behavior of ink drop (V_0 = 0.1 m/s).

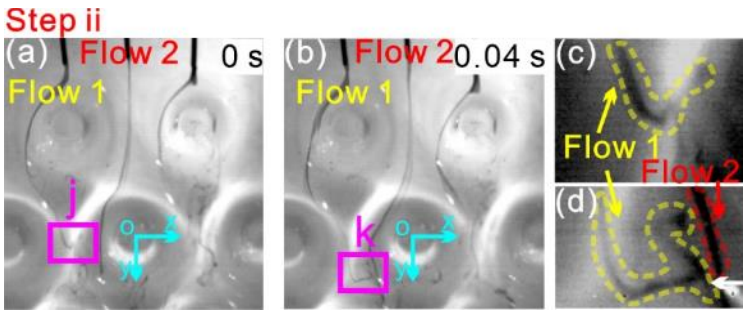

Figure 5.18 Mixing of two different ink streams – wake alternative vortex shedding in step (i) & (ii) caused the mixing (V_0 = 0.1 m/s).

The elongation of the ink drop is caused by the large velocity gradient in shear and accelerated flow areas on both sides (named as Area 3 in **Figure 5.14**), as shown in **Figure 5.24**, and the

rotation of the ink drop is caused by the pushing and sucking effect of the high- & low-pressure regions. Hence, the rotation behavior (vorticity) is weak when the flow passes the Row 1 dots, while it is distinct between Row 2 and Row 3 as the ink drop acquires vorticity from dots in Row 1. **Figure 5.17** & **Figure 5.18** illustrate the arc-shaped ink drop behavior affected by the velocity gradient and vorticity. By comparing **Figure 5.17**, the angle of the arc increases as the velocity on the right side is higher. Also, the formation of the arc is due to the sucking effect of the low-pressure region in Row 1 – the sucking force decreases the velocity of the right side of the ink drop which causes the curvature of the ink drop. The higher velocity on the right side then increases the angle of the arc. **Figure 5.18** depicts the mixing point of two adjacent ink drops. Due to the alternative vortex shedding effect of the flow after the dots, Flow 1 moves to the right part when compared to the position in **Figure 5.18a**. Together with the velocity induced rotation, Flow 1 and 2 start to mix.

Steps (iii) & (iv) contribute to the distribution behavior of the network structure by the high- & low-pressure regions. Thirdly, when the elongated ink drop is approaching the high-pressure region, the blockage by the reinforcement dots spilts the ink drop into two parts, as shown in **Figure 5.19**. Fourthly, each spilt part of the ink drop enters the wake of the dot - occupied by vortices that can enhance mixing in the low-pressure region. Together with the acceleration effect in Area 3, the ink drop becomes split again, as shown in **Figure 5.20**.

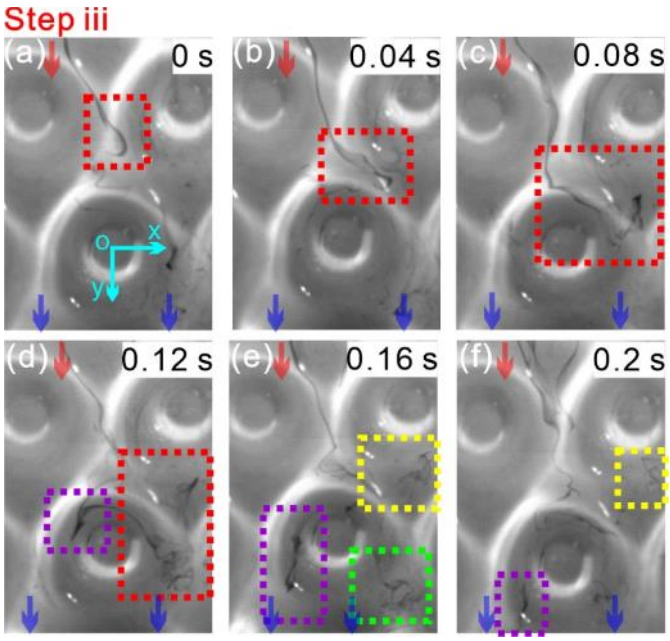

Figure 5.19 Flow visualization of ink stream split by high-pressure region – step (iii) & (iv) (V_0 = 0.1 m/s), (a-c) marked in red showed the streamline is approaching the high-pressure region, (d-f) marked in purple and red showed the split stream line by high-pressure region and the sucked ink by low-pressure region, the stream line was finally divided into three parts.

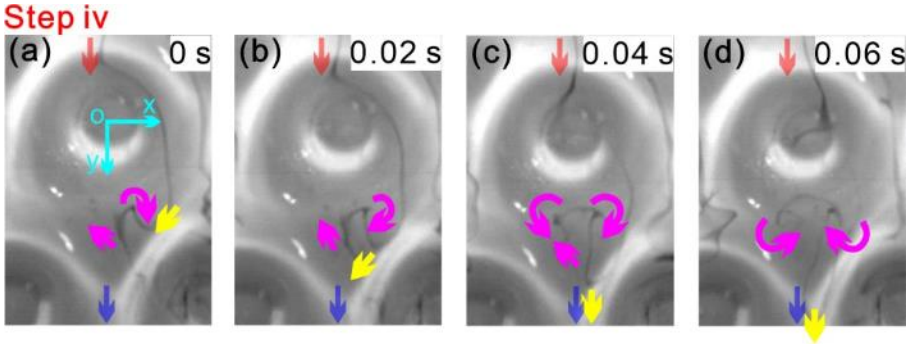

Figure 5.20 Flow visualization of ink stream sucked by low-pressure region – step (iv) (V_0 = 0.1 m/s), the ink marked in pink was sucked by low-pressure region and the ink marked in yellow went forward, the stream line was divided into two parts.

After the step (i) & (ii), the ink drop is approaching the high-pressure region. As the red mark shows in **Figure 5.19a**, due to blockage by the reinforcement dots and the alternative vortex shedding effect mentioned in step (ii), the ink streamline turns right, and some part of the ink drop is affected by the low-pressure region. The high-pressure region then splits the following ink streamline to the left (purple marked in **Figure 5.19d**). Finally, as shown in **Figure 5.19e**, the ink streamline is divided into 3 parts: 1. Left side ink stream (purple); 2. Right side ink stream (red); 3. Ink drop remaining inside the previous low-pressure region (red). The velocity inside the low-pressure region is low, but this region also contributes to the mass mixing and further splits the ink streamline. When the ink drop is approaching the boundary of the triangular mixing and distribution area, the sucking force of the low-pressure area sucks part of the ink drop into the low-pressure region (pink arrow in **Figure 5.20**) while the remaining part of the ink drop goes forward. However, due to the large area of the low-pressure region, the lee side area shows low velocity magnitude and mass transfer is poor in this area.

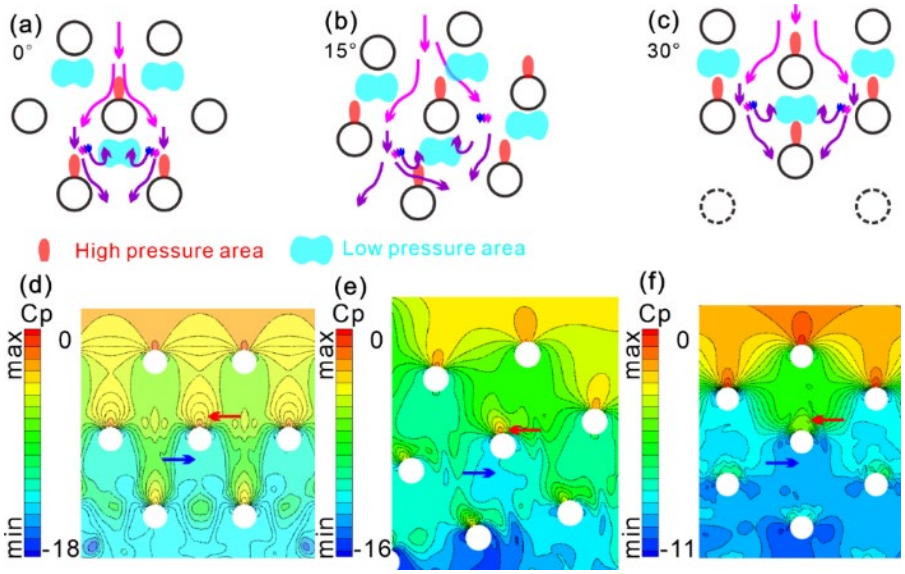

Figure 5.21 Self-homogeneity adjusted flow field with location of high- & low-pressure area with different attack angles when V_0 = 0.1 m/s: (a,d) 0 °; (b,e) 15 °; (c,f) 30 °.

This 4-step mass mixing mechanism has a significant effect on improving the flow velocity evenness (uniform temperature distribution) and enhancing the performance stability of network-structured devices. The general mixing effect can be seen in **Figure 5.16** after the flow passes three rows of dots, as the arrow 4 depicts, and the yellow and blue ink streamlines become diffused. All these phenomena show that the hexagonal unit cell cluster-network structure can enhance mass mixing. This self-homogeneity adjusted mixing mechanism ensures velocity evenness and further enhances the uniform heat transfer performance of the whole heat transfer panel.

5.3.4 Analysis of time-averaged flow field of network structure

This part focuses on the time-averaged simulation results of network structure. Previous results vividly show us the flow field evolution and the mass transfer mechanism. But the wearable heat transfer panel need to work for at least several minutes and the instantaneous results cannot show the long-time flow field evolution and the impact on wearable heat transfer panels.

The fluid field inside the wide fabric channel easily becomes uneven without an appropriate network structure (**Figure 4.27**). Compared to conventional single tube fluidic fabrics (**Figure 4.5**), the flow field inside the network structure mirrors the flow around a special-shaped cylindrical array. Flow field evolution strongly relies on the shape of the curved walls formed by dots. The flow field around the reinforcement dots can also be divided into 4 typical regions (**Figure 5.14**): a narrow area of decelerating flow (Area 1); a boundary layer region attached to the surface of the structure on both sides (Area 2); shear and accelerated flow areas on both sides (Area 3); the downstream separation flow area of the wake (Area 4)[174]. Due to the curved-wall structure, Area 3 on the two flanks of the reinforcement dot shows a bat-like shape

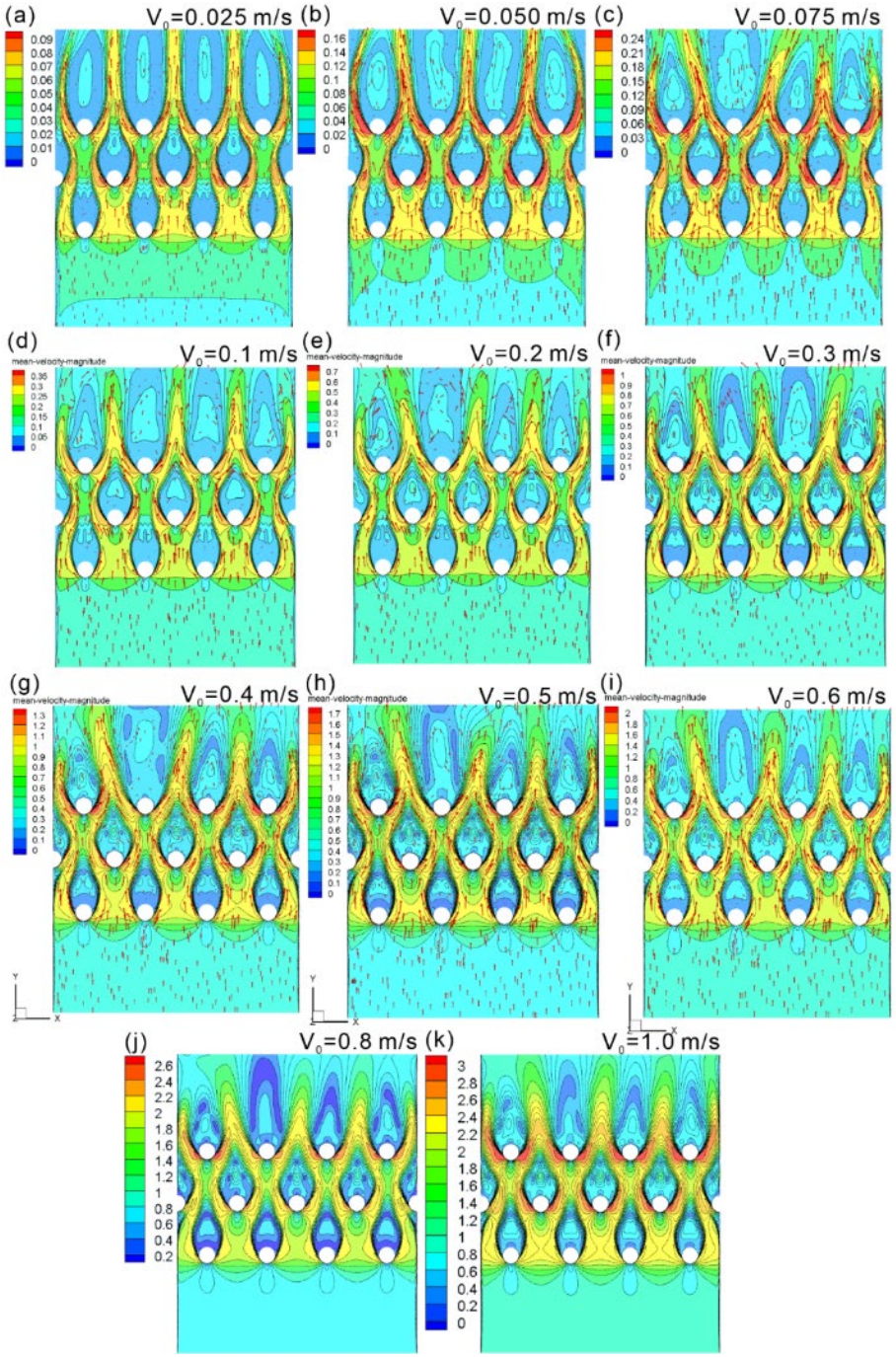

Figure 5.22 CFD time-averaged simulation results of velocity magnitude contour in the x-y plane. (a) V_0 = 0.025 m/s; (b) V_0 = 0.05 m/s; (c) V_0 = 0.075 m/s; (d) V_0 = 0.1 m/s; (e) V_0 = 0.2 m/s; (f) V_0 = 0.3 m/s; (g) V_0 = 0.4 m/s; (h) V_0 = 0.5 m/s; (i) V_0 = 0.6 m/s; (j) V_0 = 0.8 m/s; (k) V_0 = 1.0 m/s.

(**Figure 5.22** & **Figure 5.24a**). The corresponding instantaneous velocity field result is shown in **Figure 5.9**, **Figure 5.11** & **Figure 5.13**. The wake behind the dots is obviously squeezed due to the stream guidance effect of the following row of dots. In the region between Area 3 and Area 4, the velocity gradient is high. Due to the viscosity of water, the velocity in Area 4 behind the reinforcement dot is low and even turns into the reverse direction that further forms a recirculation bubble. Also, the velocity magnitudes in the experiments and simulation results are compared in **Figure 5.22** & **Figure 5.24a**, which shows the simulation results are reliable; details of the validation can be found in the Methodology part.

As shown in **Figure 5.23** & **Figure 5.24b**, the pressure evidently drops when the water passes one row of dots. These reinforcement dots form a curved wall structure contributing mainly to the power loss inside the network structure. The high- & low-pressure regions on the windward side (Area 1) and lee side (Area 4) show relatively low velocity magnitude. The pressure inside the recirculation bubble core is low. The pressure difference and velocity gradient between the high- & low-pressure regions together contribute to mass transfer inside the network structure. The time-averaged velocity along three lines marked in **Figure 5.1e** shows there is almost no difference when the local velocity is nondimensionalized (**Figure 5.25**).

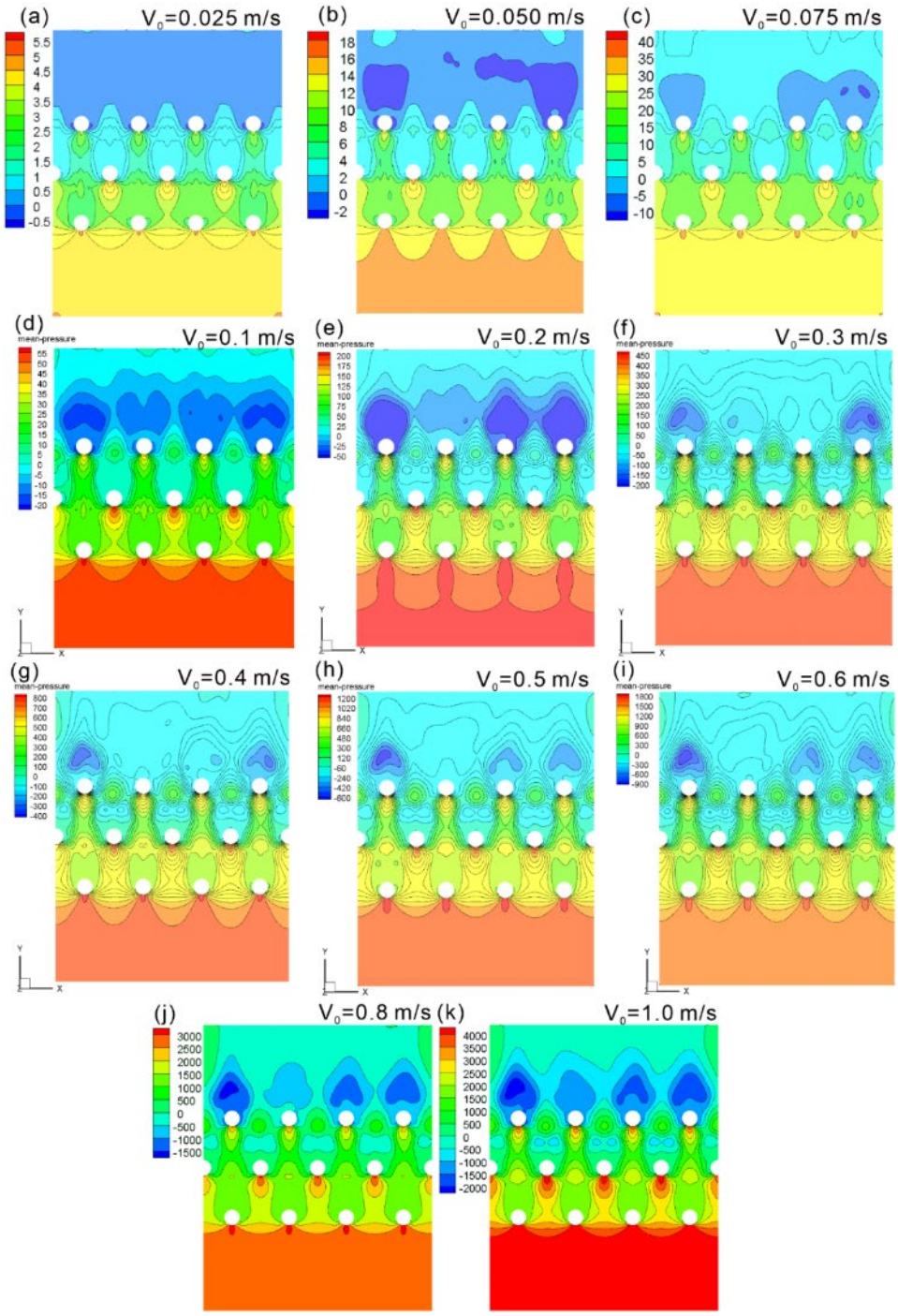

Figure 5.23 CFD time-averaged simulation results of pressure contour in the x-y plane. (a) V_0 = 0.025 m/s; (b) V_0 = 0.05 m/s; (c) V_0 = 0.075 m/s; (d) V_0 = 0.1 m/s; (e) V_0 = 0.2 m/s; (f) V_0 = 0.3 m/s; (g) V_0 = 0.4 m/s; (h) V_0 = 0.5 m/s; (i) V_0 = 0.6 m/s; (j) V_0 = 0.8 m/s; (k) V_0 = 1.0 m/s.

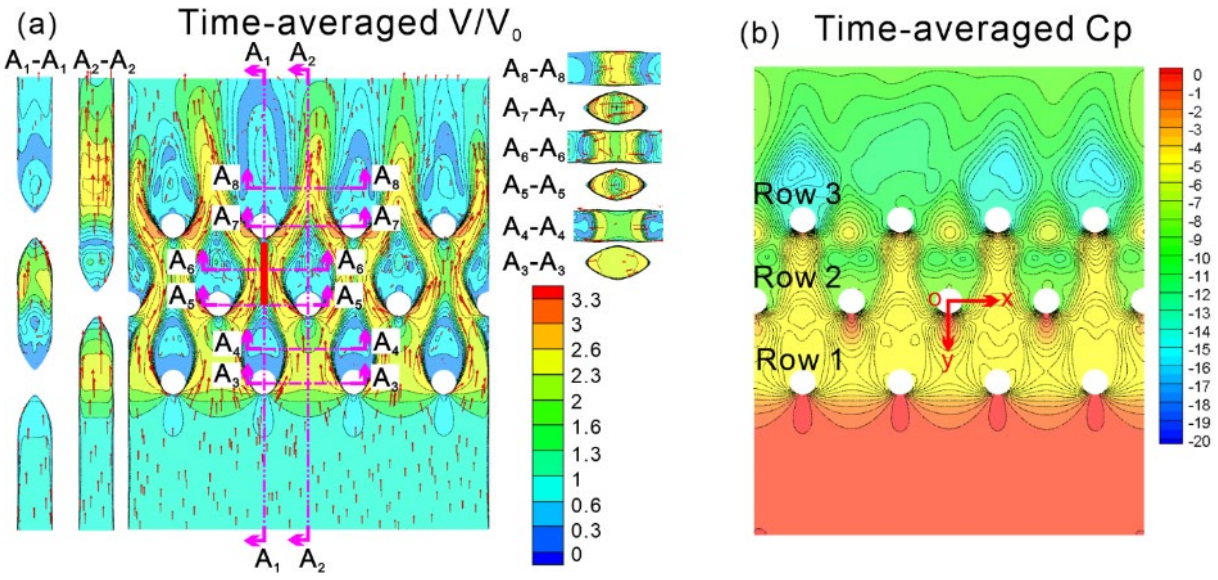

Figure 5.24 (a) Time-averaged V/V_0 magnitude contour in the x-y plane (V_0 = 0.1 m/s) and the velocity magnitude comparison of simulation and experiments results at the place marked by red broad line , regions with high velocity gradient around the dots are mixing area; (b) Time-averaged pressure coefficient (Cp) depicted the crossed layout of high- & low- pressure region (V_0 = 0.1 m/s).

The nature of the 4-step mixing mechanism is the crossed layout of the high- & low-pressure regions. The four mixing steps are not separate and two adjacent steps are usually performed simultaneously. The hexagonal layout of dots is six-fold symmetrical and can completely overlap with the pattern after each rotation of 30°, making this layout show good isotropy. As the incident angle of flow inside the network structure is not always directly vertical to the layout shown in **Figure 5.21a**, this hexagonal layout can ensure that every dot inside network structure has the capability of mass mixing. **Figure 5.21** shows the location of the high- & low-pressure regions when the incident angle is different. All these three incident angle results show

the existence of high- & low-pressure regions; the only difference is that the pressure drop is the highest when the incident angle is 0° and the lowest when 30°. This means that the energy loss decreases when the incident angle is approaching 30°, which may weaken the mass mixing effect. As the distance of two adjacent rows decreases (from $\frac{\sqrt{3}R}{2}$ to $\frac{R}{2}$) and the distance between two adjacent column dots in one row increases. It weakens the interactive effect of these surrounding dots. As the 4-step mass mixing mechanism relies on the interaction of fluid and dots, the mixing behaviour of the mass tends to occur in Area 3 of these dots where the momentum in the X & Z directions can be given to the mass nearby. When the distance between two adjacent column dots increases, the unaffected region between the two column dots also expands where the flow resistance is much lower. Also, with the distance decreasing between two adjacent rows, the dots of the following rows become inside Area 4 of front row dots where the velocity is quite low and the interactive effect with fluid is weak. This means the flow resistance caused by this dot is low.

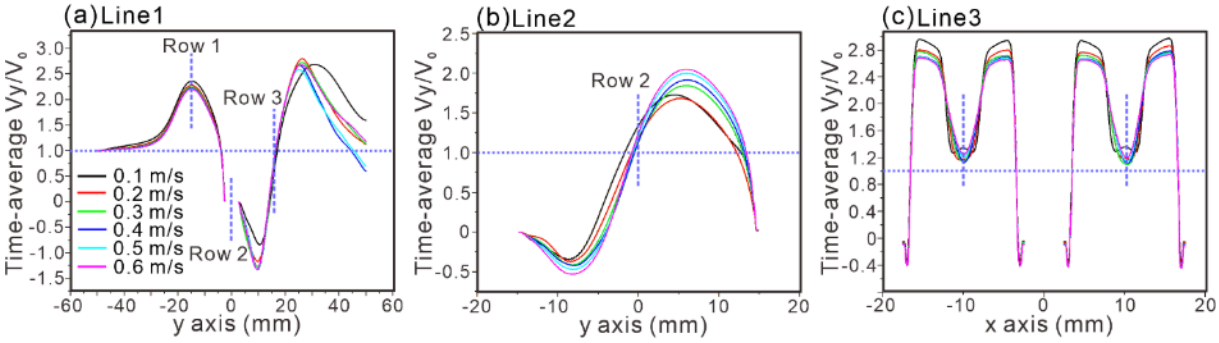

Figure 5.25 Time-averaged Vy/V_0 distribution along line 1,2 & 3 marked in **Figure 5.1**.

In general, the hexagonally arranged network structure can self-adjust the homogeneity of the network structure fluid field by the crossed layout of the high- & low-pressure regions. This can also be explained by the 4-step mass mixing mechanism and further ensures the rapid uniform temperature distribution in the heat transfer panel.

5.4 Summary

In this chapter, the flow field evolution and mass transfer mechanism of a network structure is detailed investigated. The flow field of network structure can be divided into three different regimes with different inlet velocity: pure laminar, transition flow and transition flow with more turbulent factors. The mass transfer mechanism works based on the crossed layout of the high- & low-pressure regions located in the windward side and lee side of the reinforcement dots. The mass transfer process can be divided into 4 continuous steps: (i) The velocity gradient and vorticity induced rotation mixing and elongation; (ii) Wake alternative vortex shedding induced mixing; (iii) High-pressure region splitting; (iv) Low-pressure region sucking. Due to this uniform mass transfer mechanism, the time-averaged flow field shows homogeneity velocity distribution and appropriate convection between fluid in x-y plane and boundary layer.

CHAPTER 6 Flow Field Manipulation by Head Loss Control of Network-Structured Fluidic Fabrics with Different Parameters

6.1 Introduction

Wearable thermal management systems are advanced technologies integrated into clothing and accessories to regulate body temperature efficiently. These systems enhance comfort, improve performance, and safeguard health by preventing overheating or hypothermia. They find applications in sports[175], healthcare[176], and military contexts[47], ensuring optimal temperature management in various conditions.

Fluid circulation cooling/heating systems are an advanced type of wearable thermal management technology that regulate body temperature through a network of thin tubes embedded in garments[177]. These tubes circulate a temperature-controlled fluid, such as water or a water-glycol mixture, moved by lightweight pumps. The fluid is cooled or heated using external heat transfer panels before flowing through the garment, managed by an integrated control unit that adjusts the fluid temperature based on sensor data. This system efficiently provides precise thermal regulation by absorbing body heat when cooling or transferring warmth when heating, ensuring uniform and consistent temperature control, and enhancing comfort and performance in various conditions.

Traditional water-based systems face challenges such as high head loss and suboptimal heat transfer due to the fluid dynamics within limited fluid channels. To enhance these systems, previous chapters focus on developing thin, lightweight, and flexible heat transfer panels that

can operate efficiently with limited power sources while ensuring safety and energy efficiency. Additionally, a comprehensive analysis of flow fields within these systems is conducted to improve heat transfer capabilities, utilizing computational fluid dynamics (CFD) simulations and fluid field visualization experiments.

However, the nature of fluid field manipulation is by controlling the velocity and pressure field. This involves the energy transfer during the fluid circulation and further requires another important area to investigate is optimizing kinetic energy transfer and managing flow resistance to maintain uniform heat performance and efficient fluid velocity. In fluid dynamics, energy loss—often referred to as head loss—describes the dissipation of energy as fluid flows through a system and is influenced by several factors, significantly impacting the efficiency of fluid movement and heat transfer[178]. The two main types of energy loss are frictional losses (major losses) caused by friction between the fluid and the walls of the pipe or channel, and minor losses associated with components like valves, fittings, and bends that introduce resistance and turbulence. Viscosity, a measure of a fluid's resistance to flow, plays a crucial role in these losses, with higher viscosity fluids experiencing more frictional resistance[179]. Additionally, turbulence in fluid flow, as opposed to laminar flow, leads to greater resistance and higher energy losses, further affecting the system's efficiency[180]. Understanding these factors is essential for optimizing fluid systems to minimize energy loss and enhance overall performance.

Based on previous chapters results, this chapter further investigates the energy transfer during the process of water circulation. Firstly, the power loss calculation of a specific network structure (fluid field investigated in chapter 5) with inlet velocity ranging from 0.025 m/s to 1.0 m/s. The calculation is performed by using the energy balance equation deduced directly from the Navier-Stokes equations. Secondly, the analysis on the energy loss type is performed. The

power loss constitution under different kinds of flow field is investigated and then the power loss type is visualized to show the location where it is generated. Thirdly, the effect of power loss on heat transfer is performed. This can help us know how to choose the most suitable inlet velocity for a desirable heat transfer capability. Last, other four representative network structures are analysed to help us know the effect of different network structures and give the guidance on designing the wearable heat transfer panels.

6.2 Methodology

6.2.1 Numerical simulation set up

The numerical simulation results are processed based on the results in chapter 5. Details of the numerical simulation can be found in section 5.2.2.

6.2.2 Analysis method of power loss for network structure

Power loss can be calculated by approaches such as total pressure loss, entropy production theory[181] and energy balance equation. The total pressure loss analysis cannot offer sufficient internal information from simulation results, while the entropy theory not only includes hydraulic loss but also involves the transfer of internal energy. The theory chosen for this work was the energy balance equation that was deduced directly from the Navier-Stokes equations[182–184], since viscosity and turbulence are two key factors for power loss analysis, and the power loss calculated here is the power loss of water. The energy balance equation is:

$$P_L = -\iiint_V \frac{\partial\left(-\overline{u_i}\overline{\rho u_i' u_j'}\right)}{\partial x_j} dV + \iiint_V \mu \frac{\partial\left(-\overline{u_i}\overline{D_{ij}}\right)}{\partial x_j} dV + \iiint_V \left(-\overline{\rho u_i' u_j'}\right)\frac{\partial \overline{u_i}}{\partial x_j} dV + \iiint_V \mu \overline{D_{ij}} \frac{\partial \overline{u_i}}{\partial x_j} dV \tag{6-1}$$

where

$$D_{ij} = \frac{\partial u_i}{\partial x_j} + \frac{\partial u_j}{\partial x_i} \tag{6-2}$$

$$\overline{-\rho u_i' u_j'} = \mu_t \left(\frac{\partial \overline{u_i}}{\partial \overline{x_j}} + \frac{\partial \overline{u_j}}{\partial \overline{x}_i}\right) - \frac{2}{3}\delta_{ij}\rho k \tag{6-3}$$

where $\overline{u_i}$ is the Reynolds averaged velocity vector; μ represents the dynamic viscosity; δ_{ij} represents the Kronecker delta symbol; ρ represents the fluid density, kg/m^3; k is the turbulent energy, m^2/s^2; $\overline{-\rho u_i' u_j'}$ is the section for Reynolds stress tensor; u_i' in term $\rho\overline{u_i' u_j'}$ is the fluctuating component of the flow velocity; μ_t represents the turbulent viscosity.

The power loss is the sum of the four items (PL1-PL4) on the right side of Eq. (6). PL1 is the diffusion loss of the kinetic energy due to Reynolds stress; PL2 is the diffusion loss of the kinetic energy due to viscous stress; PL3 is the turbulent kinetic energy produced due to the transformation of the kinetic energy to the turbulent kinetic energy; PL4 is the viscous energy dissipation of mean kinetic energy.

6.3 Results and discussion

6.3.1 Power loss calculation and visualization

After the discussions on mass transfer and flow field evolution, this section reveals the energy dispersion in the network structure. To evaluate the power loss of a particular parameter defined hexagonal unit cell, a three-dimensional (3D) network-structured flow field with 4 × 3 reinforcement dots layout (**Figure 5.1**) was set up. The inside wall shape of network structure can be controlled by changing the three parameters, D*, R* and *r*, defined previously. Parameter chosen for power loss calculation and visualization: 5-20-25 (*D* = 5mm, *R* = 20mm, *r* = 25mm). Then the power loss of different network structures can be determined by the energy balance equation (6) derived from the Navier-Stokes equations (see in Methodology). **Figure 6.1** shows the integration results of power loss density in spatial region of heat transfer panel restricted by hexagonal prism 12 (HP12), HP13, HP22, HP32, HP33 mentioned in **Figure 5.1**.

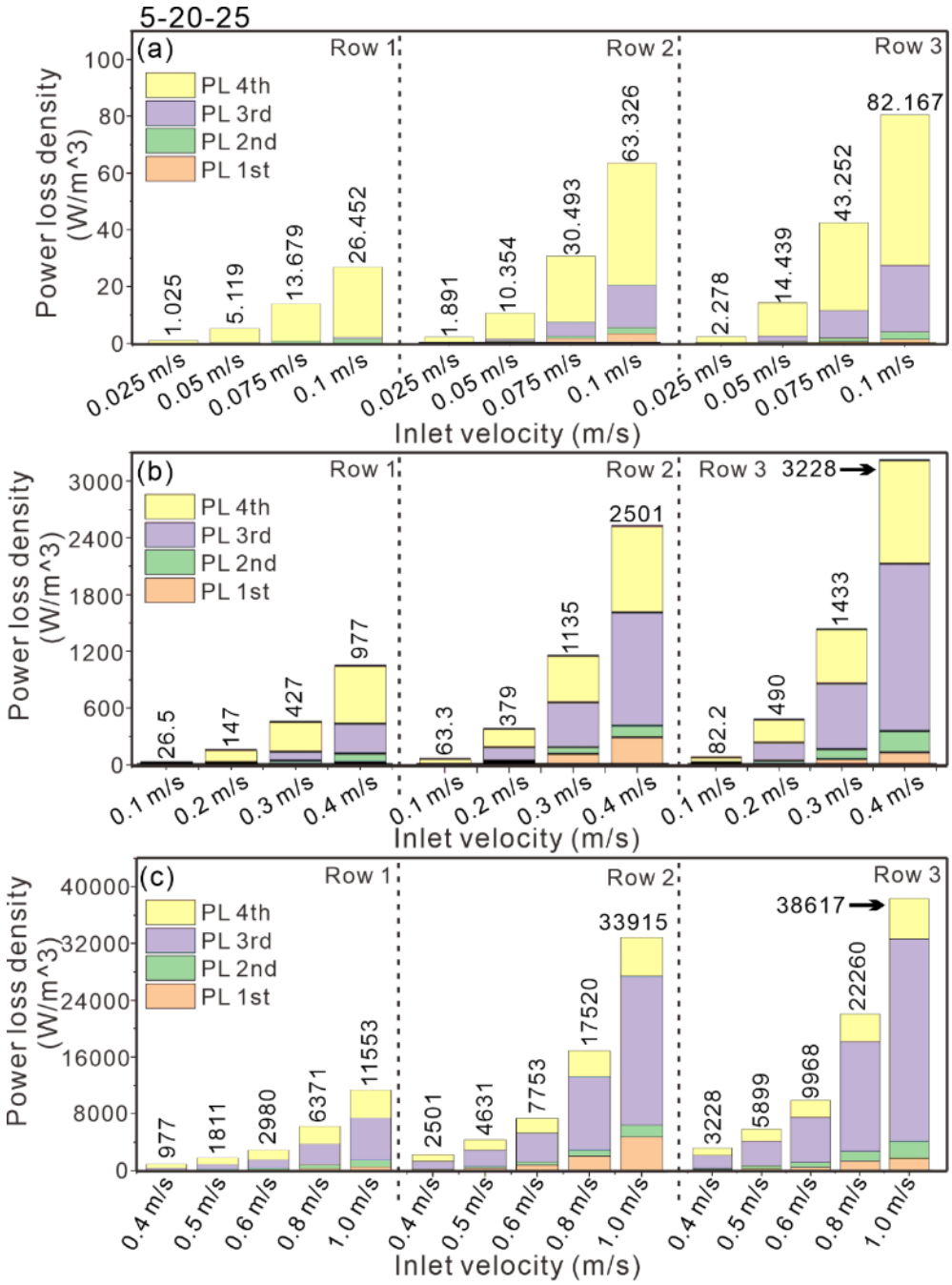

Figure 6.1 Average power loss density of hexagon region (D = 5mm, R = 20mm, r = 25mm; 5-20-25) at each row of reinforcement dots shown in **Figure 5.1**, the power loss increases with the increasement of inlet velocity and the major power loss types in network structure are PL 3 and PL 4.

The calculation results are divided into three groups which corresponds to the previous three kinds of fluid evolution regime: pure laminar flow regime (**Figure 6.1a**), transition flow regime (**Figure 6.1b**) and transition flow with more turbulent factors (**Figure 6.1c**). As shown in **Figure 6.1a**, the total power loss is quite low. This is because the flow regime is pure laminar. Head loss during a pure laminar flow regime is primarily due to friction, and is directly proportional to the fluid's viscosity, the pipe length, and the flow velocity, and inversely proportional to the fluid density, the pipe diameter squared, and gravity[185]. Since the pipe shape, fluid physical parameters and gravity are fixed, the increasing of head loss is mainly due to the increasement of flow velocity. When the flow regime is pure laminar, most of the head loss is contributed by the viscosity caused friction (PL4). When the inlet velocity increases to higher than 0.075 m/s, the turbulence factors occur in the head loss when the flow passes through the second row. This means the first reinforcement dots contribute the turbulence. But the velocity is still not high enough to trigger turbulence only with one arrow of reinforcement dots. In the transition flow regime, the contribution of PL3 and PL4 are nearly equivalent. However, when in the transition flow regime with more turbulent factors, PL3 becomes the dominant head loss type due to higher velocity. The PL4 also increased in this flow regime but with smaller increasement. The total power-loss density increases with the increasing velocity (**Figure 6.1**).

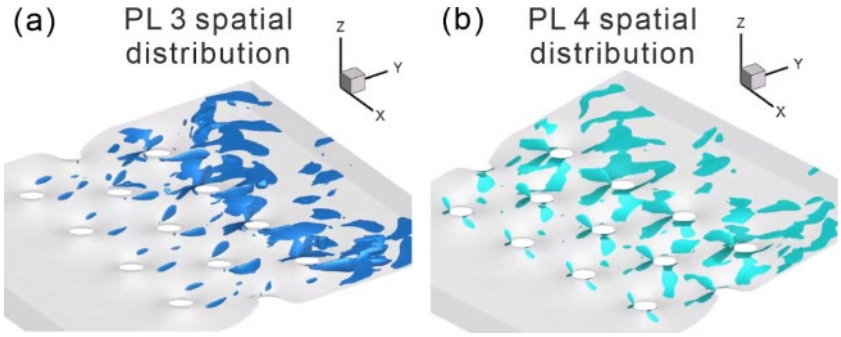

Figure 6.2 (a) PL3 distribution in spatial region, mainly occurs at inner part of network structure (5-20-25); (b) PL4 distribution in spatial region, mainly occurs near the walls of network structure (5-20-25).

In general, the flow inside network structure is transitional flow, which contains both features for the laminar and turbulent flows. The major power loss sections are power loss section 3 (PL3) and PL4, which were induced by transformation of the laminar to the turbulent kinetic energy in the central part of flow field and viscosity dissipation at the boundary layer region of flow field (**Figure 6.2**), which are contributed by inertial and viscous forces, respectively. The PL3 increases much faster and is the dominant head loss type when the flow is pure laminar, PL3 and PL4 are nearly equivalent when flow is transition flow, the PL4 increases faster and is the dominant head loss type when the flow contains more turbulent factors (**Figure 6.3**). PL1 and PL2 are not the key factors for head loss in network-structured flow field. The frequency and inlet pressure increase with the increasing of inlet velocity while the drag coefficient decreases (**Figure 6.4**). The power loss of this network structure parameter is 82.2 W/m^3 when the inlet velocity is 0.1 m/s (**Figure 6.1b**). This means the total power loss is quite small and the results show this structure is suitable for most parts of this wearable heat transfer panel. As

the velocity in FA4 is much smaller when comparing the that at the inlet, the velocity in FA4 after dispersion is around 0.1 m/s.

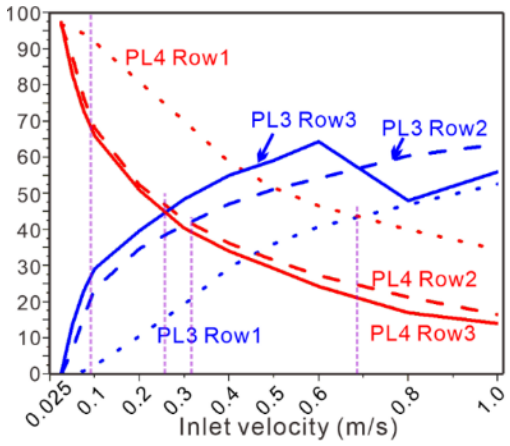

Figure 6.3 The power loss constitution of different rows at different inlet velocities.

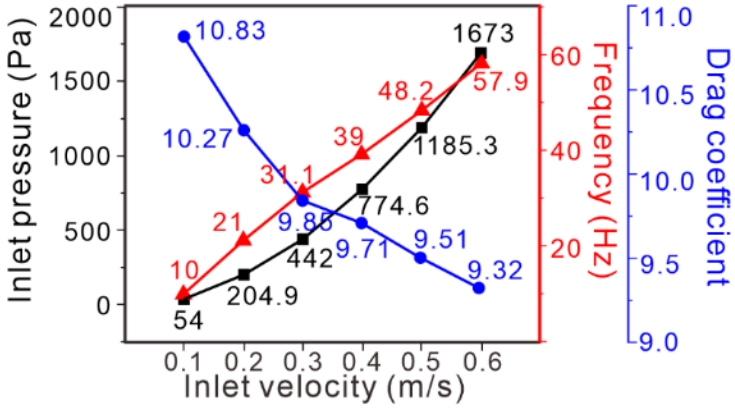

Figure 6.4 Frequency, pressure & drag coefficient vs. different inlet velocity of 5-20-25 network structure, the inlet pressure and vortex shedding frequency increase with the increasement of inlet velocity magnitude.

As shown in **Figure 6.5**, **Figure 6.6**, PL3 is mainly induced by the disturbance of reinforcement dots, which corresponds to the step (i) & (ii) in mixing & distribution mechanism - large flow velocity gradient behind the separating point (pink arrow 2 in **Figure 6.7**) and previous vorticity induced rotation (pink arrow 1 in **Figure 6.6i**). PL3 contributes to the mass mixing in the x-y plane for the improvement of velocity evenness. Power loss induced by viscosity dissipation (PL4) mainly occurs at the windward side walls of the dots because of the curved wall structure caused by the "balloon effect". When the flow passes the curved walls around dots, the thickness of channel (length in z-axis) decreases, and the flow is forced to go along the x-y plane of the flow network. Boundary laminar flow layers near the walls are destroyed and the heating performance of heat transfer panel is enhanced. By comparing the instantaneous and time-averaged results, the power loss density pattern is almost the same when the inlet flow velocity is lower than 0.05 m/s. It shows that the flow is pure laminar, which corresponds to the flow regime analysis previous. However, when the inlet flow velocity is larger than 0.075 m/s, the instantaneous power loss density contour starts to turn into chaos. It shows the turbulence factors starts to occur from this flow regime. Although the flow density map shows the calculated results of all kinds of power loss type, most power loss in x-y plane is contributed by PL3. By comparing the results of vorticity map in previous section and the power loss density, the PL3 is mainly caused by the turbulent of the rotation of the vortex.

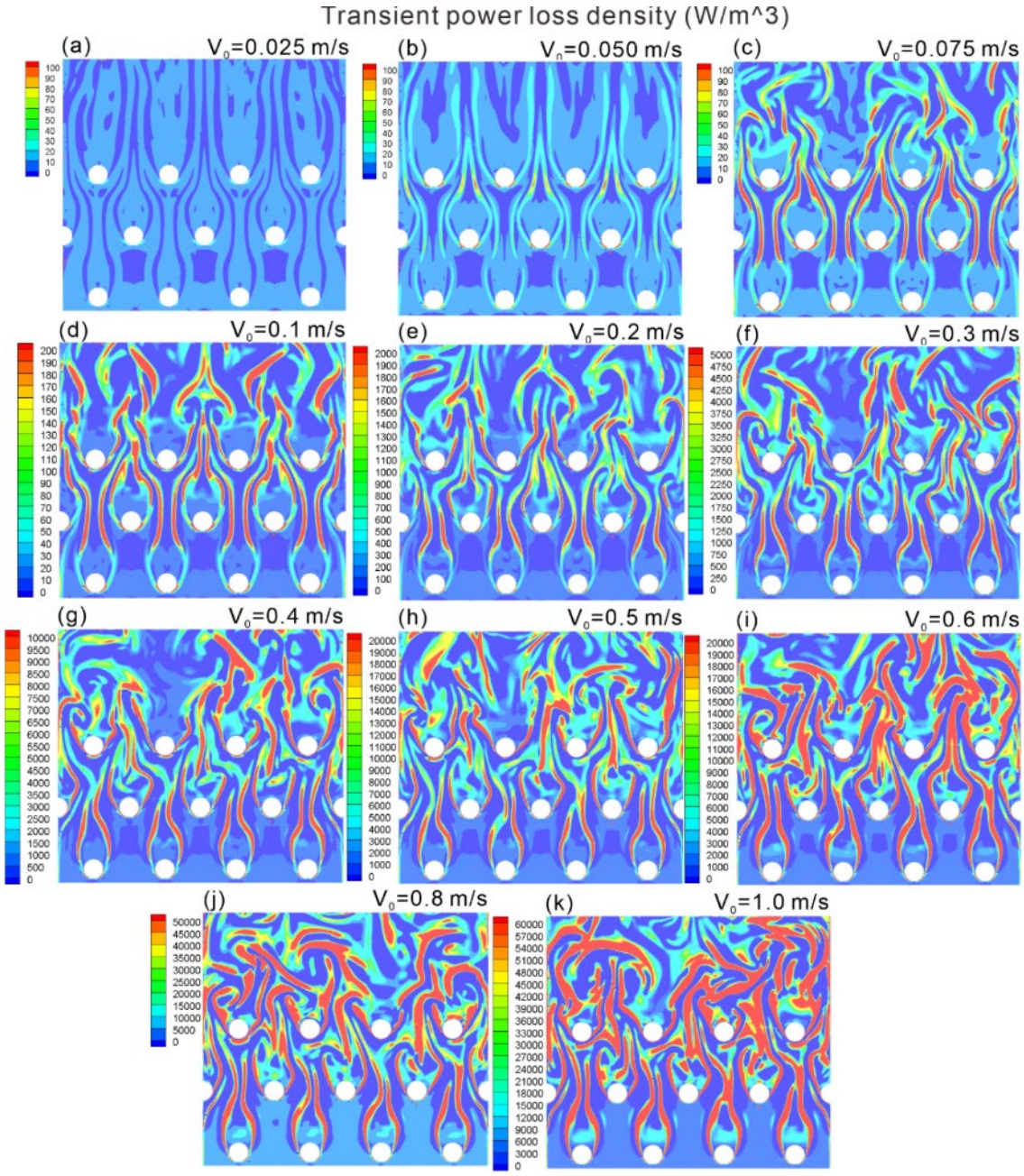

Figure 6.5 Visualization of total power loss density in instantaneous flow field in x-y plane, the power loss mainly occurs where velocity gradient is high together with significant mass mixing. (a) V_0 = 0.025 m/s; (b) V_0 = 0.05 m/s; (c) V_0 = 0.075 m/s; (d) V_0 = 0.1 m/s; (e) V_0 = 0.2 m/s; (f) V_0 = 0.3 m/s; (g) V_0 = 0.4 m/s; (h) V_0 = 0.5 m/s; (i) V_0 = 0.6 m/s; (j) V_0 = 0.8 m/s; (k) V_0 = 1.0 m/s.

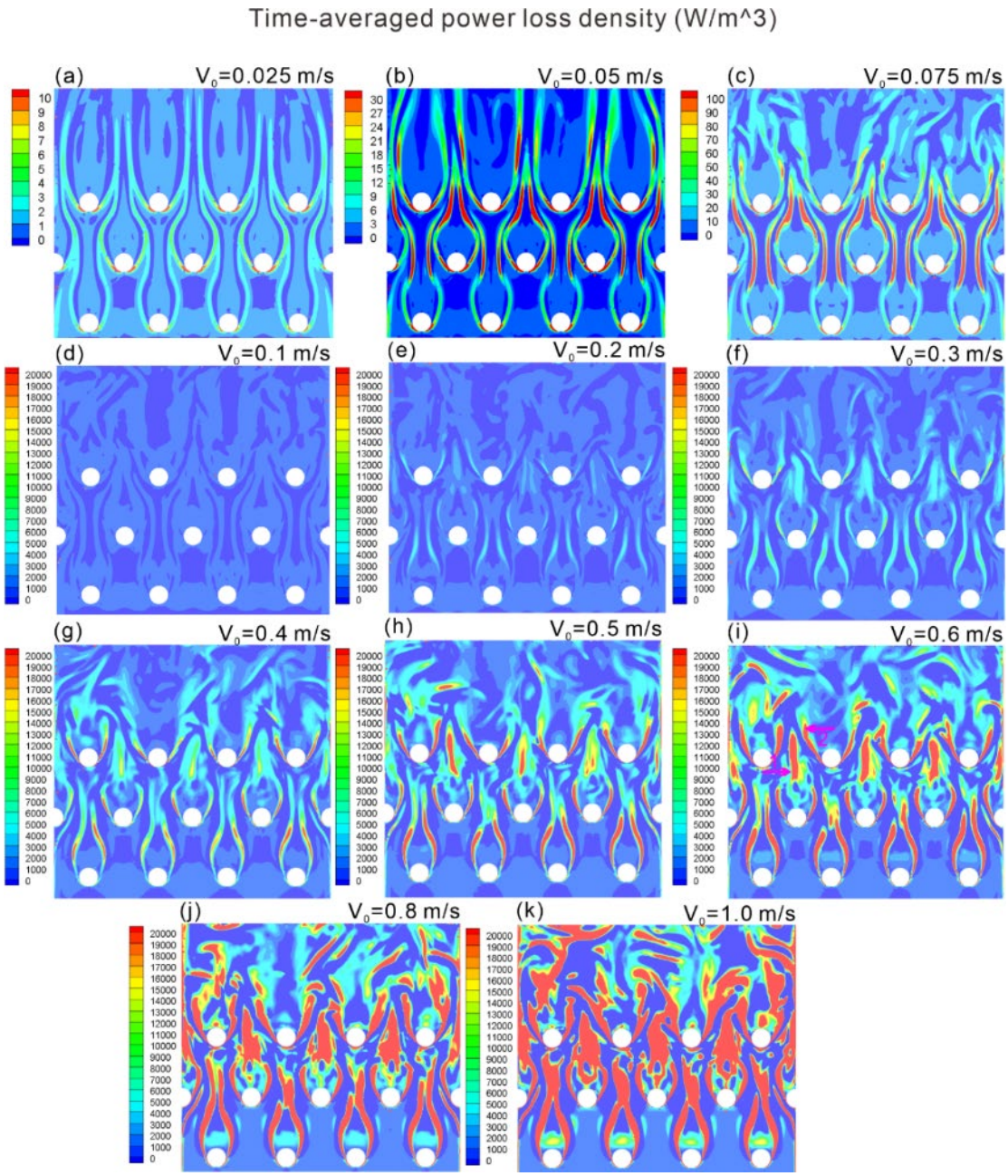

Figure 6.6 Visualization of total power loss density in time-averaged flow field in x-y plane. (a) V_0 = 0.025 m/s; (b) V_0 = 0.05 m/s; (c) V_0 = 0.075 m/s; (d) V_0 = 0.1 m/s; (e) V_0 = 0.2 m/s; (f) V_0 = 0.3 m/s; (g) V_0 = 0.4 m/s; (h) V_0 = 0.5 m/s; (i) V_0 = 0.6 m/s; (j) V_0 = 0.8 m/s; (k) V_0 = 1.0 m/s.

6.3.2 Heat transfer performance of network structure

The wearable heat transfer panel needs to transfer energy between the skin surface and the internal fluid and works locally based on the 4-step mass transfer and curved wall structure. This part investigates the heat performance of network structures based on previous analysis on flow field evolution and power loss density. The inlet temperature is set as 5ºC and the temperature outside the network structure is set as 38ºC. The network structure assumed by fully covered by an aluminium shell of 0.3 mm thickness. The setting is different from the actual using scenarios of wearable heat transfer panels (watertight fabric constructed network structure covering on skin surface), the purpose of this setting is just to find out the heat transfer capability on different parts of the network structure.

Figure 6.7 is the water temperature distribution inside network structure of x-y plane by time-averaged simulations with different inlet velocity. In all calculation cases, the temperature in areas without reinforcement dots are much lower, while higher in the lee side of reinforcement dots. The temperature is the highest in the lee side of the first row of reinforcement dots and the lee side of the last row of reinforcement dots is the lowest. This can be explained by the contribution of turbulence caused convection. When the inlet flow velocity is 0.1 m/s, the temperature at lee side is the highest, but the temperature at this place show no obvious difference when the inlet velocity is higher than 0.2 m/s. It shows that the effect of convection for heat transfer under this thermal transfer condition has reached to a choke. On considering the power loss is much higher if we try to increase the velocity magnitude inside the network structure. The velocity 0.1 m/s is very suitable for this parameter network structure since the power loss is acceptable and the convention for heat transfer is enough. Also, even though the temperature is high at the lee side of reinforcement dots, the actual condition is that this part do

not directly contact with the skin surface and the thermal transfer is mainly conducted by radiation.

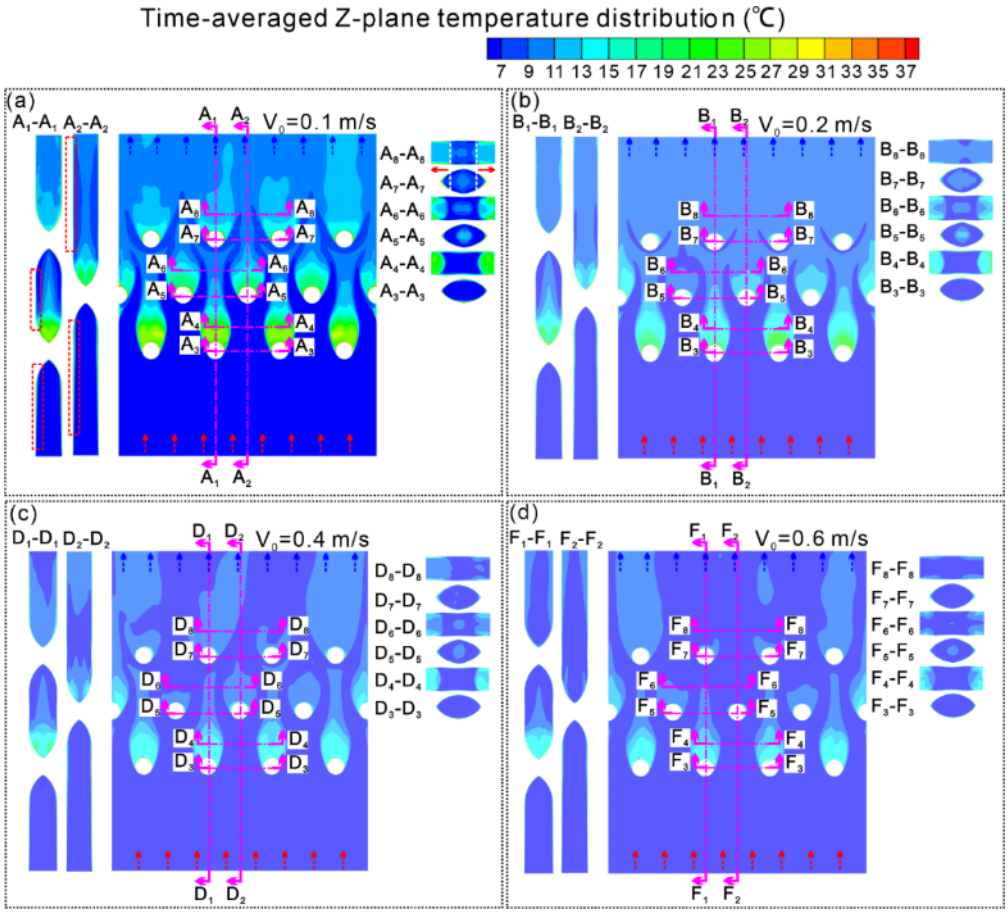

Figure 6.7 Water temperature distribution inside network structure of x-y plane by time-averaged simulations with different inlet velocity. (a) V_0 = 0.1 m/s; (b) V_0 = 0.2 m/s; (c) V_0 = 0.4 m/s; (d) V_0 = 0.6 m/s.

Figure 6.8 is the temperature distribution on the surface network structure of by time-averaged simulations with different inlet velocity. The results show almost the same conclusion in previous paragraph. The heat transfer ability shows no obvious change when the inlet velocity

is higher than 0.2 m/s in most part of areas without reinforcement dots. The temperature is the lowest at the place with high power loss consumption. This surface temperature results can be further analysed by the surface Nusselt number.

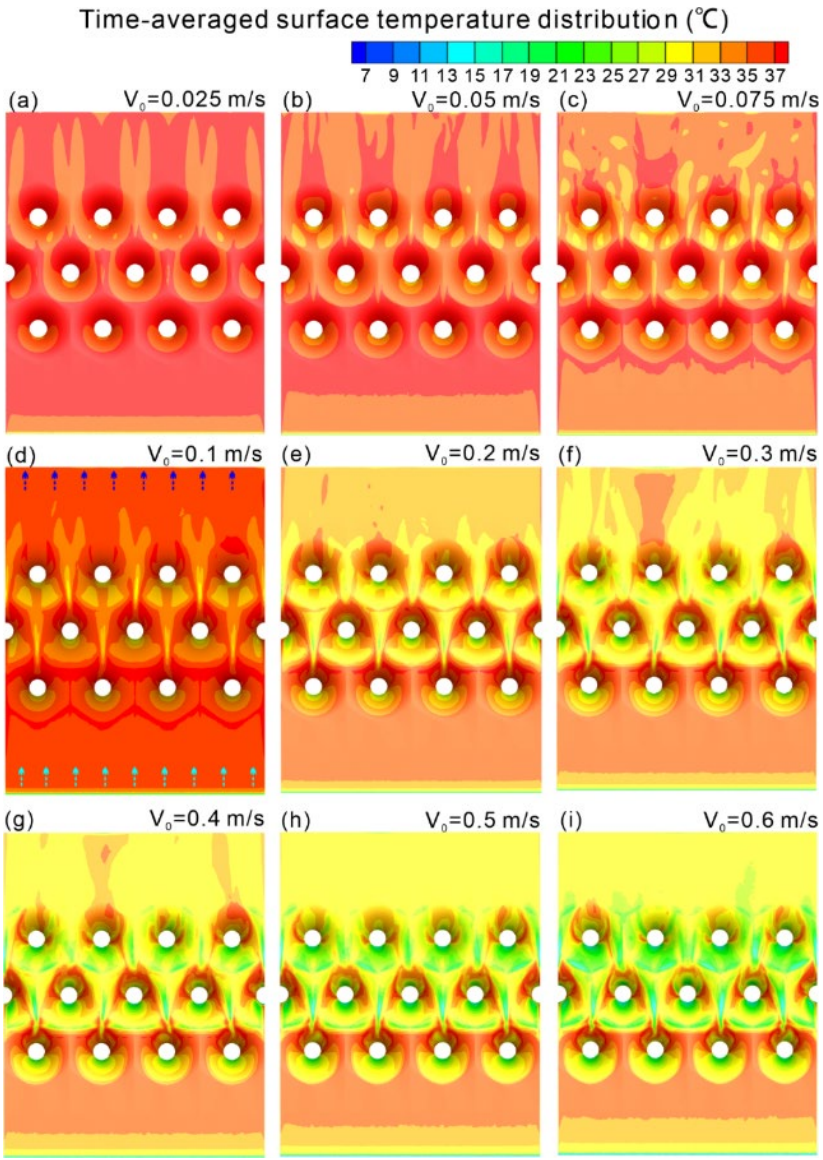

Figure 6.8 Temperature distribution on the surface network structure of by time-averaged simulations with different inlet velocity. (a) V_0 = 0.025 m/s; (b) V_0 = 0.05 m/s; (c) V_0 = 0.075 m/s; (d) V_0 = 0.1 m/s; (e) V_0 = 0.2 m/s; (f) V_0 = 0.3 m/s; (g) V_0 = 0.4 m/s; (h) V_0 = 0.5 m/s; (i) V_0 = 0.6 m/s.

Figure 6.9 shows the surface Nusselt values (Nu) of the heat transfer panel. There are 3 regions with relatively high Nu values, which mean better heat exchange ability. The vertical "line" shaped high Nu region, which corresponds to the mass transfer steps (i) & (ii). The rotation, elongation and alternative vortex shedding effect in this region contribute to the heat convection by destroying the boundary layer (**Figure 6.7**). High Nu regions in front of the reinforcement dots are caused by mass transfer steps (iii) & (iv), together with the curved wall structure. Because on the windward side, the shrinking thickness of the tunnel near the dots decreases the local divergence and increases the local curl, this further enhances heat convection. **Figure 6.8** shows that the temperature is higher on the lee side of the reinforcement dots (low-pressure region) due to the low flow velocity. The Nusselt values are extreme low when the inlet velocity is lower than 0.05 m/s. Because in these conditions, the flow is pure laminar and the convention in vertical direction is very weak. When the velocity is between 0.075 m/s and 0.1 m/s, most parts of network structure surface show relatively high Nusselt value. Although the Nusselt value is much higher when the inlet velocity is larger than 0.2 m/s, the power loss is also very high under these conditions.

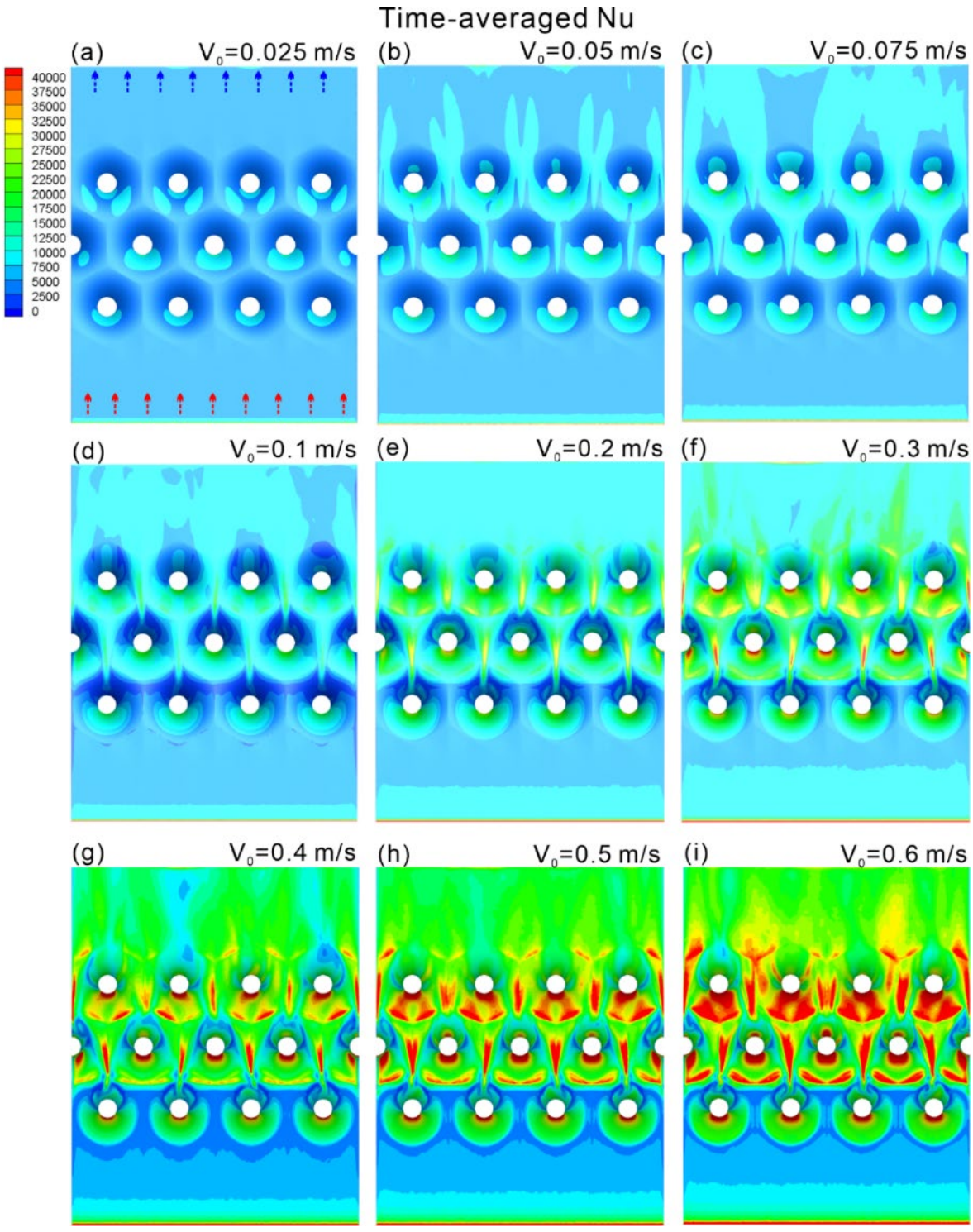

Figure 6.9 Surface Nusselt number of network structure of by time-averaged simulations with different inlet velocity. (a) V_0 = 0.025 m/s; (b) V_0 = 0.05 m/s; (c) V_0 = 0.075 m/s; (d) V_0 = 0.1 m/s; (e) V_0 = 0.2 m/s; (f) V_0 = 0.3 m/s; (g) V_0 = 0.4 m/s; (h) V_0 = 0.5 m/s; (i) V_0 = 0.6 m/s.

6.3.3 Comparison of different network structures

Chapter 5 detailed investigates the flow field evolution of network structure with parameter 5-20-25. Previous part of chapter 6 detailed analyses the power loss and thermal transfer of network structure with parameter 5-20-25. The basic fluid field condition of this novel network structure is comprehensive understanded by previous contents. The following section focuses on the analysis of four representative network structures and study the effects of parameters on power loss consumption, flow field evolution and heat transfer ability. The four representative network structures' parameters: 5-15-25; 5-20-45; 5-25-45; 5-30-45.

6.3.3.1 Time-averaged flow field analysis of the four network structures

As shown in **Figure 6.10** is the time-averaged V/V_0 magnitude contour in the x-y plane (V_0 = 0.1 m/s) of different network structure parameters. These flow fields are like that of 5-20-25 network structure. The V/V_0 value is different when changing the parameters. The highest V/V_0 value of 5-15-25 network structure is ~4. It is higher when comparing to the V/V_0 value ~3.3 of 5-20-25 network structure. The difference between 5-15-25 and 5-20-25 network structure is the parameter "R" (**Figure 6.10a**). The thickness and reinforcement dots diameter of the two network structures are the same. The distance between reinforcement dots of 5-15-25 network structure is smaller. This makes the channel narrower and the interconnection of adjacent reinforcement dots stronger. The fluctuation of flow field around the one reinforcement dot can easily affect the flow field around the reinforcement dots nearby. Since the fluid channels are narrow, the fluid velocity in accelerating area is larger and resulting in the higher V/V_0 value of 5-15-25 network structure. The difference between 5-20-45 and 5-20-25 network structure is the parameter "r" (**Figure 6.10c**). The reinforcement dots' diameter and distance of the two network structures are the same. The thickness of 5-15-25 network structure is smaller. This

makes the water consumption smaller and the boundary layer constitution higher inside the network structure basin. The reason for this phenomenon is the same as that in 5-15-25 network structure. Their fluid channel is narrow when comparing to the one of 5-20-25 network structure. The difference between 5-25-45, 5-30-45 and 5-20-45 network structure is also the parameter "R" (**Figure 6.10c**). Obviously, the V/V_0 value decreases with the increasement of "R" value. This is because the fluid channel is wider.

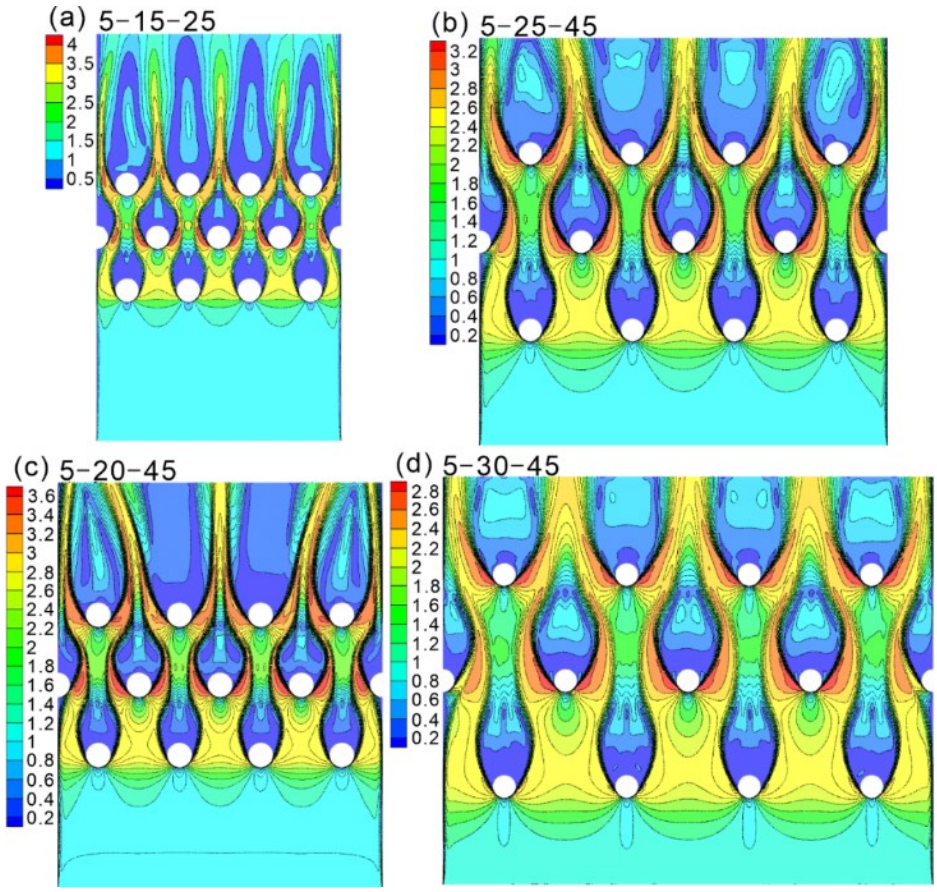

Figure 6.10 Time-averaged V/V_0 magnitude contour in the x-y plane (V_0 = 0.1 m/s) of different network structure parameters. (a) D = 5mm, R = 15mm, r = 25mm, 5-15-25; (b) D = 5mm, R = 25mm, r = 45mm, 5-25-45; (c) D = 5mm, R = 20mm, r = 45mm, 5-20-45; (d) D = 5mm, R = 30mm, r = 45mm, 5-30-45.

Figure 6.11 shows the time-averaged pressure coefficient (Cp) in the x-y plane (V_0 = 0.1 m/s) of different network structure parameters. Obviously, the pressure drop of 5-15-25 network structure is the highest while the pressure drop of 5-30-45 is the lowest. This phenomenon can also be understood as the "block" density formed by reinforcement dots is the highest in 5-15-25 network structure. Since extra reinforcement dots can cause more flow resistance inside the fluid channel. However, time-averaged results can only tell us the general behaviour of flow field. Instantaneous simulation results need to be analysed for more details.

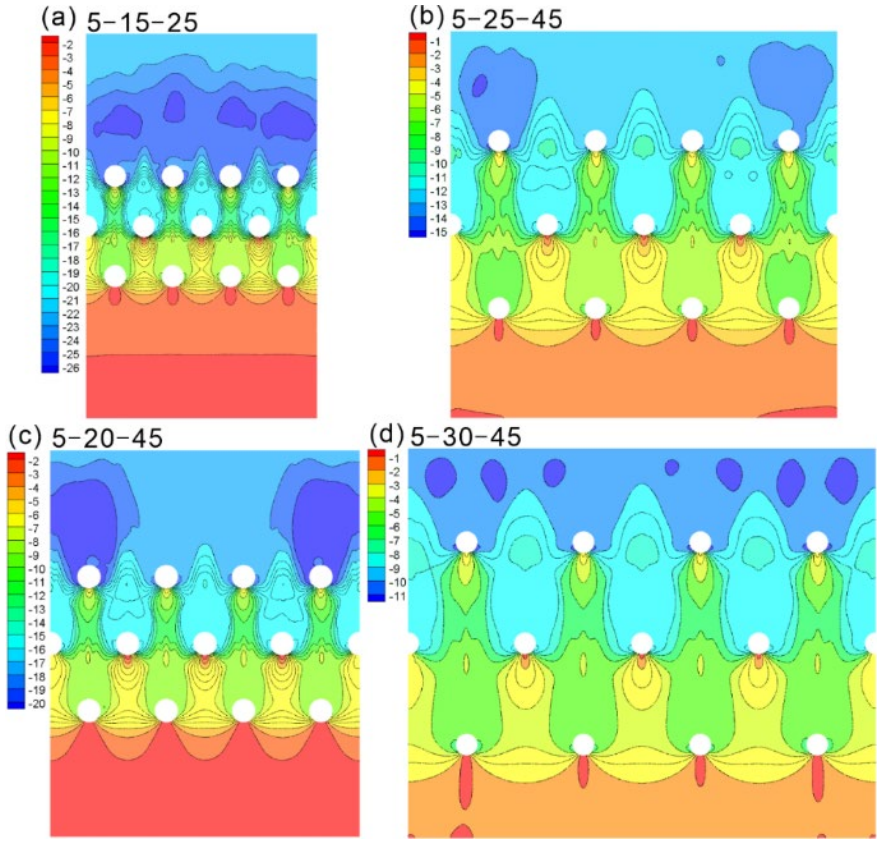

Figure 6.11 Time-averaged pressure coefficient (Cp) in the x-y plane (V_0 = 0.1 m/s) of different network structure parameters. (a) D = 5mm, R = 15mm, r = 25mm, 5-15-25; (b) D = 5mm, R = 25mm, r = 45mm, 5-25-45; (c) D = 5mm, R = 20mm, r = 45mm, 5-20-45; (d) D = 5mm, R = 30mm, r = 45mm, 5-30-45.

6.3.3.2 Instantaneous flow field analysis and power loss visualization of the four network structures

As shown in **Figure 6.12** is the CFD instantaneous simulation results of velocity magnitude contour of 5-15-25 network structure in the x-y plane with different inlet velocity. Different from the instantaneous simulation results of 5-20-25 network structure, no obvious vortex shedding is observed in all cases of 5-15-25 network structure. This can be explained by the narrow fluid channel of this network structure. As the distance between two reinforcement dots are too small to develop the alternative vortex shedding and the boundary layer constitution is high, vortex shedding cannot happen in all these cases. **Figure 6.13** is the visualization of total power loss density in time-averaged flow field in x-y plane of 5-15-25 network structure with different inlet velocity. The power loss mainly occurs at the wake of these reinforcement dots. This is caused by the friction between the low velocity fluid at the lee side of reinforcement dots and the high velocity fluid in the accelerating area. Then, small vortices are formed in this long and narrow friction area. As shown in **Figure 6.14** is the CFD instantaneous simulation results of velocity magnitude contour of 5-20-45 network structure in the x-y plane with different inlet velocity. The fluid field is very similar to that inside the 5-15-25 network structure. No obvious alternative vortex shedding in all cases except the case of 0.6 m/s inlet velocity. **Figure 6.15** is the visualization of total power loss density in time-averaged flow field in x-y plane of 5-20-45 network structure with different inlet velocity. The results show the same power loss behavior when comparing to that of 5-15-25 network structure. This is also due to the narrow fluid channel of this 5-20-45 network structure.

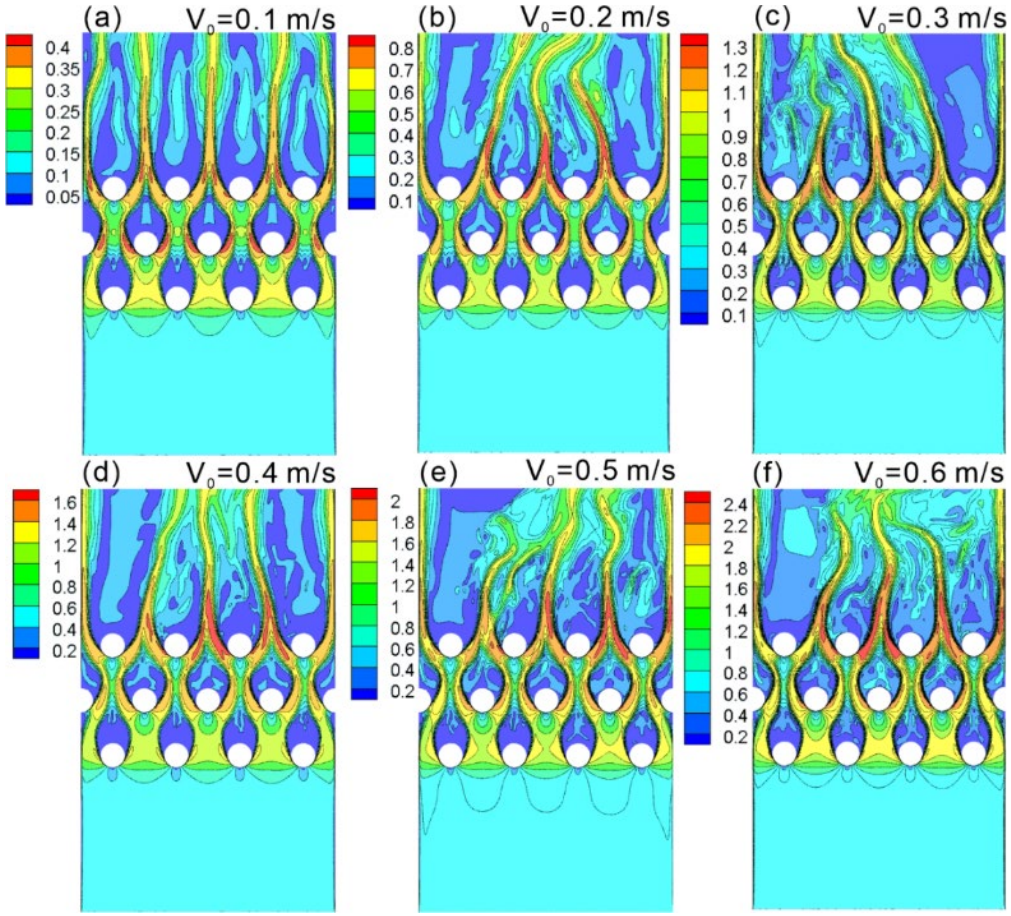

Figure 6.12 CFD instantaneous simulation results of velocity magnitude contour of 5-15-25 network structure in the x-y plane with different inlet velocity. (a) V_0 = 0.1 m/s; (b) V_0 = 0.2 m/s; (c) V_0 = 0.3 m/s; (d) V_0 = 0.4 m/s; (e) V_0 = 0.5 m/s; (f) V_0 = 0.6 m/s.

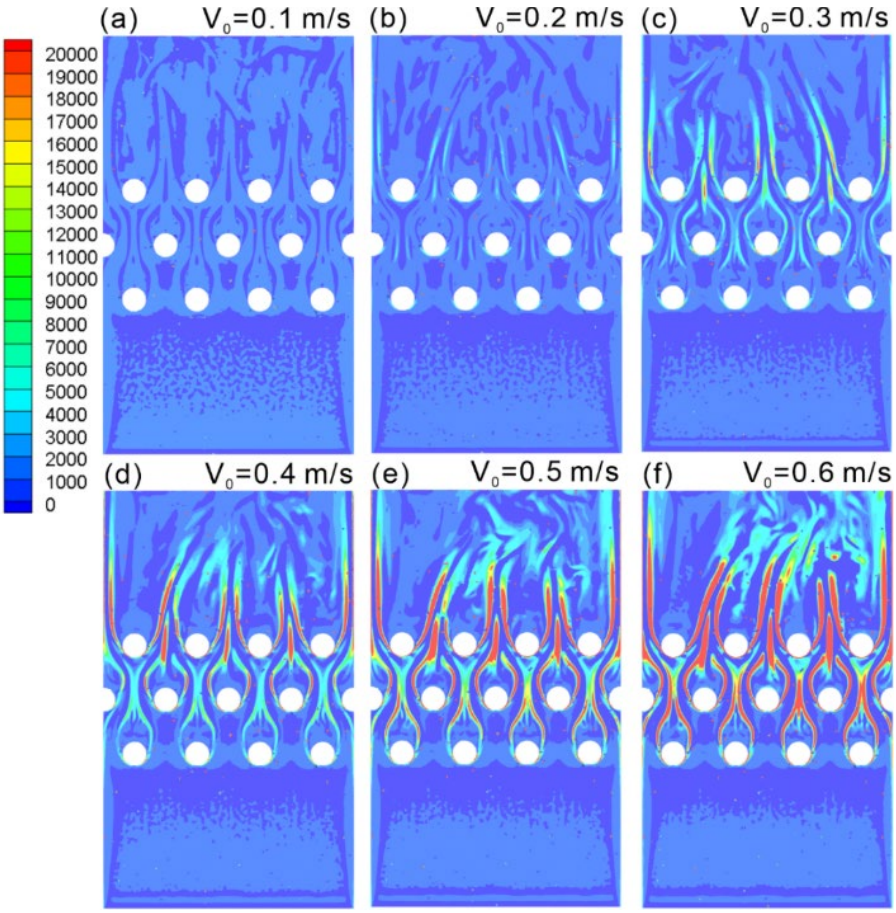

Figure 6.13 Visualization of total power loss density in time-averaged flow field in x-y plane of 5-15-25 network structure with different inlet velocity. (a) V_0 = 0.1 m/s; (b) V_0 = 0.2 m/s; (c) V_0 = 0.3 m/s; (d) V_0 = 0.4 m/s; (e) V_0 = 0.5 m/s; (f) V_0 = 0.6 m/s.

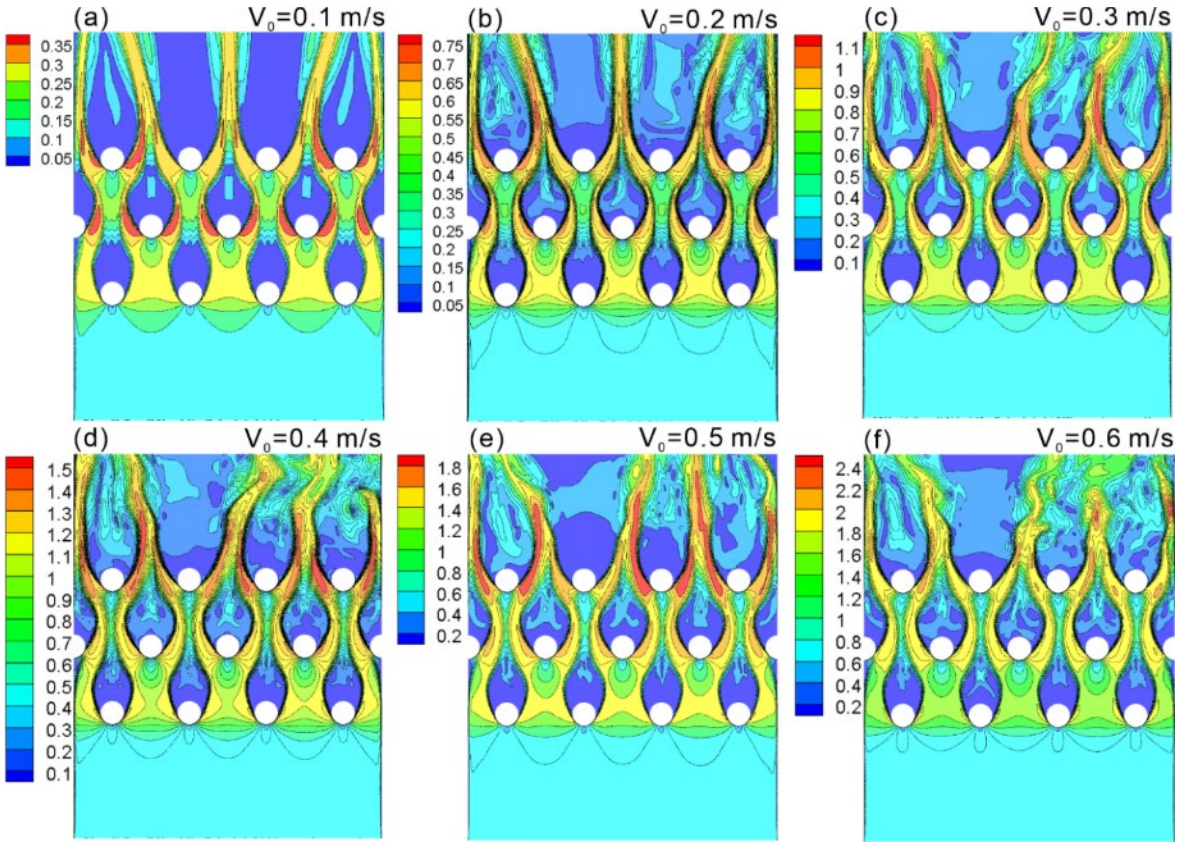

Figure 6.14 CFD instantaneous simulation results of velocity magnitude contour of 5-20-45 network structure in the x-y plane with different inlet velocity. (a) V_0 = 0.1 m/s; (b) V_0 = 0.2 m/s; (c) V_0 = 0.3 m/s; (d) V_0 = 0.4 m/s; (e) V_0 = 0.5 m/s; (f) V_0 = 0.6 m/s.

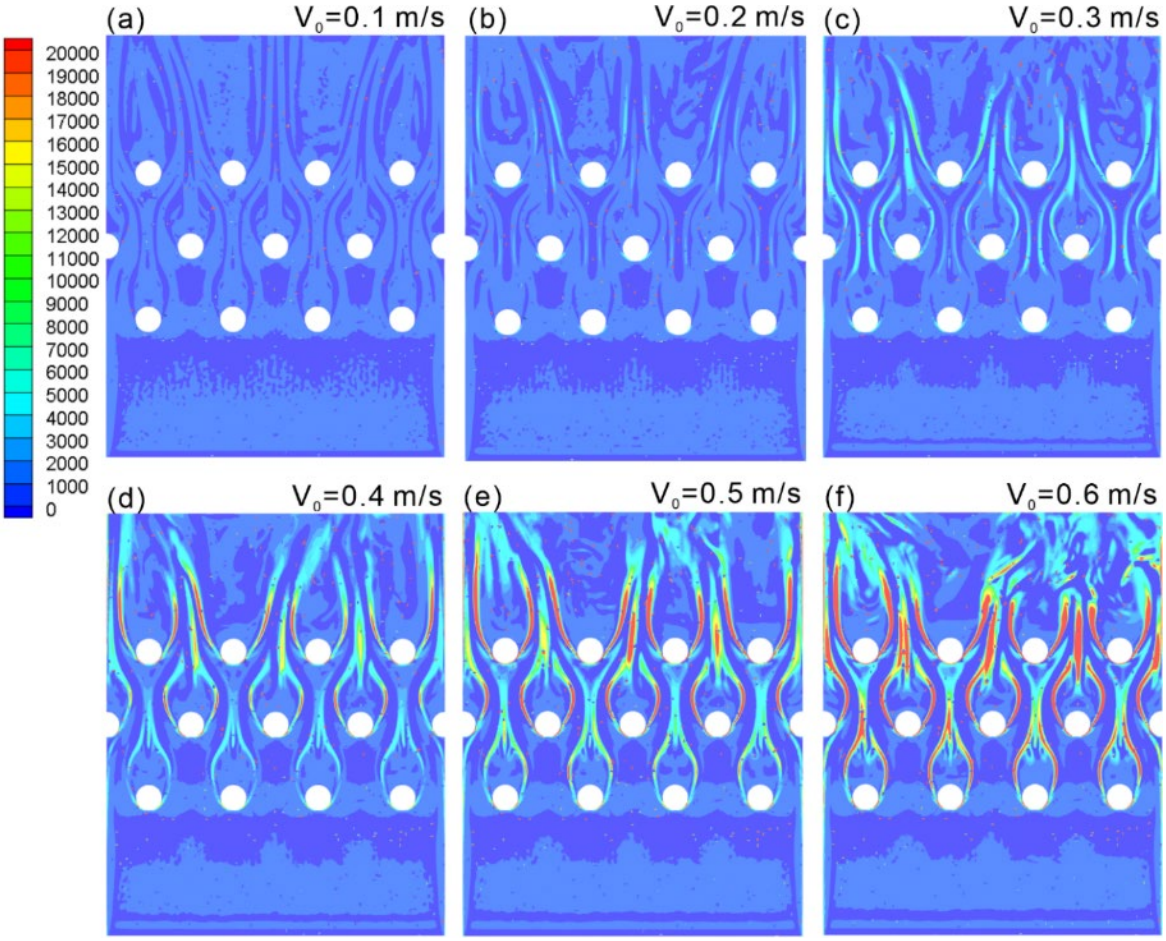

Figure 6.15 Visualization of total power loss density in time-averaged flow field in x-y plane of 5-20-45 network structure with different inlet velocity. (a) V_0 = 0.1 m/s; (b) V_0 = 0.2 m/s; (c) V_0 = 0.3 m/s; (d) V_0 = 0.4 m/s; (e) V_0 = 0.5 m/s; (f) V_0 = 0.6 m/s.

Figure 6.16 is the CFD instantaneous simulation results of velocity magnitude contour of 5-25-45 network structure in the x-y plane with different inlet velocity. Different from previous two network structures, the vortex shedding occurs when the inlet velocity reaches 0.2 m/s. And the vortex shedding even occurs behind the second row when the velocity increased to 0.3 m/s. The maximum velocity increases with the increasing of inlet velocity. The vortex cannot be generated just after one row of reinforcement dots under network structured heat transfer panels scenerios. Even though the vorticity of vortex generated by the closest two reinforcement dots

are entirely in two opposite directions, the vortex generated in the previous row of reinforcement dots seems do not fade away, the magnitude is even enhanced in the accelerating region of the next row of reinforcement dots. The mechanism cannot be clarified just based on current simulation data, but it explains the reason why vortex always do not occur after the first row of reinforcement dots. It shows that this kind of arrangement of reinforcement dots can amplifiy the turbulence generated by previous rows of reinforcement dots. **Figure 6.18** is the CFD instantaneous simulation results of velocity magnitude contour of 5-30-45 network structure in the x-y plane with different inlet velocity. With the increasement of reinforcement dots distance, the occurance of vortex shedding is advanced to the inlet velocity 0.1 m/s. Also, the ovality of the vortex is decreasing, and the magnitude of vorticity is increasing. **Figure 6.17** is the visualization of total power loss density in time-averaged flow field in x-y plane of 5-25-45 network structure with different inlet velocity. The vertical line shape high power loss region only appears after the second row is because the downstream is suqeezed by the following flow field of the next row of reinforcement dots and the turbulence generated by previous provides enough vorticity. **Figure 6.19** is the visualization of total power loss density in time-averaged flow field in x-y plane of 5-30-45 network structure with different inlet velocity. Due to the similar structure parameter to the 5-25-45 network structure, the power loss mapping shows almost the same features.

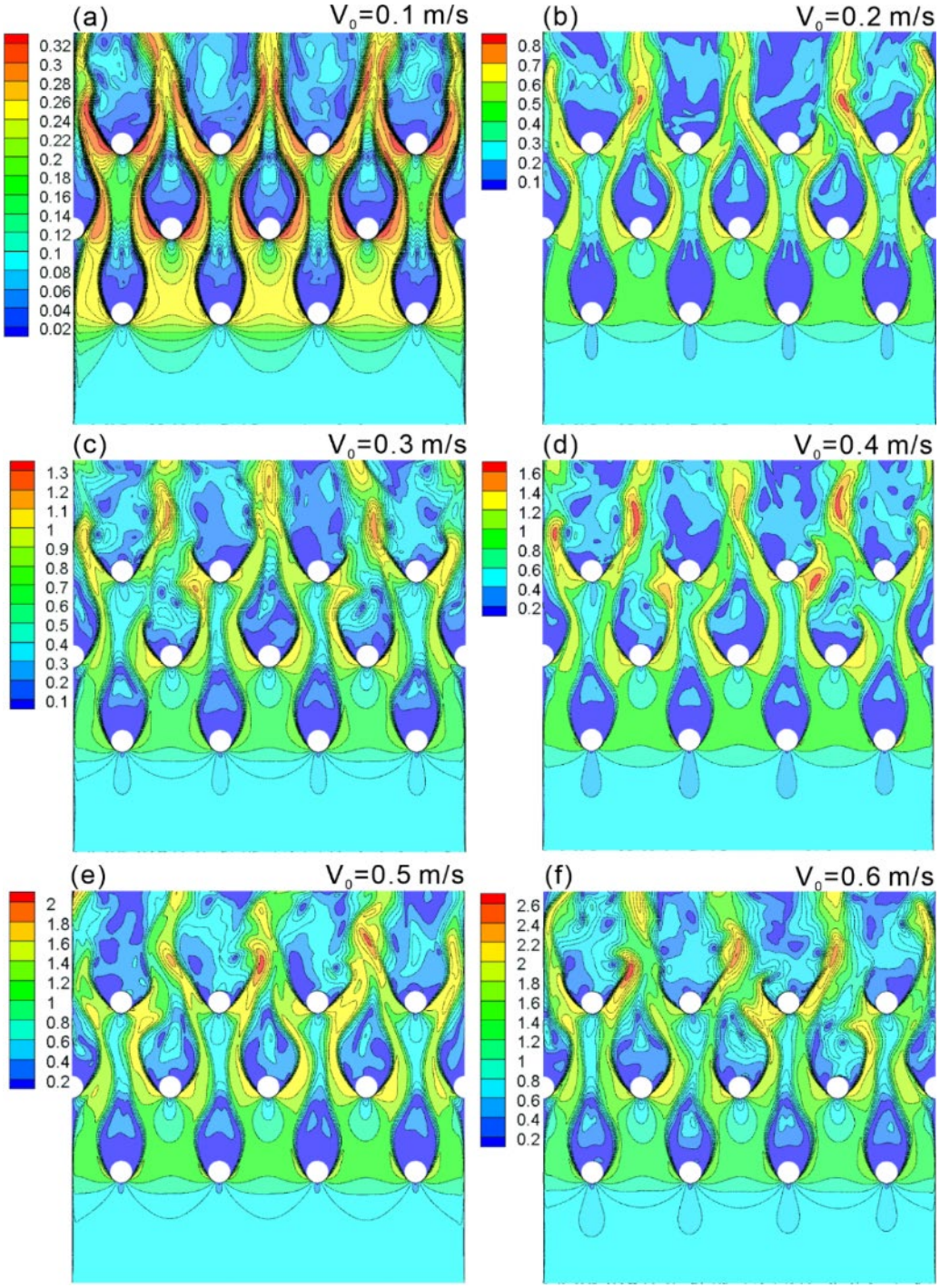

Figure 6.16 CFD instantaneous simulation results of velocity magnitude contour of 5-25-45 network structure in the x-y plane with different inlet velocity. (a) V_0 = 0.1 m/s; (b) V_0 = 0.2 m/s; (c) V_0 = 0.3 m/s; (d) V_0 = 0.4 m/s; (e) V_0 = 0.5 m/s; (f) V_0 = 0.6 m/s.

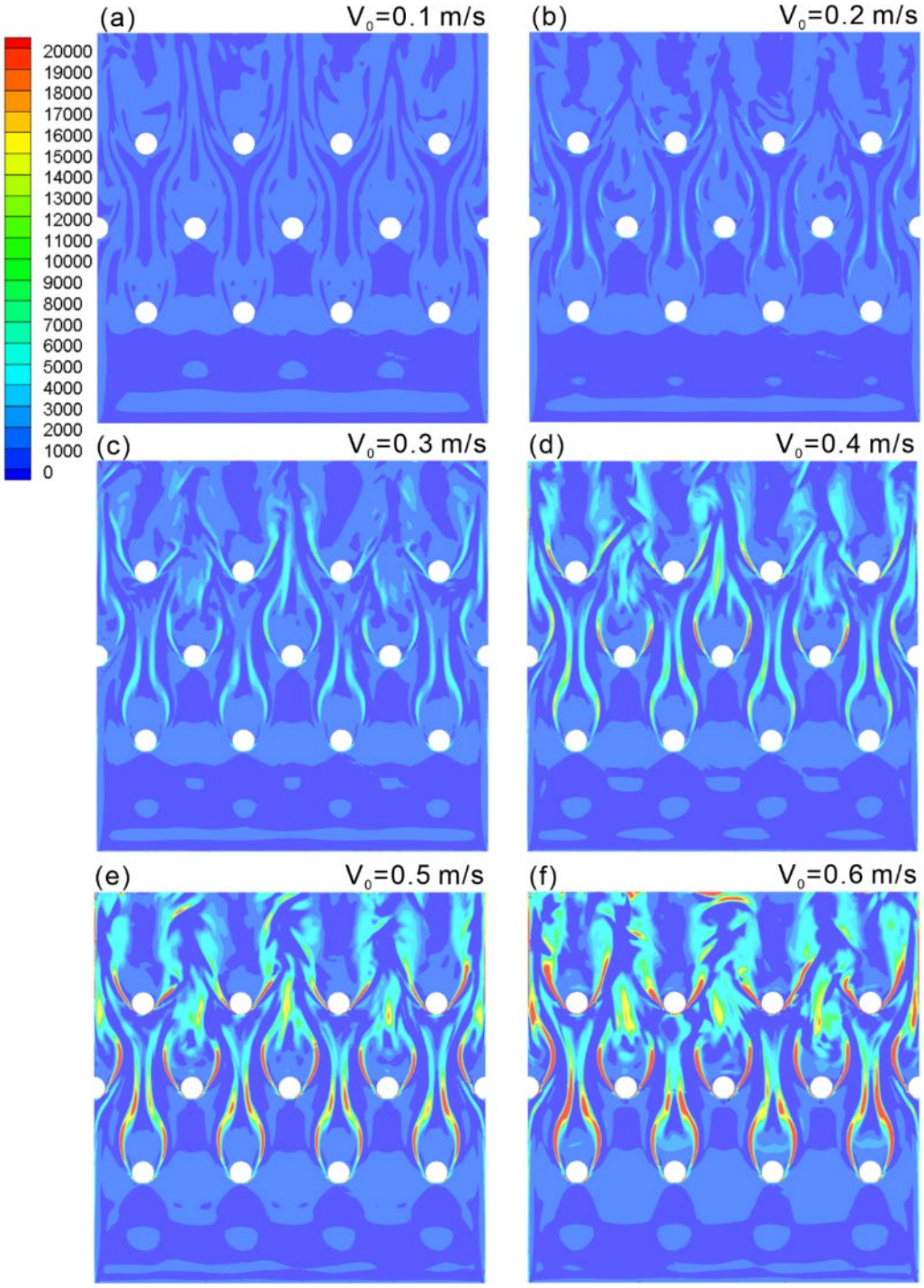

Figure 6.17 Visualization of total power loss density in time-averaged flow field in x-y plane of 5-25-45 network structure with different inlet velocity. (a) V_0 = 0.1 m/s; (b) V_0 = 0.2 m/s; (c) V_0 = 0.3 m/s; (d) V_0 = 0.4 m/s; (e) V_0 = 0.5 m/s; (f) V_0 = 0.6 m/s.

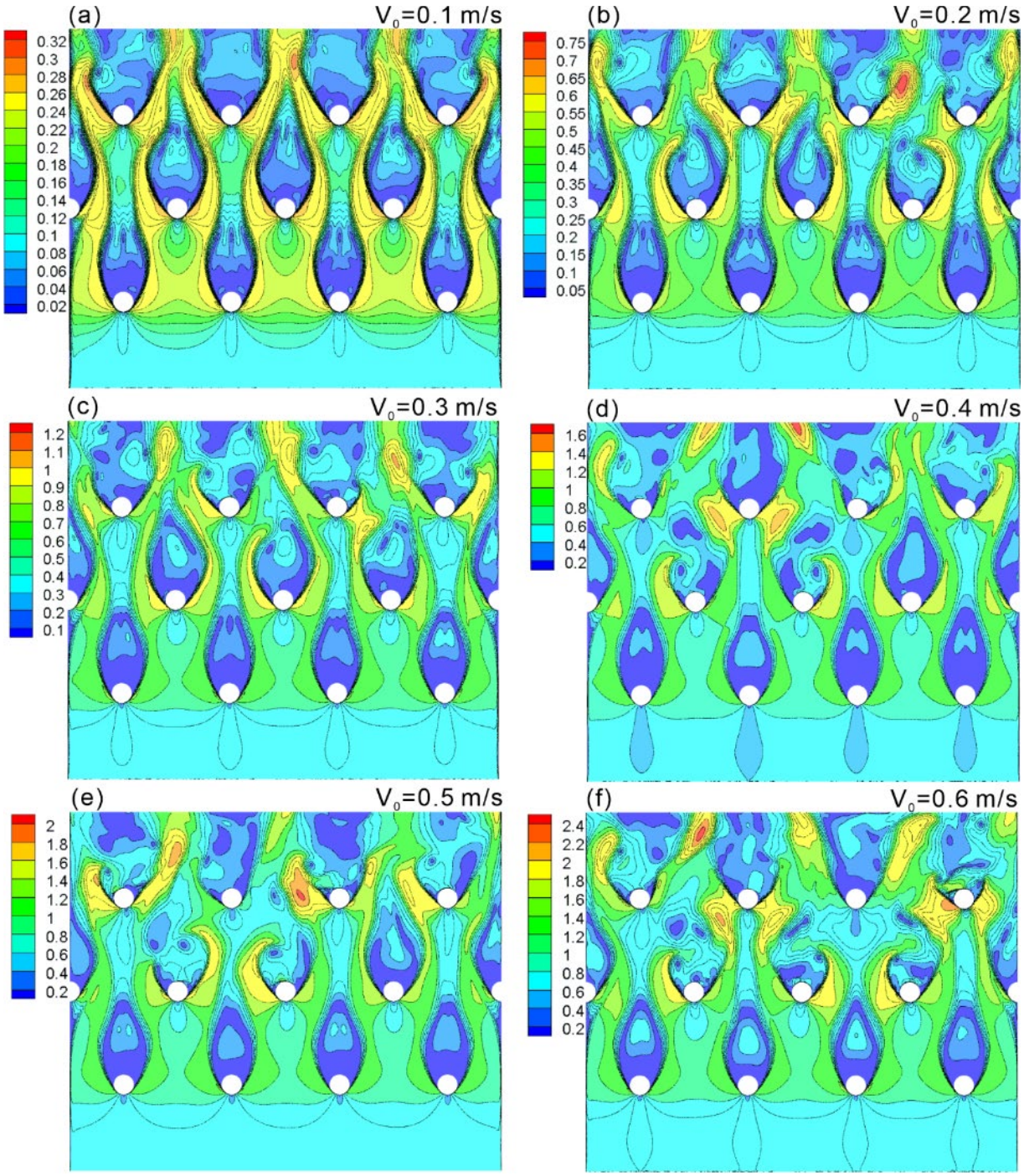

Figure 6.18 CFD instantaneous simulation results of velocity magnitude contour of 5-30-45 network structure in the x-y plane with different inlet velocity. (a) V_0 = 0.1 m/s; (b) V_0 = 0.2 m/s; (c) V_0 = 0.3 m/s; (d) V_0 = 0.4 m/s; (e) V_0 = 0.5 m/s; (f) V_0 = 0.6 m/s.

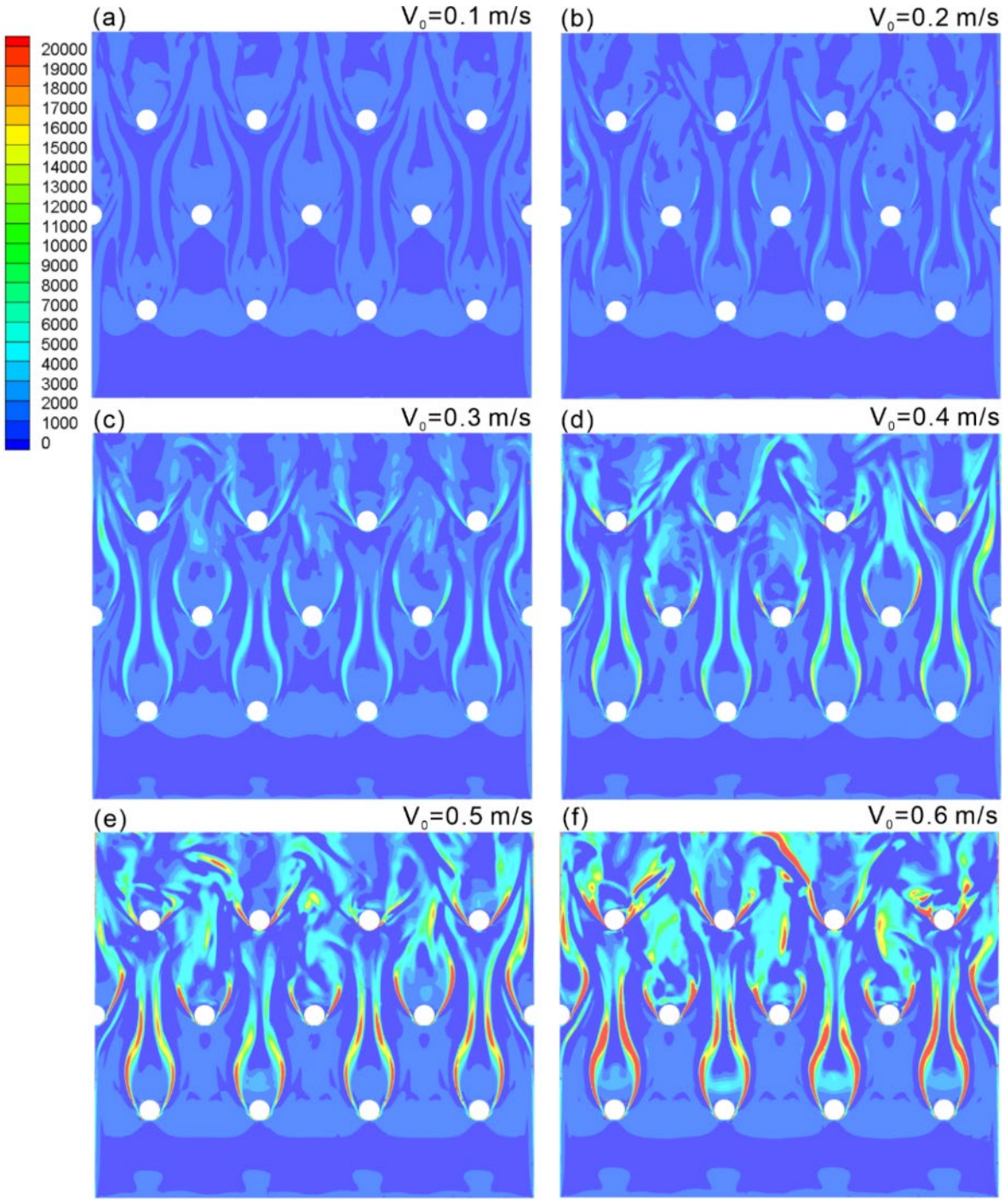

Figure 6.19 Visualization of total power loss density in time-averaged flow field in x-y plane of 5-30-45 network structure with different inlet velocity. (a) V_0 = 0.1 m/s; (b) V_0 = 0.2 m/s; (c) V_0 = 0.3 m/s; (d) V_0 = 0.4 m/s; (e) V_0 = 0.5 m/s; (f) V_0 = 0.6 m/s.

6.3.3.3 Power loss calculation comparison of the four network structures

As shown in **Figure 6.20**, different network structures display various behaviors in power loss density. The 5-15-25 network structure shows the largest power loss density in all scenarios. This is caused by the high PL3 and PL4 of the narrow water tunnel. However, the 5-30-45 network structure shows extremely low power loss density having the lowest PL4 constitution. This means that the effect of inertial and viscous forces is different when changing the network structure and inlet velocity. Thus, the power loss can be controlled. When the network structure is narrow and thin, the volume proportion of boundary layer increases and more PL4 is generated. Additionally, the viscous force plays a key role in the total power loss consumption. When the network structure is thick with intensive dots, turbulence will contribute more to the total power loss, and this results in the increase of PL3. The total energy loss increases when the inlet velocity is increasing (**Figure 6.1** & **Figure 6.20**), while the drag coefficient decreases, together with an increase of fluid vibration frequency (**Figure 6.4**). A higher fluid velocity can improve the mixing effect in the mass mixing steps (i) & (ii) and further improve the heat performance. Obviously, the velocity magnitude is higher in the place with a higher power loss density, which causes higher consumption of transformation of the kinetic energy (PL3) and viscosity dissipation (PL4). Thus, appropriate control of the network structure can manipulate the categories of power loss – contributed by inertial and viscous forces – to achieve the desired local pressure drop at the different function areas of this wearable heat transfer panel.

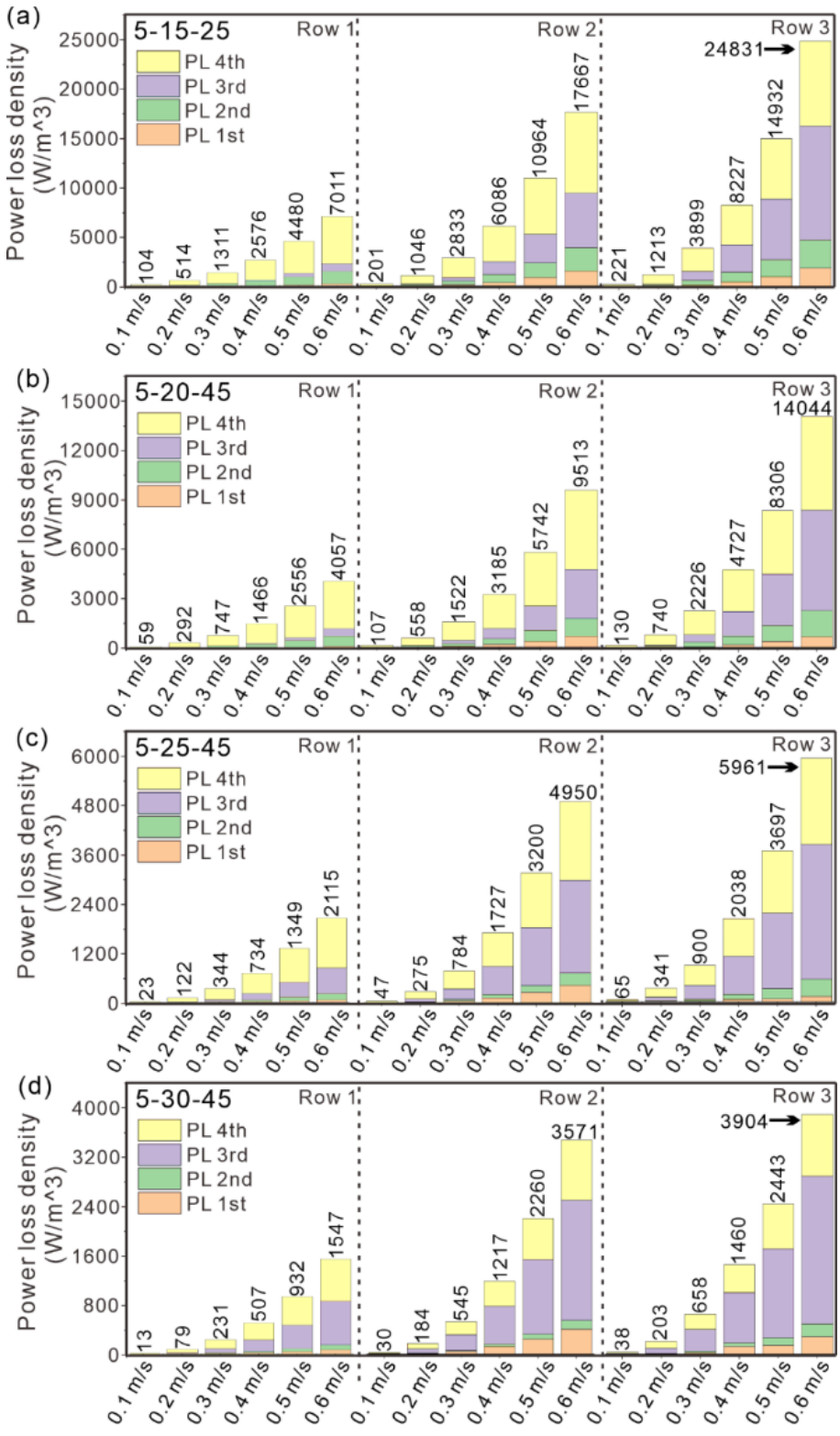

Figure 6.20 Average power loss density of different parameters network structure hexagon region at each row of reinforcement dots shown in **Figure 5.1**. (a) D = 5mm, R = 15mm, r =

25mm, 5-15-25; (b) D = 5mm, R = 20mm, r = 45mm, 5-20-45; (c) D = 5mm, R = 25mm, r = 45mm, 5-25-45; (d) D = 5mm, R = 30mm, r = 45mm, 5-30-45.

The inlet pressure of 5-20-25 & 5-30-45 network structures is low, which makes them suitable for placing at FA4 and FA1 (**Figure 6.21**). The velocity magnitude in FA1 is high as it is close to the inlet. Also, this area needs to distribute large volumes of water. The 5-30-45 network structure can transfer large volumes of water with low energy loss together with the function of water decentralization (FA1). Moreover the 5-20-25 network structure is suitable for large area heat transfer since this network structure shows both low power loss and water volume consumption. Other network structures can be placed in FA2 & FA3 for the manipulation of flow resistance to control the rate of flow of different dendrites.

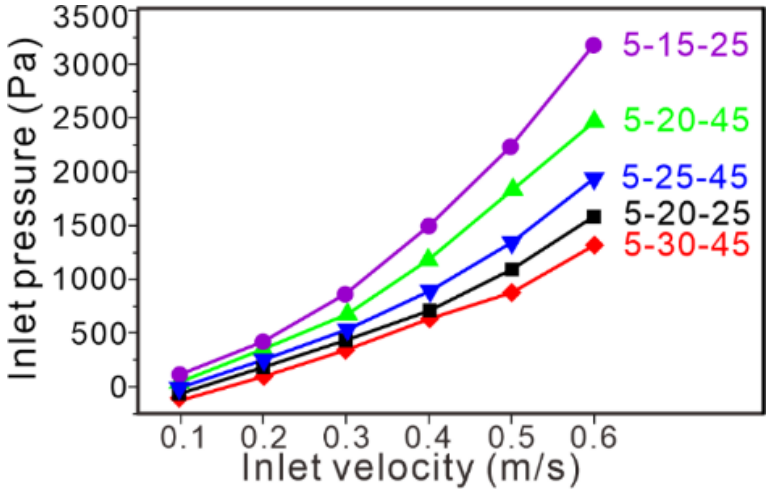

Figure 6.21 Inlet pressure vs. inlet velocity of different network structures, the 5-20-25 network structure shows the low inlet pressure with relative lower water consumption (suitable parameter for FA4) while the 5-30-45 network structure shows the lowest power loss

density together with relative lower inlet pressure (suitable parameter for FA1), other network structures can be used for control the mass rate of flow in other FAs for the purpose of uniform heat performance and fast velocity.

6.4 Summary

In this chapter, power loss calculations for different network structures of flow field homogenization guide the manipulation of pressure drops due to inertial and viscous forces in the transitional flow field. The constitution of power loss type is different under different flow regime. PL4 dominates the total power loss in pure laminar regime while PL3 in transition flow with more turbulent factors. The two power loss types show equivalent contribution when the flow regime is transition flow. The power loss during the fluid moving process further causes convection and increase the surface Nusselt number for enhanced heat transfer ability. The flow field evolution of different flow regime is affected strongly by the fluid channel shape - defined by “D”, “R”, “r” three different parameters. This further affects the pressure drop caused by power loss of these network structures. This character of network structure sheds new light on engineering design and optimization of fluidic fabric heat transfer panels and finally help us fabricate the novel nature-inspired wearable heat transfer panels which can perform two different temperatures switching uniformly in 10 s.

CHAPTER 7 Conclusions and Suggestions for Future Research

7.1 Conclusions

In this thesis, a nature-inspired network structure has been proposed for wearable thermal transfer fluidic fabric devices by flow field manipulation to achieve a uniform temperature rapidly with large coverage area. Three such engineered wearable heat transfer panels were fabricated for rapid contrast temperature therapy showed a fast-switching time of less than 10 s from hot (40^{o}C) to cold (5^{o}C) temperatures, over 6 times that of a conventional single-tube heat transfer panel. The excellent performance of these heat transfer panels is realized by the design of appropriate network structures in different parts of the heat transfer panels. This work investigates the 4-step mass mixing mechanism inside the network structure, induced by the cross layout of the high- & low-pressure regions inside the network structure flow field thus facilitating the homogeneity-adjusted flow field. Power loss calculation results of different network structures were analyzed to reveal energy transfer in the fluid circuit manipulation, energy dissipation, fluid velocity. Major findings and contributions of the research are listed as follows:

(1) The investigation into fast contrast therapy has yielded a comprehensive strategy for optimizing temperature control and energy efficiency in water immersion systems. Through thermal modeling and simulations, we identified water cooling and heating as the optimal approach for managing the significant heat transfer involved in this therapy. To address the challenge of mixing different temperature water, an innovative switch

logical design has been proposed, enhancing energy efficiency by optimizing the sucking and reflux periods. Among various portable heating and cooling methods tested, the combination of directly adding ice for cold therapy and using a heating rod for heat therapy emerged as the most effective solution for onsite applications. In contrast, thermoelectric (TE) modules, due to their high energy consumption and inefficiency in scenarios requiring rapid and significant temperature changes, are better suited for scenarios with minimal thermal transfer demands. This research provides a robust framework for implementing fast contrast therapy effectively, balancing thermal efficiency and practicality.

(2) The development of three innovative nature-inspired wearable heat transfer panels for the full leg, thigh, and calf has demonstrated significant advancements in rapid temperature switching and energy efficiency. By drawing inspiration from natural flow fields and mass transfer processes, the redesign of the fluid channels—with a reduced number of corners—has effectively minimized energy loss. The extension of reinforcement dots' functionality has further optimized flow manipulation, ensuring fluid delivery to targeted regions and reducing water consumption. The engineered network structure has resulted in improved fluid circulation velocity and more uniform temperature distribution, highlighting the superiority of these wearable heat transfer panels over conventional designs lacking structured flow channels and guide vane arrangements. This breakthrough offers promising potential for enhanced performance in wearable thermoregulation technologies.

(3) The comprehensive investigation into the flow field evolution and mass transfer mechanism within a network structure has unveiled distinct behavioral regimes based

on inlet velocity: pure laminar, transitional flow, and transitional flow with increased turbulence. The innovative mass transfer mechanism leverages the strategic configuration of high- and low-pressure regions around reinforcement dots to enhance fluid dynamics. This mechanism unfolds in four steps: rotation mixing and elongation induced by velocity gradient and vorticity, mixing from wake alternative vortex shedding, splitting of the high-pressure region, and suction in the low-pressure region. Together, these processes establish a uniform mass transfer that ensures a consistent and homogeneous velocity distribution across the flow field. The resulting flow field demonstrates effective convection between the fluid layers in the x-y plane and the boundary layer, indicating a well-balanced and efficient transfer system that could enhance performance in various applications relying on network-structured fluid dynamics.

(4) The exploration of power loss calculations across various network structures has provided valuable insights into managing pressure drops influenced by inertial and viscous forces within transitional flow fields. The research highlights that power loss type PL4 predominates in pure laminar flow regimes, whereas PL3 is more significant in transition flows with more turbulence. When the flow regime falls within a transitional state, both power loss types contribute equally. This understanding enhances our ability to predict and control the associated convection processes, thereby increasing the surface Nusselt number which is crucial for improved heat transfer. The shape of fluid channels, determined by parameters "D", "R", and "r", significantly influences flow field evolution and consequent pressure drops within these network structures. These findings illuminate new possibilities in the engineering design and optimization

of fluidic fabric heat transfer panels. Ultimately, this research contributes to the development of innovative, nature-inspired wearable heat transfer panels capable of uniformly switching between two temperatures in just 10 seconds, offering promising advancements in wearable thermoregulation technology.

This work sheds new light on the development of fluidic fabric heat transfer panels. It illustrates their great potential in other thermal management devices with large cover area such as air-conditioned clothing, thermal management systems in space exploration, quick charging lithium batteries in electric automobiles, effective cooling of computers and other machines and so on. However, future work is required on the influence of fluid type, material and structural parameters of the network structure, especially with consideration of buckling/wrinkles of the shell in such fabric-fluid structures. As the wrinkles are located at the boundary of the inner fluid field, they contribute to heat convection but also cause large extra power loss (by comparing the power loss consumed in fluid field homogenization). The following section detailed listed the limitations of current work and the suggestions for future research.

7.2 Limitations and Suggestions for Future Research

This thesis introduces a novel wearable heat transfer panel for fast temperature switching with high flow velocity and uniform temperature mapping. The above 4 chapters detailed demonstrated the thermal management system set up, network-structured wearable heat transfer panels design and fabrication, network structure flow field evolution, local head loss control for entirety flow field manipulation. However, owing to the insufficient time and resources, this research remains several limitations, and they need improvement in the further work. Here

are three main aspects of limitations of current work and corresponding suggestions for improvement:

(1) Device: Firstly, we finally fabricated three wearable heat transfer panels which can perform different temperature switching in 10 s with a 30-watt inlet water pump, the water can be filled uniformly into the heat transfer panel in less than 6 s, but the flow field in FA4 is still not perfect uniform. Especially the wearable heat transfer panel for thigh, the velocity at the margin is lower than that close to the inlet guide vanes. This means the flow resistance manipulation inside the wearable heat transfer panel need further optimization for higher energy efficiency. Secondly, despite the three heat transfer panels for full leg, thigh and calf, rapid-contrast-therapy heat transfer panels for other parts of human body are still under the designing process. They are heat transfer panels for knee, ankle, shoulder and elbow. All these parts of body are no need for large coverage but need to be covered with large curvature. This poses a new key factor on designing these wearable heat transfer panels – how flow field evolves in a curved network structure. Thirdly, the application of this nature inspired network-structured fluidic fabrics just focused on the rapid contrast therapy for elite athletes. This device can be used for any scenario with the requirement large area heat transfer and other potential applications still need exploring.

(2) Experiments: Flow field visualization are performed by temperature mapping for entirety wearable heat transfer panel captured by thermal camera and ink streamline for local network structure captured by high-speed camera. Firstly, all these flow field experiment results only show the flow field in x-y direction. The cross-section flow field visualization experiments are needed. Because in this direction, heat transfer is of great

importance and largely affected by the flow field. Secondly, the temperature mapping can only roughly show the flow field. Transparent fluidic fabrics can be used for observing the flow behavior inside the network structure. Thirdly, more advanced flow field visualization methods can be tried such as tomographic particle image experiments to get more accurate results of this network structure flow field. Fourth, research on guide vanes effect need to be done as this thesis only conducted the research on reinforcement dots.

(3) Theory: The whole flow field manipulation is based on the control of local head loss of different network structures allocated in different function areas of fluidic fabrics. Firstly, the parameters of network structures investigated in this work is limited, only 5-15-25, 5-20-25, 5-20-45, 5-25-45, 5-30-45 five groups of representative network structures. Due to the limitation of the tedious calculation period, modifications are needed for the simulation. Secondly, the network structure is defined by three parameters. A new parameter for describe the network structure needs to be proposed for simplification and nondimensionalization like Reynolds number and so on. The key point for affecting the flow behavior is the shape of fluid channel – gap between these reinforcement dots. Thus D and R together affect the width of the fluid channel and d(r) affects the thickness of the fluid channel. This further results in the dimensionless process of these parameters – '(D*d)/R' – the "Hydraulic radius" of heat transfer panel. Thirdly, the vortex evolution in network structure clusters is very important as this can directly affect the total head loss and the convection of heat transfer, it still need to be further investigated since this work only scratches the surface power loss.

References

[1] G.P. Kenny, O. Jay, Thermometry, calorimetry, and mean body temperature during heat stress, Compr. Physiol. 3 (2011) 1689–1719.

[2] S.S. Cheung, T.M. McLellan, Heat acclimation, aerobic fitness, and hydration effects on tolerance during uncompensable heat stress, J. Appl. Physiol. 84 (1998) 1731–1739.

[3] C.J. Gronlund, Racial and socioeconomic disparities in heat-related health effects and their mechanisms: a review, Curr. Epidemiol. Reports 1 (2014) 165–173.

[4] A. Mazloumi, F. Golbabaei, S.M. Khani, Z. Kazemi, M. Hosseini, M. Abbasinia, S.F. Dehghan, Evaluating effects of heat stress on cognitive function among workers in a hot industry, Heal. Promot. Perspect. 4 (2014) 240.

[5] H.M.M. Lumingu, P. Dessureault, Physiological responses to heat strain: A study on personal monitoring for young workers, J. Therm. Biol. 34 (2009) 299–305.

[6] G.P. Kenny, A.R. Schissler, J. Stapleton, M. Piamonte, K. Binder, A. Lynn, C.Q. Lan, S.G. Hardcastle, Ice cooling vest on tolerance for exercise under uncompensable heat stress, J. Occup. Environ. Hyg. 8 (2011) 484–491.

[7] Y. Peng, Y. Cui, Advanced Textiles for Personal Thermal Management and Energy, Joule 4 (2020) 724–742. https://doi.org/10.1016/j.joule.2020.02.011.

[8] R. Hu, Y. Liu, S. Shin, S. Huang, X. Ren, W. Shu, J. Cheng, G. Tao, W. Xu, R. Chen, Emerging materials and strategies for personal thermal management, Adv. Energy Mater. 10 (2020) 1903921.

[9] X. Zhang, X. Chao, L. Lou, J. Fan, Q. Chen, B. Li, L. Ye, D. Shou, Personal thermal

management by thermally conductive composites: A review, Compos. Commun. 23 (2021) 100595.

[10] U. Sajjad, N. Abbas, K. Hamid, S. Abbas, I. Hussain, S.M. Ammar, M. Sultan, H.M. Ali, M. Hussain, C.C. Wang, A review of recent advances in indirect evaporative cooling technology, Int. Commun. Heat Mass Transf. 122 (2021) 105140.

[11] A.P.C. Chan, W. Song, Y. Yang, Meta-analysis of the effects of microclimate cooling systems on human performance under thermal stressful environments: potential applications to occupational workers, J. Therm. Biol. 49 (2015) 16–32.

[12] W.E.S. Jose, Compliant Heat Exchange Panel, US 7,198,093 B1, 2007.

[13] Lawrence H. Kuznetz, Control of thermal balance by a liquid circulating garment based on a mathematical representation of the human thermoregulatory system, University of California at Berkeley, 1976.

[14] M. Rothmaier, M. Weder, A. Meyer-Heim, J. Kesselring, Design and performance of personal cooling garments based on three-layer laminates, Med. Biol. Eng. Comput. 46 (2008) 825–832. https://doi.org/10.1007/s11517-008-0363-6.

[15] U. Sajjad, K. Hamid, Tauseef-ur-Rehman, M. Sultan, N. Abbas, H.M. Ali, M. Imran, M. Muneeshwaran, J.Y. Chang, C.C. Wang, Personal thermal management - A review on strategies, progress, and prospects, Int. Commun. Heat Mass Transf. 130 (2022) 105739. https://doi.org/10.1016/j.icheatmasstransfer.2021.105739.

[16] H. Cao, D.H. Branson, S. Peksoz, J. Nam, C.A. Farr, Fabric Selection for a Liquid Cooling Garment, Text. Res. J. 76 (2006) 587–595.

https://doi.org/10.1177/0040517506067375.

[17] S.A. Nunneley, Water cooled garments: A review, Space Life Sci. 2 (1970) 335–360. https://doi.org/10.1007/BF00929293.

[18] L. Li, W. Di Liu, W. Sun, D.Z. Wang, L.C. Yin, M. Li, X.L. Shi, Q. Liu, Z.G. Chen, Performance Optimization of a Thermoelectric-Water Hybrid Cooling Garment, Adv. Mater. Technol. 2301069 (2023). https://doi.org/10.1002/admt.202301069.

[19] M. Bellon, D. Michelet, N. Carrara, T. Vacher, B. Gafsou, B. Ilhareborde, K. Mazda, E. Ferrero, A.L. Simon, F. Julien-Marsollier, S. Dahmani, Efficacy of the Game Ready® cooling device on postoperative analgesia after scoliosis surgery in children, Eur. Spine J. 28 (2019) 1257–1264. https://doi.org/10.1007/s00586-019-05886-6.

[20] J. Qi, F. Gao, G. Sun, J.C. Yeo, C.T. Lim, HaptGlove—Untethered Pneumatic Glove for Multimode Haptic Feedback in Reality–Virtuality Continuum, Adv. Sci. 10 (2023) 1–12. https://doi.org/10.1002/advs.202301044.

[21] C.T. O'Neill, C.M. McCann, C.J. Hohimer, K. Bertoldi, C.J. Walsh, Unfolding Textile-Based Pneumatic Actuators for Wearable Applications, Soft Robot. 9 (2022) 163–172. https://doi.org/10.1089/soro.2020.0064.

[22] Y. Luo, K. Wu, A. Spielberg, M. Foshey, D. Rus, T. Palacios, W. Matusik, Digital Fabrication of Pneumatic Actuators with Integrated Sensing by Machine Knitting, Conf. Hum. Factors Comput. Syst. - Proc. (2022). https://doi.org/10.1145/3491102.3517577.

[23] V. Sanchez, C.J. Walsh, R.J. Wood, Textile Technology for Soft Robotic and Autonomous Garments, Adv. Funct. Mater. 31 (2021) 1–55.

https://doi.org/10.1002/adfm.202008278.

[24] H.D. Yang, A.T. Asbeck, A Layered Manufacturing Approach for Soft and Soft-Rigid Hybrid Robots, Soft Robot. 7 (2020) 218–232. https://doi.org/10.1089/soro.2018.0093.

[25] E. Siéfert, E. Reyssat, J. Bico, B. Roman, Programming stiff inflatable shells from planar patterned fabrics, Soft Matter 16 (2020) 7898–7903. https://doi.org/10.1039/d0sm01041c.

[26] K.W. Oh, K. Lee, B. Ahn, E.P. Furlani, Design of pressure-driven microfluidic networks using electric circuit analogy, Lab Chip 12 (2012) 515–545. https://doi.org/10.1039/c2lc20799k.

[27] Q. Zhang, M. Zhang, L. Djeghlaf, J. Bataille, J. Gamby, A.M. Haghiri-Gosnet, A. Pallandre, Logic digital fluidic in miniaturized functional devices: Perspective to the next generation of microfluidic lab-on-chips, Electrophoresis 38 (2017) 953–976. https://doi.org/10.1002/elps.201600429.

[28] D. Bierbach, L. Gómez-nava, A. Fritz, J. Grinham, M.J. Hancock, K. Kumar, M. Bechthold, Bioinspired design and optimization for thin film wearable and building cooling systems Bioinspired design and optimization for thin film wearable and building cooling systems, Bioinspir. Biomim. 17 (2022) 15003. https://doi.org/10.1088/1748-3190/ac2f55.

[29] L.M. Jonsson, B. Björlenius, Dynamic and initial head loss in full-scale wastewater filtration and measures to prevent long-term initial head loss, Water Pract. Technol. 17 (2022) 1390–1405. https://doi.org/10.2166/wpt.2022.064.

[30] F. Gu, L. Shi, X. Shen, D. Zhang, B.P.M. (Bart) van Esch, Research on the suppression mechanism of a tip leakage vortex over a hydrofoil with double-control-hole structure, Ocean Eng. 293 (2024) 116610. https://doi.org/10.1016/j.oceaneng.2023.116610.

[31] B. Wang, J.J. Klemeš, N. Li, M. Zeng, P.S. Varbanov, Y. Liang, Heat exchanger network retrofit with heat exchanger and material type selection: A review and a novel method, Renew. Sustain. Energy Rev. 138 (2021). https://doi.org/10.1016/j.rser.2020.110479.

[32] D.J. Preston, H.J. Jiang, V. Sanchez, P. Rothemund, J. Rawson, M.P. Nemitz, W.K. Lee, Z. Suo, C.J. Walsh, G.M. Whitesides, A soft ring oscillator, Sci. Robot. 4 (2019) 1–10. https://doi.org/10.1126/scirobotics.aaw5496.

[33] P. Rothemund, A. Ainla, L. Belding, D.J. Preston, S. Kurihara, Z. Suo, G.M. Whitesides, A soft, bistable valve for autonomous control of soft actuators, Sci. Robot. 3 (2018) 1–11. https://doi.org/10.1126/SCIROBOTICS.AAR7986.

[34] D.J. Preston, P. Rothemund, H.J. Jiang, M.P. Nemitz, J. Rawson, Z. Suo, G.M. Whitesides, Digital logic for soft devices, Proc. Natl. Acad. Sci. U. S. A. 116 (2019) 7750–7759. https://doi.org/10.1073/pnas.1820672116.

[35] R.A. Shveda, A. Rajappan, T.F. Yap, Z. Liu, M.D. Bell, B. Jumet, V. Sanchez, D.J. Preston, A wearable textile-based pneumatic energy harvesting system for assistive robotics, Sci. Adv. 8 (2022) eabo2418. https://doi.org/10.1126/sciadv.abo2418.

[36] M. Smith, V. Cacucciolo, H. Shea, Fiber pumps for wearable fluidic systems, Science (80-.). 379 (2023) 1327–1332. https://doi.org/10.1126/science.ade8654.

[37] A. Rajappan, B. Jumet, D.J. Preston, Pneumatic soft robots take a step toward autonomy,

Sci. Robot. 6 (2021) 1–3. https://doi.org/10.1126/SCIROBOTICS.ABG6994.

[38] M. Wehner, R.L. Truby, D.J. Fitzgerald, B. Mosadegh, G.M. Whitesides, J.A. Lewis, R.J. Wood, An integrated design and fabrication strategy for entirely soft, autonomous robots, Nature 536 (2016) 451–455. https://doi.org/10.1038/nature19100.

[39] K. Luo, J.P. Moiwo, Sensitivity of the land surface hydrological cycle to human activities in China, Gondwana Res. 123 (2023) 255–264. https://doi.org/10.1016/j.gr.2022.04.006.

[40] M. Deb, J.T. Kirby, F. Shi, A. Abdolali, Tidal hydrodynamics in a multi-inlet wetland system: toward improved modeling of salt marsh flooding and draining, 2020.

[41] J.H. Knox, K.A. McCormack, Temperature effects in capillary electrophoresis. 1: Internal capillary temperature and effect upon performance, Chromatographia 38 (1994) 207–214. https://doi.org/10.1007/BF02290338.

[42] A.D. Flouris, G.P. Kenny, Heat remains unaccounted for in thermal physiology and climate change research, F1000Research 6 (2017).

[43] J.R. Allan, The liquid conditioned suit: A physiological assessment, Flying Personnel Research Committee, 1966.

[44] M. Mokhtari Yazdi, M. Sheikhzadeh, Personal cooling garments: a review, J. Text. Inst. 105 (2014) 1231–1250.

[45] C. Gao, K. Kuklane, I. Holmér, Cooling vests with phase change materials: the effects of melting temperature on heat strain alleviation in an extremely hot environment, Eur. J. Appl. Physiol. 111 (2011) 1207–1216. https://doi.org/10.1007/s00421-010-1748-4.

[46] K.J. Chua, S.K. Chou, W.M. Yang, J. Yan, Achieving better energy-efficient air conditioning – A review of technologies and strategies, Appl. Energy 104 (2013) 87–104. https://doi.org/https://doi.org/10.1016/j.apenergy.2012.10.037.

[47] F.L. Zhu, Q.Q. Feng, Recent advances in textile materials for personal radiative thermal management in indoor and outdoor environments, Int. J. Therm. Sci. 165 (2021) 106899.

[48] A.S. Farooq, P. Zhang, Fundamentals, materials and strategies for personal thermal management by next-generation textiles, Compos. Part A Appl. Sci. Manuf. 142 (2021) 106249.

[49] X.-L. Shi, J. Zou, Z.-G. Chen, Advanced thermoelectric design: from materials and structures to devices, Chem. Rev. 120 (2020) 7399–7515.

[50] H.N. Choi, S.H. Jee, J. Ko, D.J. Kim, S.H. Kim, Properties of surface heating textile for functional warm clothing based on a composite heating element with a positive temperature coefficient, Nanomaterials 11 (2021) 904.

[51] S. Lepak-Kuc, P. Taborowska, T.Q. Tran, H.M. Duong, T. Gizewski, M. Jakubowska, J. Patmore, A. Lekawa-Raus, Washable, colored and textured, carbon nanotube textile yarns, Carbon N. Y. 172 (2021) 334–344.

[52] T. Tian, X. Wei, A. Elhassan, J. Yu, Z. Li, B. Ding, Highly flexible, efficient, and wearable infrared radiation heating carbon fabric, Chem. Eng. J. 417 (2021) 128114.

[53] J. Reese, M. Vorhof, G. Hoffmann, K. Böhme, C. Cherif, Joule heating of dry textiles made of recycled carbon fibers and PA6 for the series production of thermoplastic composites, J. Eng. Fiber. Fabr. 15 (2020) 1558925020905828.

[54] T. Ruiz-Calleja, M. Bonet-Aracil, J. Gisbert-Payá, E. Bou-Belda, Analysis of the influence of graphene and phase change microcapsules on thermal behavior of cellulosic fabrics, Mater. Today Commun. 25 (2020) 101557.

[55] I. Bramhecha, J. Sheikh, Antibacterial and waterproof breathable waterborne polyurethane functionalised by graphene to develop UV and NIR-protective cotton fabric, Carbon Trends 4 (2021) 100067.

[56] N.P. Klochko, K.S. Klepikova, D.O. Zhadan, V.R. Kopach, S.M. Chernyavskaya, S.I. Petrushenko, S. V Dukarov, V.M. Lyubov, A.L. Khrypunova, Thermoelectric textile with fibers coated by copper iodide thin films, Thin Solid Films 704 (2020) 138026.

[57] P.-C. Hsu, X. Liu, C. Liu, X. Xie, H.R. Lee, A.J. Welch, T. Zhao, Y. Cui, Personal thermal management by metallic nanowire-coated textile, Nano Lett. 15 (2015) 365–371.

[58] J. Billingham, Heat exchange between man and his environment on the surface of the moon, J. Br. Interplanet. Soc 17 (1959) 297–300.

[59] C.L. Lim, Fundamental concepts of human thermoregulation and adaptation to heat: a review in the context of global warming, Int. J. Environ. Res. Public Health 17 (2020) 7795.

[60] P.-A. Dubé, D. Imbeau, D. Dubeau, I. Auger, Worker heat stress prevention and work metabolism estimation: comparing two assessment methods of the heart rate thermal component, Ergonomics (2019).

[61] J.P. KNOCHEL, L.N. DOTIN, R.J. HAMBURGER, Heat stress, exercise, and muscle injury: effects on urate metabolism and renal function, Ann. Intern. Med. 81 (1974) 321–

328.

[62] Y. Takahashi, A. Nomoto, S. Yoda, R. Hisayama, M. Ogata, Y. Ozeki, S. Tanabe, Thermoregulation model JOS-3 with new open source code, Energy Build. 231 (2021) 110575.

[63] J.A.J. Stolwijk, A mathematical model of physiological temperature regulation in man, NASA, 1971.

[64] Y. Kobayashi, S. Tanabe, Development of JOS-2 human thermoregulation model with detailed vascular system, Build. Environ. 66 (2013) 1–10.

[65] S. Tanabe, K. Kobayashi, J. Nakano, Y. Ozeki, M. Konishi, Evaluation of thermal comfort using combined multi-node thermoregulation (65MN) and radiation models and computational fluid dynamics (CFD), Energy Build. 34 (2002) 637–646.

[66] M. Ichihara, Measurement of convective and radiative heat transfer coefficients of standing and sitting human body by using a thermal manikin, J. Archit. Plan. Environ. Eng. 501 (1997) 45–51.

[67] Y. Kurazumi, J. Ishii, K. Fukagawa, Y. Yamato, K. Tobita, T. Tsuchikawa, N. Matsubara, Body heat balance for evaluation of sleep environment-Measurement of radiative and convective heat transfer coefficients of the human body with supine position by using a thermal mannequin, Japanese J. Physiol. Anthropol. 13 (2008) 17–26.

[68] J. Lee, H. Zhang, E. Arens, Typical clothing ensemble insulation levels for sixteen body parts, (2013).

[69] A. Nomoto, Y. Takahashi, S. Yoda, M. Ogata, S. Tanabe, S. Ito, Y. Aono, Y. Yamamoto,

K. Mizutani, Measurement of local evaporative resistance of a typical clothing ensemble using a sweating thermal manikin, Japan Archit. Rev. 3 (2020) 113–120.

[70] Z.J. Schlader, The human thermoneutral and thermal comfort zones: Thermal comfort in your own skin blood flow, Temperature 2 (2015) 47–48.

[71] A.D. Flouris, Human thermoregulation, Heat Stress Sport Exerc. Thermophysiology Heal. Perform. (2019) 3–27.

[72] G.P. Kenny, A.D. Flouris, The human thermoregulatory system and its response to thermal stress, in: Prot. Cloth., Elsevier, 2014: pp. 319–365.

[73] K. Nagashima, K. Tokizawa, S. Marui, Thermal comfort, Handb. Clin. Neurol. 156 (2018) 249–260.

[74] T. Fukazawa, G. Havenith, Differences in comfort perception in relation to local and whole body skin wettedness, Eur. J. Appl. Physiol. 106 (2009) 15–24.

[75] R. Raad, M. Itani, N. Ghaddar, K. Ghali, A novel M-cycle evaporative cooling vest for enhanced comfort of active human in hot environment, Int. J. Therm. Sci. 142 (2019) 1–13.

[76] S. Byun, J.H. Yun, S. Heo, C. Shi, G.J. Lee, K. Agno, K. Jang, J. Xiao, Y.M. Song, J. Jeong, Self-Cooling Gallium-Based Transformative Electronics with a Radiative Cooler for Reliable Stiffness Tuning in Outdoor Use, Adv. Sci. 9 (2022) 2202549.

[77] M.J. Luomala, J. Oksa, J.A. Salmi, V. Linnamo, I. Holmér, J. Smolander, B. Dugué, Adding a cooling vest during cycling improves performance in warm and humid

conditions, J. Therm. Biol. 37 (2012) 47–55.

[78] G. Erkan, Enhancing the thermal properties of textiles with phase change materials, Res. J. Text. Appar. 8 (2004) 57–64.

[79] E. Kamon, W.L. Kenney, N.S. Deno, K.I. Soto, A.J. Carpenter, Readdressing personal cooling with ice, Am. Ind. Hyg. Assoc. J. 47 (1986) 293–298.

[80] I.H. Muir, P.A. Bishop, P. Ray, Effects of a novel ice-cooling technique on work in protective clothing at 28 C, 23 C, and 18 C WBGTs, Am. Ind. Hyg. Assoc. J. 60 (1999) 96–104.

[81] J. Smolander, K. Kuklane, D. Gavhed, H. Nilsson, I. Holmér, Effectiveness of a light-weight ice-vest for body cooling while wearing fire fighter's protective clothing in the heat, Int. J. Occup. Saf. Ergon. 10 (2004) 111–117.

[82] R. Duffield, B. Dawson, D. Bishop, M. Fitzsimons, S. Lawrence, Effect of wearing an ice cooling jacket on repeat sprint performance in warm/humid conditions, Br. J. Sports Med. 37 (2003) 164–169.

[83] L. Taylor, C.J. Stevens, H.R. Thornton, N. Poulos, B.C.R. Chrismas, Limiting the rise in core temperature during a rugby sevens warm-up with an ice vest, Int. J. Sports Physiol. Perform. 14 (2019) 1212–1218.

[84] J.K.W. Lee, R.W. Kenefick, S.N. Cheuvront, Novel cooling strategies for military training and operations, J. Strength Cond. Res. 29 (2015) S77–S81.

[85] J.D. Countryman, D.E. Dow, Historical development of heat stroke prevention device in the military, in: 2013 35th Annu. Int. Conf. IEEE Eng. Med. Biol. Soc., IEEE, 2013: pp.

2527–2530.

[86] J.D. Cotter, G.G. Sleivert, W.S. Roberts, M.A. Febbraio, Effect of pre-cooling, with and without thigh cooling, on strain and endurance exercise performance in the heat, Comp. Biochem. Physiol. Part A Mol. Integr. Physiol. 128 (2001) 667–677.

[87] S.A. Konz, Personal cooling garments-a review, ASHRAE Trans 90 (1984) 499–517.

[88] H. Dehghan, S. Gharebaei, Effectiveness of Ice Gel Cooling Vest on Physiological Indices in Hot and Dry Conditions in a Climate Chamber, (2017).

[89] L.S. Chesterton, N.E. Foster, L. Ross, Skin temperature response to cryotherapy, Arch. Phys. Med. Rehabil. 83 (2002) 543–549.

[90] L. Teunissen, E. Janssen, J. Schootstra, L. Plaude, K. Jansen, Evaluation of phase change materials for personal cooling applications, Cloth. Text. Res. J. 41 (2023) 208–224.

[91] C. Zhang, W. Lin, Q. Zhang, Z. Zhang, X. Fang, X. Zhang, Exploration of a thermal therapy respirator by introducing a composite phase change block into a commercial mask, Int. J. Therm. Sci. 142 (2019) 156–162.

[92] Y. Jing, Z. Zhao, N. Zhang, X. Cao, Q. Sun, Y. Yuan, T. Li, Ultraflexible, cost-effective and scalable polymer-based phase change composites for wearable thermal management, Available SSRN 4150536 (2023).

[93] M. Itani, N. Ghaddar, D. Ouahrani, K. Ghali, B. Khater, An optimal two-bout strategy with phase change material cooling vests to improve comfort in hot environment, J. Therm. Biol. 72 (2018) 10–25.

[94] W. Li, Y. Liang, C. Liu, Y. Ji, L. Cheng, Study of ultra-light modular phase change cooling clothing based on dynamic human thermal comfort modeling, Build. Environ. 222 (2022) 109390.

[95] Y. Yan, W. Li, R. Zhu, C. Lin, R. Hufenus, Flexible phase change material fiber: a simple route to thermal energy control textiles, Materials (Basel). 14 (2021) 401.

[96] W. Tomaszewski, K. Twarowska-Schmidt, A. Moraczewski, M. Kudra, M. Szadkowski, B. Pałys, Nonwoven with Thermal Storage Properties Based on Paraffin–Modified Polypropylene Fibres, Fibres Text. East. Eur. (2012).

[97] J. Lei, K. Kumarasamy, K.T. Zingre, J. Yang, M.P. Wan, E.-H. Yang, Cool colored coating and phase change materials as complementary cooling strategies for building cooling load reduction in tropics, Appl. Energy 190 (2017) 57–63.

[98] V. Skurkyte-Papieviene, A. Abraitiene, A. Sankauskaite, V. Rubeziene, J. Baltusnikaite-Guzaitiene, Enhancement of the thermal performance of the paraffin-based microcapsules intended for textile applications, Polymers (Basel). 13 (2021) 1120.

[99] J. Shi, W. Aftab, Z. Liang, K. Yuan, M. Maqbool, H. Jiang, F. Xiong, M. Qin, S. Gao, R. Zou, Tuning the flexibility and thermal storage capacity of solid–solid phase change materials towards wearable applications, J. Mater. Chem. A 8 (2020) 20133–20140.

[100] Z. Yang, Y. Ma, S. Jia, C. Zhang, P. Li, Y. Zhang, Q. Li, 3D-printed flexible phase-change nonwoven fabrics toward multifunctional clothing, ACS Appl. Mater. Interfaces 14 (2022) 7283–7291.

[101] Z. Niu, W. Yuan, Smart nanocomposite nonwoven wearable fabrics embedding phase

change materials for highly efficient energy conversion–storage and use as a stretchable conductor, ACS Appl. Mater. Interfaces 13 (2021) 4508–4518.

[102] Y.F. Zhang, B.K. Sun, Development of Outlast Fiber and Study about Its Character of Thermoregulation, Adv. Mater. Res. 557 (2012) 979–982.

[103] W.B. Grant, Water vapor absorption coefficients in the 8–13-μm spectral region: a critical review, Appl. Opt. 29 (1990) 451–462.

[104] J.K. Tong, X. Huang, S. V Boriskina, J. Loomis, Y. Xu, G. Chen, Infrared-transparent visible-opaque fabrics for wearable personal thermal management, Acs Photonics 2 (2015) 769–778.

[105] P.-C. Hsu, A.Y. Song, P.B. Catrysse, C. Liu, Y. Peng, J. Xie, S. Fan, Y. Cui, Radiative human body cooling by nanoporous polyethylene textile, Science (80-.). 353 (2016) 1019–1023.

[106] Y. Peng, J. Chen, A.Y. Song, P.B. Catrysse, P.-C. Hsu, L. Cai, B. Liu, Y. Zhu, G. Zhou, D.S. Wu, Nanoporous polyethylene microfibres for large-scale radiative cooling fabric, Nat. Sustain. 1 (2018) 105–112.

[107] M.C. Larciprete, Y.S. Gloy, R.L. Voti, G. Cesarini, G. Leahu, M. Bertolotti, C. Sibilia, Temperature dependent emissivity of different stainless steel textiles in the infrared range, Int. J. Therm. Sci. 113 (2017) 130–135.

[108] J.-S. Roh, Y.-S. Chi, T.J. Kang, Thermal insulation properties of multifunctional metal composite fabrics, Smart Mater. Struct. 18 (2009) 25018.

[109] L. Cai, A.Y. Song, P. Wu, P.-C. Hsu, Y. Peng, J. Chen, C. Liu, P.B. Catrysse, Y. Liu, A.

Yang, Warming up human body by nanoporous metallized polyethylene textile, Nat. Commun. 8 (2017) 496.

[110] X. Yue, T. Zhang, D. Yang, F. Qiu, Z. Li, G. Wei, Y. Qiao, Ag nanoparticles coated cellulose membrane with high infrared reflection, breathability and antibacterial property for human thermal insulation, J. Colloid Interface Sci. 535 (2019) 363–370.

[111] Z. Yu, Y. Gao, X. Di, H. Luo, Cotton modified with silver-nanowires/polydopamine for a wearable thermal management device, RSC Adv. 6 (2016) 67771–67777.

[112] A. Yang, L. Cai, R. Zhang, J. Wang, P.-C. Hsu, H. Wang, G. Zhou, J. Xu, Y. Cui, Thermal management in nanofiber-based face mask, Nano Lett. 17 (2017) 3506–3510.

[113] P.-C. Hsu, C. Liu, A.Y. Song, Z. Zhang, Y. Peng, J. Xie, K. Liu, C.-L. Wu, P.B. Catrysse, L. Cai, A dual-mode textile for human body radiative heating and cooling, Sci. Adv. 3 (2017) e1700895.

[114] A. Hazarika, B.K. Deka, D. Kim, H.E. Jeong, Y.-B. Park, H.W. Park, Woven Kevlar Fiber/Polydimethylsiloxane/Reduced Graphene Oxide Composite-Based Personal Thermal Management with Freestanding Cu–Ni Core–Shell Nanowires, Nano Lett. 18 (2018) 6731–6739. https://doi.org/10.1021/acs.nanolett.8b02408.

[115] A. Hazarika, B.K. Deka, C. Jeong, Y.-B. Park, H.W. Park, Biomechanical Energy-Harvesting Wearable Textile-Based Personal Thermal Management Device Containing Epitaxially Grown Aligned Ag-Tipped-NiCo1−Se Nanowires/Reduced Graphene Oxide, Adv. Funct. Mater. 29 (2019) 1903144. https://doi.org/https://doi.org/10.1002/adfm.201903144.

[116] B. Choudhary, Udayraj, F. Wang, Y. Ke, J. Yang, Development and experimental validation of a 3D numerical model based on CFD of the human torso wearing air ventilation clothing, Int. J. Heat Mass Transf. 147 (2020) 118973. https://doi.org/https://doi.org/10.1016/j.ijheatmasstransfer.2019.118973.

[117] L. Heqing, G. Liying, Y. Bo, L. Tianyu, O. Congying, Experimental Study on the Effect of Air Cooling Garment on Skin Temperature and Microclimate BT - Proceedings of the 11th International Mine Ventilation Congress, in: X. Chang (Ed.), Springer Singapore, Singapore, 2019: pp. 742–752.

[118] T. Guo, B. Shang, B. Duan, X. Luo, Design and testing of a liquid cooled garment for hot environments, J. Therm. Biol. 49–50 (2015) 47–54. https://doi.org/https://doi.org/10.1016/j.jtherbio.2015.01.003.

[119] R.G. Revaiah, T.M. Kotresh, B. Kandasubramanian, Technical textiles for military applications, J. Text. Inst. 111 (2020) 273–308. https://doi.org/10.1080/00405000.2019.1627987.

[120] P. Guo, Y. Wang, M. Duan, D. Pang, N. Li, Research and application of methods for effectiveness evaluation of mine cooling system, Int. J. Min. Sci. Technol. 25 (2015) 649–654. https://doi.org/https://doi.org/10.1016/j.ijmst.2015.05.020.

[121] X. Ni, T. Yao, Y. Zhang, Y. Zhao, Q. Hu, A.P.C. Chan, Experimental Study on the Efficacy of a Novel Personal Cooling Vest Incorporated with Phase Change Materials and Fans, Materials (Basel). 13 (2020). https://doi.org/10.3390/ma13081801.

[122] L. Lou, Y.S. Wu, Y. Zhou, J. Fan, Effects of body positions and garment design on the

performance of a personal air cooling/heating system, Indoor Air 32 (2022) e12921. https://doi.org/https://doi.org/10.1111/ina.12921.

[123] L. Lou, D. Shou, H. Park, D. Zhao, Y.S. Wu, X. Hui, R. Yang, E.C. Kan, J. Fan, Thermoelectric air conditioning undergarment for personal thermal management and HVAC energy saving, Energy Build. 226 (2020) 110374. https://doi.org/https://doi.org/10.1016/j.enbuild.2020.110374.

[124] W. He, G. Zhang, X. Zhang, J. Ji, G. Li, X. Zhao, Recent development and application of thermoelectric generator and cooler, Appl. Energy 143 (2015) 1–25. https://doi.org/https://doi.org/10.1016/j.apenergy.2014.12.075.

[125] Z. Yang, C. Zhu, Y.-J. Ke, X. He, F. Luo, J. Wang, J.-F. Wang, Z.-G. Sun, Peltier effect: From linear to nonlinear, J. Mech. Eng. 70 (2021) 108402–108418. https://doi.org/10.7498/aps.70.20201826.

[126] D. Zhao, G. Tan, A review of thermoelectric cooling: Materials, modeling and applications, Appl. Therm. Eng. 66 (2014) 15–24. https://doi.org/https://doi.org/10.1016/j.applthermaleng.2014.01.074.

[127] S. Lv, Z. Qian, D. Hu, X. Li, W. He, A Comprehensive Review of Strategies and Approaches for Enhancing the Performance of Thermoelectric Module, Energies 13 (2020). https://doi.org/10.3390/en13123142.

[128] Y. Xu, Z. Li, J. Wang, M. Zhang, M. Jia, Q. Wang, Man-portable cooling garment with cold liquid circulation based on thermoelectric refrigeration, Appl. Therm. Eng. 200 (2022) 117730. https://doi.org/https://doi.org/10.1016/j.applthermaleng.2021.117730.

[129] T.C. Ernst, S. Garimella, Demonstration of a wearable cooling system for elevated ambient temperature duty personnel, Appl. Therm. Eng. 60 (2013) 316–324. https://doi.org/https://doi.org/10.1016/j.applthermaleng.2013.06.019.

[130] J.I. Priego-Quesada, A. Gandia-Soriano, M.T. Pellicer-Chenoll, I. Catalá-Vilaplana, J.L. Bermejo-Ruiz, A. Encarnación-Martínez, R. Salvador-Palmer, R. Cibrián Ortiz de Anda, Reproducibility of Skin Temperature Response after Cold Stress Test Using the Game Ready System: Preliminary Study, Int. J. Environ. Res. Public Health 18 (2021). https://doi.org/10.3390/ijerph18168295.

[131] A. De Bie, R. Siboni, M.F. Smati, X. Ohl, S. Bredin, Enhanced recovery after lumbar fusion surgery: Benefits of using Game Ready©, Orthop. Traumatol. Surg. Res. 107 (2021) 102953. https://doi.org/https://doi.org/10.1016/j.otsr.2021.102953.

[132] C. Al Sayed, L. Vinches, O. Dupuy, W. Douzi, B. Dugue, S. Hallé, Air/CO2 cooling garment: Description and benefits of use for subjects exposed to a hot and humid climate during physical activities, Int. J. Min. Sci. Technol. 29 (2019) 899–903. https://doi.org/https://doi.org/10.1016/j.ijmst.2019.02.010.

[133] Y. Zhang, P.A. Bishop, J.M. Green, M.T. Richardson, R.E. Schumacker, Evaluation of a Carbon Dioxide Personal Cooling Device for Workers in Hot Environments, J. Occup. Environ. Hyg. 7 (2010) 389–396. https://doi.org/10.1080/15459621003785554.

[134] L.P.J. Teunissen, L.-C. Wang, S.-N. Chou, C. Huang, G.-T. Jou, H.A.M. Daanen, Evaluation of two cooling systems under a firefighter coverall, Appl. Ergon. 45 (2014) 1433–1438. https://doi.org/https://doi.org/10.1016/j.apergo.2014.04.008.

[135] B. Yang, X. Ding, F. Wang, A. Li, A review of intensified conditioning of personal micro-environments: Moving closer to the human body, Energy Built Environ. 2 (2021) 260–270. https://doi.org/https://doi.org/10.1016/j.enbenv.2020.06.007.

[136] M. Valant, Electrocaloric materials for future solid-state refrigeration technologies, Prog. Mater. Sci. 57 (2012) 980–1009. https://doi.org/https://doi.org/10.1016/j.pmatsci.2012.02.001.

[137] R. Ma, Z. Zhang, K. Tong, D. Huber, R. Kornbluh, Y.S. Ju, Q. Pei, Highly efficient electrocaloric cooling with electrostatic actuation, Science (80-.). 357 (2017) 1130–1134. https://doi.org/10.1126/science.aan5980.

[138] T. Gottschall, A. Gràcia-Condal, M. Fries, A. Taubel, L. Pfeuffer, L. Mañosa, A. Planes, K.P. Skokov, O. Gutfleisch, A multicaloric cooling cycle that exploits thermal hysteresis, Nat. Mater. 17 (2018) 929–934. https://doi.org/10.1038/s41563-018-0166-6.

[139] J. Ding, W. Zhao, W. Jin, C. Di, D. Zhu, Advanced Thermoelectric Materials for Flexible Cooling Application, Adv. Funct. Mater. 31 (2021) 2010695. https://doi.org/https://doi.org/10.1002/adfm.202010695.

[140] W. Sun, W.-D. Liu, Q. Liu, Z.-G. Chen, Advances in thermoelectric devices for localized cooling, Chem. Eng. J. 450 (2022) 138389. https://doi.org/https://doi.org/10.1016/j.cej.2022.138389.

[141] W.-Y. Chen, X.-L. Shi, J. Zou, Z.-G. Chen, Thermoelectric Coolers: Progress, Challenges, and Opportunities, Small Methods 6 (2022) 2101235. https://doi.org/https://doi.org/10.1002/smtd.202101235.

[142] Z. Lu, H. Zhang, C. Mao, C.M. Li, Silk fabric-based wearable thermoelectric generator for energy harvesting from the human body, Appl. Energy 164 (2016) 57–63. https://doi.org/https://doi.org/10.1016/j.apenergy.2015.11.038.

[143] D. Madan, Z. Wang, P.K. Wright, J.W. Evans, Printed flexible thermoelectric generators for use on low levels of waste heat, Appl. Energy 156 (2015) 587–592. https://doi.org/https://doi.org/10.1016/j.apenergy.2015.07.066.

[144] V. Leonov, Thermoelectric Energy Harvesting of Human Body Heat for Wearable Sensors, IEEE Sens. J. 13 (2013) 2284–2291. https://doi.org/10.1109/JSEN.2013.2252526.

[145] S. Hong, Y. Gu, J.K. Seo, J. Wang, P. Liu, Y.S. Meng, S. Xu, R. Chen, Wearable thermoelectrics for personalized thermoregulation, Sci. Adv. 5 (2024) eaaw0536. https://doi.org/10.1126/sciadv.aaw0536.

[146] D. Fiala, K.J. Lomas, M. Stohrer, A computer model of human thermoregulation for a wide range of environmental conditions: the passive system, J. Appl. Physiol. 87 (1999) 1957–1972. https://doi.org/10.1152/jappl.1999.87.5.1957.

[147] Y. Ke, F. Wang, P. Xu, B. Yang, On the use of a novel nanoporous polyethylene (nanoPE) passive cooling material for personal thermal comfort management under uniform indoor environments, Build. Environ. 145 (2018) 85–95. https://doi.org/https://doi.org/10.1016/j.buildenv.2018.09.021.

[148] Y. Li, H. Zhu, Y. Wang, U. Ray, S. Zhu, J. Dai, C. Chen, K. Fu, S.-H. Jang, D. Henderson, T. Li, L. Hu, Cellulose-Nanofiber-Enabled 3D Printing of a Carbon-Nanotube

Microfiber Network, Small Methods 1 (2017) 1700222. https://doi.org/https://doi.org/10.1002/smtd.201700222.

[149] Y. Guo, C. Dun, J. Xu, J. Mu, P. Li, L. Gu, C. Hou, C.A. Hewitt, Q. Zhang, Y. Li, D.L. Carroll, H. Wang, Ultrathin, Washable, and Large-Area Graphene Papers for Personal Thermal Management, Small 13 (2017) 1702645. https://doi.org/https://doi.org/10.1002/smll.201702645.

[150] J. Huang, Y. Li, Z. Xu, W. Li, B. Xu, H. Meng, X. Liu, W. Guo, An integrated smart heating control system based on sandwich-structural textiles, Nanotechnology 30 (2019) 325203. https://doi.org/10.1088/1361-6528/ab15e8.

[151] P. Won, J.J. Park, T. Lee, I. Ha, S. Han, M. Choi, J. Lee, S. Hong, K.-J. Cho, S.H. Ko, Stretchable and Transparent Kirigami Conductor of Nanowire Percolation Network for Electronic Skin Applications, Nano Lett. 19 (2019) 6087–6096. https://doi.org/10.1021/acs.nanolett.9b02014.

[152] D. Hao, B. Xu, Z. Cai, Polypyrrole coated knitted fabric for robust wearable sensor and heater, J. Mater. Sci. Mater. Electron. 29 (2018) 9218–9226. https://doi.org/10.1007/s10854-018-8950-2.

[153] X. Yue, T. Zhang, D. Yang, F. Qiu, G. Wei, H. Zhou, Multifunctional Janus fibrous hybrid membranes with sandwich structure for on-demand personal thermal management, Nano Energy 63 (2019) 103808. https://doi.org/https://doi.org/10.1016/j.nanoen.2019.06.004.

[154] K. Li, T.-H. Chang, Z. Li, H. Yang, F. Fu, T. Li, J.S. Ho, P.-Y. Chen, Biomimetic MXene

Textures with Enhanced Light-to-Heat Conversion for Solar Steam Generation and Wearable Thermal Management, Adv. Energy Mater. 9 (2019) 1901687. https://doi.org/https://doi.org/10.1002/aenm.201901687.

[155] W.S. Suen, G. Huang, Z. Kang, Y. Gu, J. Fan, D. Shou, Development of wearable air-conditioned mask for personal thermal management, Build. Environ. 205 (2021) 108236. https://doi.org/https://doi.org/10.1016/j.buildenv.2021.108236.

[156] S. Yousefi, A. Jamekhorshid, S. Tahmasebi, S.M. Sadrameli, Experimental and numerical performance evaluation of a cooling vest subtending phase change material under the extremely hot and humid environment, Therm. Sci. Eng. Prog. 26 (2021) 101103. https://doi.org/https://doi.org/10.1016/j.tsep.2021.101103.

[157] G. Bartkowiak, A. Dabrowska, A. Marszalek, Assessment of an active liquid cooling garment intended for use in a hot environment, Appl. Ergon. 58 (2017) 182–189. https://doi.org/https://doi.org/10.1016/j.apergo.2016.06.009.

[158] C.C.W.G. Bongers, M.T.E. Hopman, T.M.H. Eijsvogels, Cooling interventions for athletes: An overview of effectiveness, physiological mechanisms, and practical considerations, Temperature 4 (2017) 60–78. https://doi.org/10.1080/23328940.2016.1277003.

[159] G. Dingle, C. Mallen, Sport and environmental sustainability, New YorN (2020).

[160] C. Multiphysics, Heat Transfer Module, © 1998–2018 Comsol (2015) 1–222.

[161] H. Morris, R. Murray, Medical textiles, Text. Prog. 52 (2020) 1–127. https://doi.org/10.1080/00405167.2020.1824468.

[162] V. Ramachandran, F. Schilling, A.R. Wu, D. Floreano, Smart Textiles that Teach: Fabric-Based Haptic Device Improves the Rate of Motor Learning, Adv. Intell. Syst. 3 (2021) 2100043. https://doi.org/https://doi.org/10.1002/aisy.202100043.

[163] P. Weiss, M.P. Mohamed, T. Gobert, Y. Chouard, N. Singh, T. Chalal, S. Schmied, M. Schweins, T. Stegmaier, G.T. Gresser, G. Groemer, N. Sejkora, S. Das, R. Rampini, M. Hołyńska, Advanced Materials for Future Lunar Extravehicular Activity Space Suit, Adv. Mater. Technol. 5 (2020) 2000028. https://doi.org/https://doi.org/10.1002/admt.202000028.

[164] COMSOL AB, CFD Module User ’s Guide, COMSOL Multiphysics (2016) 598.

[165] J. Li, Q. Ma, A.H.S. Chan, S.S. Man, Health monitoring through wearable technologies for older adults: Smart wearables acceptance model, Appl. Ergon. 75 (2019) 162–169. https://doi.org/https://doi.org/10.1016/j.apergo.2018.10.006.

[166] H. Kim, Y.-T. Kwon, H.-R. Lim, J.-H. Kim, Y.-S. Kim, W.-H. Yeo, Recent Advances in Wearable Sensors and Integrated Functional Devices for Virtual and Augmented Reality Applications, Adv. Funct. Mater. 31 (2021) 2005692. https://doi.org/https://doi.org/10.1002/adfm.202005692.

[167] S.N. Joshi, Y.S. Gujarathi, A review on active and passive flow control techniques, Int. J. Recent Technol. Mech. Electr. Eng. 3 (2016) 1–6.

[168] M. Souri, A. Mojra, A nexus between active and passive control methods for reduction of aerodynamic noise of circular cylinder, Int. J. Mech. Sci. 200 (2021) 106446. https://doi.org/https://doi.org/10.1016/j.ijmecsci.2021.106446.

[169] O. Delabroy, E. Haile, F. Lacas, S. Candel, A. Pollard, A. Sobiesiak, H.A. Becker, Passive and active control of NOx in industrial burners, Exp. Therm. Fluid Sci. 16 (1998) 64–75. https://doi.org/https://doi.org/10.1016/S0894-1777(97)10013-9.

[170] M. Schäfer, S. Turek, F. Durst, E. Krause, R. Rannacher, Benchmark Computations of Laminar Flow Around a Cylinder BT - Flow Simulation with High-Performance Computers II: DFG Priority Research Programme Results 1993–1995, in: E.H. Hirschel (Ed.), Vieweg+Teubner Verlag, Wiesbaden, 1996: pp. 547–566. https://doi.org/10.1007/978-3-322-89849-4_39.

[171] B. Launder, S. Poncet, E. Serre, Laminar, transitional, and turbulent flows in rotor-stator cavities, Annu. Rev. Fluid Mech. 42 (2010) 229–248.

[172] T. a. Oliver, A High-Order , Adaptive , Discontinuous Galerkin Finite Element Method for the Reynolds-Averaged Navier-Stokes Equations, Massachusetts Institute of Technology, 2008.

[173] F.R. Menter, Two-equation eddy-viscosity turbulence models for engineering applications, AIAA J. 32 (1994) 1598–1605. https://doi.org/10.2514/3.12149.

[174] M.M. Zdravkovich, P.W. Bearman, Flow around circular cylinders—Volume 1: Fundamentals, (1998).

[175] C. Yang, M.Y. Yao, L. LI, Development of a flexible wearable thermal textile accessory for winter sports, Text. Res. J. 91 (2021) 2707–2723. https://doi.org/10.1177/00405175211001803.

[176] R. Bahru, A.A. Hamzah, M.A. Mohamed, Thermal management of wearable and

implantable electronic healthcare devices: Perspective and measurement approach, Int. J. Energy Res. 45 (2021) 1517–1534. https://doi.org/https://doi.org/10.1002/er.6031.

[177] G.B. Delkumburewatte, T. Dias, Wearable cooling system to manage heat in protective clothing, J. Text. Inst. 103 (2012) 483–489. https://doi.org/10.1080/00405000.2011.587647.

[178] C. Wang, W. Shi, X. Wang, X. Jiang, Y. Yang, W. Li, L. Zhou, Optimal design of multistage centrifugal pump based on the combined energy loss model and computational fluid dynamics, Appl. Energy 187 (2017) 10–26. https://doi.org/https://doi.org/10.1016/j.apenergy.2016.11.046.

[179] T. Schaefer, Fluid dynamics and viscosity in strongly correlated fluids, Annu. Rev. Nucl. Part. Sci. 64 (2014) 125–148.

[180] A. Leonard, Energy Cascade in Large-Eddy Simulations of Turbulent Fluid Flows, in: F.N. Frenkiel, R.E.B.T.-A. in G. Munn (Eds.), Turbul. Diffus. Environ. Pollut., Elsevier, 1975: pp. 237–248. https://doi.org/https://doi.org/10.1016/S0065-2687(08)60464-1.

[181] L. Ji, W. Li, W. Shi, H. Chang, Z. Yang, Energy characteristics of mixed-flow pump under different tip clearances based on entropy production analysis, Energy 199 (2020) 117447. https://doi.org/https://doi.org/10.1016/j.energy.2020.117447.

[182] S. Wilhelm, G. Balarac, O. Métais, C. Ségoufin, Analysis of Head Losses in a Turbine Draft Tube by Means of 3D Unsteady Simulations, Flow, Turbul. Combust. 97 (2016) 1255–1280. https://doi.org/10.1007/s10494-016-9767-9.

[183] G. Lu, Z. Zuo, D. Liu, S. Liu, Energy balance and local unsteady loss analysis of flows

in a low specific speed model pump-turbine in the positive slope region on the pump performance curve, Energies 12 (2019). https://doi.org/10.3390/en12101829.

[184] X. Luo, W. Ye, R. Huang, Y. Wang, T. Du, C. Huang, Numerical investigations of the energy performance and pressure fluctuations for a waterjet pump in a non-uniform inflow, Renew. Energy 153 (2020) 1042–1052. https://doi.org/10.1016/j.renene.2020.02.081.

[185] M. Everts, Heat transfer and pressure drop of developing flow in smooth tubes in the transitional flow regime, (2015).